**CZECH TECHNICAL UNIVERSITY IN PRAGUE**

Faculty of Biomedical Engineering

Department of Natural Sciences

# Essential elements towards the development of diamond-based biosensors for bacteria detection in water

Doctoral thesis

**Ing. Lucie Dubovská**

Kladno, October 2023

Ph.D. Programme: Biomedical and Clinical Technology

**Supervisor: Dr. Vincent Mortet, Ph.D.**

**Supervisor-Specialist: Prof. Abdelkrim Talbi, Ph.D.**

**Thesis supervisor:**

Dr. Vincent Mortet, Ph.D.

Institute of Physics, CAS
Na Slovance 1999/2
Prague 8, 182 00
Czech Republic

**Thesis supervisor-specialist:**

Prof. Abdelkrim Talbi, Ph.D.

Institute of Electronics, Microelectronics and Nanotechnology
Centrale Lille
Cité Scientifique
Avenue Henri Poincaré
CS 60069
59 652 Villeneueve d'Ascq Cedex
France

# Abstract

Detection of pathogenic bacteria is an inherent part of environmental and industrial safety. In spite of good selectivity of conventional methods, they are time-consuming and labor-intensive. Biosensors are good candidates for real-time monitoring and fast detection of pathogenic agents.

The first part of this Thesis resumes the state of the art of whole cell bacteria detection including conventional and biosensor methods. We summarize recent developments in biosensing technologies for bacteria detection in aqueous solutions and food matrices based on different transduction methods (optical, electrochemical and acoustic). Their advantages and disadvantages are discussed and compared.

In the second part, studies towards the development of the proposed biosensor: diamond coated Love wave surface acoustic wave sensor as a transducer and Escherichia coli binding proteins as a bioreceptor, are presented. Theoretical simulations of LW-SAW sensors are carried out for three different piezoelectric substrates – ST-cut quartz, 36°YX $LiNbO_3$ and 36°YX $LiTaO_3$, that can support the propagation of shear waves. Phase velocity $v_p$ and electromechanical coupling coefficient $K^2$ dispersion curves were simulated and $v_p$ was compared to experimental results for the diamond/$SiO_2$/ST-cut quartz and diamond/$SiO_2$/36°YX $LiTaO_3$ structures. Experimental results have shown disagreement with the theoretical ones which is attributed to the different mechanical properties used in simulations and real samples.

Two different approaches of sensitivity enhancement were studied - experimental deposition of diamond grains on LW-SAW sensors instead of continuous layer and simulation study of use of diamond phononic metamaterials on surface of LW-SAW sensors. A short simulation chapter is dedicated also to the use of diamond and silicon carbide layers as a passivation layer for package less sensors and the usability of both materials were confirmed.

*E.coli* binding his-tagged proteins gp17, gp12 and ORF26 were successfully produced and purified. Immunofluorescent assays confirmed that ORF26 and gp17 bind specifically to the *E.coli* cells, gp12 showed binding also to the *Salmonella* cells. Two different approaches of attachment of these proteins to the boron doped diamond surface has been successfully developed: 1/ direct electrodeposition of nickel nanoparticles and 2/ electrochemical grafting followed by EDC/NHS chemistry for attachment of NTA acid that

chelates nickel ions. Further experiments must be carried out to confirm bacteria binding on biosensors. The last part is devoted to the study of boron doped diamond coated QCM sensors for the biosensing applications. We successfully deposited BDD layers on the QCM crystals, but the functionalization of the layers followed by attachment of the bacteria was not successfully finished so far and it needs further attention and development.

Even though the work did not lead to the development of the working diamond-based biosensors, it laid important building stones. Sensitivity of diamond-coated LW-SAW sensors is not reduced that much as was expected from the theoretical simulations, as the Young modulus of thin CVD diamond layer grown at low temperature is much lower than for the bulk diamond. The his-tagged tail fibers were successfully produced and two different protocols for their attachment to the boron doped diamond layers were developed. Also the deposition of low temperature BDD layers on QCMs sensors were successfully achieved. Results of this Thesis are promising for development of biosensors with dual-read out system - coupled electrochemical and acoustic detection.

**Keywords:**

Surface acoustic waves, Love-waves, Bacteria detection, Biosensing, CVD diamond, BDD diamond, His-tagged protein, Bioreceptor

# Abstrakt

Detekce patogenních bakterií je nedílnou součástí environemtální a průmyslové bezpečnosti. Navzdory dobré selektivitě, jsou konvenční metody časově náročné a vyžadují specializovaný personál a laboratorní vybavení. Biosenzory jsou dobrými kandidáty pro monitorování v reálném čase a rychlou detekci patogenních agens.

První část této práce shrnuje současný stav detekce celých bakteriálních buněk včetně konvenčních metod a biosenzorů. Je shrnut nejnovější vývoj v technologiích biosenzorů pro detekci bakterií ve vodních roztocích a potravinových vzorcích založených na různých transdukčních metodách (optických, elektrochemických a akustických). Jsou také diskutovány jejich výhody a nevýhody a jednotlivé metody jsou porovnány.

Ve druhé části je věnována pozornost vývoji navrhovaného biosenzoru - diamantem pokrytý senzor s povrchovými Loveho akustickými vlnami (LW-SAW) jako převodník signálu a bakteriofágové proteiny vázající se na buňky *E. coli* jako bioreceptor. Teoretické simulace LW-SAW senzorů byli provedeny pro tři různé piezoelektrické substráty - křemen (ST-řez), tantalát litný a niobát litný, které podporují šíření horizontálních vln. Byli provedeny simulace disperzních křivek fázové rychlosti a elektromechanického vazebního koeficientu a fázová rychlost byla porovnána s experimentálními výsledky pro diamantem pokryté senzory z křemene a tantalátu litného s oxidem křemičitým jako vedoucí vrstvou. Experimentální výsledky se neshodují s teoretickými, což je výsledkem rozdílných mechanických vlastností materiálů použitých v simulacích a reálných vzorcích.

Dva různé způsoby zvýšení citlivosti navrhovaných biosenzorů byly studovány - experimentální depozice diamantových zrn na LW-SAW senzory místo spojité vrstvy a simulace použití diamantových fononových metamateriálů na povrchu LW-SAW senzorů. Krátká kapitola je také věnována použití vrstvy diamantu a karbidu křemíku jako pasivační vrstvy pro senzory bez nutnosti ochranného obalu, kdy byla potvrzena použitelnost obou materiálů.

Byli úspěšně vyrobeny proteiny s his-tag značkou gp17, gp12 a ORF26 vázající bakteriální buňky *E.coli*. Imunofluorescenční test potvrdil, že ORF26 a gp17 se specificky vážou na bakterie *E.coli*, zatímco protein gp12 se vázal i na buňky bakterie *Salmonella*. Dva různé přístupy navázání těchto proteinů s his-tag značkou na bórem dotované diamantové vrstvy byli úspěšně vyvinuty: 1/ přímá elektrodepozice nikelnatých nanočástic a 2/ elektrochemická funkcionalizace následovaná chemií EDC/NHS pro navázání kyseliny NTA,

která chelatuje ionty niklu. Pro potvrzení úspěšného navázání bakterií na funkcionalizované vrstvy musí být provedeny další experimenty. Poslední část je věnována studiu QCM senzorů s borem dotovanými diamantovými vrstvami pro biosenzorické aplikace. BDD vrstvy byli úspěšně nadeponované na QCM krystaly, ale funkcionalizace vrstev s následným přichycením bakteriálních buněk nebyla dosud úspěšně dokončena a vyžaduje další pozornost a vývoj.

Přestože tato práce nevedla k vývoji fungujících biosenzorů na bázi diamantů, položila důležité stavební kameny. Citlivost LW-SAW senzorů s diamantovým povlakem není snížena natolik, jak se očekávalo z teoretických simulací, protože Youngův modul tenké CVD diamantové vrstvy je mnohem nižší než u objemového diamantu. His-tagované proteiny byly úspěšně vyrobeny a byly vyvinuty dva různé protokoly pro jejich připojení k borem dotovaným diamantovým vrstvám. Úspěšně bylo také dosaženo depozice nízkoteplotních BDD vrstev na senzory QCM. Výsledky této práce jsou slibné pro vývoj biosenzorů s duálním odečítacím systémem - spřaženou elektrochemickou a akustickou detekcí.

**Klíčová slova:**

Povrchové akustické vlny, Loveho vlny, Detekce bakterií, Biosenzory, CVD diamant, Borem dotovaný diamant, Proteiny s his-tag značkou, Bioreceptor

# Acknowledgements

This Thesis is the result of my doctoral studies at the Faculty of Biomedical Engineering at Czech Technical University in Prague and the experimental work has been carried out at the Institute of Physics, Czech Academy of Sciences within the group Materials for Nanosystems and Biointerfaces under the leadership of Dr. Vincent Mortet, Ph.D. This work would not be possible without the guidance, help and support of many colleagues and friends. I would like to take this opportunity to express my gratitude to all of them.

My greatest thanks belongs to my supervisor Vincent Mortet for his guidance, patience and willingness. He always tried to support me and gave his opinion and advice when I encountered any problem during my doctoral journey. He helped me not only with the problems related to my research topic, but also gave me insight into the science related topics and skills, such as articles and grants writing or preparation of the conference papers. This endeavor would not have been possible without the help of my colleagues from the Materials and Nanosystems and Biointerfaces research groups. They were there always for me with valuable advice, when I needed help in the lab or for the scientific discussion. My special thanks belongs to the Andrew Taylor and Petr Ashcheulov for the diamond layers depositions and Simona Baluchová for her incredible help with electrochemical experiments.

I would like to express my gratitude to my co-supervisor Abdelkrim Talbi for sharing his knowledge on acoustic sensors modelling with me and his valuable advice. My thanks also belong to his colleagues from the Institute of Electronics, Microelectronics and Nanotechnology, Lille, France who guided me during my six months (within Erasmus+ program) stay there. My thanks belongs to Yuxin Liu for her patience and advice when explaining me the basics of acoustic modelling in COMSOL Multiphysics software.

I am very grateful to Mark J Van Raaij from the National Center for Biotechnology, Madrid, Spain, for his heartwarming welcome into his research group for my six months stay. Many thanks belongs to Mara Laguna Castro and Mateo Seoane Blanco for their patience and all the help when teaching me how to produce and purify the proteins. I really appreciate this opportunity to gain insight into another research field. Proteins produced within this group were integral part to achieve goals of this Thesis. This stay was supported by the IoP researchers mobility project with the registration number CZ.02.2.69/0.0/0.0/16_027/0008215.

My special thanks belongs to all of the people, that make this Thesis possible, such as Zbyněk Šobáň and Jiří Bulíř (IoP) for different layers depositions, Ladislav Fekete (IoP) for AFM measurements, Ladislav Klimša (IoP) for SEM measurements, Martin Kempa and Viktor Bovtun (IoP) that provided me the access to their Network Analyzer, so I could do all of the frequency characterization of SAW sensors. I am also grateful to Imrich Gablech (CEITEC) for SAW sensors fabrication, Petr Novák (University of West Bohemia) for ZnO layers deposition, Mariia Uzhytchak (IoP) for her willingness and help with preparation of proteins at Institute of Physics. My great gratitude goes also to Marek Cebecauer from J. Heyrovský Institute of Physical Chemistry for his willingness and access to his lab to perform the experiments with bacterial cells.

Thanks should also go to my friends and colleagues from FBME, CTU, Kateřina Žambochová and Tomáš Parkman, for all of their mental support during the whole doctoral studies.

Last but not least thanks belongs to my husband Jakub and daughter Anna, parents, siblings and parents-in-law, for their love, patience, understanding and everlasting support. Without them, completing this Thesis, would simply not have been possible.

This work was financially supported by projects of Grant Agency of the Czech republic 13-31783S2013, 17-15319S, 19-09784Y and 20-03187S, from Technology Agency of the Czech Republic project TH2030874 and ADE2-TG02010056, project from Ministry of Insdustry and Trade FV10312, and by my two CTU students grants competition SGS20/084/OHK4/1T/17 and SGS21/082/OHK4/1T/17.

**Declaration**

Hereby I declare, that this thesis entitled "Essential elements towards the development of diamond-based biosensors for bacteria detection in water" has been written by me in its entirety as the result of my own original research. I have acknowledged all the sources of information which have been used in the Thesis in compliance with the Methodological Instruction No. 1/2009 - On maintaining ethical principles when working on a university final project.

Prohlašuji, že jsem tuto Doktorskou práci vypracovala samostatně na základě vlastního výzkumu a že jsem uvedla veškeré použité informační zdroje v souladu s Metodickým pokynem č. 1/2009 o dodržování etických principů při přípravě vysokoškolských závěrečných prací.

| | |
|---|---|
| ..... | ..... |
| Prague (date) | author's signature |

# List of Figures

# List of Tables

# Contents

# Motivation

Detection and identification of pathogens is an important goal in food safety, medicine, public health or national security. Rapid detection of pathogens in medical samples can mean the difference between life and death of patients. Pathogen detection in food, water or air samples is an important part to maintain public health [1, 2]. It is estimated, that about 15 % of total mortality in the world is caused by infectious diseases. It became even bigger problem with change of the modern lifestyle, when the spread of the disease around the world is accelerated [3]. Bioterrorism is also huge concern, as food and water can be an excellent carrier of the pathogenic bacteria [4]. Each of us has experienced the need for fast, inexpensive and selective pathogen detection method, when we came through the global pandemic of the disease COVID-19 in recent years and this pandemic paralyzed the world and greatly affected our lives.

Water-borne diseases are caused mainly by viruses, fungi, bacteria and protozoan parasites [5]. *Escherichia coli, Salmonella typhimurium, Campylobacter jejuni, Legionella pneumonia* or *Staphylococcus aureus* are few bacteria strains, that can cause serious health problems. Among them, *E. coli* is reported to cause large scale life loss [6]. *E. coli* O157:H7 strains produce Shiga toxins, that can cause stomach pain, diarrhea, inflammation or even extreme instances like hemorrhagic enteritis and hemolysis, mainly found in babies and young children. Quality water monitoring is based on the testing of presence of *E.coli* cells, as it is still the best indicator of fecal contamination. According to WHO, water is considered as intermediate risk, when it contains only 10 to 100 viable *E.coli* cells per ml [7].

A detection method for water quality monitoring should be quick, sensitive, selective and ideally real-time. As conventional detection methods are time-consuming and labor intensive, researchers are focusing on the development of biosensing methods. In general, biosensors should be inexpensive, easy to operate, label-free with minimal sample

processing, selective with the ability to distinguish between bacterial serotypes. The key requirement for close-to-real-time monitoring is the stability of the bioreceptor [1, 6].

In this Thesis, we propose the use of Love wave-SAW biosensor with integrated CVD diamond layer as an interface for the attachment of bacteriophage tail fibers as bioreceptor for the bacteria detection in water. LW-SAW sensors can monitor cells behavior in liquids in the simple and non-invasive way with avoiding contact of the liquid with electrodes, and they are a promising probing method in biology and biomedical research. The proposed structure should also fulfill the requirements stated above. Acoustic wave devices are easy to fabricate and the use of Love waves allows sensing in liquids. Additionally, LW-SAW sensors possess the highest sensitivity among acoustic sensors [8]. Diamond has advantageous good chemical inertness together with multiple various surface functionalization possibilities. Reported prolonged stability of attached biomolecules is important to ensure close-to-real-time monitoring [9–11]. The specificity of the sensor is addressed by the functionalization of the diamond surface using bacteriophage tail fibers.

This Thesis is divided into four main chapters. The first chapter is theoretical and reviews the state of the art of whole cell bacteria detection, including the biosensor with bacteriophages or bacteriophage tail fibers as bioreceptor, then the acoustic-wave sensors are discussed with focus onto Love-wave acoustic devices. The last subchapter is devoted to diamond, its properties, synthesis and use in the biosensing technology.

Chapter 2 establishes the Thesis objectives.

Chapter 3 presents the main methods used within this Thesis. It describes models in COMSOL Multiphysics software used for FEM simulations, SAW devices fabrication and characterization and diamond layers deposition and characterizations.

Chapter 4 resumes the experimental results of presented thesis. It consists of eight different subchapters and each of them is devoted to the different topic. Subchapter 1 describes FEM simulations of LW-SAW devices properties after diamond coating, subchapter 2 gives experimental details on LW-SAW devices with continuous and discrete diamond coating. Subchapter 3 provides FEM simulations focused on enhancing the sensitivity of LW-SAW devices by using the diamond phononic metamaterials. Subchapter 4 is a shorter chapter giving the FEM simulations on use of diamond and silicon carbide layer as passivation layer for LW-SAW sensing technology. Subchapter 5 gives the ex-

perimental results on the behavior of diamond-coated LW-SAW sensors fabricated with different piezoelectric substrates and guiding layer materials. Subchapter 6 describes the fabrication of our bioreceptor - bacteriophage tail fibers. Subchapter 7 focuses on functionalization of diamond surface via attachment of produced bacteriophage tail fibers from previous chapter. The last subchapter 8 is devoted to the fabrication of boron doped diamond-coated QCM sensors for the biosensing applications.

Chapter 5 resumes the conclusions of this work and provides guidelines for future development.

# 1 Introduction and state of the art

## 1.1 State of the art of bacteria detection

To date, there are a plethora of reports on biosensors for pathogen detection. This review focuses on detection of whole-cell pathogenic bacteria in liquid environments. After a brief description of bacteria and conventional methods of their detection, we review the main biosensor's transduction methods including optical, electrochemical and acoustic ones. The last subchapter focuses on the use of bacteriophages and their tail fibers as a biorecognition element.

### 1.1.1 Bacteria

Bacteria are ubiquitous microorganisms which are present in air, soil, water, as well as on the human skin and in the gastrointestinal tract. Despite the fact, that the majority of them are not pathogenic, but harmless and useful [12], they are the major cause of infectious diseases [13].

Bacteria are single-cell prokaryotic organisms. The chromosomal apparatus is not separated from the cytoplasm by the membrane and consists of a circular double-stranded deoxyribonucleic acid (dsDNA). This chromosomal DNA contains information that is necessary for the cell life. The bacterial cell may also contain another type of dsDNA – plasmids. They can carry the important information, for example, for an antibiotic resistance. The surface of the bacterial cell is formed by the cell wall composed mainly of peptidoglycan (murein) [12, 14]. According to the amount of peptidoglycan (5 – 90 %) in the cell wall mass, we can distinguish between Gram−positive and Gram-negative bacteria. Gram−positive bacteria have more peptidoglycan, and their cell wall is much thicker and more robust than at Gram−negative bacteria [13, 15].

The bacterium *Escherichia coli* is used as a model organism in this study. It belongs to

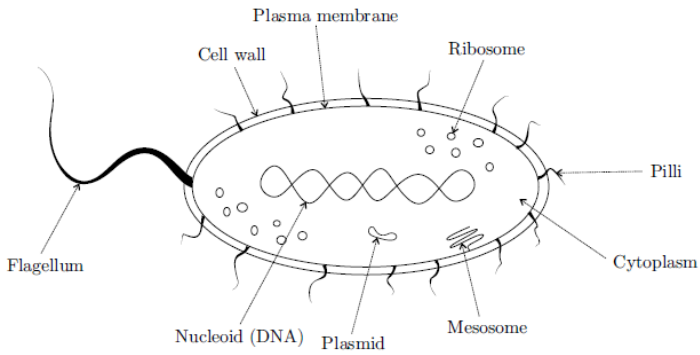


Figure 1.1: Schematic of the prokaryotic cell [13]

the large family of gram-negative bacteria called Enterobacteriaceae. Most of the *E. coli* strains are non-pathogenic and they are common commensals of the human intestine. However, some of the *E. coli* strains are pluripotent pathogens that can cause various diseases, such as diarrhea, the hemolytic-uremic syndrome or dysentery. They are also a major cause of the nosocomial infections [13, 16].

### 1.1.2 Conventional methods of bacteria detection

The detection and identification of bacteria have been traditionally performed by conventional microbiological techniques, namely, optical microscopy and cell culture, immunological tests, biochemical assays and genetic analysis. Microscopy involves staining of bacteria followed by observation of staining pattern and its morphology. This technique is relatively quick, but not very specific [1]. Culture methods are based on the growing ability of bacteria on selective culture media. Although these methods provide reliable results, they can take several days up to weeks [17]. The enzyme-linked immunosorbent assay (ELISA) is a widely accepted immunological test. It is based on the interaction of the targeted molecule with primary antibody followed by the addition of secondary antibody to form a "sandwich." The development is done by reaction of the chromogenic substrate with an enzyme linked to the secondary antibody [18]. Genetic analysis, such as polymerase chain reaction (PCR), is an extremely sensitive technique based on the identification of bacterial genetic material. Targeted bacterial sequences are paired with the preselected genetic probe. Despite its selectivity, it is still a time-consuming and expensive procedure. Real-time PCR analysis can be completed within several hours but requires expensive equipment and reagents [1]. All these mentioned techniques are time-consuming

and require sample preparation, particular reagents, skilled personnel and therefore are expensive [1, 2].

Nowadays, there is an urgent demand for the cost-effective, efficient, rapid and sensitive analytical techniques to detect pathogens [1,5]. Sensitivity and selectivity are key features for detection of water-born pathogens, as the presence of even single pathogenic bacteria may cause an infection [5].

### 1.1.3 Biosensors for whole bacterial cell detection

Biosensors are devices comprising biorecognition element coupled with a signal transducer. The transducer converts the biological event into measurable electrical, optical or mechanical signal. Most common biorecognition elements are enzymes, antibodies, aptamers, oligonucleotide probes, cell-surface molecules and phages, but any molecule which recognize or attach bacteria can be used as a bioreceptor [1, 2, 5, 9]. In general, biosensors should be inexpensive, easy to operate, small and label-free [1]. Key requirements for bacterial biosensors are given in Table 1.1. The important unit in microbiology is colony forming unit per milliliter (CFU/ml), that is used to estimate the number of viable bacteria cells in a sample.

Table 1.1: Requirements for an ideal bacterial biosensor [1, 6]

| **Parameter** | **Value or quality** |
|---|---|
| Sensitivity | Better than $10^3$ CFU/ml |
| Assay time | 5 - 10 min for a single test |
| Sample processing | Label-free with minimal sample processing, no reagent addition needed |
| Specificity | Ability to distinguish different serotypes of bacteria in the presence of other microorganism or cells |
| Size | Compact, hand-held, portable, design for field use |
| Stability | Biorecognition element must be stable at temperatures up to 45 °C for several months |
| Viable cell count | Should discriminate between live and dead cells |
| Skill of operator | No specialist training needed |

Two main classes of biosensors have been developed for bacteria detection: 1) biosensors based on detection of bacteria's DNA, RNA or intracellular proteins, and 2) biosensors

targeting whole bacteria cells. The main disadvantage of the first type is that they require sample preparation to achieve bacterial lysis to liberate targeted bacterial components, which is time-consuming and increase costs [1, 2, 5, 19]. The following review focuses on the detection of whole bacteria cells.

### Optical biosensors

In optical biosensors, a change in optical properties is detected, e.g., absorption, emission, refractive index variations, upon binding of the bacteria. The most common types of optical biosensors are based on surface plasmon resonance (SPR), evanescent field sensing via functionalized optical fiber, fluorescence, chemiluminescence or colorimetry. Optical biosensors are often divided into two categories – labeled and label-free biosensors [1,5,17].

SPR is an optical technique which uses plane-polarized light propagating through a glass prism at a fixed (resonant) angle. The light excites surface plasmon waves at the deposited thin noble metal layer. This metal layer is functionalized by bioreceptors. When target biomolecule is trapped by bioreceptors, variation in refractive index occurs. It is determined as a change of the resonance angle of the surface plasmon [1, 5, 20], see Figure 1.2. However, detection of live bacteria by SPR technique yields lower sensitivity caused by limited penetration of bacteria by the electromagnetic field and low difference between refractive index of bacteria cytoplasm and aqueous solution [21]. Another disadvantage is the need for relatively large equipment [22]. Enhancement of the sensitivity can be achieved by localized surface plasmon resonance by using noble metal nanoparticles [23].

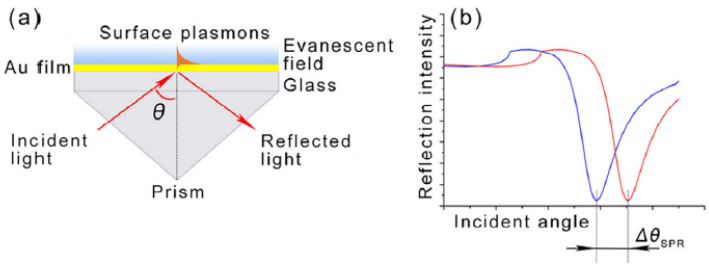


Figure 1.2: Principle of SPR sensor, a) a simplified diagram of Kretschmann configuration for SPR sensor, b) change in SPR angle caused by variation of refractive index [24]

Another type of optical biosensors is using the evanescent field. This electromagnetic field is generated at the interface fiber/sample by propagation of light within a core-only high-index ($n_{fiber} > n_{sample}$) optical fiber by total internal reflection. Evanescent field decays exponentially with the distance from the interface and can excite, e.g., fluores-

cence in fluorescently-labeled biomolecules attached to the fiber surface [5], see Figure 1.3. Colorimetric sensors are attractive optical sensors because it is possible to observe the presence of pathogenic bacteria in the sample through a color change by the naked eye. Their major disadvantage is low sensitivity, that can be enhanced for example by pre-concentration of cells [22]. Fluorescence and chemiluminescence biosensors represent a powerful analytical technique with high sensitivity, easy read-out, and ease of operation. These technologies have evolved from typical immunoassays, where the target molecule is trapped by immobilized biorecognition element. A secondary reagent, such as a fluorescently labeled antibody, is captured to the target molecule and generate the optical signal. The main disadvantage is a requirement for sample labeling with the fluorescent reagent. It adds time and cost to the test [1].

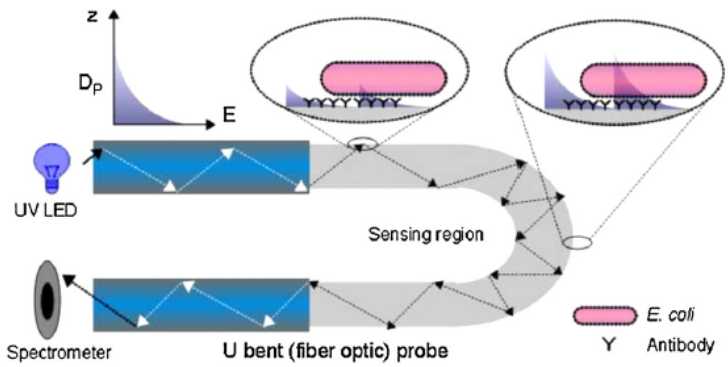


Figure 1.3: U-bent optical fiber for enhancement of penetration depth of evanescent field [25]

Table 1.2 shows examples of several studies carried out on optical sensors for whole bacteria detection. Sensitivity lower or equal to $10^3$ CFU/ml have been achieved using SPR, evanescent wave absorbance as well as fluorescence detection technique. Most of the studies were carried out in different liquid solution (NaCl, PBS buffer, LB media) containing only the bacteria strain to be detected. Few studies, such as [26] and [27], demonstrated the bacterial detection in the complex sample with the LOD equal or lower to $10^3$ CFU/ml. Vaisocherová et al. [26] reported detection time lower than 80 min without bacteria enrichment using gold nanoparticles to enhance SPR signal. Ohk et al. [27] reported the detection of three different pathogens in complex food samples within 24 hours, that is still a shorter time than the one needed using conventional methods.

Table 1.2: Examples of optical sensors for detection of whole bacterial cells

| **Target analyte** | **Transducer signal** | **Sensor assembly** | **Bioreceptor** | **LOD** (CFU/ml) | **Analyte** | **REF** |
|---|---|---|---|---|---|---|
| *E. coli* ATCC 25922 | SPR | Au-3-MPA-polymiyxin B modified SPR chip | Antibiotic Polymiyxin B | $1 \cdot 10^2$ | Bacteria in NaCl | [28] |
| *E. coli* O157:H7, *Salmonella* | SPR | SPR signal enhanced by streptavidin-coated gold nanoparticles | pCBAA, biotinylated secondary antibody | $7.4 \cdot 10^3$, $11.7 \cdot 10^3$ | Complex cucumber and hamburger samples | [26] |
| *E. coli* K12 | SPR | Functionalized gold SPR chip, gold nanoparticles functionalized SPR chip | goat polyclonal IgG anti-E. coli (ab13627) | $10^4$, $10^3$ | Bacteria in PBS buffer | [29] |
| *E. coli* O157:H7 | SPR | Sensor chip CM5 modified with carboxymethyl dextran | Lectin from Triticum vulgaris | $3 \cdot 10^3$ | Bacteria culture in Luria broth solution | [30] |
| *P. aeruginosa S. typhimurium* | SPR | Au-silica NP dielectric layer on a glass slide | aptamer | 30 CFU/assay | Bacteria culture | [31] |
| *E. coli* ATCC-35218 | Evanescent wave absorbance | U-bent optical fiber | Anti-*E. coli* monoclonal antibody | $10^3$ | Bacteria in buffer | [25] |
| *E. coli* O157:H7 | Fluorescence | Immune MNPs separation, immune QD visualization | Anti-*E. coli* monoclonal antibody | 14 | Bacteria in buffer | [32] |
| *Desulfovibrio alaskensis* | Evanescent wave absorbance | U-bent plastic optical fiber | Anti-SRB antibodies | $10^4$ MPN/ml | Bacteria in buffer | [33] |
| *Salmonella Typhimurium* | Mie light scattering | Immunoagglutination assay with polystyrene microparticles | Anti-*Salmonella* polyclonal antibody | 10 | Liquid from raw chicken | [34] |
| *Listeria monocytogenes*, *E. coli* O157:H7, *Salmonella enterica* | Fluorescence | Antibodies linked via streptavidin/biotin to the optical fiber | Polyclonal antibody for capture, Alexa-Fluor 647-labeled monoclonal antibodies to visualize | $10^3$ | Ready-to-eat beef, chicken and turkey meats | [27] |
| *Salmonella Typhimurium* | Colorimetric Fluorescent Magnetic | Magnetic separation and chromatography by antibody labeled $Fe_3O_4$ and quantum dots nanospehers | Mouse monoclonal antibody | $10^3$ | tap water, milk, FBS, whole blood | [35] |
| *E. coli* Dh5$\alpha$ | evanescent field sensing | dielectrophoretic cell-collecting with waveguide structure | label-free | $10^2$ | artifical urine | [36] |
| *E. coli* O157:H7 | Surface-enhanced Raman scattering | Core/shell of Au-Ag nanoparticles with two-layer Raman reporter molecules | monoclonal antibody | $7{\cdot}10^1$ | food matrices (milk, beef) | [37] |

### Electrochemical biosensors

Based on their operation mechanism, electrochemical sensors are classified into voltammetric, potentiometric, amperometric and impedance-based biosensors. Advantages of the electrochemical sensors are their fast response, possibility to operate in turbid solutions and possible miniaturization. However, the main difficulty to apply electrochemical biosensors for the detection of foodborne pathogens is the complexity of food samples [5, 38].

Amperometric/voltammetric sensors detect an analyte by determining the change in current or potential, that is caused by oxidation or reduction reactions in the electrochemical system. In amperometric sensors, the current is measured at the fixed potential. In voltammetric sensors, the current is measured when the applied potential is changed under controlled variations. Different voltammetric techniques have been used for analysis of environmental samples, such as cyclic voltammetry (CV), differential pulse voltammetry (DPV) or square wave voltammetry (Figure 1.4a) [5, 38]. Nowadays, amperometric sensors are commonly used for the detection of glucose limit in blood [1]. Potentiometric sensors measure the electrical potential between working and reference electrode in an electrochemical cell. Ideally, there should be no significant current flow between these electrodes. The potential difference is generated by the accumulation of the charge density at the surface of working electrode, that is usually ion-selective electrode (ISE), see (Figure 1.4b). The potential of the reference electrode is kept invariant during measurement. Within the impedance-based biosensors, an advanced technique known as electrochemical impedance spectroscopy (EIS) is often used for electrochemical measurements. Low voltage sinusoidal potentials are applied to the electrochemical system and the resulting current is measured as a function of excitation frequency (Figure 1.4c). Electrochemical parameters, such as charge transfer resistance, bulk solution resistance, double layer capacitance, can be obtained by fitting of obtained data into an equivalent circuit [5, 38].

All reported electrochemical sensors (see Table 1.3) have a limit of detection lower than $10^2$ CFU/ml, which makes them more sensitive than optical sensors. Most of these sensors are label-free, without the addition of a secondary antibody, which makes the detection time shorter and also their price lower.

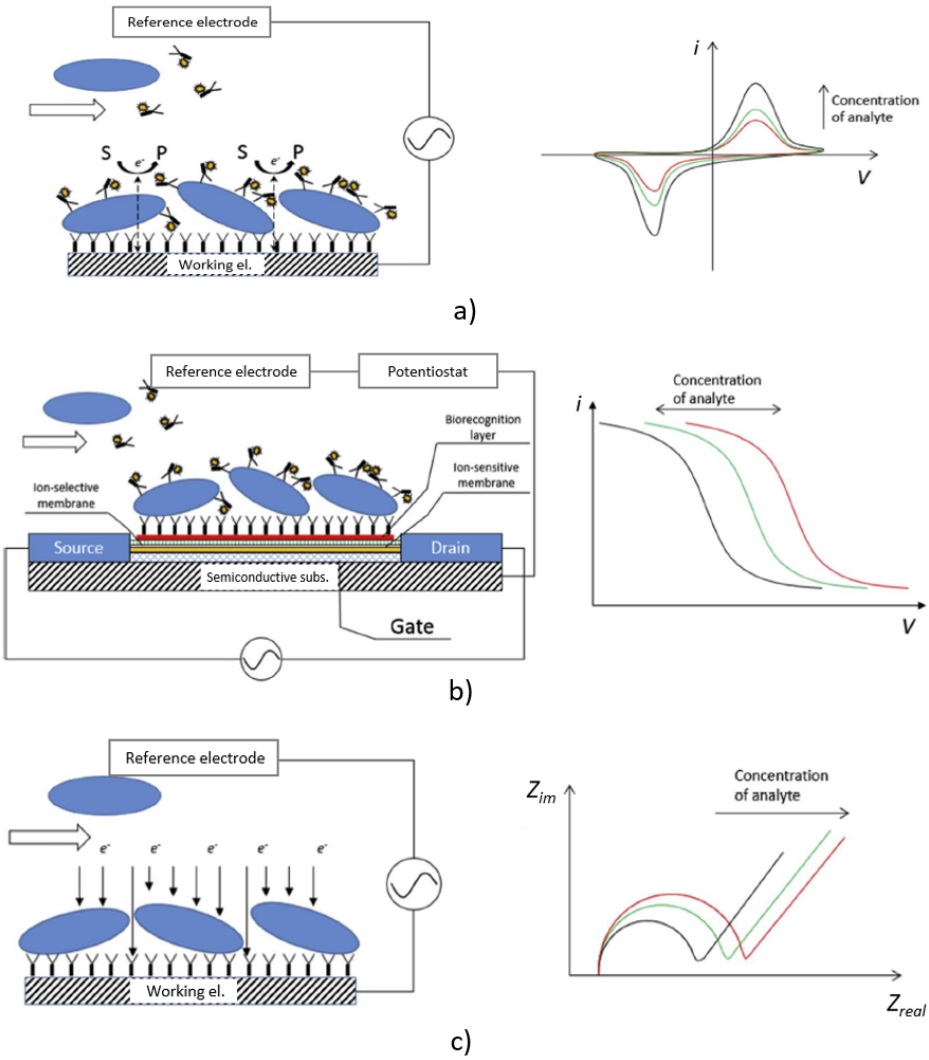


Figure 1.4: Schematic of electrochemical sensors: a) voltammetric sensor, b) ISFETs potentiometric biosensor, c) impedimetric sensor [38]

Table 1.3: Examples of electrochemical sensors for detection of whole bacterial cells

| **Target analyte** | **Transducer signal** | **Sensor assembly** | **Bioreceptor** | **LOD** (CFU/ml) | **Analyte** | **REF** |
|---|---|---|---|---|---|---|
| *E. coli* O157:H7 | EIS | The gold electrode coated by PANI/Glu/antibody | Monoclonal anti-*E. coli* antibody | $10^2$ | Bacteria in buffer | [39] |
| *E. coli* | Amperometric | An array of 8 Au electrodes | Polyclonal rabbit anti-*E.coli* antibody | 50 | Bacteria in water | [40] |
| *E. coli* O157:H7 | Impedance | MNPs for bacteria separation, gold NP with urease for hydrolysis | Polyclonal antibodies for separation, the aptamer to attach gold NP | 12 | Bacteria in a buffer or spiked milk | [41] |
| *Staphylococcus aureus* | Potentiometry | Single-walled carbon nanotubes | Anti-*S. aureus* aptamer | $8{\cdot}10^2$ | Contaminate pig skin | [42] |
| *Salmonella Typhimurium* | Impedance | Gold disk coated by poly[pyrrole-co-3-carboxyl-pyrrole] copolymer film | Aptamer | $10^2$ | Spiked apple juice | [43] |
| *Staphylococcus aureus* | Pulse voltammetry | single walled carbon nanotubes bioconjugates | Polyclonal rabbit anti-*S. aureus* antibody | 13 | spiked milk | [44] |
| *E.coli* K12 | pulse voltammetry and EIS | Sandwich assay of AuNPs on the surface of polypyrrole-reduced graphen oxide and ferrocene doped polypyrrole antibody-AuNPs | polyclonal antibodies | 10 | spiked water and milk | [45] |
| *E. coli* O157:H7 | amperometric | nickel oxide thin film matrix | mouse monoclonal antibody | 10 | milk samples | [46] |
| Bacterial culture from sewage sludge | EIS | carbon electrodes printed on hydrophobic paper | Concanavalin A | $1.9{\cdot}10^3$ | water | [47] |
| *Streptococcus Pneumoniae* | EIS | glassy carbon electrode with lead nanoparticles | DNA probe | 622 | - | [48] |

### Acoustic biosensors

Acoustic sensors are based on the perturbation of the acoustic waves by the attachment over their surface. Perturbation of the acoustic wave caused by the addition of mass to the surface results in a change of the operating frequency of the sensor. This change in the frequency can be measured with high precision [2, 5]. Acoustic devices are promising among the label-free sensors because of their ability to obtain pure mass and viscosity of the deposited layer [49]. Particular types of acoustic sensors are discussed more deeply in the section 1.2 Overview of Acoustic-Wave sensors.

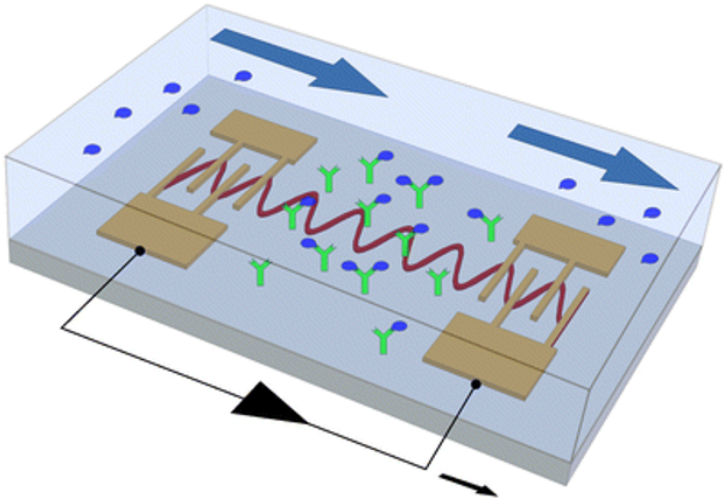

Figure 1.5: SAW biosensor. Analyte molecules present in a liquid bind to the immobilized antibodies on the sensor surface. The velocity of the SAW is influenced and hence the output signal is generated [50]

Table 1.4 presents examples of the few studies carried out on acoustic devices as biosensors. Acoustic devices can achieve sensitivity lower than $10^3$ CFU/ml. For both reported QCM sensors with a low limit of detection were used gold nanoparticles for signal enhancement. Salam et al. [51] proposed a QCM sensor, that is able to detect 10 CFU/ml within 12 minutes. Acoustic devices have not been studied as extensively as optical and electrochemical biosensors, however, they offer good sensitivity and fast detection times as well as simplicity of manufacturing.

Table 1.4: Examples of acoustic devices for whole cell bacteria detection

| **Target analyte** | **Transducer signal** | **Bioreceptor** | **LOD** (CFU/ml) | **Analyte** | **REF** |
|---|---|---|---|---|---|
| *E. coli*, *Legionella* | LW-SAW sensors from ST-cut quartz with a $SiO_2$ guiding layer | Antibodies | $10^5$ | Bacteria in PBS buffer | [52] |
| *E. coli* O157:H7 | QCM with immobilized antibody for capture and antibody-functionalized nanoparticles for signal enhancement | Antibodies | $10^6$ | Bacteria in buffer | [53] |
| *Salmonella Typhimurium* | QCM sensor with immobilized antibody, gold nanoparticles for signal enhancement | Monoclonal Antibodies | 10 | Bacteria spiked into meat samples | [51] |
| *Campylobacter jejuni* | QCM immunosensor sandwich assay with gold nanoparticles for signal enhancement | Rabbit polyclonal antibody | 150 | Bacteria in PBS buffer | [54] |
| *E. coli* | aluminium nitride based SAW sensor on recyclable polyethylene naphthalate | Protein A/polyclonal antibody | $6{\cdot}10^5$ | Bacteria in PBS buffer | [55] |
| *E. coli* | Ultra-high frequency electromagnetic piezoelectric acoustic sensor (AT-cut quartz QCM) | aptamer | 35 and 8 | PBS buffer or cow milk | [56] |
| *E. coli* | ZnO/GaAs BAW sensor | alkanethiol self-assembled monolayer with *E.coli* antibodies | $10^3$ | PBS buffer | [57] |
| *Legionella pneumophila* | ultra-high frequency SAW device from 128°YX $LiNbO_3$ | anti-*L. pneumophilla* antibody | $2{\cdot}10^6$ | water | [58] |

For these reasons, SAW sensors were studied for bacterial detection in combination with a new and emerging type of bioreceptor: bacteriophage tail fiber proteins.

### 1.1.4 Bacteriophages as a sensing element

#### Bacteriophages

Bacteriophages are viruses that infect bacteria and replicate within them. The majority of all known bacteriophages belongs to the *Caudovirales* order, and they have the similar structure – genetic information (double-stranded DNA) encapsulated in an icosahedral capsid with attached a tail with fibers [59]. Figure 1.6 shows the structure of bacteriophage T7, member of *Caudovirales* order [13].

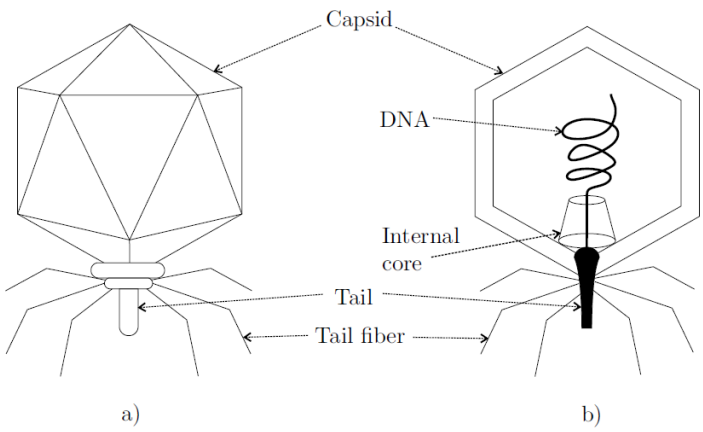


Figure 1.6: a) schematic picture and b) cross-section of bacteriophage T7 [13]

Bacteriophages replicate only within the living bacterial host. The first step is based on the electrostatic attraction of positively charged bacteriophage's tail fibers towards the negatively charged bacteria surface. Recognition of host bacteria is then done via specific receptor binding proteins [60]. After bonding to the host bacteria, bacteriophages insert their nucleic acid via their tail into the bacterial cell and use the intercellular machinery host cells to reproduce [14]. Several hundreds of new virions are reproduced within a single bacterial cell, and at some point, the bacteria cell is disrupted, and new virions are released. This bacteriophages reproduction is called the lytic cycle, as shown in Figure 1.7. A second reproduction cycle of phages called lysogenic cycle exists. Lysogenic phages insert their genome in host DNA. Integrated DNA is called prophage. It is not infectious and replicates as a part of bacteria chromosome until some stress starts the production of bacteriophages [13, 14, 61, 62].

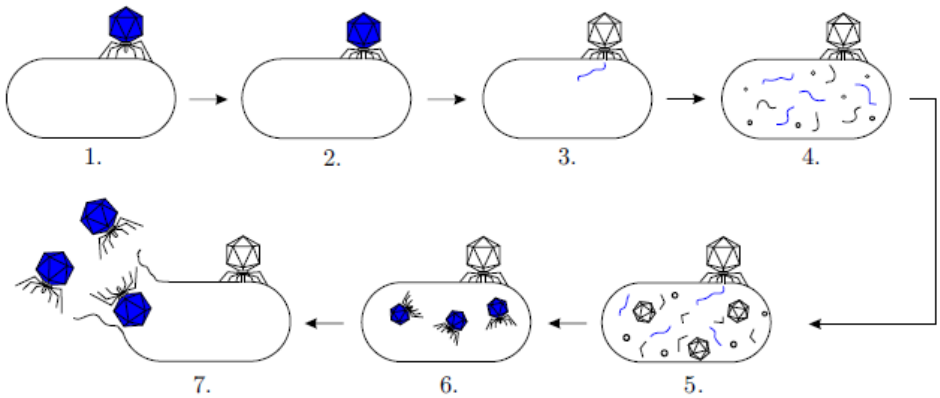


Figure 1.7: Lytic cycle of bacteriophage: 1) bonding of virion to the bacteria-host cell, 2) penetration into the host cell, 3) insertion of nucleic acid via tail into the host cell, 4) replication of bacteriophage's nucleic acid, 5) synthesis of bacteriophage's proteins, 6) maturation of virions, 7) release of new virions from host cell [13]

### Phage-based bacterial detection

Bacteriophages have become an interesting alternative to antibodies in the field of bacteria detection for several reasons. One of the main advantages of bacteriophages is their high specificity to their host bacteria. It is possible to choose a bacteriophage that selectively detects a single species or even a single bacterial strain. Additionally, some of them are robust, and they can keep their activity even after exposure of organic solvents or high temperatures (up to 76 °C). Another advantage is the simplicity of their production [61, 63].

There are several strategies of bacteriophage-based bacteria detection. First, the lysis of infected bacteria releases its intracellular compounds, which can be used as a marker of bacteria presence. Capture of bacteria by immobilized phages on the sensor's surface can be detected as the variation of the surface physical properties. Bacteriophages can also be immobilized on nanoparticles and used for separation of bacteria from complex samples and/or as a tool for bacteria detection. All mentioned ways of using bacteriophages for bacteria detection are summarized in Figure 1.8 [61].

For biosensing applications, several approaches to attach bacteriophages to the sensor's surface have been discussed in the literature: physical adsorption of virions on the surface, covalent bonding, entrapment of virions into porous matrices or utilization of specific interactions – biotin-streptavidin or electrostatic interaction [62, 64]. Several conditions must be fulfilled to obtain a functional bacteriophage coated surface. Immobilized bacteriophages must retain their infectivity. Even though bacteriophages are more robust

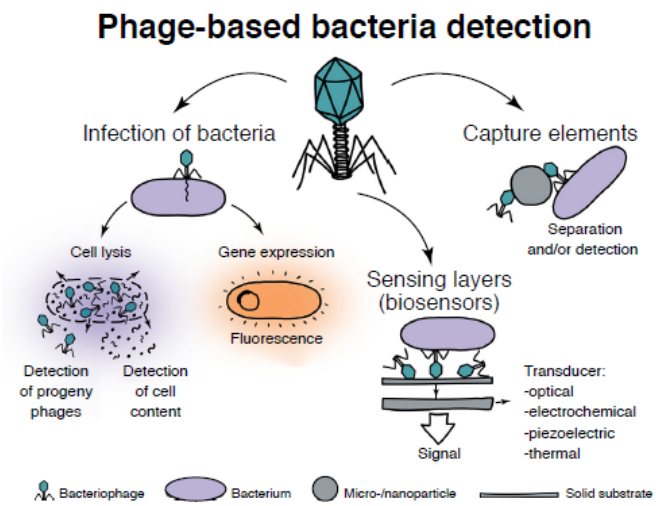


Figure 1.8: Different ways of using bacteriophages for bacteria detection [61]

than commonly used biorecognition elements (antibodies, aptamers, enzymes, etc.), they can be inactivated by harsh conditions (pH, chemical, temperature) or by drying. Another requirement is high surface density and uniform distribution of the bacteriophages as well as proper arrangement of asymmetric bacteriophages to retain availability of virion's receptors. Another crucial issue is the prevention of bacteriophages desorption during sensor operation [62, 63]. Several examples of biosensors using bacteriophages as sensing element are listed in Table 1.5.

To overcome the issues of the orientation of immobilized bacteriophages, bacteriophage might be replaced by their receptor binding proteins (RBPs). These proteins are long tail fibers or short tail spikes attached to the baseplate of tailed bacteriophages. There are just a few studies on bacteriophage tail fibers and short tail spike attachment on a solid surface. Available examples are given in Table 1.6.

Table 1.5: Examples of biosensors using bacteriophages as sensing element for bacteria detection

| **Bacteria** | **Phage** | **Detection technique** | **Assay scheme** | **Means of immobilization** | **LOD** (CFU/ml) | **REF** |
|---|---|---|---|---|---|---|
| *Salmonella* | M13 | Capacitive | Capacitance change when bacteria bind to immobilized phage | Polytyramine | 200 | [65] |
| *E. coli* K12 | T4 | Impedimetric | Magnetically separated E. coli detection at a screen-printed carbon electrode | Carboxylic groups | $10^3$ | [66] |
| *Pseudomonas aeruginosa* | PaP1 | Electrochemi-luminescence | Inhibition of luminescence caused by bacteria binding | Carboxylic groups | 56 | [67] |
| *M. smegmatis*, *M. tuberculosis* | D29 | Piezoelectric | Phages immobilized on gold IDTs, detection of variations in oscillation frequency | Covalent | $10^3$ | [68] |
| *S. aureus* | 12600 | Piezoelectric | QCM with dissipation monitoring | Physisorption | n. a. | [69] |
| *S. aureus* | 12600 | Magnetoelastic | METGLAS 2826 MB alloy ribbon with chromium/gold layer to attach phages, variation in resonant frequency | Physisorption | 3log (linear range not provided) | [70] |
| *E. coli* O157:H7 *S. aureus* | T4, BP14 | SPR | Phages attached to the gold surface of SPR sensors | Physisorption | $10^3$ | [71] |
| *Salmonella* | SEP37 | EIS | AuNPs modified gold disk electrode | Cysteamine as a crosslinker | 17 | [72] |
| *S. aureus* | SATA-8505 | EIS | carbon nanotube-based sensor | immobilization by electric field | $10^2$ | [73] |
| *E. coli* | T4 | EIS | screen printed electrodes functionalized with a nanocomposite made from gold, tungsten oxide and carbon nanotubes | covalent | 3 | [74] |
| *E. coli* | M13 | | gold IDTs with reduced graphene oxide nanosheet | carboxylic groups | 45 | [75] |

Table 1.6: Examples of biosensors using phage receptor binding proteins

| **Bacteria** | **Phage** | **RSB** | **Detection technique** | **Assay scheme** | **LOD** (CFU/ml) | **REF** |
|---|---|---|---|---|---|---|
| *Campylobacter jejuni* | NCTC 12673 | Gp48 | SPR | Glutathione S-transferase-Gp48 immobilized onto SPR chip using glutathione SAM | $10^2$ | [76] |
| *Campylobacter jejuni* | NCTC 12673 | Gp48 | PCR | Immobilized GST-Gp48 protein onto magnetic beads for separation and pre-enrichment of bacteria, detection by PCR | $10^2$ | [77] |
| *Campylobacter jejuni, Campylobacter coli* | NCTC 12673 | Gp47 | Agglutination assay | Immobilized Gp47 on gold chip, agglutination in different buffers | n.a. | [78] |
| *E. coli* K-12 | Lambda | J protein | SPR | His-tagged J protein immobilized on SPR sensor chip | $2{\cdot}10^4$ | [79] |
| *Salmonella enterica* ser. Typhimurium | Det7 | Det7T | SPR | Amine-coupling immobilized phage tail to gold surface of SPR sensor | $5{\cdot}10^4$ | [80] |

### 1.1.5 Comparison of biosensing techniques and their challenges

As mentioned before, the main requirements for reliable pathogen detection and analysis are the sensitivity and the specificity that include the ability to distinguish even between bacterial strains, reproducibility of biosensor and reliability of the obtained results as well as detection speed, low cost, and ease of use [5].

Electrochemical sensors thank to their high robustness, ease of preparation and low cost became a "workhorse" within biosensors. Their problem is the possibility of the influence of the obtained signal by electroactive interferents, e.g., unwanted redox reactions. Optical sensors are getting the main alternative transducer to the electrochemical sensors, but they are dealing with the problem of reducing their size [5]. Acoustic sensors, particularly SAW sensors, are easy to fabricate, easy to use and they can be easily miniaturized. Compared to another type of sensors, they can be easily designed as passive wireless sensors [81]. Table 1.7 summarizes the advantages and disadvantages of most studied transduction methods – optical, electrochemical and acoustic.

All of the types of biosensors mentioned in this review have to face the same challenges. 1/ The difficulty to achieve specificity and sensitivity in the complex samples such as blood or food. Nonspecific interactions and adsorptions limit the sensitivity, reliability and also lifetime of the biosensor. This can be overcome by a careful choice of the bioreceptor and proper surface functionalization. The sensitivity of the sensors can be enhanced using functionalized nanoparticles and/or pre-concentration steps. 2/ The difficulty to reduce the size and cost of some systems, such as SPR or QCM [1, 5].

Real-time detection of bacteria in drinking water brings other challenges. One problem is, how to deal with the large volumes of water to be analyzed. Another problem is how to achieve that the possibly present bacteria will get close enough to the sensor's surface to be captured by the bioreceptor. A possible solution is passing the liquid through the charged membrane to filter the bacteria or pre-concentration step using functionalized magnetic nanoparticles.

Generally speaking, there is a great effort by scientists to develop a biosensor for bacteria detection in real-world aqueous solutions. But there are still many challenges to be addressed before possible commercialization of such type of sensors.

Table 1.7: Summary of advantages and disadvantages of the biosensor with different transduction method [1]

| Transduction method | Advantages | Disadvantages |
|---|---|---|
| **Optical** | • High sensitivity<br>• Rapid<br>• Suitable for real time detection | • Problem with miniaturization (SPR)<br>• The need for labeling with fluorescent reagents (Fluorescence) – adds time and cost<br>• The limited penetration depth of bacteria by an electromagnetic field (SPR)<br>• The similarity in the refractive index of bacteria and aqueous environment<br>• Expensive |
| **Electrochemical** | • High sensitivity<br>• Low cost<br>• Point of care testing<br>• Miniaturization capacity<br>• Not affected by the presence of other analytes (Impedimetric) | • The signal from unwanted redox reactions (Amperometric)<br>• The need for an enzymatic substrate (Amperometric)<br>• Bad reproducibility |
| **Acoustic** | • Miniaturization capacity<br>• Low cost<br>• Quick processing times without the need for sample processing<br>• Can operate wirelessly (SAW)<br>• Suitable for real-time detection | • Lower sensitivity |

## 1.2 Overview of Acoustic-Wave sensors

Surface acoustic waves (SAWs) and bulk acoustic waves (BAWs) are two of MEMS technologies of industrial relevance and can been found in a myriad of devices. Acoustic RF filters, for instance, are integral parts of wireless communication systems. SAW devices have been also adapted as sensors which can be configured to operate both passively and wirelessly.

Acoustic devices can be divided into three groups depending on their propagation mode – devices using Bulk Acoustic Waves (BAW) and Surface Generated Acoustic Waves (SGAW), that contain Surface Acoustic Waves (SAW) and Acoustic Plate Modes (APM) devices [82]. Classification of acoustic wave devices is shown in figure 1.9. Table 1.8 summarizes key parameters of different acoustic devices and gives the advantages and disadvantages of each type.

As all of the acoustic devices use piezoelectric substrates to generate acoustic waves, the brief descricption of piezoelectricity is given in next section followed by discussion of two types of acoustic sensors relevant for this thesis - QCM sensors belonging to BAW devices and Love wave SAW sensors from the family of surface generated acoustic wave devices.

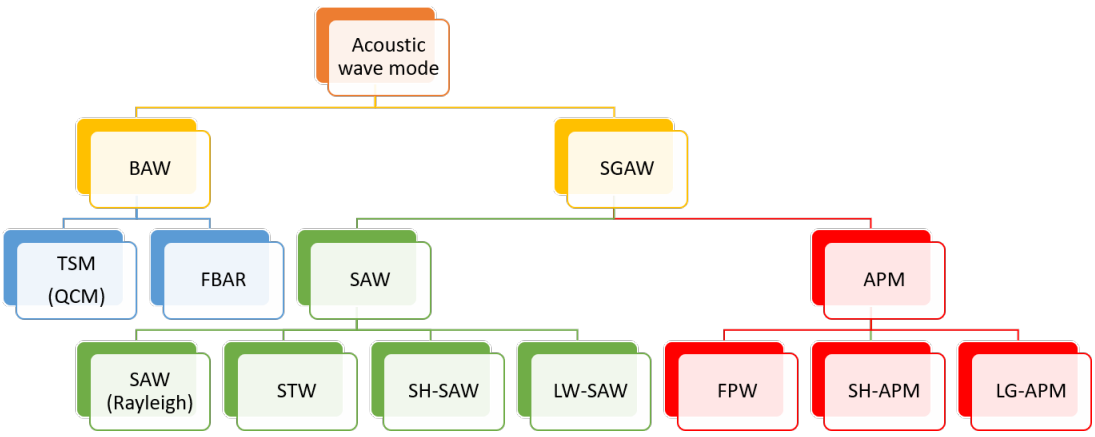


Figure 1.9: Classification of different acoustic wave modes (reproduced from [82]). The two types of BAW sensors are Thickness Shear mode (TSM)- Quartz Crystal Microbalance (QCM) and Film Bulk Acoustic Wave (FBAR). SAW group include Rayleigh SAW, Surface Transverse Wave (STW), Shear-Horizonatal SAW (SH-SAW) and Love wave SAW (LW-SAW). APM devices include Flexural Plate Wave (FPW), Shear-Horizontal APM (SH-APM) and Layer-Guided APM (LG-APM).

Table 1.8: Key parameters for different acoustic devices (reproduced from [83])

| Wave mode | Res. frequency | Sensitivity | Advantages | Disadvantages | Materials |
|---|---|---|---|---|---|
| **QCM** 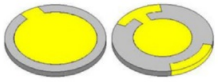 | kHz to a few MHz | 12-70 $cm^2/g$ [84] | • Detection in humid and liquid environment<br>• Easy to operate<br>• Inexpensive equipment<br>• high Q factor | • Low detection resolution due to low operating frequency<br>• Sensors with higher operating frequency are fragile due to lower thickness of the substrate | • Quartz plates<br>• Au electrodes |
| **Rayleigh SAW** 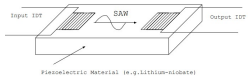  [85] | A few MHz-GHz | 100-200 $cm^2/g$ [86] | • Low power consumption<br>• Relatively low cost<br>• Wireless control<br>• Easy processing | • High attenuation in humid conditions<br>• Significant wave damping in a liquid environment | • 41°YX cut $LiNbO_3$<br>• ST-cut quartz<br>• 128° Y-cut $LiNbO_3$<br>• ZnO, AlN and PZT thin film devices |
| **FPW sensor** 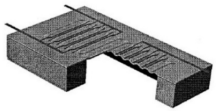 [87] | 2 - 20 MHz (few hundreds MHz to 1 GHz for thin film based higher Lamb modes) | 200-1000 $cm^2/g$, 200 $cm^2/g$ in liquids [84, 86] | • Supports two propagation modes - symmetric and antisymmetric<br>• Wireless control<br>• Able to operate in liquid environment | • Radiation loss can occur in liquid<br>• Fragile structure due to the low thickness of the device<br>• Temperature sensitivity | • ZnO, AlN, and PZT multilayer membranes |

*Continued on next page*

Table 1.8 – *Continued from previous page*

| Wave mode | Res. frequency | Sensitivity | Advantages | Disadvantages | Materials |
|---|---|---|---|---|---|
| **SH-SAW** 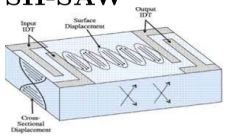 | 30 - 500 MHz [86] | 100-180 $cm^2/g$ [86] | • Low power consumption<br>• Wireless control<br>• Operate in liquid environment<br>• Low cost | • Often not pure shear wave when excited<br>• Part of the energy is lost to a bulk acoustic wave<br>• Depends on crystal orientation | • Quartz<br>• 36° and 64 °YX-cut $LiNbO_3$ |
| **Love-wave** 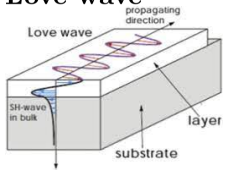  | 80 - 300 MHz | 150 - 950 $cm^2/g$ [84,86] | • Highest sensitivity among SAW sensors due to wave guiding effect<br>• Able to work in liquid environments | • Significant guiding layer effect | • Substrates: Quartz, 36° YX-cut $LiTaO_3$, 64° YX-cut $LiNbO_3$<br>• Guiding layer: $SiO_2$, ZnO, PMMA, SU-8, Photoresist, $TiO_2$ |
| **Back trench FBAR** 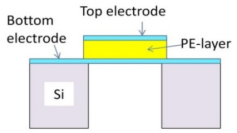  [87] | Sub- or a few GHz | 400 - 700 $cm^2/g$ [84] | • Small dimensions<br>• Very high sensitivity<br>• Ability to fabricate using standard CMOS processing, materials and circuitry<br>• Significantly reduced size | • Large noise/signal ratio<br>• Sensitive to many different parameters<br>• Fragile membrane | • Si, $Si_3N_4$ or $SiO_2$ membrane<br>• ZnO and AlN membrane |

### 1.2.1 Piezoelectricity

The direct piezoelectric phenomenon was discoverd by brothers Pierre and Paul-Jacques Curie in 1880 followed by the discovery of inverse piezoelectric effect by Gabriel Lippman in 1881. The word *piezoelectricity*, that means *"electricity by pressure"*, is derived from the Greek word *piezein* with meaning to press or squeeze [88, 89].

Direct piezoelectric phenomenon refers to the ability of some materials to produce an electric charge when the mechanical stress is applied. The reciprocal phenomenon when the applied electric field to a piezoelectric material cause a mechanical stress is called the converse piezoelectric effect. Piezoelectric materials always exhibit both of them. A molecular model of piezoelectricity is shown in the figure 1.10. When the piezoelectric material is not under applied mechanical stress, the external effect of negative and positive charges is reciprocally cancelled resulting in electrically neutral molecule. When the mechanical stress is applied, the internal structure of molecule is deformed causing the separation of positive and negative charges and hence the small dipoles are generated [88, 89].

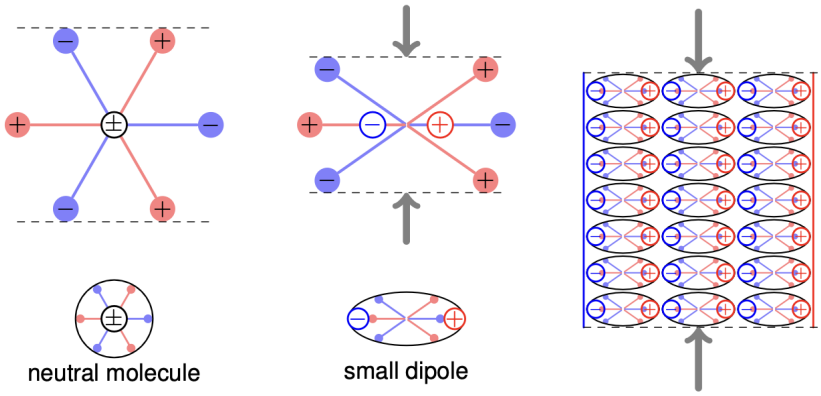


Figure 1.10: A molecular model of piezoelectricity, reproduced from [88]

#### Piezoelectric constitutive equations

Mathematically, the coupling between electric and mechanical parameters is expressed in the form of a connection between the material strain and its permittivity at constant strain. These equations are called *piezoelectric constitutive equations* and are given below:

$$T_{ij} = c^{E}_{ijkl} S_{kl} - e_{kij} E_k, \tag{1.1}$$

$$D_i = e_{ikl} S_{kl} + \epsilon^S_{ik} E_k, \tag{1.2}$$

where $T_{ij}$ is tensor of mechanical stress, $S_{kl}$ is strain tensor, $E_k$ is vector of electric field intensity, $D_i$ is vector of electric field induction, $c^E_{ijkl}$ is elasticity tensor in the absence of electric field ($\boldsymbol{E} = 0$), $e_{ikl}$ is piezoelectric coupling tensor and $\epsilon^S_{ij}$ is dielectric tensor in the absence of strains ($\boldsymbol{S} = 0$) [88, 90, 91].

If we want to write piezoelectric and elastic tensors in the matrix form, we need to use Voight-Kelvin notation for index substitution, see table 1.9. This notation allows us to represent the $4^{th}$-rank tensor of elasticity $\boldsymbol{c}$ as 6x6 matrix, the $3^{rd}$-rank tensor of piezoelectric coupling $\boldsymbol{e}$ as 3x6 matrix, the $2^{nd}$-rank tensor of dielectric constants $\epsilon$ as 3x3 matrix and the $2^{nd}$-rank tensors of strain $\boldsymbol{S}$ and stress $\boldsymbol{T}$ as 6x1 vectors. Using the Voight-Kelvin notation and writing out the components, the piezoelectric constitutive equations will appear as follows.

Table 1.9: Voight-Kelvin notation for index substitution

| Indexes in tensor - *ij, kl* | Voight indexes - *p, q* |
|---|---|
| 11 | 1 |
| 22 | 2 |
| 33 | 3 |
| 23 or 32 | 4 |
| 31 or 13 | 5 |
| 12 or 21 | 6 |

$$\begin{bmatrix} T_1 \\ T_2 \\ T_3 \\ T_4 \\ T_5 \\ T_6 \end{bmatrix} = \begin{bmatrix} c^E_{11} & c^E_{12} & c^E_{13} & c^E_{14} & c^E_{15} & c^E_{16} \\ c^E_{21} & c^E_{22} & c^E_{23} & c^E_{24} & c^E_{25} & c^E_{26} \\ c^E_{31} & c^E_{32} & c^E_{33} & c^E_{34} & c^E_{35} & c^E_{36} \\ c^E_{41} & c^E_{42} & c^E_{43} & c^E_{44} & c^E_{45} & c^E_{46} \\ c^E_{51} & c^E_{52} & c^E_{53} & c^E_{54} & c^E_{55} & c^E_{56} \\ c^E_{61} & c^E_{62} & c^E_{63} & c^E_{64} & c^E_{65} & c^E_{66} \end{bmatrix} \begin{bmatrix} S_1 \\ S_2 \\ S_3 \\ S_4 \\ S_5 \\ S_6 \end{bmatrix} - \begin{bmatrix} e_{11} & e_{21} & e_{31} \\ e_{12} & e_{22} & e_{32} \\ e_{13} & e_{23} & e_{33} \\ e_{14} & e_{24} & e_{34} \\ e_{15} & e_{25} & e_{35} \\ e_{16} & e_{26} & e_{36} \end{bmatrix} \begin{bmatrix} E_1 \\ E_2 \\ E_3 \end{bmatrix} \tag{1.3}$$

$$\begin{bmatrix} D_1 \\ D_2 \\ D_3 \end{bmatrix} = \begin{bmatrix} e_{11} & e_{12} & e_{13} & e_{14} & e_{15} & e_{16} \\ e_{21} & e_{22} & e_{23} & e_{24} & e_{25} & e_{26} \\ e_{31} & e_{32} & e_{33} & e_{34} & e_{35} & e_{36} \end{bmatrix} \begin{bmatrix} S_1 \\ S_2 \\ S_3 \\ S_4 \\ S_5 \\ S_6 \end{bmatrix} + \begin{bmatrix} \epsilon_{11}^S & \epsilon_{12}^S & \epsilon_{13}^S \\ \epsilon_{21}^S & \epsilon_{22}^S & \epsilon_{23}^S \\ \epsilon_{31}^S & \epsilon_{32}^S & \epsilon_{33}^S \end{bmatrix} \begin{bmatrix} E_1 \\ E_2 \\ E_3 \end{bmatrix} \tag{1.4}$$

For each cut of particular piezoelectric material, we obtain unique set of piezoelectric, elastic and dielectric constants, that can be written in elasto-piezo-dielectric matrix:

$$\left[\begin{array}{cccccc|ccc} c_{11}^E & c_{12}^E & c_{13}^E & c_{14}^E & c_{15}^E & c_{16}^E & e_{11} & e_{21} & e_{31} \\ c_{21}^E & c_{22}^E & c_{23}^E & c_{24}^E & c_{25}^E & c_{26}^E & e_{12} & e_{22} & e_{32} \\ c_{31}^E & c_{32}^E & c_{33}^E & c_{34}^E & c_{35}^E & c_{36}^E & e_{13} & e_{23} & e_{33} \\ c_{41}^E & c_{42}^E & c_{43}^E & c_{44}^E & c_{45}^E & c_{46}^E & e_{14} & e_{24} & e_{34} \\ c_{51}^E & c_{52}^E & c_{53}^E & c_{54}^E & c_{55}^E & c_{56}^E & e_{15} & e_{25} & e_{35} \\ c_{61}^E & c_{62}^E & c_{63}^E & c_{64}^E & c_{65}^E & c_{66}^E & e_{16} & e_{26} & e_{36} \\ \hline e_{11} & e_{12} & e_{13} & e_{14} & e_{15} & e_{16} & \epsilon_{11}^S & \epsilon_{12}^S & \epsilon_{13}^S \\ e_{21} & e_{22} & e_{23} & e_{24} & e_{25} & e_{26} & \epsilon_{21}^S & \epsilon_{22}^S & \epsilon_{23}^S \\ e_{31} & e_{32} & e_{33} & e_{34} & e_{35} & e_{36} & \epsilon_{31}^S & \epsilon_{32}^S & \epsilon_{33}^S \end{array}\right] \tag{1.5}$$

where the elasticity matrix $c^E$ is in the order $10^{11}$ N/m$^2$, the piezoelectric constants $e$ are generally between 0.1 to 10 C/m$^2$ and the permittivity $\epsilon$ at constant strain is in values of $10^{-12}$ F/m. The knowledge of these parameters is essential for the modelling of the behavior of piezoelectric devices [90, 92]. As all of the piezoelectric substrates are anisotropic, values in elasto-piezo-dielectric matrix will vary depending on the cut of the crystal, because the cut change the reference system in the calculation and the matrix coefficient must be recalculated in the new reference system.

Piezoelectric materials are crystalline materials. Atomic structure of crystals is determined by the lattice and the atomic group assigned to each nodes. There are 14 Bravais lattices, 7 crystal systems and 32 point symmetry classes of crystals, as is shown in the figure 1.11 and table 1.10.

Table 1.10: The 7 crystal systems and 14 Bravais lattices [88]

| ***System*** | ***Lattices*** | | |
|---|---|---|---|
| 1. Triclinic | P | $\alpha \neq \beta \neq \gamma \neq 90°$ | $a \neq b \neq c$ |
| 2. Monoclinic | P, C | $\alpha = \gamma = 90°$, $\beta \neq 90°$ | $a \neq b \neq c$ |
| 3. Orthorhombic | P, I, C, F | $\alpha = \beta = \gamma = 90°$ | $a \neq b \neq c$ |
| 4. Trigonal (rhombohedral) | P (or R) | $\alpha = \beta = \gamma \neq 90°$ | $a = b = c$ |
| 5. Tetragonal (quadratic) | P, I | $\alpha = \beta = \gamma = 90°$ | $a = b \neq c$ |
| 6. Hexagonal | P | $\alpha = \beta = 90°$, $\gamma = 120°$ | $a = b \neq c$ |
| 7. Cubic | P, I, F | $\alpha = \beta = \gamma = 90°$ | $a = b = c$ |

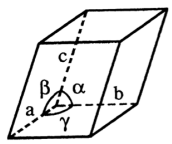


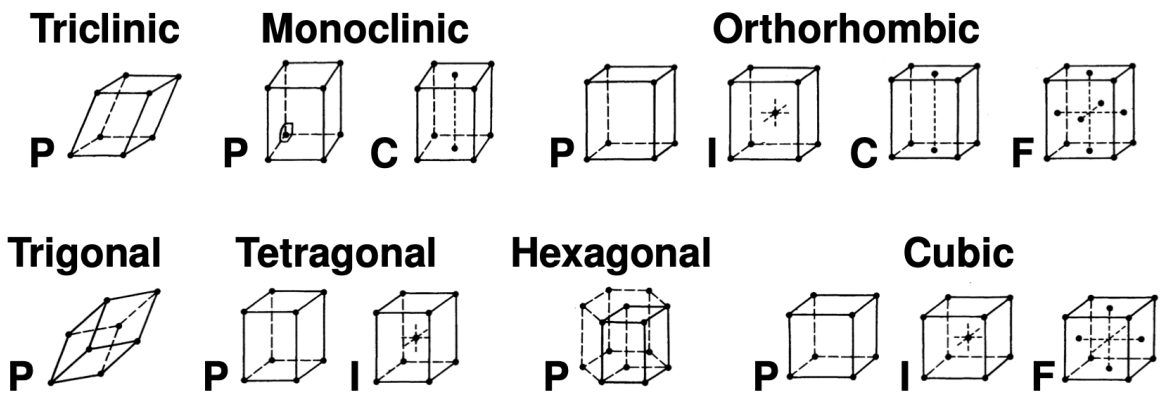


Figure 1.11: The 7 crystal systems and 14 Bravais lattices, reproduced from [88]

The constitutive matrices vary for each class of anisotropy. Based on the crystal symmetry, the number of independent material constants is different. In this work, four piezoelectric materials were used - lithium tantalate, lithium niobate, quartz and zinc oxide. Lithium tantalate and lithium niobate belongs to the trigonal system with the $3m$ symmetry class, quartz belongs to the same crystal system with the symmetry class 32 and zinc oxide has hexagonal system with 6 $mm$ class. [88,92] Components of constitutive matrices for beforementioned materials are shown in the figure 1.12. Symmetry with respect to the main diagonal is not indicated. The three numbers at the bottom right of the matrices represent the numbers of independent elastic, piezoelectric and dielectric constants. Tables 1.11 and 1.12 give the values of elastic or piezoelectric and dielectric constants respectively for materials used in this work. It is important to note, that it is necessary to make a transformation of the constitutive matrices according to the coordinate system given by the particular cut of the piezoelectric material.

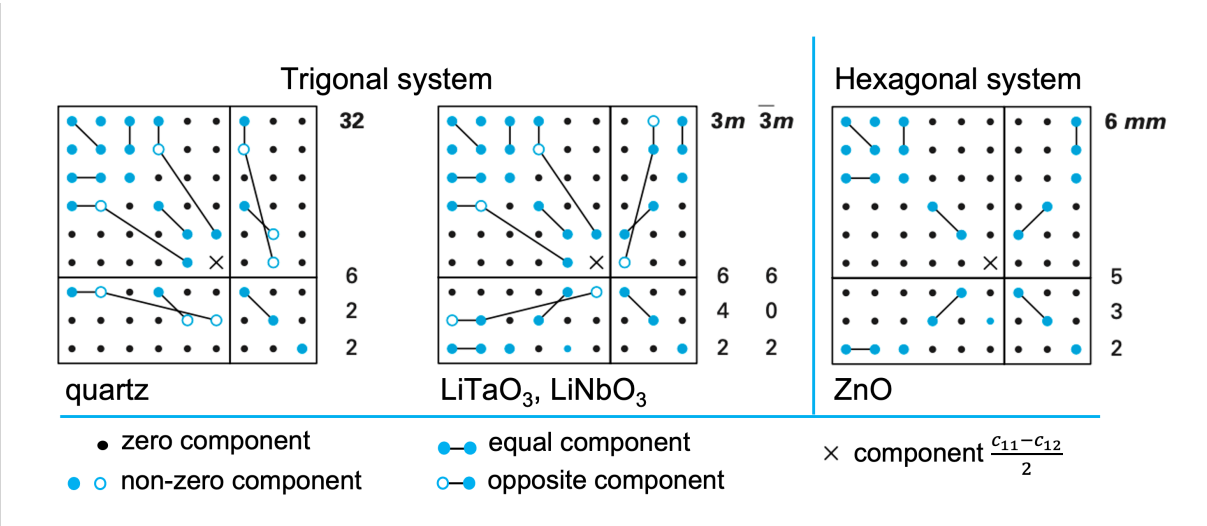


Figure 1.12: The components of constitutive matrices for trigonal system and symmetry classes 32 and $3m$ and hexagonal system and symmetry class 6 $mm$, [92]

Table 1.11: Elastic constants of materials employed in creation of elastic waves [92]

| **Material** | **System** | **Class** | **Stiffness** (in $10^{10}$ N/m$^2$) | | | | | | | |
|---|---|---|---|---|---|---|---|---|---|---|
| | | | $c_{11}$ | $c_{12}$ | $c_{13}$ | $c_{33}$ | $c_{44}$ | $c_{66}$ | $c_{16}$ | $c_{14}$ |
| Silice ($SiO_2$) | isotropic material | - | 7.85 | 1.61 | - | - | - | - | - | - |
| ZnO* | hexagonal | $6mm$ | 20.97 | 12.11 | 10.51 | 21.09 | 4.25 | - | - | - |
| $LiNbO_3$* | trigonal | $3m$ | 20.3 | 5.3 | 7.5 | 24.5 | 6.0 | - | - | 0.9 |
| $LiTaO_3$* | trigonal | $3m$ | 23.3 | 4.7 | 8.0 | 27.5 | 9.4 | - | - | -1.1 |
| Quartz* ($SiO_2$) | trigonal | 32 | 8.67 | 0.7 | 1.19 | 10.72 | 5.79 | - | - | -1.79 |

* piezoelectric material

Table 1.12: Piezoelectric and dielectric constants of materials employed in creation of elastic waves [92]

| **Material** | **Piezoelectric constants** (C/m$^2$) | | | | | | **Permittivity** ($10^{-11}$ F/m) | | **Density** $\rho$ ($10^3$ kg/m$^3$) |
|---|---|---|---|---|---|---|---|---|---|
| | $e_{11}$ | $e_{14}$ | $e_{15}$ | $e_{22}$ | $e_{31}$ | $e_{33}$ | $\epsilon_{11}$ | $\epsilon_{33}$ | |
| ZnO | -0.59 | - | -0.61 | - | - | 1.14 | 7.38 | 7.83 | 5.676 |
| $LiNbO_3$ | - | - | 3.7 | 2.5 | 0.2 | 1.3 | 38.9 | 25.7 | 4.7 |
| $LiTaO_3$ | - | - | 2.6 | 1.6 | $\approx 0$ | 1.9 | 36.3 | 38.1 | 7.45 |
| Quartz | 0.171 | -0.0406 | - | - | - | - | 3.92 | 4.1 | 2.648 |

### Electromechanical coupling coefficient

Electromechanical coupling coefficient $K^2$ provides the information on the ability of piezoelectric materials to generate elastic waves [92]. It is the measure of the efficiency of the

piezoelectric substrate in converting the electric signal into mechanical energy, that results in propagation on acoustic waves [91].

$K^2$ can be defined in terms of elastic, piezoelectric and dielectric constants and the value depends on the appropriate cut of the crystal [83, 91]. The example of the $K^2$ variation as a function of different crystal cut of $LiNbO_3$ is shown in figure 1.13.

$$K^2 = \frac{e_{31}^2}{c_{11}\epsilon_{33}} \tag{1.6}$$

$K^2$ can be also derived experimentally using the equation:

$$K^2(\%) = -\frac{2\Delta v}{v} \cdot 100, \tag{1.7}$$

where $|\Delta v|$ is the change in the SAW velocity caused by shorting the free piezoelectric surface by thin highly conductive metal film and $v$ is unperturbed SAW velocity [91].

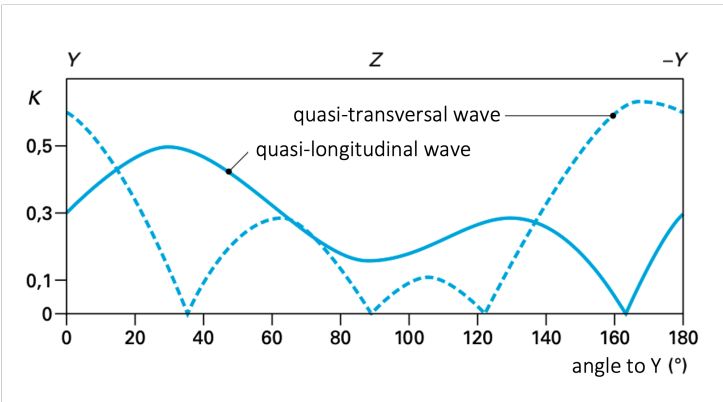


Figure 1.13: Variation of the coupling coefficient $K^2$ of lithium niobate as a function of the direction in the plane YZ, reproduced from [92]

### 1.2.2 Bulk acoustic wave devices

#### Quartz Crystal Microbalance (QCM)

The best-known representative among the BAW devices is Quartz Crystal Microbalance (QCM). It has two metallic circular electrodes on both parallel surfaces of the piezoelectric material, most commonly AT-cut quartz crystal. Acoustic waves are generated by applying the high frequency signal on electrodes, with waves propagating within the bulk of crystal [93]. Advantages of QCMs are the simplicity of manufacturing, good temperature stability and the possibility to operate in a harsh environment and liquids. Typical

resonant frequency is in the range from 5 to 30 MHz for the fundamental mode and is inversely proportional to the QCM thickness, the sensitivity might be increased by fabrication of very thin and fragile plates. For this reason, their sensitivity is limited [89] and relative sensitivity to mass loading is given by equation:

$$S_r = \frac{-2f_0}{\rho_p v} = -\frac{1}{\rho_p h_0}, \tag{1.8}$$

where $f_0$ is resonant frequency given by $f_0 = \frac{v}{2h_0}$, $h_0$ is quartz crystal thickness, $v$ is the acoustic velocity and $\rho_p$ is the piezoelectric material density [83].

### 1.2.3 Surface generated acoustic wave devices

SAW-based sensors are highly sensitive because the acoustic energy is strongly confined close to the surface of the device. The acoustic wave is generated by interdigital transducers electrode (IDTs) by conversion of the electrical signal and propagates across the transducer's surface to another IDTs, that convert acoustic wave back to the electrical signal via the piezoelectric effect. There exist several types of SAW sensors: Rayleigh-SAW sensor, Lamb wave sensor, and Love wave sensor. Rayleigh-type SAW sensor suffer from high attenuation due to particle displacement perpendicular to the surface causing that acoustic energy is radiated in the liquid. They are not suitable for bacterial detection in aqueous solutions or buffer solutions [50, 94, 95]. Lamb devices are composed of thin membrane deposited on the piezoelectric substrate and waves are guided in the free upper and lower surfaces of the membrane. They can operate in liquids as the Lamb waves velocity is lower than the compressional velocity of sound in liquids and therefore only minor energy dissipation occurs. Their disadvantage is the thin and fragile membrane necessary to achieve high sensitivity [86, 96]. Particle motion of Rayleigh, Lamb and Love waves are shown in the figure 1.14. Love waves will be discussed in the following subchapter devoted to the LW-SAW sensors.

#### Love-Wave Surface Acoustic Wave (LW-SAW)

Love wave sensors use primarily shear-horizontal polarized waves (SH-SAW) or a surface skimming bulk wave (SSBW) depending on the piezoelectric material. Both waves have shear horizontal particle displacement, where the particle movement is in parallel to the

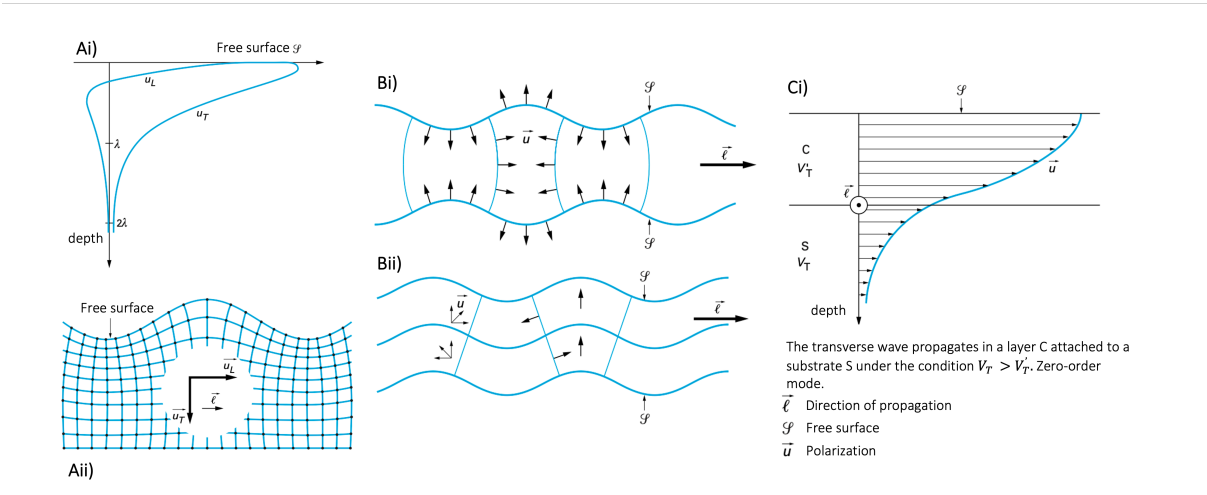


Figure 1.14: Schematic representation of different types of surface acoustic waves: A) Rayleigh waves in isotropic semi-infinite medium where i) is decrease in the longitudinal component $u_L$ and the transverse component $u_T$ as a function of the depth and ii) undulation of the surface as the wave passes, B) Lamb waves, where i) represents deformation of the plate in symmetric mode and ii) is deformation of the plate in antisymmetric mode and C) Love waves, reproduced from [92]

surface. This prevents radiation losses to the liquid [8, 94], see Figure 1.5. They are considered to be the most sensitive ones among the acoustic devices [96]. Love waves are obtained by trapping the shear waves in the guiding layer deposited on piezoelectric substrate and the guiding layer has to have lower acoustic velocity than the piezoelectric substrate, see figure 1.14C) [97]. The LW-SAW sensors consist of three main elements - piezoelectric substrate, guiding layer and IDTs electrodes that are sandwiched between the beforementioned materials. This important elements will be discussed in the following sections.

*Interdigital electrodes*

Interdigital electrodes (ITDs) were firstly proposed for generation of SAW by White and Voltmer in 1965 [98]. IDTs consists of two metal comb-like structure, one acting as generator and second as receiver. Center-to-center distance between two consecutive electrode fingers is called a period $p$ and the overlap between the fingers is the acoustic aperture $W$. The simplest IDTs electrodes consist of two fingers per period, where the finger width is equal to the space between them ($p/4$), shown in the figure 1.15a). One finger is connected to the ground and second one to the RF signal [82, 99].

Figure 1.15B) shows typical frequency response of IDTs. The highest electrical amplitude $A_f$ occurs, when the acoustic wavelength $\lambda$ is equal to the IDTs period $p$. Bandwidth $B$ of the IDTs frequency response is influenced by number of finger pairs $N$, where higher

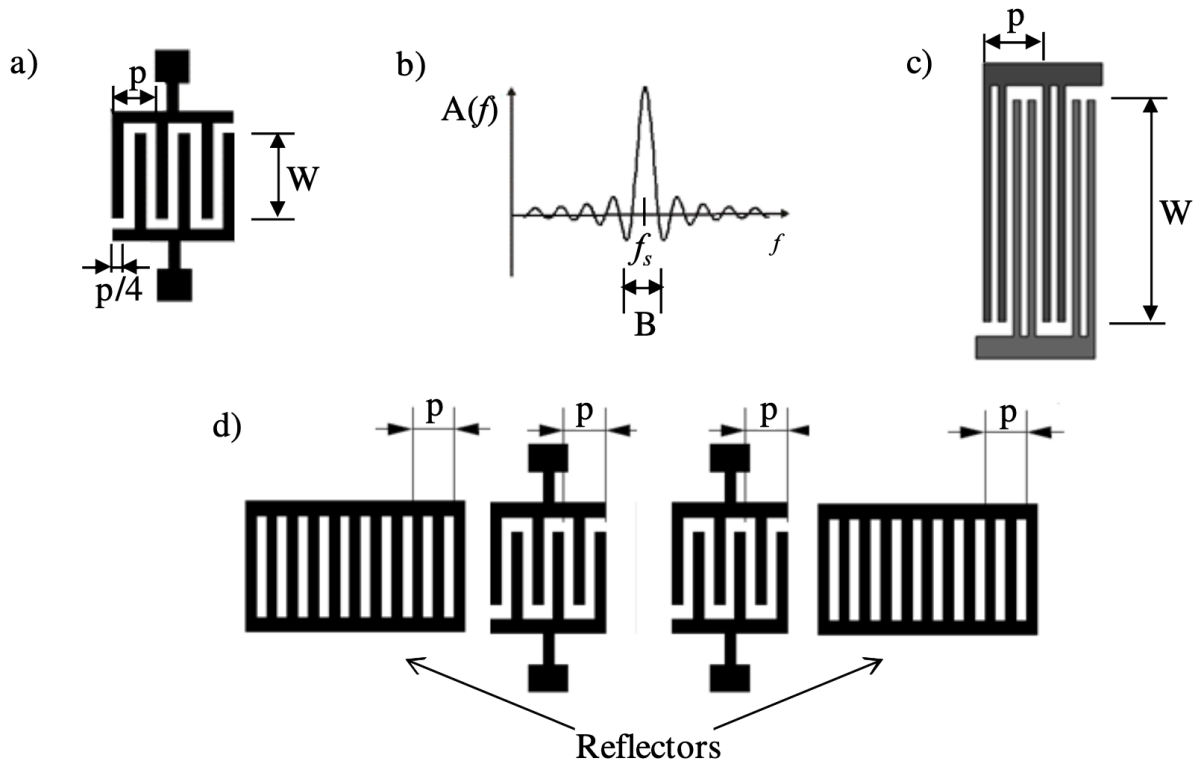


Figure 1.15: Schematic representation of different IDTs electrodes, a) simple IDT electrode with shown period $p$ and acoustic aperture $W$, b) frequency response of an IDT, where $A_f$ is electrical amplitude, $B$ is the bandwith and $f_s$ is synchronous frequency c) double-IDTs electrodes with split fingers and d) single IDTs electrodes with two grating reflectors, reproduced from [82]

$N$ results in narrower $B$. Practically, the maximum $N$ is recommended equal to 100 as higher $N$ causes losses associated with mass loading and scattering from the electrodes. Inherent loss of 3 dB in the frequency response is caused by propagation of the acoustic waves to both direction from the IDTs electrodes, that is caused by the symmetry of IDTs electrodes. In two-port devices, such as LW-SAW sensors, the inherent loss value is 6 dB. [82]

There are several second-order effect, that affect transducer frequency response and are significant in practice. For a single-electrode IDTs, scattered unwanted waves are in phase and cause very strong, so called Bragg reflections. This phenomenon occurs at the resonance condition $\lambda = p$. To avoid Bragg reflection, split electrodes are used (see figure 1.15c)). The disadvantage of split electrodes is an increase in lithographic resolution needed for their fabrication [91]. Triple-transit signal is another second-order effect, that occurs in two-port devices, as so LW-SAW sensors. The output IDT generates a reflected wave, that is reflected second time by the input IDT. This reflected wave travels to the output IDT after traversing the substrate three times, resulting in output signal known

as triple transit echo. The path difference between the main and doubly reflected wave results in amplitude and phase ripple [91]. Unwanted reflections can be reduced by using reflectors, metal gratings with the same configuration (space periodicity) as IDT, see figure 1.15d) [82].

*Piezoelectric substrates*

When choosing a material as the substrate for Love Wave devices, there are several important properties that need to be taken into account. First of them is the electromechanical coupling coefficient ($K^2$). Higher $K^2$ leads to the lower insertion loss, which implies higher sensitivity of LW-SAW device [82]. Second important parameter is temperature coefficient of frequency (TCF), which gives the temperature stability of the substrate. The minimization of the temperature influence on the sensor's response can improve the limit of detection [100]. The third property is the ability to excite shear horizontal polarized acoustic wave required for the operation of LW-SAW sensors in the liquid media [82]. For sensors operating in aqueous solutions, dielectric constant $\epsilon$ is another important parameter. In order to minimize a capacitive shortcuts of the electrical field of the IDTs, $\epsilon$ should be close to the dielectric constant of water ($\epsilon_w \sim 80$) [86].

36°YX $LiNbO_3$ substrate has very high coupling factor, but it has also the highest *TCF* and the substrate breaks extremely easily when exposed to abrupt thermal shock, which makes it difficult to handle during fabrication process including high temperature diamond deposition. The 36°YX $LiTaO_3$ substrate possesses low insertion loss and large $K^2$, which provide advantages over the other substrates, such as quartz cuts. The main shortcomings of $LiTaO_3$ substrate are 1) its poor thermal stability caused by high *TCF* and 2) it excites leaky waves, which leads to the increase of damping in liquid environment [101]. Quartz is the only common substrate material that offers cuts generating purely shear horizontal polarized waves. Most used quartz cuts that can generate pure SH waves are AT-cut and ST-cut. Both of them possess weak coupling coefficient. [82] From the fabrication point of view, Curie temperature needs to be taken into account. It is the temperature point, where phase transition from ferroelectric to paraelectric phase occurs and the material loses their piezoelectric properties [102]. Properties of the discussed piezoelectric materials are listed in the following table 1.13, dielectric constants are listed in the table 1.12.

*Guiding layers*

In the LW-SAW sensors, guiding layers play the crucial role in the improvement of the

Table 1.13: Properties of piezoelectric substrates materials

| **Material** | **Cut** | $v_s$ (m/s) | $K^2$ (%) | **TCF** (ppm/°C) | **Curie temperature** (°C) | **Ref** |
|---|---|---|---|---|---|---|
| **Quartz** | ST-cut (42.75°) | 5060 | 1.9 | 40 | 573 | [82, 103] |
| **Quartz** | AT-cut (32.25°) | 5099 | 1.4 | 0-1 | 573 | [82, 103] |
| **$LiNbO_3$** | 36°YX | 4800 | 16 | -75 to - 80* | 1140 | [82, 102] |
| **$LiTaO_3$** | 36°YX | 4160 | 5 | -30 to -45 | 665 | [82, 104] |
| **ZnO** | (11-20) | 2650 | 1.1 | 59-42 | | [82, 105, 106] |

*Approximate value, TCF - temperature coefficient of the frequency, $v_s$ - shear wave velocity

device performance, as it ensures higher sensitivity due to the wave entrapment closer to the sensor's surface [107]. The difference between the mechanical properties of piezoelectric substrate and the guiding layer material is crucial for the wave confinement. For the existence of Love modes, the shear wave velocity in the guiding layer ($v_L = \frac{\mu_L}{\rho_L}^{1/2}$) has to be lower than the shear wave velocity in the piezoelectric substrate ($v_S = \frac{\mu_S}{\rho_S}^{1/2}$).

The guiding layer material has to possess a low acoustic velocity. The most used are polymers, silicon oxide, gold or zinc oxide, their density $\rho$ and shear wave velocity $v_s$ are listed in the table 1.14.

Table 1.14: Properties of several guiding layer materials, [82]

| **Material** | $v_s$ (m/s) | $\rho$ (kg/m$^3$) |
|---|---|---|
| **$SiO_2$** | 2850 | 2200 |
| **ZnO** | 2650 | 5720 |
| **Au** | 1215 | 19300 |
| **PDMS** | 16 | 965 |
| **PMMA** | 1200 | 1180 |
| **Diamond** | 12820 | 3500 [105] |

Polymers, such as PDMS, PMMA or novolac, are interesting from the sensitivity point of view, as they have very low acoustic velocity. But they can cause high acoustic damping due to their viscoelastic properties, which is clearly a disadvantage for biosensing applications [8, 107]. Gold is often used guiding layer. It provides strong wave guiding and its surface can be easily modified by biomolecules, which is definitely advantage in

biosensing applications [82].

Zinc oxide guiding layers are suitable for biosensing applications, as ZnO is biocompatible and biomolecules immobilized on ZnO retain their conformation. ZnO possesses lower acoustic velocity than $SiO_2$, which results in higher sensitivity of LW-SAW devices [108]. Its deposition can be carried out at relatively low temperatures, low film stress and good adhesion onto many different substrates. [109] Main shortcoming of ZnO for our application is its weak chemical stability, when the layer is etched in hydrogen plasma used for diamond deposition and also in the majority of photoresist developers.

Silicon oxide offers low damping, excellent chemical and mechanical resistance and its acoustic velocity is sufficiently low. Its stability at higher temperatures is important property for successful coating by NCD layer [8, 110]. The main shortcoming of $SiO_2$ material as guiding layer to obtain optimal sensitivity of LW-SAW sensor is, that it is necessary to use thick $SiO_2$ films, which complicates the fabrication process [82]. Despite this fact, we consider $SiO_2$ material to be the most suitable guiding layer material for the diamond-coated LW-SAW sensors.

The guiding layer on top of piezoelectric substrate affects the LW-SAW device's properties, as it increases the electromechanical coupling coefficient $K^2$ and it also has the influence on the temperature behavior, as it modifies the TCF coefficient [82, 111]. Guiding layers brings one more advantage as it serves as protective coating of IDTs against the liquid environment, which improves the sensor's performance [108].

## 1.3 Diamond

Diamond is one form of Carbon C, which is the element with the atomic number $Z = 6$ located in the fourth group of the periodic system. In the ground state, its electron configuration is $1s^2 2s^2 2p^2$ [112]. The $1s^2$ state contains two strongly bounded core electrons. Remaining four electrons in the $2s^2 2p^2$ states are called valence electrons and are involved in formation of chemical bonds. In crystalline state the $2s$, $2p_x$, $2p_y$ *and* $2p_z$ orbitals are formed, as is shown in the figure 1.16 a). Because the energy difference between $2s$ and $2p$ orbitals is smaller (4 eV) than the energy gain in forming the chemical bond, the electronic wave-functions of these four electrons can mix with each other forming new hybrid orbitals. Carbon atoms forms three different hybrid orbitals - $sp$, $sp^2$ and $sp^3$ which allows to form many different forms called allotropes. The *carbon family* of inorganic carbon materials consists of diamond ($sp^3$ hybridization, see figure 1.16 b)), graphite ($sp^2$ hybridization), fullerenes and carbines [112, 113].

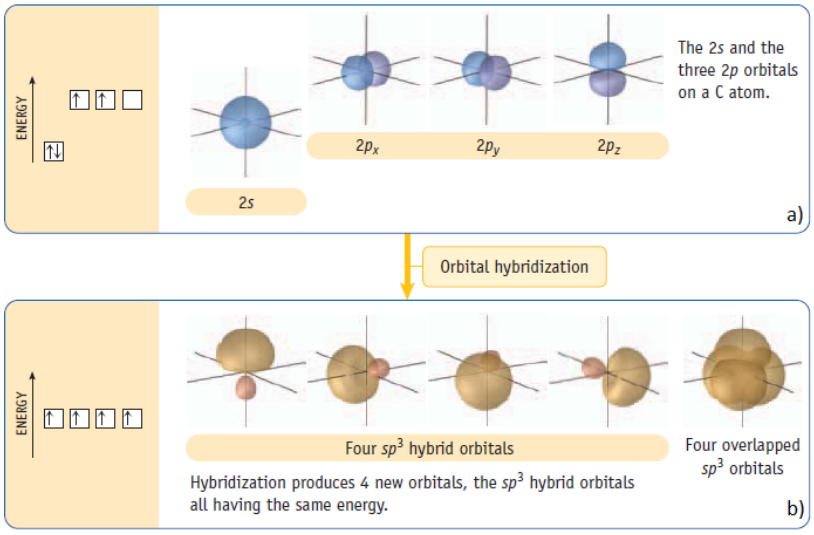


Figure 1.16: a) $2s$ and $2p$ orbitals in ground state of carbon atom and b) $sp^3$ hybridization of atomic orbitals [112]

### 1.3.1 Properties

Diamond has the face-centered cubic lattice with $sp^3$-hybridized tetrahedrally bonded atoms. Covalent bond lengths of the carbon-carbon atoms is equal, thus diamond builds strong three-dimensional network of covalent bonds. Due to this hexagonal structure, diamond exhibits the highest hardness and thermal conductivity in comparison with any

bulk material. Diamond has many other extraordinary properties, such as chemical inertness, high wear resistance, optical transparency from ultraviolet to far-infrared, the lowest thermal expansion coefficient. Intrinsic diamond is an electrical insulator, but can become a wide-band-gap semiconductor when suitably doped. Moreover, diamond is biologically inert and non-toxic material, which makes it suitable for various biosensing and biomedical applications [114–116].

Different elements can incorporate in the diamond lattice resulting in wide variety of crystallographic defects and color centers. The most common impurity elements are nitrogen and boron. The diamond type classification system divides diamonds into different categories based on the presence or absence of nitrogen and boron impurities. There are two main categories: 1) Type I diamonds contains sufficient amount of nitrogen, that is detectable using IR spectroscopy and 2) Type II diamond do not contains IR detectable amount of N impurities. Both types of diamond are further subdivided, as is shown in the figure 1.17. In type I group belongs type Ia, that has aggregated nitrogen impurities and is the most common natural diamond type. It contains up to 0.3 % of nitrogen. Type IaA consists of pairs of aggregated N atoms and type IaB are made up of four N atoms and vacancy V in the middle. Type Ib contains isolated single N impurities. This type is very rare in nature (less than 0.1 %) but almost all of the synthetic diamond belongs here and contains nitrogen concentration up to 500 ppm. Type II does not contain any nitrogen impurities and is divided into two subgroups - Type IIa contains very little nitrogen and is also very rare in nature. Type IIb contains even lower nitrogen concentration than type IIa, but it has boron impurities, that makes the diamond p-type semiconductor with a blue color. This type is extremely rare in the nature [114, 115, 117].

### 1.3.2 Diamond synthesis

Diamonds can be obtain from nature by mining, but they are in limited amount and for high prices. But the exceptional properties of diamond suitable for many applications led to the discovery of different ways to synthesize diamond artificially. Diamond is metastable (kinetically stable, but thermodynamically unstable) material and the conversion from graphite to diamond is extremely difficult at room temperature and pressure, as graphite is thermodynamically stable allotrope of carbon in these conditions. There is large activation barrier between these two phases that needs to be overcome to form dia-

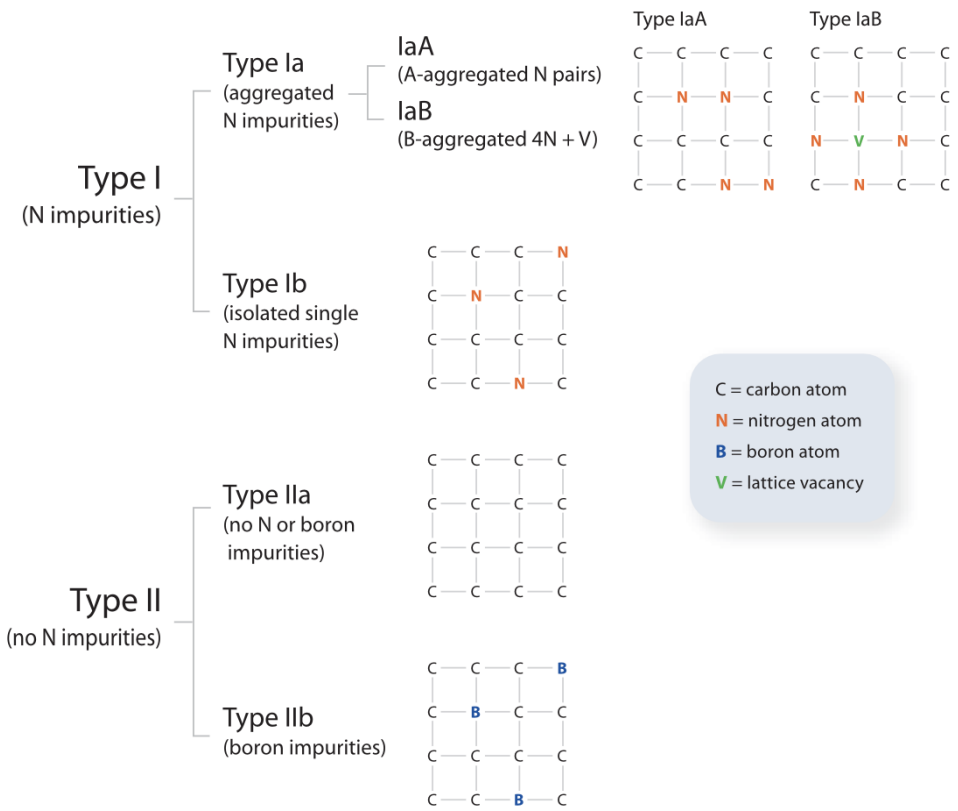


Figure 1.17: Schematic configuration of the diamond lattice impurities according to the diamond type classification system, reproduced from [117]

mond from graphite. Nowadays, two methods are commonly used to synthesize diamond from graphite - high-pressure high-temperature (HPHT) method and chemical vapor deposition (CVD) method. These methods will now be discussed. Figure 1.18 shows the phase diagram of carbon. It also shows the conditions used for different methods of synthesis. [114, 116]

### HPHT synthesis

HPHT method was used in 1954 by General Electric for the first time and it has been used to synthesize "industrial" diamond for decades. This method is used to produce diamond crystals ranging from nanometers to millimeters sizes. In this method, graphite is compressed in the hydraulic press at pressure of tens to thousands of atmospheres and the temperature over 2000 K in the presence of suitable metallic catalyst. HPHT-grown diamond are almost all of type Ib and they are used mainly in the industry such as cutting tools or for polishing and grinding in optics. [114, 116, 117]

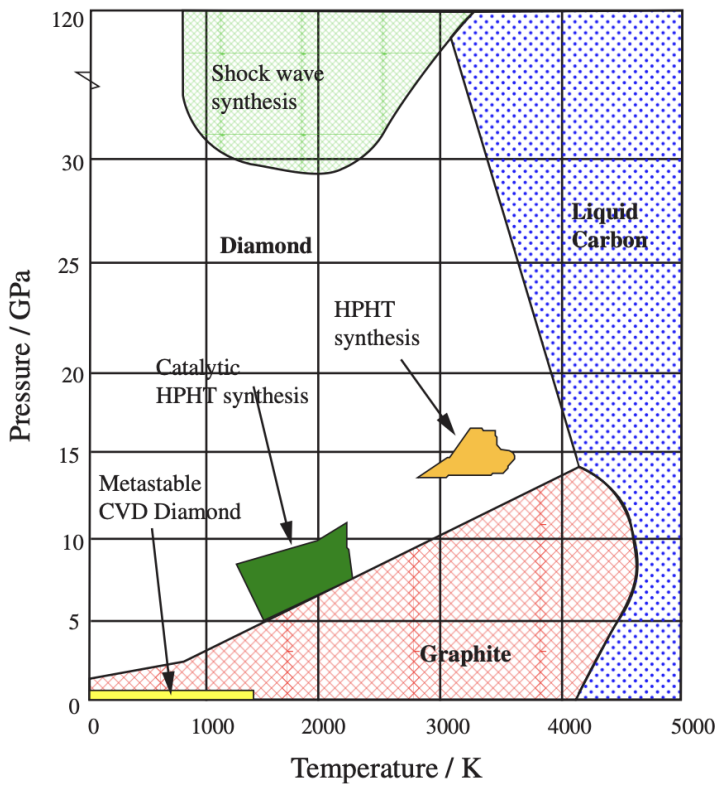


Figure 1.18: The phase diagram for carbon, reproduced from [114]

### Chemical vapor deposition

Chemical vapor deposition method is used to grow either polycrystalline diamond thin films or epitaxial diamond layers. CVD-grown diamonds are most commonly type IIa and are typically almost colorless or light brown [117]. This method is using conditions at which diamond is not thermodynamically stable, so it is also called metastable synthesis [115]. The CVD growth occurs in a low vacuum reactor using activated process gases (commonly methane $CH_4$ diluted in hydrogen $H_2$) at the temperature usually higher than 800 °C. Diamond thin films are grown from nucleation sites on the substrate by atom-by-atom and layer-by-layer process. The process involves decomposition of process gases and chemical reactions. This process is presented in the figure 1.19. Different approaches can be used to activate process gases, such as thermal activation (using a hot filament), electric discharge (e.g. DC, RF or microwave) or a combustion flame (oxyacetylene torch) [114, 116]. In this work, diamond layers were grown using microwave plasma enhanced chemical vapor deposition methods (MW-PECVD).

*Diamond doping*

During the CVD diamond growth process, different precursors gases can be added to the

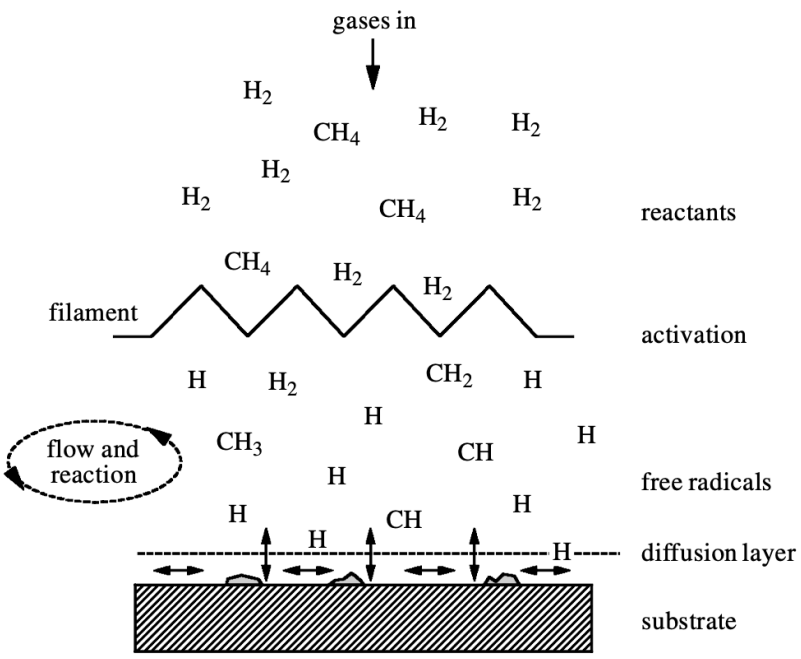


Figure 1.19: Schematic of physical and chemical processes occurring during the CVD diamond deposition, reproduced from [116]

reactant mixture to incorporate dopants in the growing layer, such as nitrogen, boron, phosphorous or some other metallic ions. The different dopants change the mechanical, electrical or electrochemical properties of the resulting diamond film [114]. Doping with nitrogen, silicon or nickel leads to the formation of luminescent color centers in diamond, which are used in photonics and quantum applications. Diamond layers are semiconductive when doped with boron (p-type semiconductor), phosphorous or nitrogen (n-type semiconductor) [114]. The activation energy of boron-doped diamond is 0.37 eV and the band gap is 5.47 eV, for the phospohorous-doped diamond the activation energy is 0.57 eV. Carrier mobility decreases with increasing number of incorporated boron or phosphorous atoms, which causes reduction of the diamond film resistivity. For boron concentrations higher than $10^{19}$, conduction by free holes in valence bands is dominant. The metal-insulator transition and superconductivity arise at the boron concentration higher than $3{\cdot}10^{20}$ atoms/cm$^3$. The resistivity of such heavily boron-doped 100 film is 10 m$\Omega$/cm or less at room temperature. In comparison, the resistivity of heavily phosphorous-doped diamond 111 film ($10^{20}$ P atoms/cm$^3$) is 70 $\Omega$/cm. [118]

### 1.3.3 Surface terminations

Surface functionalization via attachment of different biomolecules is important part of producing biosensing devices. Surface termination of diamond layers is starting point for further functionalization and will be briefly discussed here. As-grown fresh CVD diamond has hydrogen terminated surface, this H-termination is very stable and makes the diamond layer very hydrophobic. Hydrophobicity of H-terminated diamond layer can be an issue for further functionalization processes. The H-layer can be removed by annealing in vacuum providing surface with unsaturated dangling bonds. Second important termination is oxygen-terminated surface, which can be obtained from oxygen plasma, ozone ($O_3$) treatment or wet chemical treatment. By plasma treatment, the "ketone" (O atom si double-bonded to C atom (C=O)) and "carbonyl" (O atom bridges to surface C atoms (C-O-C)) termination is likely obtained. Chemically oxidized atoms provides hydroxyl (-OH) or carboxyl (-COOH) termination. These groups makes the diamond surface hydrophilic. Several methods have been developed to introduce different groups on its surface, such as termination of diamond by halogens, fluorine and chlorine, or amino groups ($NH_2$). Halogen termination can be achieved by UV irradiation of the sample in the suitable environment (e.g. $Cl_2$ for chlorinated surface) Anyway, to obtain amino groups on the surface, the halogen termination is starting point. Diamond surface terminations give sufficient options for activation and introduction of biomolecules to its surface. Standard chemical methods (cross-linking) can be applied to couple biomolecules to the amino-, hydroxyl or carboxyl terminated diamond surfaces. [13, 119–121]

### 1.3.4 Diamond in biosensing

Thanks to it chemical inertness, biocompatibility and low toxicity, diamond is promising material in many engineering, medical and biotechnology applications. It can be used either in the form of nanoparticles, or thin nanocrystalline coating. Despite its chemical inertness, diamond surface can be functionalized with different surface termination (as discussed above) in order to attach different drugs or biomolecules [122]. Bio-applications of diamond are very wide, this part will discuss the use of diamond in biosensing technology.

Development of biosensors involves integration biomolecules within microelectronic devices. This needs to develop an interface compatible with microelectronic fabrica-

tion methods that also enables biofunctionalization and provides stability and selectivity when exposed to biological environment [123]. Protocols for biofunctionalization of microelectronic-compatible materials, such as silicon, glass or gold, has been well developed. However, the interface between these materials and biomolecules is not stable and its degradation is problem mainly for real-time and long-term monitoring [123, 124]. Diamond became a competitive material, as it is compatible with microelectronic processing methods and provides stable immobilization of biomolecules, such as DNA [125, 126] or aptamers [127] via covalent attachment [128]. Radadia *et. al.* showed that proteins attached to the UNCD surfaces has extended stability and retain their activity at physiological conditions compared to glass surfaces [129]. Recently, Zhang *et. al* developed diamond solution-gate field-effect transistor using H-terminated diamond functionalized with specific antibody for detection of SARS-CoV-2 N-protein [130].

As diamond possesses also extraordinary electrochemical properties, such as low background current and wide potential window, it was successfully used to develop electrochemical biosensors [131]. In addition to its excellent properties, diamond showed less propensity to fouling during electrochemical measurement in comparison to other conventional electrodes materials, such as metallic electrodes, metal oxides or glassy carbon electrodes. The electrode fouling is problem, that can cause passivation of the electrochemically active surface and thus deterioration of sensing performance [132]. Bijnens *et. al.* developed a fast and label-free immunosensor for C-reactive protein (CRP) detection using H-terminated NCD layer functionalized with anti-CRP antibodies [133]. BDD electrodes were also used to eliminate water's micropollutants and resistant bacteria. It was shown, that the electrochemical oxidation treatment using BDD electrode was able to decrease analyzed pharmaceutical and drugs concentrations by more than 51 %, and for coliform bacteria and staphylococci the efficiency reached almost 100 % in the Slovakia and Czech Republic wastewater [134]. BDD electrodes are often used for inactivation of bacteria in water, see review of Martínez-Huitle and Brillas [135]. EIS method was successfully used to detect SARS-CoV-2 virus using N protein antibody-modified BDD electrodes [136]. BDD electrodes are also used for dopamine and melatonin detection, that are neurotransmitters and their detection is important in investigation of neurodegenerative diseases. [137, 138]

### Diamond-based acoustic sensors for biosensing

This Thesis studies the acoustic sensors with integrated diamond coating for biosensing applications. As was written in the previous section, diamond is widely used in bio-applications, but there are only few studies on diamond-based biosensors. In the acoustic technology, diamond is more often used in high-frequency applications as a substrate due to the very high diamond's acoustic velocity [139].

The idea of integrating of diamond with acoustic devices for the biosensing is not new, but the low Curie temperature of quartz was long time an issue for the NCD layer depositions [140]. Procházka *et. al* showed that intrinsic diamond coated QCMs with H-NCD or O-NCD termination possesses enhanced sensing performance for bovine serum albumin and fibronectin proteins in comparison to bare QCM sensors [140]. Manai *et. al* developed BDD diamond micro-cantilever for odorant detection in liquid phase by immobilization of two olfactory receptors - mouse M17 and chimpanzee OR7D4 [141]. SAW resonator coated with diamond nanoparticles with Major Urinary Proteins from mouse as recognition element was developed for artificial olfaction applications [142]. To my knowledge, there has been no previous studies on the integrating of diamond coating with LW-SAW sensors for biosensing application for bacteria detection.

# 2 | Aims of the Thesis

This work aims to carry out essential research on diamond-coated LW-SAW sensors to determine their suitability for pathogenic bacteria detection in aqueous solutions.

The research directions are more particularly specified as follows:

1. Theoretical investigation of diamond-coated LW-SAW sensors
    - To study the effect of different materials on the properties of diamond-coated LW-SAW sensors, such as phase velocity, electromechanical coupling coefficient and sensitivity
    - To discuss the possibilities to obtain high sensitive LW-SAW sensor with diamond coating
2. Fabrication and characterization of diamond coated LW-SAW sensors
    - To fabricate LW-SAW sensors, study its properties and evaluate the accuracy of theoretical results
    - To fabricate LW-SAW sensors with different types of diamond coatings and discuss their properties
3. Functionalization of diamond surface
    - To produce N-terminated His-tagged bacteriophage's tail fibers and study their binding to the bacterial host cells
    - To attach produced tail fibers to the diamond surface

# 3 | Methods

This chapter covers the main methods used within this Thesis and it contains several parts, that can be divided like follows: 1) Numerical simulation tool for the design of acoustic wave structures: This chapter presents a numerical simulation tool used for designing and studying acoustic wave structures. This tool allows for modeling and predicting the behavior of acoustic waves in specific structures. 2) SAW devices fabrication and characterization methods. This chapter explores different material options and deposition methods to optimize the performance of acoustic wave structures. 3) CVD diamond layers deposition and characterization.

## 3.1 Theoretical simulations

### 3.1.1 Basic COMSOL model

To investigate the propagation of elastic waves in multilayered structures, we utilize a solid mechanics piezoelectric model in the COMSOL Multiphysics software. This advanced model enables us to simulate and analyze the behavior of elastic waves in intricate layered systems. By leveraging this model, we can gain valuable insights into various aspects such as wave polarization, localization, and guiding within the structure. Additionally, considering the piezoelectric properties of the materials involved allows us to explore the electrical response and characteristics of practical designs. Overall, this approach provides us with a comprehensive understanding of the dynamics and interactions involved in wave propagation in multilayered structures.

In this work, we are specifically interested in surface or guided acoustic waves, where the penetration depth is typically close to the wavelength or less. To operate within the desired frequency range of a few hundred MHz, the wavelength will be kept in the range of 10 µm to 20 µm. With this in mind, a basic unit cell model consists of 60 µm-

height piezoelectric substrate (quartz, $LiNbO_3$, $LiTaO_3$) covered by a guiding layer. Euler angles for ST-cut quartz were chosen to obtain 90 degrees rotated substrate around $z$-axis, since fast shear waves (5060 m/s) propagate along the $x$-axis ($y$-axis of ST-cut quartz substrate) and Rayleigh waves cannot be generated because of zero electromechanical coupling coefficient. The substrate was divided into two parts: the lower part includes damping material to prevent surface waves from propagating downwards, while the upper part allows for the propagation of surface waves on the top surface. This configuration enables to focus the analysis on the desired surface wave phenomena while mitigating unwanted effects from the bottom surface.

Floquet periodic conditions are a mathematical framework used to model and analyze elastic waves in periodic structures. These conditions allow us to study wave behavior in an infinitely repeating structure by imposing periodicity constraints on the wave solutions. In the context of elastic waves, Floquet periodic conditions involve expressing the displacement and stress fields as a combination of a plane wave and a periodic function. The periodic function accounts for the repeating nature of the structure, while the plane wave component represents the wave propagation direction. By applying Floquet periodic conditions, we can analyze the dispersion properties, band structures, and wave propagation characteristics in periodic elastic structures. This framework is particularly useful in understanding the interaction of waves with periodic boundaries and the formation of bandgaps, which are frequency ranges where certain wave modes are prohibited from propagating through the structure. Overall, Floquet periodic conditions provide a powerful tool for studying elastic wave phenomena in periodic structures, enabling us to explore their unique properties and design novel devices based on wave manipulation.

Floquet periodic conditions (expressed by equation (3.1)) were applied along the $y$-axis and $x$-axis to obtain whole crystal by repetition of the unit cell.

$$\vec{u_{dst}} = \vec{u_{src}} e^{-j\vec{k_F}\cdot(\vec{r_{dst}}-\vec{r_{src}})}, \tag{3.1}$$

where $\vec{u_{src}}$ and $u_{dst}\rightarrow$ were displacement vectors of the source and the destination, $\vec{r_{src}}$ and $\vec{r_{dst}}$ were vectors of the source and the destination, $\vec{k_F}$ was wave vector fixed to pi/a, which was the boundary of the irreducible Brillouin zone. From the relations $k = \frac{\pi}{a}$ and $k = \frac{2\pi}{\lambda}$ we could deduce that $\lambda$ is fixed to $2a$. The basic model is shown in the figure 3.1.

To distinguish between bulk (BAW) and surface acoustic waves (SAW), the wavelength

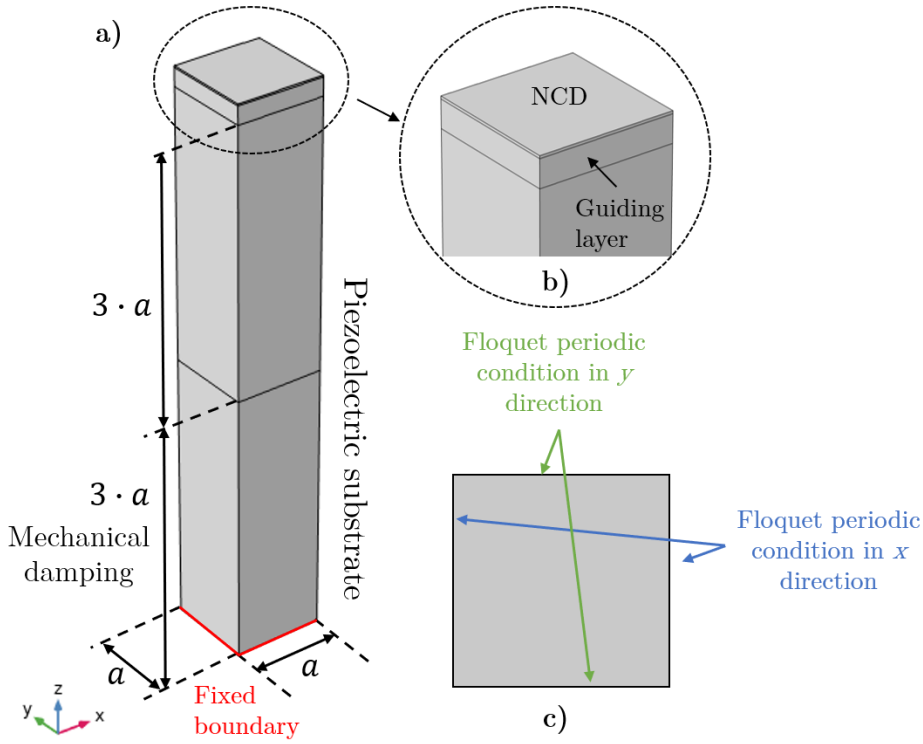


Figure 3.1: Basic COMSOL model used for theoretical calculations: a) whole structure, b) detail of the upper part with the guiding and diamond layers c) top view with shown periodic conditions

normalized energy depth ($NED$) was calculated to select surface modes:

$$NED = \frac{\iiint_V \frac{1}{2} T_{ij} S^*_{ij}(-z) dxdydz}{n\lambda \iiint_D \frac{1}{2} T_{ij} S^*_{ij} dxdydz}, \tag{3.2}$$

where $T_{ij}$ and $S_{ij}$ are the stress and strains components, star symbol denotes complex conjugate. $D$ means that we integrate across whole domain, $\lambda$ is the wavelength. For the continuous guiding layer, $n = 1$. The average depth of the acoustic energy is less than a wavelength for surface acoustic modes resulting in $NED < 1$,. As SAW includes SH type and Rayleigh type waves, the $R_{SH}$ was calculated to distinguish between them, according to equation 3.3:

$$R_{SH} = \frac{\iiint_V v_{SH} v^*_{SH} dxdydz}{\iiint_V (u_x u^*_x + v_y v^*_y + w_z w^*_z) dxdydz} \tag{3.3}$$

where $u_x, v_y$ and $w_z$ are displacement component in $x$, $y$ and $z$ direction respectively, $v_{SH}$ is SH component of the displacement, $V$ denotes the whole volume of unit cell. Complex conjugate is marked with the star symbol (*) [143].

### 3.1.2 Model with IDTs electrodes

For some simulations, model with IDTs electrodes were used. The unit cell model was the same as described above, only electrodes were added on top of the piezoelectric substrate. One electrode was set to potential 1 V and the second one was grounded.

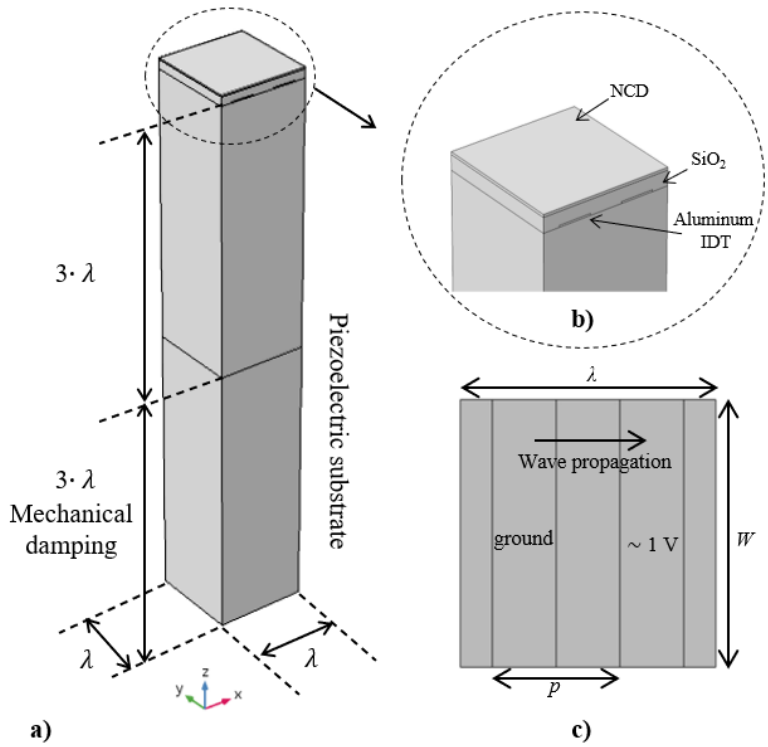


Figure 3.2: COMSOL model with IDTs electrodes: a) whole structure, b) detail of the IDTs electrode and c) top view with shown parameters of wavelength $\lambda$ and acoustic aperture $W$

### 3.1.3 Phononic crystal model

A 30 µm-height 90ST-cut quartz substrate [Euler angles = (90°, 132.75°, 0°), LH 1978 IEEE] for generation of fast shear (SH) waves propagating along the x-axis was used. To calculate the dispersion curves of the band structure, unit cell of the PnMs with the square array period with lattice constant $a$, resulting in the wave wavelength $\lambda = 2a$, was constructed in COMSOL Multiphysics software. The irreducible Brillouin zone (BZ) was square bounded by Γ-X-M-Y-Γ and the band structures were calculated only in the Γ-X direction. The model setup was then the same as described in previous section 3.1 Theoretical simulations. The NED was calculated according to equation 3.2, where for the pillar PnMs $n = 1 + h_p/\lambda$ because of the pillar height, and SH ratio was calculated

according to equation 3.3. COMSOL model of different configurations used in this study is shown on the Figure 3.3, where $a$ is lattice constant, $h_{SiO2}$ is thickness of guiding silica layer, $r$ is pillar radius and $h_p$ is height of the pillar.

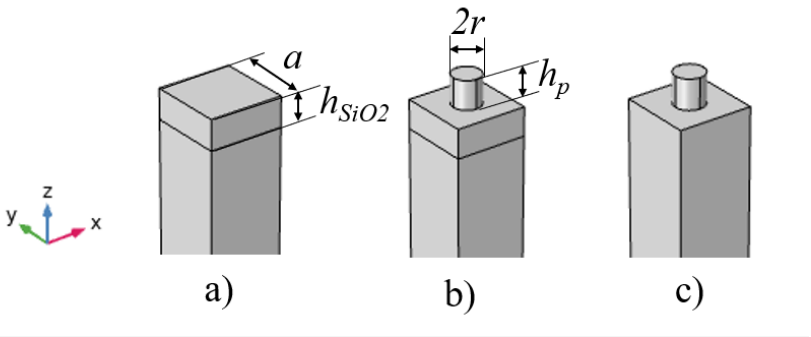


Figure 3.3: Different configurations of COMSOL model for calculation of phononic crystals band structures: a) 90ST-cut quartz substrate with silica guiding layer, b) quartz substrate with silica guiding layer and diamond or $SiO_2$ PnMs and c) quartz substrate directly with diamond or $SiO_2$ PnMs

### 3.1.4 Transmission model

The phononic band structures show the resonance and polarization of the PnCs. To better understand the band structures, the transmission spectra of 3D PnCs were calculated in COMSOL Multiphysics.

The simulation was realized by using the SAW device model consisting of two parts of IDTs and PnC located between the IDTs electrodes. As the model was symmetrical along the y-axis, the boundary periodic conditions were applied to the y-axis reducing the model to only one period. To avoid undesired reflections, the model was surrounded by perfectly matched layer and lateral and bottom sides were kept fixed. To obtain the fast shear acoustic waves, 20 pairs of 200 nm thick IDTs aluminum electrodes were added on top of the piezoelectric 90ST-cut quartz substrate. To excite the acoustic waves in the quartz substrates, the harmonic voltage $V_0 = 1$ V was applied on the even fingers of the IDTs acting as a transmitter. Odd fingers were grounded. Generated acoustic waves confined in the $SiO_2$ guiding layer propagated through the phononic crystals, consisted of 10 pillars, to the second set of IDTs fingers acting as a receiver. The output signal was obtained by averaging voltage variations between the even and odd IDTs fingers, where odd fingers were grounded and even fingers were set to zero surface charge accumulation. The transmission spectra were calculated at the fixed wavelength and the width of the

IDTs was calculated according to the relation $L_{IDT} = \frac{\lambda}{4} = \frac{v}{4f}$, where $v$ was the velocity of the Love waves resulting from the dispersion relation of the Love waves and $f$ was the frequency of the pillar resonance obtained from the band structure.

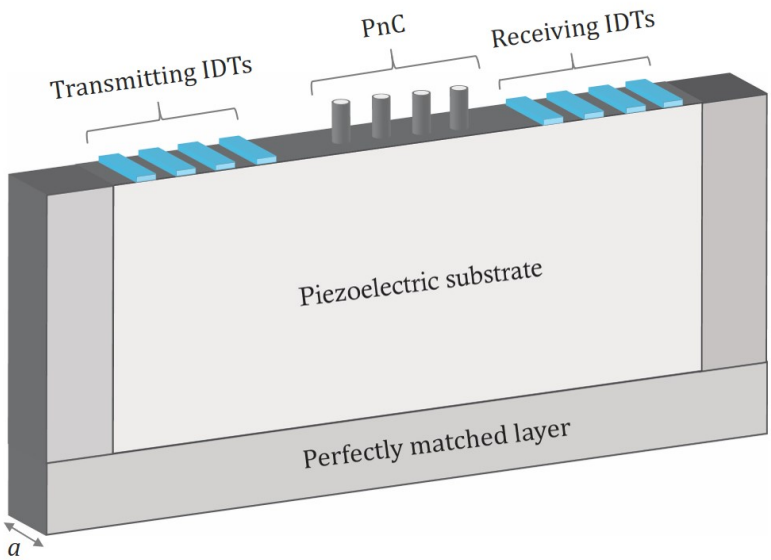


Figure 3.4: Model of the SAW device used for the calculation of the transmission through PnC

The dispersion curve for velocity of Love waves as a function of the frequency was calculated using COMSOL Multiphysics for the 90ST-cut quartz substrate with 1.5 or 2 thick µm $SiO_2$ guiding layer. To obtain exact velocity for the pillar resonance frequency, the dispersion curve was fitted using Matlab software, as is shown in the figure 3.5.

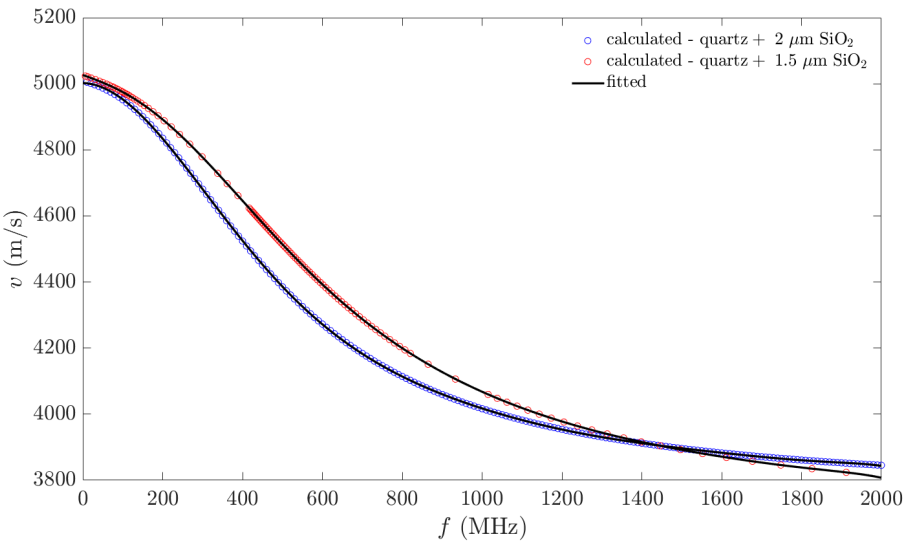


Figure 3.5: Dispersion curve of the velocity of Love waves for two different $SiO_2$ guiding layer thicknesses with shown fitted curve obtained in Matlab

## 3.2 SAW device fabrication & characterization

Piezoelectric wafers were purchased from Krystaly, Hradec Králové. Schematic pictures of the fabricated LW-SAW sensors with IDTs electrodes, a guiding layer and thin NCD layer is shown in figure 3.6. For the fabrication of LW-SAW sensor used in this Thesis, the simple IDT geometry was chosen. It means that IDTs consist of alternating polarity (single finger) with unapodized fingers (equal finger's length) and with equal finger width and gap resulting in metallization ratio 0.5.

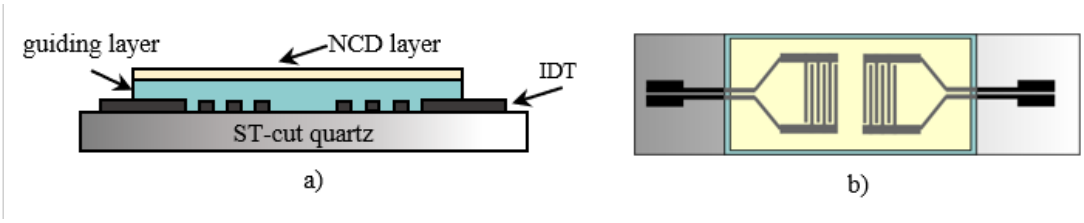


Figure 3.6: Structure of diamond coated LW-SAW sensor: a) cross-section, b) top view

LW-SAW sensors were fabricated using conventional microtechnology techniques at Institute of Physics CAS and at CEITEC (Central European Institute of Technology) in cooperation with Ing. Imrich Gablech, Ph.D., as described below. SAW device fabrication at IoP was done to test device's design one by one, larger scale production was done at CEITEC in their clean room lab, as their equipment is more suitable for work with wafer size samples.

### 3.2.1 SAW device fabrication at IoP

#### Metal deposition

Prior to aluminum metal deposition, piezoelectric substrates were cleaned by sonication in acetone, isopropyl alcohol and hot deionized water for 5 minutes each followed by cleaning in mixture of sulfuric acid $H_2SO_4$ (98%) and hydrogen peroxide (30%) (mixture ratio 1:1) for 10 minutes and rinsed 5x in the deionized water. 200 nm thick aluminum layers were deposited by a sputtering method in homemade magnetron sputtering system. Used deposition conditions are written in table 3.1.

Table 3.1: Used conditions for Al layers deposition by magnetron sputtering

| Pressure | Gas | Power | Voltage | Distance target - substrate | Target diameter | Deposition rate |
|---|---|---|---|---|---|---|
| 0.5 Pa | Ar, 16 sccm | 420 W | 450 V | 10 cm | 100 mm | 100 nm/min |

### Patterning of IDTs electrodes

Interdigital transducers (IDTs) electrodes were patterned using optical photolithography technique followed by chemical wet etching. The design of the mask was done in the CleWin5 software. Negative photoresist ma-N 1410 (purchased from Micro resist technology GmbH) was deposited on metal coated piezoelectric substrates by spin coating at 3000 rpm for 30 s followed by baking at 110 ° for 150 s on a hot plate. Exposure of photoresist was done using laser writing MicroWriter (from Durham) apparatus followed by hard baking at 120 ° for 150 s. Exposure conditions are given in the table 3.2. The exposed pattern was developed in ready-to-use developer ma-D 533/S (purchased from Micro resist technology GmbH) for 40 s and thoroughly rinsed in deionized water and dried using the cleaned and dry compressed air. The final pattern was obtained by wet chemical etching of aluminum layer in the mixture of $H_3PO_4$ : $CH_3COOH$ : $HNO_3$ : $H_2O$ with the mixing ratio 19:1:1:2 for 4 minutes. Then the samples were rinsed in isopropyl alcohol and DI water before being dried using cleaned and dry compressed air.

Table 3.2: Used exposure conditions for negative photoresist ma-N 1410 at MicroWriter photolithography apparatus

| Laser diameter | Laser wavelength | Quality of exposure | Focus correction | Exposure mode | Exposure dose |
|---|---|---|---|---|---|
| 1 µm | 405 nm | 0.5 µm/pixel | 0.4 | X raster | 300 mJ/cm$^2$ |

### Deposition of guiding layers

To obtain SAW sensor with Love waves, two materials were used as a guiding layers - silicon oxide and zinc oxide.

***Deposition of $SiO_2$ guiding layers***

Amorphous silicon oxide layers were deposited in cooperation with J. Bulíř at IoP by radiofrequency magnetron sputtering method or at Institute of Electronics, Microelectronics and Nanotechnology (IEMN), Lille, France using low temperature plasma enhanced

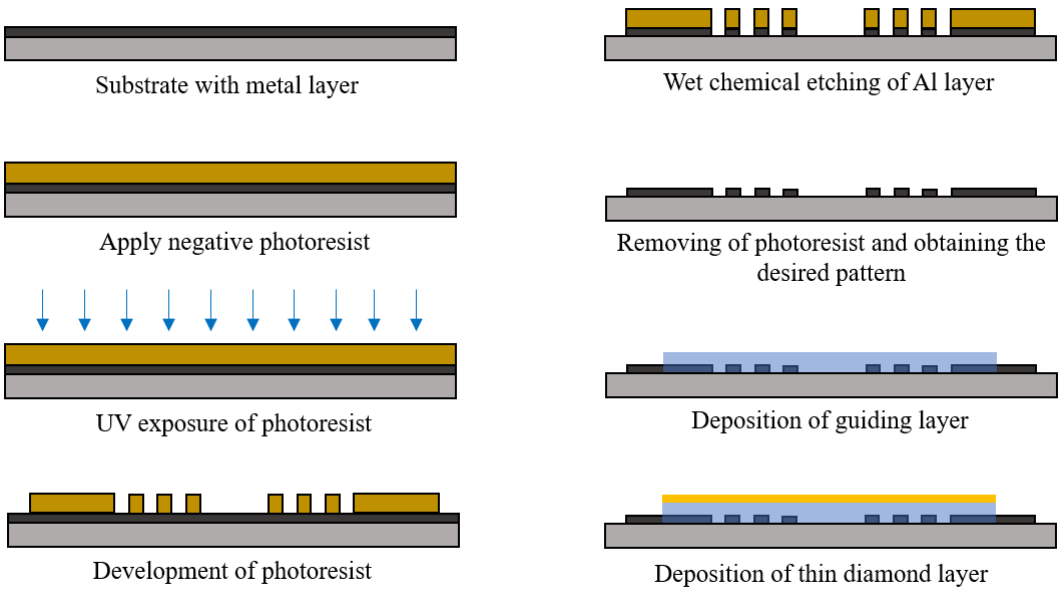


Figure 3.7: Scheme of a process for patterning IDTs electrodes followed by guiding and diamond layer deposition

chemical vapor deposition (PECVD) Plasmalab 80 plus deposition system from Oxford Instruments. Used conditions are reported in table 3.3. IDTs pads were mechanically protected during all the depositions.

Table 3.3: Amorphous $SiO_2$ layers deposition conditions

| | **$SiO_2$ (IEMN)** | **$SiO_2$ (IoP)** |
|---|---|---|
| Gas composition | 150 sccm $SiH_4$, 700 sccm $N_2O$ | 10 sccm Ar, 2 sccm $O_2$ |
| Power | MW, 20 W | RF, 200 W |
| Process pressure | 1.3 mbar | 1 Pa |
| Substrate temperature | 300 °C | RT |
| Growth rate | 67.5 nm/min | 8 nm/min |

***Deposition of ZnO guiding layers***

Zinc oxide layers were deposited in cooperation with Ing. Petr Novák Ph.D. from University of West Bohemia in Pilsen. The deposition was performed in a BOC Edwards TF 600 coating system equipped with two magnetrons connected to a radio-frequency (RF) and direct-current (DC) power supplies. The films were deposited from metallic Zinc target (3 inches in diameter) placed on RF magnetron and samples were placed in the center of a rotating holder, but not directly opposite to the sputtering target. This layout allows eliminating the influence of the high-energy negative ions accelerated by cathode sheet voltage. These high energy ions lead to deterioration of structure. The distance

between the target and substrate was 150 mm and the substrate holder was on a floating potential. The mixture of argon and oxygen was used to ensure complete oxidation of the film, thereby simulating oxygen-rich conditions. The substrates were heated on 350 °C to ensure good crystalline quality and strong preferential orientation. Conditions used for ZnO layers deposition are listed in the table 3.4.

Table 3.4: Conditions used for deposition of zinc oxide layers using magnetron sputtering

| **RF power (W)** | **Discharge voltage (V)** | **Gas composition** | | **Pressure (Pa)** | **Temperature (°C)** |
|---|---|---|---|---|---|
| | | **$O_2$** (sccm) | **Ar** (sccm) | | |
| 600 | 860-1060 | 4 | 3 | 1 | 350 |

### 3.2.2 SAW device fabrication at CEITEC

SAW devices were fabricated using physical vapor deposition (PVD) for Ti/Al electrodes and plasma-enhanced chemical vapor deposition (PECVD) for $SiO_2$ guiding layer.

#### Metal deposition

For metal deposition, the substrate was loaded in ion-beam sputtering instrument equipped with two Kaufman ion-beam sources (IBS). Primary IBS was used for deposition and the secondary IBS was used for substrate pre-cleaning to remove adsorbed impurities on wafer. The pre-cleaning procedure was done for 5 minutes with Ar ions at low energy of 36 eV. Such low energy is safe for substrate and cannot cause damage or changes of electrical and mechanical parameters. Then was used primary IBS for deposition of 3 nm thick Ti adhesion layer using Ar ions with energy of 600 eV. This step was followed by deposition of 200 nm thick Al layer employing Ar ions with energy of 900 eV.

#### Patterning of IDTs electrodes

Shaping of interdigitated electrodes was done using UV lithography employing positive photoresist and etching using $BCl_3/Cl_2$ plasma mixture in RIE instrument. The photoresist was then removed using dimethylsulfoxid (DMSO) for 10 minutes at 80 °C, rinsed by demineralized water and dried by compressed nitrogen.

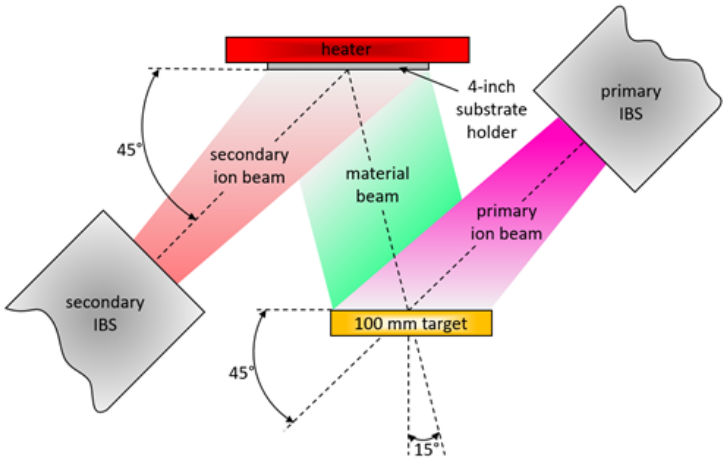


Figure 3.8: Scheme of ion-beam sputtering instrument with two Kaufman ion-beam sources (IBS)

### Deposition of $SiO_2$ guiding layer

Such cleaned wafer was then placed to the PECVD instrument for deposition of 2.5 $\mu$m thick $SiO_2$ layer. Windows on pads for electrical connections were opened using the same type of photolithography and photoresist as in previous step. Consequent etching of $SiO_2$ was done using mixture of $CHF_3$/Ar plasma using RIE method. When the etching of $SiO_2$ was done, wafer was cleaned using the same procedure as is described before. Wafer was then covered using positive photoresist and cut into single chips using dicing saw.

## 3.2.3 Frequency characterization

Fabricated LW-SAW sensors were characterized using a vector network analyzer Agilent E8364B and Summit 9000 Analytical Probe Station with Infinity probes at Institute of Physics, CAS, shown in the figure 3.9. Reflection $S_{11}$ and $S_{22}$ and transmission $S_{21}$ and $S_{12}$ scattering parameters were measured in magnitude and phase at the room temperature.

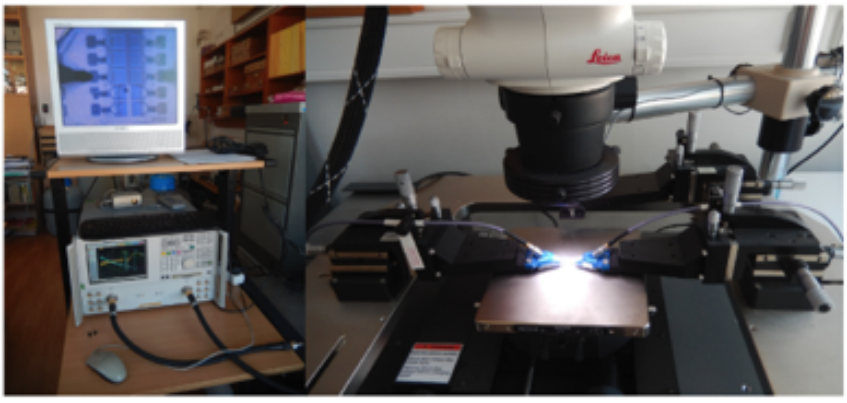

Figure 3.9: Network analyzer with a probe station

## 3.3 Diamond layers deposition & characterization

Thin nanocrystalline diamond (NCD) layers were deposited at a low temperature (< 500 °C) to preserve piezoelectric properties of the quartz substrate using microwave linear antenna plasma enhanced chemical vapor deposition (MW-LA-PECVD) apparatus for low temperature deposition and AX5010 apparatus from Seki Diamond System for conventional NCD deposition, see figure 3.10. Prior to NCD growth, LW-SAW samples were seeded with nanodiamond particle water based colloids (NanoAmando®B from NanoCarbon Research Institute Ltd., average mean crystal size of 4-6 nm) by spin coating for introduction of diamond nucleation sites on the sample's surface. The IDTs contact pads were mechanically protected by clean lab tape as solid mask (F04xx tape from Semiconductor Equipment Corp.) to ensure they would not be coated with insulating diamond. Conditions for NCD layers deposition are reported in table 3.5. Deposition conditions of used BDD layers are discussed and listed directly in the chapters in the results section.

Table 3.5: Intrinsic NCD layers deposition conditions at low temperature

| | NCD layer |
|---|---|
| Gas composition | 92 % $H_2$, 5 % $CH_4$, 3 % $CO_2$ |
| MW power | $2 \cdot 2.75$ kW |
| Process pressure | 0.25 mbar |
| Substrate temperature | $320 < T < 500$ °C |
| Growth rate | 20 nm/h |

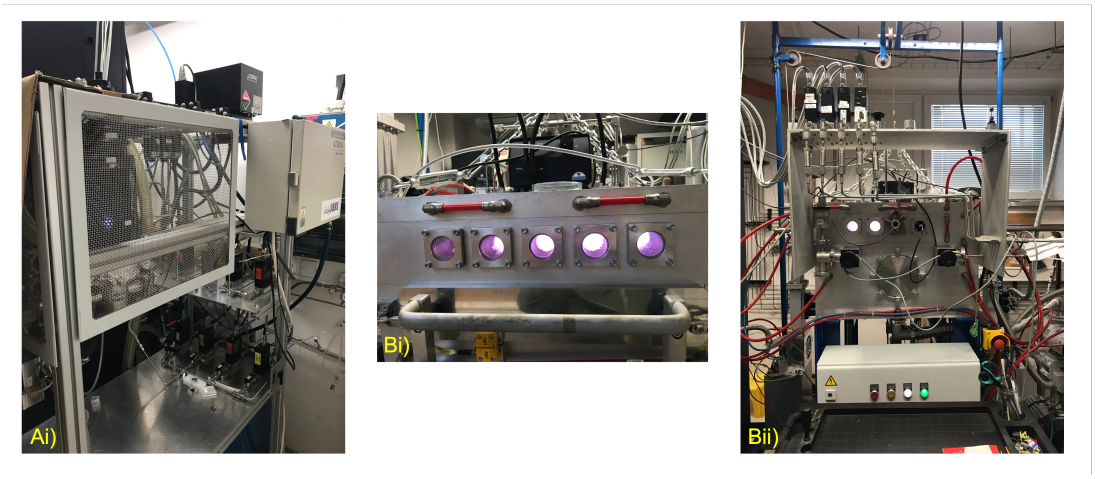


Figure 3.10: Apparatuses for CVD deposition of thin diamond layers, A) high temperature AX5010 deposition system from Seki Diamond System, Japan and B) MW-LA-PECVD apparatus from Leybold Optics Dresden, Germany for low temperature deposition

### 3.3.1 Morphology NCD layer characterization

The morphology and the roughness of the NCD layers were investigated by Atomic force microscopy (AFM) using a Dimension Icon ambient AFM in Peak Force Tapping mode with Tap150Al-g tips and Tescan FERA3 scanning electron microscope (SEM). AFM was also used to measure thickness of the diamond layers.

### 3.3.2 Raman spectroscopy

The quality of diamond layers was investigated using Raman spectroscopy using Renishaw InVia Raman microscope with a 488 nm excitation laser at a power of 25 mW at 20 °C. Raman spectra were normalized to the diamond peak. Raman spectroscopy is widely used to determine the quality of diamond, i.e. non diamond carbon concentration ($sp^2$ carbon) as well as diamond dopants, such as boron (peak at 500 $cm^{-1}$). In Raman spectra, $sp^2$ carbon fraction is responsible for peaks at 1600 $cm^{-1}$ (G band) and 1345 $cm^{-1}$ (D band), peaks at 1100 - 1150 $cm^{-1}$ and 1430 - 1470 $cm^{-1}$ are attributed to the trans-polyacetylene C-H chains at grain boundaries and surfaces, shown on figure 3.11. The diamond zone-center phonon peak is located at 1332 $cm^{-1}$ and is used as a signature of high crystalline quality [144, 145].

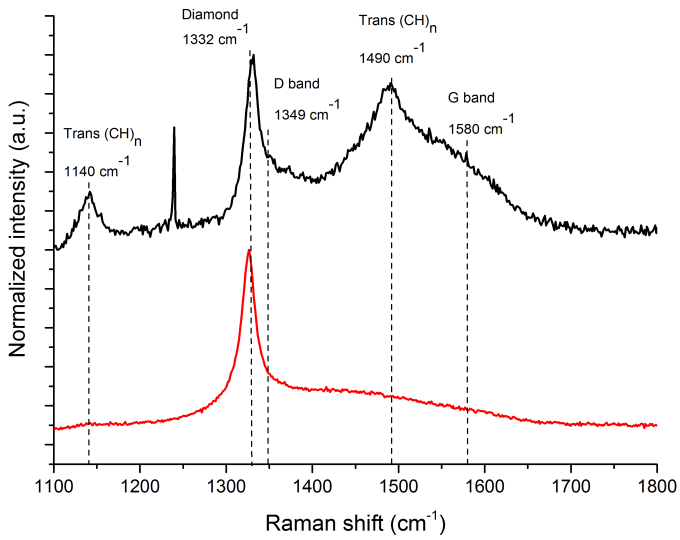


Figure 3.11: Raman spectra of CVD nanocrystalline diamond layers. Red line - CVD layer without impurities, clear diamond peak at 1332 $cm^{-1}$. Black line - NCD layer with a significant fraction of non diamond carbon (D and G band attributed to $sp^2$ carbon, peaks attributed to trans-polyacetylene), diamond peak at 1332 $cm^{-1}$ [13].

### Raman spectra of BDD layers

When diamond layers are boron doped, new peaks appear in the Raman spectra - peak at 500 $cm^{-1}$ and 1230 $cm^{-1}$ and the diamond zone-center phonon line is red shifted. The intensity of boron-related peaks increases with the increasing boron concentration, see figure 3.12, [146].

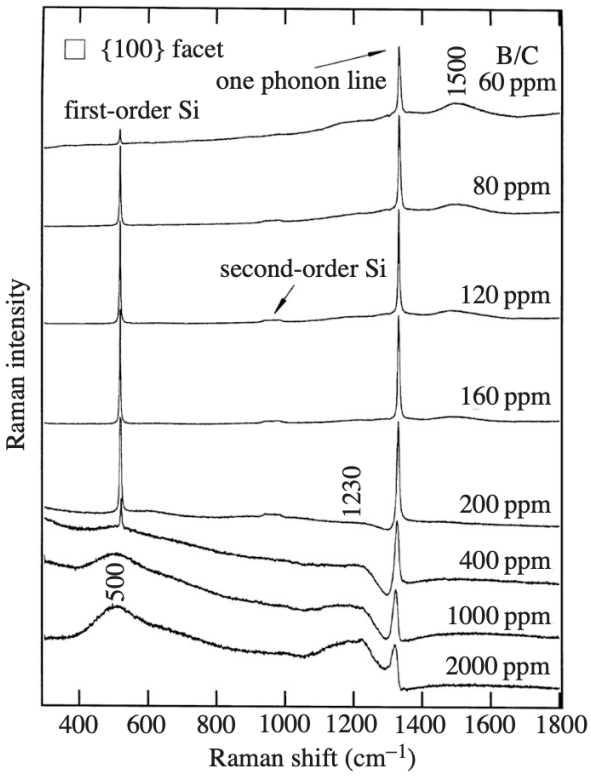


Figure 3.12: Raman spectra of BDD layers with different boron concentrations, reproduced from [146]

# 4 | Results and discussion

This chapter summarizes the work carried out within this Thesis. The development of biosensors is complex task involving optimalization and fabrication of physical transducer, production of biosensing elements and their immobilization on the surface of the transducer. All these important steps of biosensor development are discussed within the following eight chapters. Three of them are theoretical about FEM simulations of LW-SAW sensors, two chapters describes experimental work on LW-SAW sensors, one chapter is devoted to the production and purification of his-tagged bacteriophage tail fibers, one chapter focuses on functionalization of boron doped diamond layers in order to attach produced tail fibers to the BDD surface and last chapter summarizes work on the QCM sensors with BDD layer and its functionalization.

## 4.1 FEM simulations of the properties of diamond coated LW-SAW sensors

The aim of this chapter is to investigate the behavior of the LW-SAW sensors after the addition of the diamond layer on top of the sensitive area of the sensor's surface. Three most commonly used piezoelectric substrates for LW devices were investigated - quartz, lithium tantalate ($LiTaO_3$) and lithium niobate ($LiNbO_3$) in combination with two mostly used guiding layers materials - $SiO_2$ and ZnO.

### 4.1.1 Methods

Theoretical simulations were carried out using COMSOL Multiphysics software with model described in the section 3.1 Theoretical simulations, subsection 3.1.1 Basic COMSOL model. The dispersion curves were calculated for guiding layer normalized thickness $h_{guid}/\lambda$ between 0.01 and 1 by fixing $\lambda = 10$ µm and varying the thickness of $SiO_2$ layer for different thicknesses of the diamond coating $h_{NCD}$. The data calculated in COMSOL Multiphysics were processed by script in Matlab in order to filter out BAW modes (equation 3.2) and to distinguish between Rayleigh and SH modes (equation 3.3).

The FEM analysis is used to compute eigenfrequencies of the acoustic modes, the phase velocity was calculated using the basic equation:

$$v\ (m/s) = f \cdot \lambda, \tag{4.1}$$

where $v$ is the phase velocity, $f$ is the frequency of the acoustic mode and $\lambda$ is the acoustic wave wavelength. The electromechanical coupling coefficient ($K^2$) is theoretically given by:

$$K^2\ (\%) = 2 \cdot \frac{v_{free} - v_{metal}}{v_{free}} \cdot 100, \tag{4.2}$$

where $v_{free}$ and $v_{metal}$ are the free surface and metalized (short-circuited) surface phase velocities [83]. This equation was used to calculate the $K^2$ in this chapter. The surface of the piezoelectric material was grounded for the calculation of the eigenfrequencies

of short-circuited surface. The sensitivity was calculated by adding thin poly(methyl) methacrylate (PMMA) layer on top of the model structure. As the density of the PMMA is $\rho = 1.18$ g/cm$^3$, the mass per unit area could be calculated and sensitivity was then obtained by using the equation:

$$S_m = \lim_{\Delta m \to 0} \frac{\Delta f}{f_0 \cdot \Delta m}, \tag{4.3}$$

where $f_0$ is unperturbed operational frequency, $\Delta f$ is the change in the operational frequency caused by mass loading and $\Delta m$ is the mass per unit area [147].

### 4.1.2 ST-cut quartz LW-SAW sensors

Figure 4.1a) shows that the phase velocity is constant for $h_{SiO2}/\lambda$ below 0.04 for uncoated LW-SAW sensor with $SiO_2$ guiding layer and decreases above this value. This is attributed to trapping of the acoustic waves in the $SiO_2$ guiding layer with slower shear velocity (2850 m·s$^{-1}$) than the piezoelectric substrate. The phase velocity increase with the thickness of the NCD layer is attributed to the increasing stiffness of the sensor's surface. The highest sensitivity of LW-SAW sensor is obtained in the region of the largest dispersion of the phase velocity. Figure 4.1c) shows that the optimal sensitivity is obtained for silicon oxide normalized thickness $h_{SiO2}/\lambda$ between 0.1 and 0.5 and it is shifting the highest sensitivity to higher $h_{SiO2}/\lambda$ values with higher diamond coating thicknesses. Within this range of normalized thickness $h_{SiO2}/\lambda$, $K^2$ is decreasing from 0.25 to 0.1 %, (see figure 4.1b)). The last graph 4.1d) shows the sensitivity as a function of diamond normalized thickness $h_{NCD}/\lambda$ for $h_{SiO2}/\lambda$ equals to 0.15 and 0.3. Steep decrease in sensitivity is observed for increasing $h_{NCD}/\lambda$ reaching zero sensitivity at $h_{NCD}/\lambda = 0.007$ and 0.03 for $h_{SiO2}/\lambda = 0.15$ and 0.3 respectively, which confirms the graph 4.1c) and highlights the importance of thin diamond coating.

The behavior of ST-cut quartz LW-SAW sensors with ZnO guiding layer is very similar to the sensors with $SiO_2$ guiding layer. Figure 4.2a) shows that phase velocity dispersion curves are decreasing since lower values of $h_{ZnO}/\lambda$ which shifts the highest sensitivity of LW-SAW sensors to the lower and easily reachable $h_{ZnO}/\lambda$ values in fabrication process, see 4.2c). Highest sensitivity obtained for diamond uncoated sensors is at $h_{ZnO}/\lambda = 0.4$ shifting to $h_{ZnO}/\lambda = 0.8$ for 100 nm thick diamond coating. $K^2$ is higher than for LW-

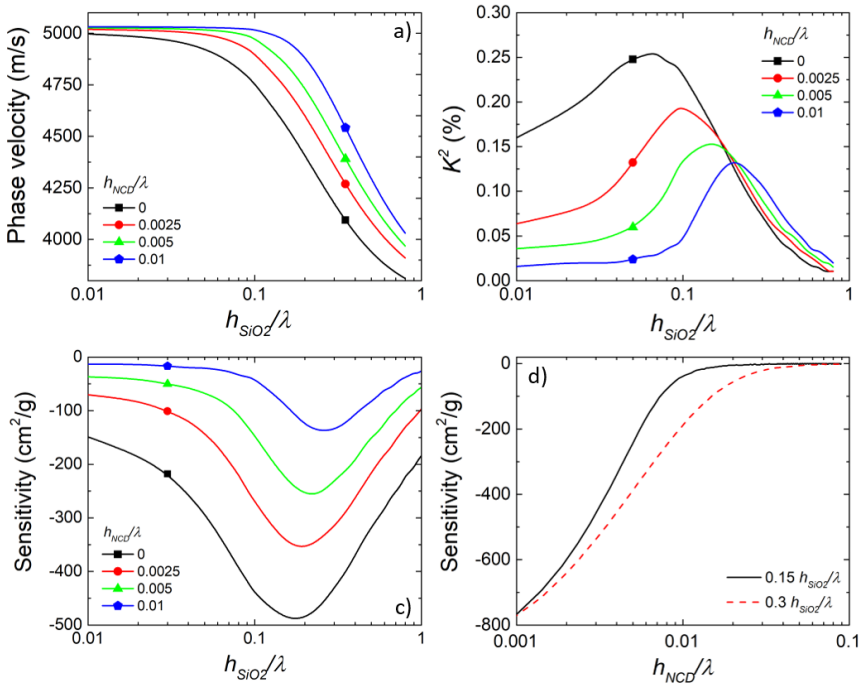


Figure 4.1: Dispersion curves for a) phase velocity, b) $K^2$, c) sensitivity as a function of silicon normalized thickness $h_{SiO2}/\lambda$ for different thicknesses of diamond coating for Diamond/$SiO_2$/ST-cut quartz structure and d) sensitivity as a function of diamond coating normalized thickness for two different silicon normalized thickness $h_{SiO2}/\lambda$

SAW with $SiO_2$ layer due to piezoelectric properties of the ZnO layer, but it also decrease with adding diamond coating, see 4.2b).

### 4.1.3 36°YX $LiTaO_3$ LW-SAW sensors

For 36°YX $LiTaO_3/SiO_2$ structure the phase velocity dispersion curves are constant to the $h_{SiO2}/\lambda = 0.2$, figure 4.3a). The cause may be that the LiTaO3 substrate does not generate pure shear waves, but leaky waves and the thickness of the guiding layer needs to be higher to trap and confine them. Phase velocity dispersion curves indicates, that the highest sensitivity is shifted to high values of $h_{SiO2}/\lambda$, see figure 4.3c). Also the drop of sensitivity after diamond coating is quite significant, as the diamond coated LW-SAW sensors almost completely loose their sensitivity. $K^2$ also decrease after diamond coating, but its value does not change much for different thicknesses of coating, figure 4.3b).

For the LiTaO3/ZnO structure the phase velocity starts to decrease earlier, as for the ST-cut quartz/ZnO. Also the ZnO layer enhances the $K^2$ which is higher than theoretical 5 % for uncoated $LiTaO_3$ substrate, but again, is reduced after adding the diamond layer,

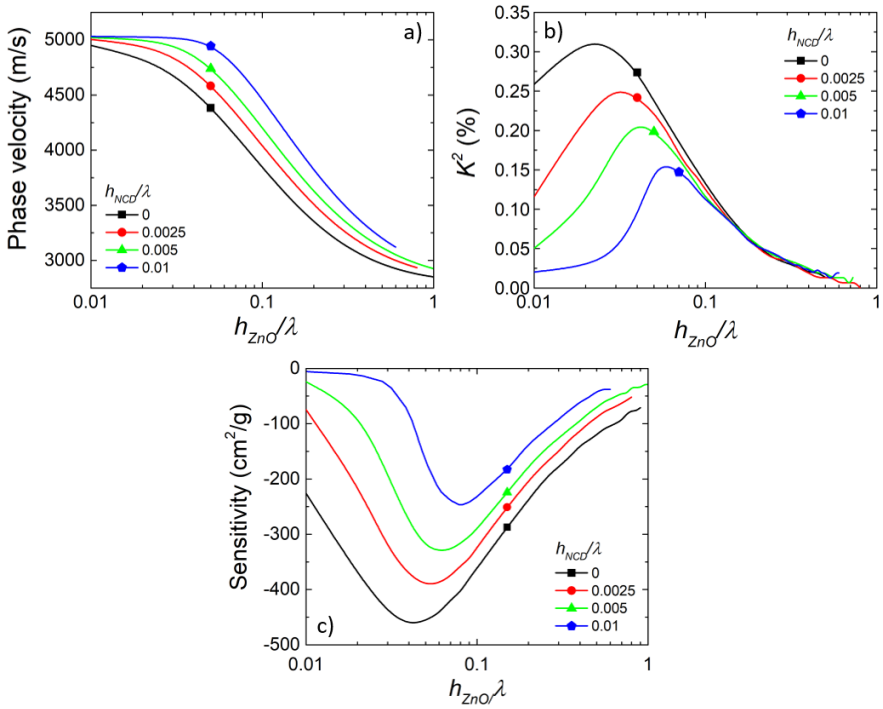


Figure 4.2: Dispersion curves for a) phase velocity, b) $K^2$ and c) sensitivity as a function of zinc oxide normalized thickness $h_{ZnO}/\lambda$ for different thicknesses of diamond coating for Diamond/ZnO/ST-cut quartz structure

figure 4.4b). The highest sensitivity is obtained for $h_{ZnO}/\lambda = 0.2$, but we can observe the same sensitivity loose after adding diamond layer as for $LiTaO_3$ with $SiO_2$ layer. This property makes $LiTaO_3$ substrate not very suitable for application in biosensing using diamond layer as interface for immobilization of biosensing elements.

### 4.1.4 36°YX $LiNbO_3$ LW-SAW sensors

Simulations were also carried out for 36°YX $LiNbO_3$ substrate with $SiO_2$ guiding layer. This substrate has the highest electromechanical coupling coefficient that after adding of diamond layer remains higher than 15 % for particular $h_{SiO2}/\lambda$ values, figure 4.5b). On the other hand, the highest sensitivity is obtained at $h_{SiO2}/\lambda = 0.25$ for uncoated LW-SAW and $h_{SiO2}/\lambda = 0.4$ for both studied thicknesses of diamond coating and the sensitive range of $h_{SiO2}/\lambda$ is very narrow, figure 4.5c). To obtain the $h_{SiO2}/\lambda = 0.4$ experimentally, we will need IDTs electrodes with small spatial periods or thick $SiO_2$ layer, which is both problematic.

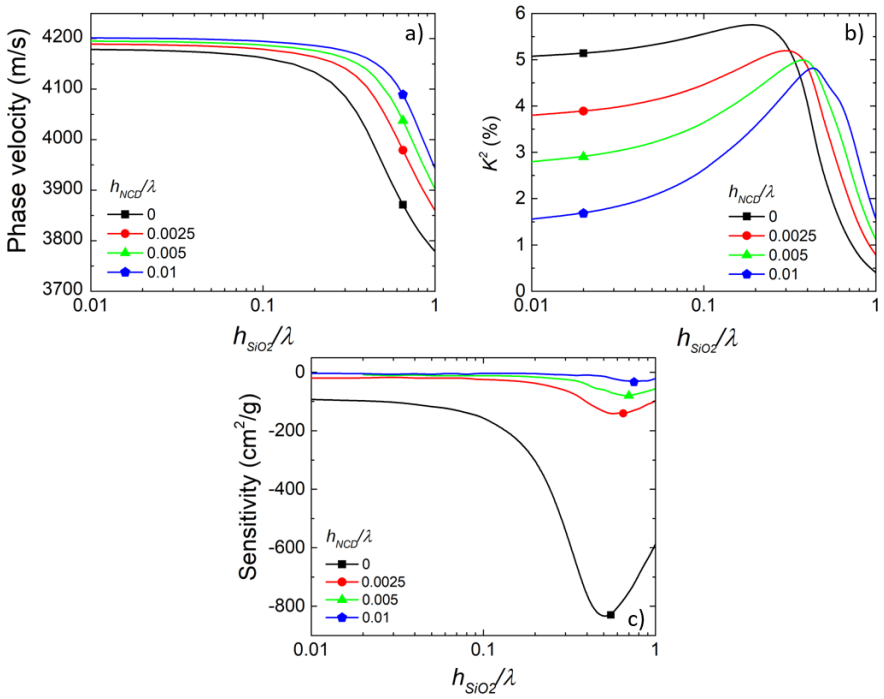


Figure 4.3: Dispersion curves for a) phase velocity, b) $K^2$ and c) sensitivity as a function of silicon oxide normalized thickness $h_{SiO2}/\lambda$ for different thicknesses of diamond coating for Diamond/$SiO_2$/36°YX $LiTaO_3$ structure

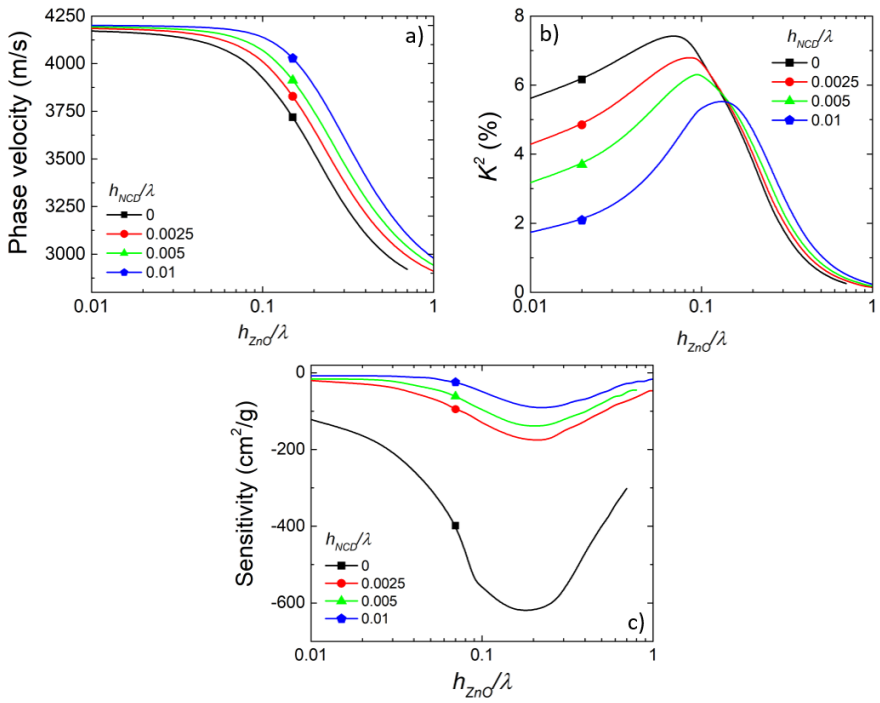


Figure 4.4: Dispersion curves for a) phase velocity, b) $K^2$ and c) sensitivity as a function of zinc oxide normalized thickness $h_{ZnO}/\lambda$ for different thicknesses of diamond coating for Diamond/ZnO/36°YX $LiTaO_3$ structure

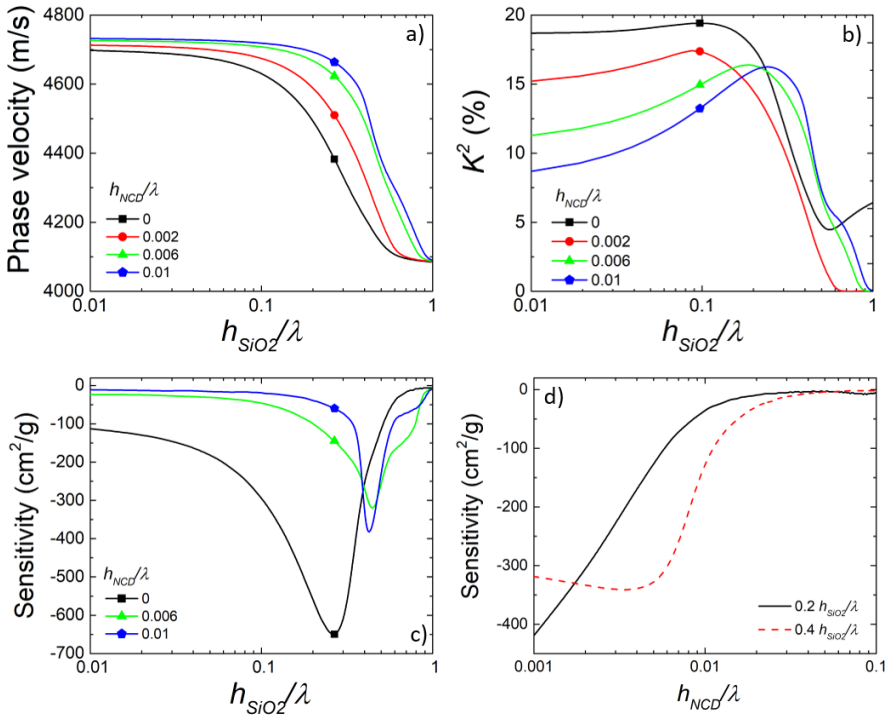


Figure 4.5: Dispersion curves for a) phase velocity, b) $K^2$ and c) sensitivity as a function of silicon oxide normalized thickness $h_{SiO2}/\lambda$ for different thicknesses of diamond coating for Diamond/$SiO_2$/36°YX $LiNbO_3$ structure and d) sensitivity as a function of diamond coating normalized thickness for two different silicon normalized thickness $h_{SiO2}/\lambda$

### 4.1.5 Conclusions

This chapter was devoted to the FEM simulations of LW-SAW sensors using different piezoelectric substrates and guiding layers materials. The aim of the chapter was to choose the materials and distinguish the parameters of the diamond coated LW-SAW sensors, such as guiding layer thickness, IDTs spatial period and diamond layer thickness, to obtain sensor with the best performance and sensitivity. The results were used to design sensors used in the following chapters.

In the design of LW-SAW sensor, it is necessary to take into account several limitations inerrant to the sensor fabrication processes. The resolution of the optical lithography method to pattern IDTs electrodes is approximately 2 µm (using the apparatus MicroWriter at IoP), which limits the IDTs spatial period to 10 µm. Deposition of $SiO_2$ guiding layer thicker than 3 µm is difficult due to high mechanical stress in the layer and the possible delamination. Deposition of very thin NCD layer is also limited, due to the necessary minimum thickness to obtain a coalesced and pin-hole free diamond layer.

The decrease of sensitivity with the addition of the continuous diamond layer on top

of LW-SAW sensors using different piezoelectric substrates lead us to think about another types of diamond coating, such as discrete diamond coating or phononic metamaterials to increase the electromechanical coupling coefficient and the sensitivity of the LW-SAW devices. These ideas will be discussed in following chapters.

## 4.2 LW-SAW devices with continuous and discrete NCD coatings

The current chapter is based on the following publication [148] and it is reprinted here with a few changes. Simulations in previous chapter showed a high decrease in sensitivity with the increasing thickness of the diamond coating. This study aims to investigate the difference between continuous and discrete NCD layer coating on LW-SAW sensors properties.

- **L. Drbohlavová**, L. Fekete, V. Bovtun, M. Kempa, A. Taylor, Y. Liu, O. Bou Matar, A. Talbi, and V. Mortet. Love-wave devices with continuous and discrete nanocrystalline diamond coating for biosensing applications. *Sensors and Actuators, A: Physical*, **298**, 2019

### 4.2.1 COMSOL simulations

Diamond/$SiO_2$/ST-cut quartz structures have been simulated using COMSOL Multiphysics software usign the basic model described in subsection 3.1.1 Basic COMSOL model. The substrate consists of an 90ST-cut quartz crystal with Euler angles (90°, 132.75°, 0°) for shear wave propagation along the x-axis and particle displacement along the y-axis. The thickness of the silicone oxide $h_{SiO2}$ and the Love wave's wavelength $\lambda$ were arbitrary fixed to 2 µm and 20 µm respectively, which corresponds to a normalized $SiO_2$ thickness $h_{SiO2}/\lambda$ of 0.1. This $h_{SiO2}/\lambda$ was chosen due to the high electromechanical coupling coefficient $K^2$ (0.26 %) of LW-SAW sensors. The theoretical study of the coalescence effect of diamond on the propagation of SH waves was carried out in three steps: 1/ deposition of an increasing number (4, 9, 16, 36, 64, 144) of diamond grains (modeled as cubes) with a fixed width (274 nm) and increasing thickness over the range of 45 nm to 200 nm (see Figure 4.11 a-b), 2/ followed by the connection of diamond grains resulting in a decreasing number (64, 36, 16, 9, 4, 1) of grains but keeping the whole surface covered (see Figure 4.11 c-d). The thickness of the diamond cubes increased over the range of 210 to 420 nm. And finally, 3/ the growth of a fully coalesced diamond layer. The results of this study were compared to the growth of a diamond layer and the effect of a rapid coalescence. The NED, equation 3.2 was calculated to filter out BAW modes

and the shear horizontal ratio ($R_{SH}$), equation 3.3 was used to distinguish waves with shear horizontal polarization among the appearing SAW.

### 4.2.2 Love-wave device fabrication

LW-SAW sensors were fabricated at IoP on ST-cut quartz substrates with a 1.6 µm thick amorphous $SiO_2$ layer and aluminum IDTs with a spatial period of 16 µm resulting in a normalized $SiO_2$ thickness of 0.1. 200 nm thick IDTs were patterned by RF sputtering, photolithography and wet etching, as is described in the chapter 3.2. Each consists of 110 finger pairs with an acoustic aperture of 840 µm and propagation length of 320 µm between input and output IDTs electrode. Fabricated electrodes are shown on figure 4.6. An amorphous $SiO_2$ layer was deposited by low temperature plasma enhanced chemical vapor deposition using a Plasmalab 80 plus from Oxford Instruments at IEMN. IDTs pads were mechanically protected during $SiO_2$ layer deposition.

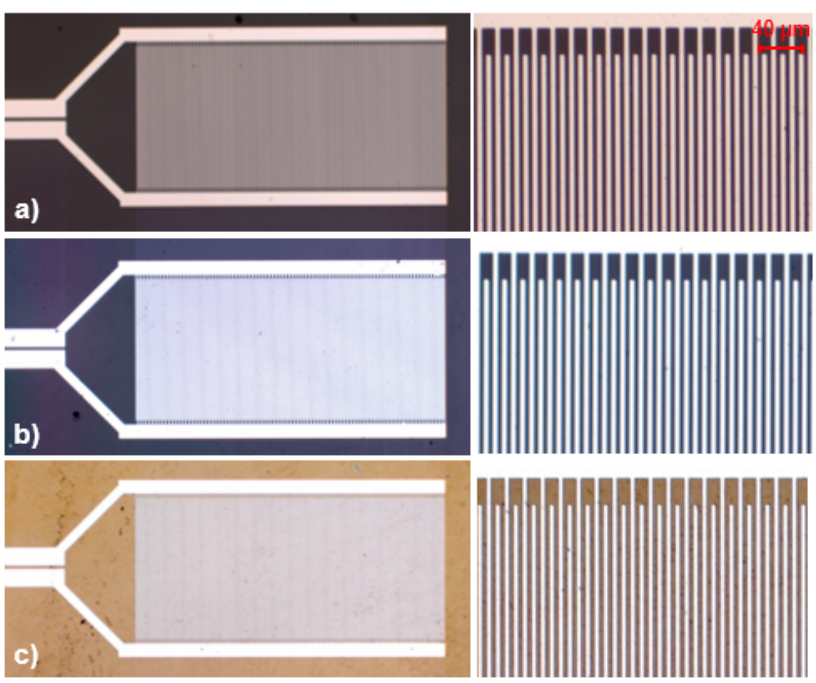


Figure 4.6: Micrographs of fabricated aluminum IDTs a) without any coating, b) with amorphous $SiO_2$ coating, c) with amorphous $SiO_2$ and NCD layers

Consecutive depositions of nano-crystalline diamond (NCD) layers were carried out at low temperature by MW-LA-PECVD apparatus [149] in order to determine the effect of diamond grain size, coalescence and diamond thickness. Prior to NCD growth, LW-SAW samples were seeded with nanodiamond particle colloids (NanoAmando®B from

NanoCarbon Research Institute Ltd.) by spin coating, to produce high and low particle densities, which act as nucleation sites for subsequent NCD growth, to enable growth of thin coalesced NCD layers and non-coalesced NCD layers. The IDT contact pads were mechanically protected by clean lab tape as solid mask (F04xx tape from Semiconductor Equipment Corp.) during spin coating to ensure they were not subsequently coated with insulating diamond. All depositions (aluminum, $SiO_2$ and NCD) were carried out at temperatures below 500 °C to preserve the piezoelectric properties of the quartz substrates.

### 4.2.3 Nanocrystalline-diamond layer characterization

NCD coatings were characterized by AFM and Raman spectroscopy. Figure 4.7 shows AFM pictures of deposited NCD coatings using two different seeding colloids. Use of the lower density colloid resulted in the growth of discrete NCD grains after the 1$^{st}$ deposition. A coalesced NCD layer was formed only after the 6$^{th}$ deposition, which corresponded to a thickness of 236 nm. Use of the higher density colloid resulted in a coalesced NCD layer after the 1$^{st}$ deposition (thickness of 30.8 nm).

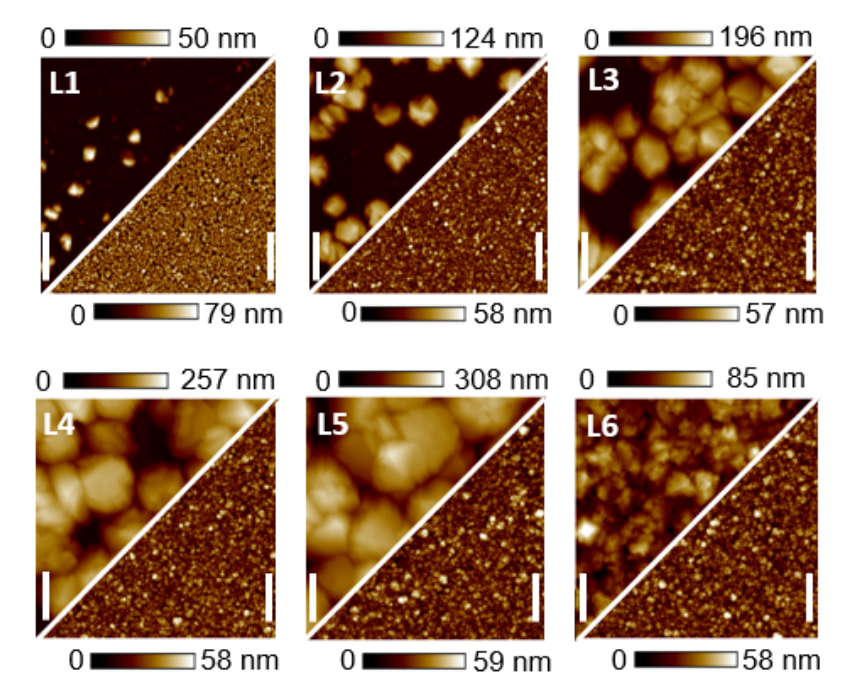


Figure 4.7: AFM images of deposited NCD layers with different nucleation density: 1) deposition of NCD grains (upper part, white bar indicates distance of 270 nm) and 2) deposition of closed NCD layers (lower part, white bar indicates distance of 1 µm)

Raman spectra of coalesced NCD layers as well as discrete NCD grains are shown in figure 4.8. The diamond zone-center phonon peak, located at 1332 cm$^{-1}$, can be seen

clearly for all NCD thicknesses, layers and grains while no significant $sp^2$ carbon fraction can be observed. Peaks at 1100 $cm^{-1}$ for NCD layer thicknesses of 30 nm is attributed to the substrate, while peaks at 1480 and 1490 $cm^{-1}$ are related to acetylene C-H chains [145].

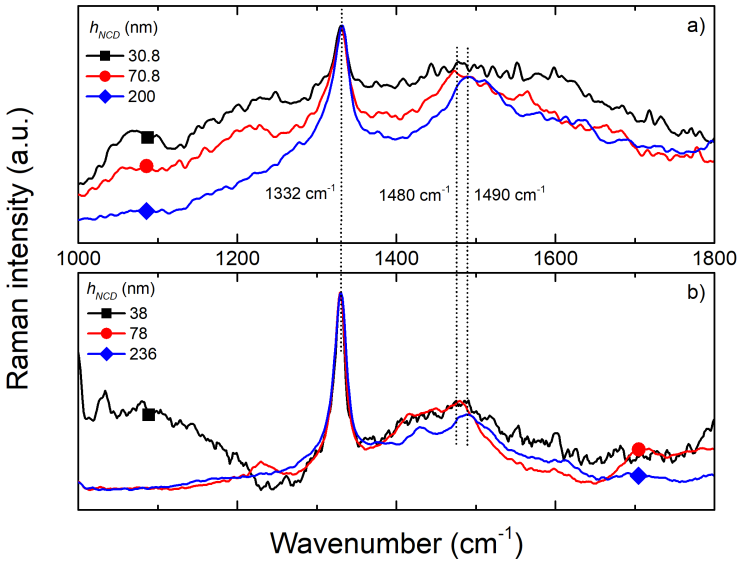


Figure 4.8: Raman spectra of a) coalesced NCD layers and b) NCD grains with different thicknesses

### 4.2.4 Love-wave device characterization

Transmission coefficient $S_{21}$ was measured as is described in the chapter 3.2.3. Responses of delay lines coated by coalesced NCD layers and NCD grains with different thicknesses are shown in figure 4.9. We can notice, first, several oscillations with presence of dips in the filter band-pass instead of perfect sin-lobe response of a periodic transducer. This behavior can be attributed to destructive interferences that occur in the presence of defects like short-circuit between IDTs. For coalesced NCD layers, an increase in the operating frequency $f_r$ can be clearly seen with increasing NCD layer thickness. It can be seen, that insertion loss decreased after deposition of NCD layer. Conversely, the delay lines coated by discrete NCD grains (see figure 4.95b) show a decrease in operating frequency $f_r$, and the insertion loss slightly increases. Once a coalesced NCD layer is formed (thickness 236 nm), $f_r$ increases and we can observe a 2 dB increase in insertion loss.

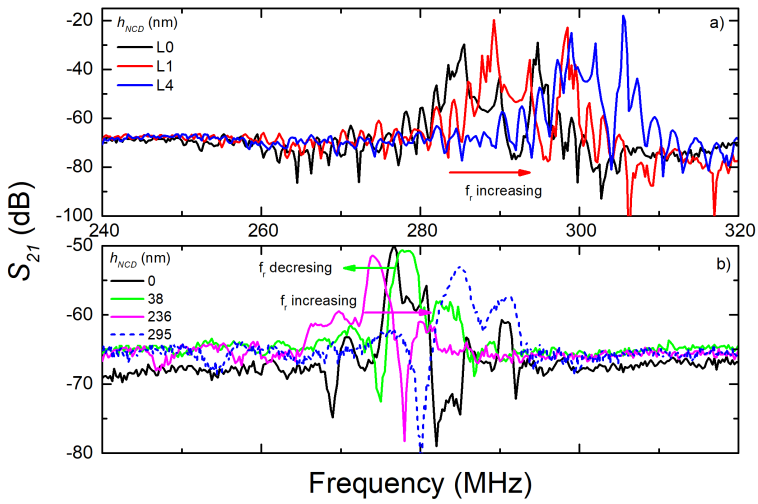


Figure 4.9: Spectra of transmission coefficient $S_{21}$ for LW-SAW sensors coated by a) coalesced NCD layer and b) NCD grains with different thicknesses. From a thickness of 236 nm, the NCD layer became coalesced.

### 4.2.5 Phase velocity dispersion

Figure 4.10 shows the effect of NCD thickness on the experimentally recorded normalized phase velocity that is compared with simulated results. Phase velocity was normalized to 4373 m/s (minimum measured velocity) and 5060 m/s (propagation velocity value for acoustic waves in ST-cut quartz substrates). For coalesced NCD layers the phase velocity steeply increases for initial values of NCD thickness and becomes almost constant as it approaches 5000 m/s. This result indicates that the Love waves are no longer trapped within the $SiO_2$ guiding layer, but that they propagate only within the quartz substrate (see figure 4.11e). However, after deposition of discrete NCD grains, the phase velocity increases slightly for the first two depositions, this is attributed to annealing of the quartz substrate and amorphous $SiO_2$ layer during diamond deposition, then the phase velocity starts to decrease until the NCD layer coalesces. The additional mass on the surface of the sensor created by isolated grains slows down the acoustic waves, which results in a decrease in operating frequency. It can also be observed, that the phase velocity is lower than for coalesced NCD coatings, which indicates improved confinement of Love waves in the guiding layer, which can be clearly observed in the figure 4.11 and therefore ensure a higher sensitivity for the discrete NCD grain coated LW-SAW sensors than for the sensors with coalesced NCD layers.

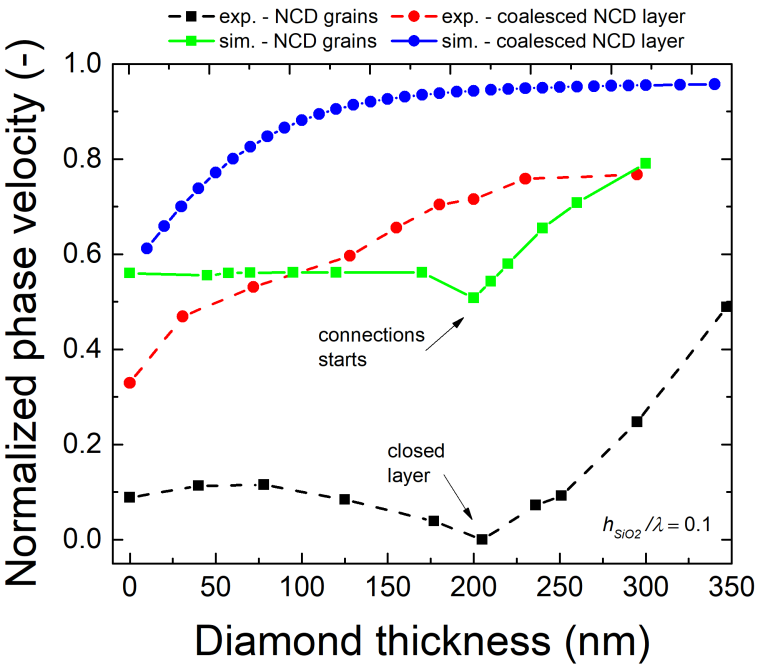


Figure 4.10: Normalized phase velocity of a Love waves as a function of NCD layer thickness from simulation (solid lines) and from experimental measurements (dashed lines) for coalesced NCD layers (circles) and discrete NCD grains (squares) on $SiO_2$/ST-cut quartz structure.

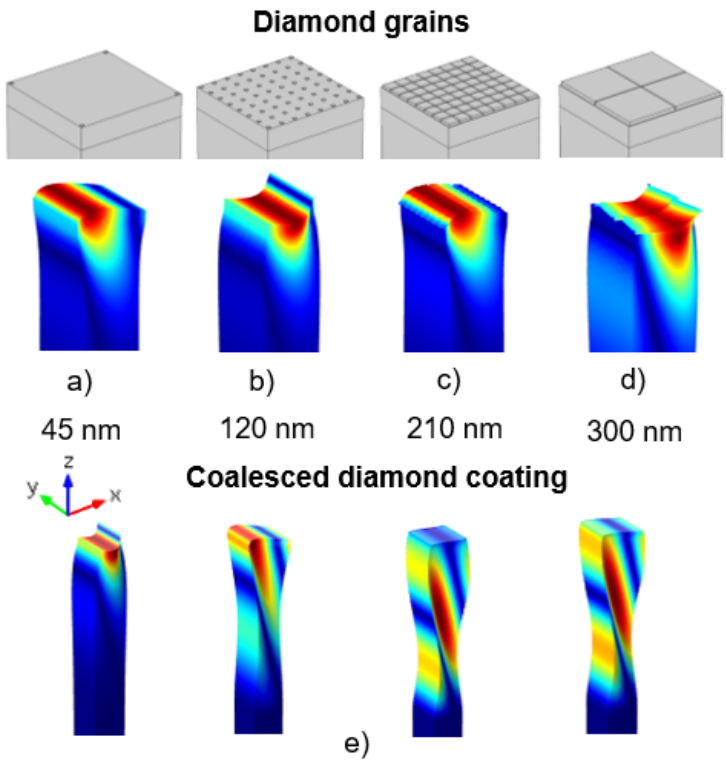


Figure 4.11: Love wave mode shapes for $SiO_2$/ST-cut quartz structures with different numbers of NCD grains: a) 4 grains, $h_{NCD}$=45 nm, b) 64 grains, $h_{NCD}$=120 nm, c) 64 grains covering whole surface, $h_{NCD}$=210 nm, d) 4 grains, $h_{NCD}$=300 nm and e) coalesced NCD layer with the same thicknesses.

### 4.2.6 Band structure of SH modes

To explain results in depth, we calculated the band structure of SH modes (SH ratio $> 0.5$) for each of the cases shown in Figure 4.11c. The result is shown in Figure 4.12, X points are the irreducible Brillouin zone limit of the unit cell in the $x$ direction (cell parameter is fixed to 10 µm). The black continuous and broken lines correspond to the shear bulk mode in quartz and $SiO_2$ substrates respectively. In the case of coalesced NCD layers, the Love mode is located above the limit of the substrate shear mode. This means that the mode radiates into the bulk of the substrate, which is confirmed by displacement field distribution (see Figure 4.11e). For discrete NCD grain coating, the Love mode is below the limit of the substrate shear mode, whilst approaching the limit of the Brillouin zone which implies a good confinement of the mode in the $SiO_2$ layer.

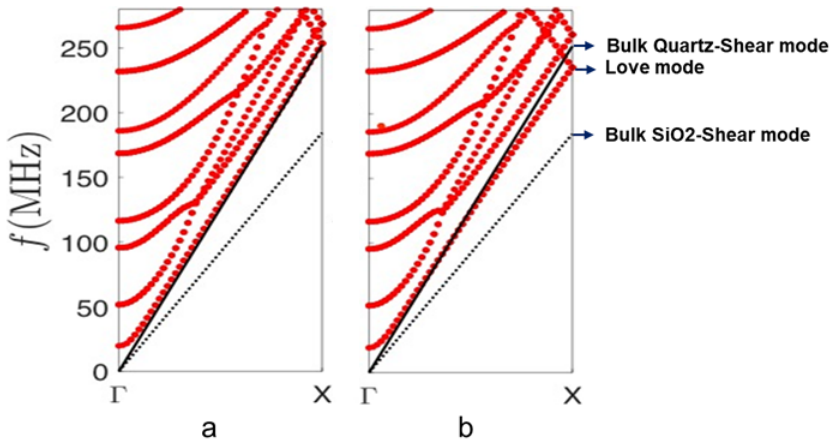


Figure 4.12: Band structure of unit cell: geometrical parameters case (Figure 5c) and cell parameter fixed to 10 µm. a) coalesced NCD layer and b) discrete NCD grains

### 4.2.7 Conclusions

This chapter focuses on experimental and by finite element simulations investigation of the effect of nucleation and the growth of diamond, in the form of nano-crystalline diamond, on the properties of $SiO_2$/ST-cut quartz LW-SAW sensors. We successfully deposited isolated diamond grains as well as coalesced diamond layers. The phase velocity is increasing due to the increasing rigidity of the surface of the sensor as well as deeper propagation of the acoustic waves in devices with coalesced diamond layers. The phase velocity is decreasing because of the prevailing effect of mass loading in devices with the growth of discrete diamond grains. As the diamond layer becomes coalesced, the phase velocity steeply

increases. An increase in phase velocity above 5060 m/s was not observed, confirming that Love waves are not propagating within the deposited diamond layer, but that it propagates within the quartz substrate. This result explains the sensitvity lost after adding of diamond coating with higher thickness, as the waves are no longer surface waves, but became a bulk waves. These results confirm the possible use of very thin diamond coating of $SiO_2$/ST-cut quartz LW-SAW sensors with two different types of diamond layers. These structures can be used for biosensing applications following appropriate diamond surface functionalization.

## 4.3 Enhancing the sensitivity of SAW sensors using the diamond surface phononic metamaterials

Part of this work has been presented on the international conference 2020 Virtual MRS Spring/Fall Meeting & Exhibit, November $27^{th}$ – December $4^{th}$ as the poster presentation and was nominated for the "Best poster Award".

Phononic metamaterials (PnMs) are analog to photonic and plasmonic in optics. Based on phononic band-gap and local resonance mechanisms, these artificial materials enabled advanced control of elastic waves in solid condensed matter including waveguiding, trapping, multiplexing, demultiplexing, etc. [150–155]. They offer the possibility to confine and focus an acoustic wave in an ultra-small region of sub-wavelength dimensions and to extend mechanical resonance lifetimes (high quality factor (Q)) [154, 156]. Therefore, combining diamond PnMs and shear surface waveguides is of great interest to enhance the performance of diamond-SAW based biosensors.

The main objective of this study is to investigate the sensitivity of LW-SAW sensors with diamond pillar PnMs using the finite element method (FEM, COMSOL Multiphysics). As an excitation of pillar discrete resonant modes depends on its geometrical parameters (radius, thickness and shape) [157], the sensitivity is investigated as a function of the pillar thickness for a set of different radii.

### 4.3.1 Band gap structure formation

As SAW devices with phononic metamaterials are not the main objective of this thesis, only brief theory insight into the formation of the band structure will be given here.

Phononic crystal can be observed as an extension of the concept of crystal in solid state physics. If we exchange the periodic atoms in crystals by elastic scatters, we get the similar influence of PnCs on elastic waves as the influence of atomic potential to electrons. From this point of view, we can use the same definitions and concepts of lattice and band theories as in solid state physics [158]. At first, it is important to introduce the term Irreducible Brillouin zone.

Crystals have a spatial periodicity and symmetry, thus its eigenvectors and eigenfrequencies has also certain symmetry. First Brillouin zone (BZ) in reciprocal space repre-

sents the smallest space divided for each point $\Gamma$. The first BZ can be further reduced, if its space has certain symmetry for a group of points. The new smaller zone is called irreducible Brillouin zone. In this work we used square lattice type, so direct lattice, reciprocal lattice and BZ are shown in the figure 4.13. If we chose the wave vector $k$ as a horizontal axis and the eigenfrequencies as the vertical axis, we will obtain band structure or dispersion diagram. To calculate band structure, $k$ is required to transverse only the boundary of irreducible BZ [158, 159].

| Lattice type | Direct lattice | Reciprocal lattice | 1st & Irreducible BZ | Direct & Reciprocal basic vectors |
|---|---|---|---|---|
| Square |  |  | 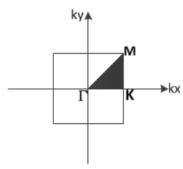 | $\begin{cases}\vec{a_1} = a(1,0)\\ \vec{a_2} = a(0,1)\end{cases}$ $\begin{cases}\vec{b_1} = \frac{2\pi}{a}(1,0)\\ \vec{b_2} = \frac{2\pi}{a}(0,1)\end{cases}$ |

Figure 4.13: Direct and reciprocal lattice and its first and irreducible Brillouin zone for PnCs with square lattice, $a$ is the lattice constant, reproduced from [158]

Phononic band gaps are the ranges of wavelength and frequencies where the acoustic waves cannot propagate through the crystal. PnCs band gaps can be classified into two types - gaps caused by Bragg diffraction or local resonance. Gaps can cover whole Brillouin zone, but can appear also only for a specific direction of the wave vector [158, 159].

Bragg diffraction is caused by the constructive interference of reflected waves from two parallel planes, that occurs if the path difference is an integer multiple of the wavelength:

$$n\lambda = 2asin\theta, \tag{4.4}$$

where $n$ is an integer, $\lambda$ is the wavelength, $a$ is lattice constant (distance between two planes) and $\theta$ is the angle between the incident wave and the crystal surface. In PnCs, Bragg scattering occurs when the wavelength is similar to the lattice parameter $a$.

Second phenomenon participating in the band gap formation is local resonance, where the wavelength corresponding to the frequency of the band gap is much higher than the lattice constant $a$. Local resonance is caused by resonance of single scatterer and elastic waves are attenuated sharply during the propagation. The local resonance band gap is the result of coupling between the intrinsic vibration of the individual particle and the propagating wave. The width of the band gap increases with the increasing filling factor and the central frequency of the hybridization band gap is anti-proportional with the

particle size [159].

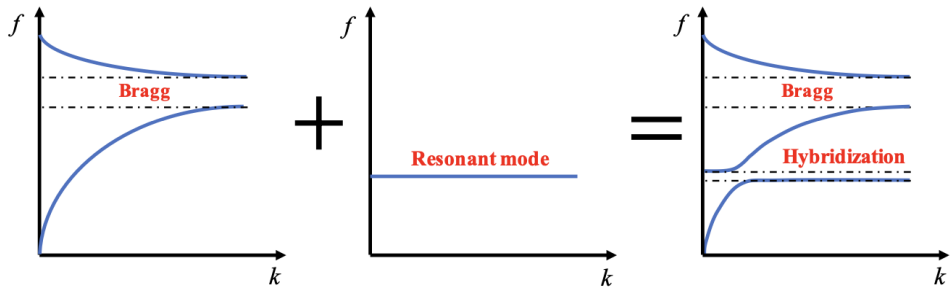


Figure 4.14: Schematic of hybridization band gap formation, reproduced from [159]

### 4.3.2 Methods

Calculation of the band structures of PnMs was carried out in COMSOL Multiphysics using model described in the chapter 3.1.3. The sensitivity was calculated at the X point of the irreducible BZ by using the add mass option in COMSOL on the top face of the PnMs and by using following equation [147]:

$$S_m = \lim_{\Delta m \to 0} = \frac{\Delta f / f_0}{\Delta m_A}, \tag{4.5}$$

where $f_0$ is unperturbed operational frequency, $\Delta f$ is the change in the operational frequency caused by mass loading and $\Delta m_A$ is the mass per unit area. The sensitivity was calculated as a function of different geometry parameters of diamond or $SiO_2$ PnMs (pillar radius, height or filling factor $r/a$) on top of 2 µm continuous $SiO_2$ guiding layer (model geometry shown in the figure 3.3b)).

Investigation of the effect of the pillar geometry was carried out at fixed lattice parameter $a$ equal to 5 µm. Pillar radius $r$ was varied in the range of 0.125 - 1.5 µm and height was $h_p$ = 0.5 - 5 µm. Sensitivity as a function of the filling factor $r/a$ was calculated for changing lattice parameter $a = 1 - 5$ µm and two different pillar radii $r = 0.25$ µm and 0.35 µm, that were fixed during the calculation. Pillar height $h_p$ was kept 750 nm for both calculations.

### 4.3.3 Diamond PnMs on $SiO_2$ guiding layer

At first, the band structure was calculated to investigate different acoustic modes for the diamond PnMS ($r_p = 250$ nm, $h_p = 750$ nm) on $SiO_2$ guiding layer ($h_{SiO2} = 1.5$ µm) with

lattice period $a = 1$ µm, and is shown in the figure 4.15).

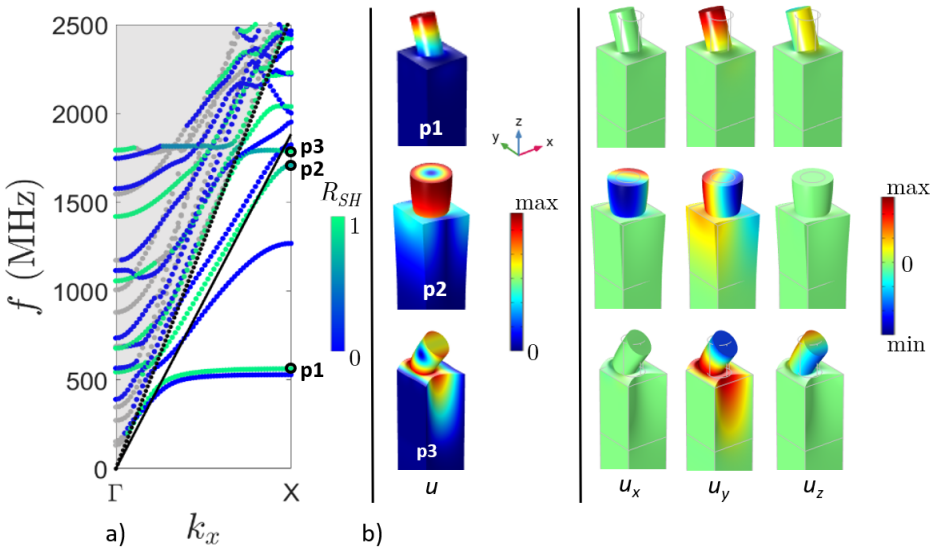


Figure 4.15: a) Band structure of PnMs based on pillar along Γ-X direction for 90ST-quartz + $SiO_2$ layer + diamond pillar (blue denotes Rayleigh wave, green color means Love waves, gray lines are bulk waves) and b) mode shapes of SH surface modes with shown $u_x, u_y$ and $u_z$ deformation components

Gray area is the radiation zone, where the waves start to propagate in the substrate bulk. Upper black dotted line is dispersion curve of the fast shear waves in the quartz substrate, lower black dotted line denotes the dispersion curve for shear waves in silica layer, calculated according to $v = \frac{2\pi f}{k}$. Modes located between these two lines are guided in silica layer. Color of modes is based on the SH ratio, blue color denotes Rayleigh waves and green color refers to the Love waves. Rayleigh waves cannot be excited in real 90ST-cut quartz because of the zero electromechanical coupling coefficient for this type of waves, only shear waves are coupled to electric field. When the frequency of the Love wave match with the resonance frequency of the pillar, we obtain wave coupling resulting in local resonance. These coupled modes are going below the dispersion curve for silica layer (lower black dotted lines), which means localization of the acoustic energy in the pillar. This is confirmed by $u_y$ displacement component of SH waves at the X point of the BZ, shown in the figure 4.15b)). p1 mode ($f = 562.3$ MHz) is localized flexion pillar mode and p3 ($f = 1789$ MHz) is Love mode guided in the $SiO_2$ layer coupled with the pillar. p2 ($f = 1706$ MHz) is indicated by petrol color in the band structure as it is the torsional mode having also $u_x$ displacement component. Based on these results, the calculation of the sensitivity was carried out for the slowest flexion pillar mode (p1), as the acoustic energy is confined well in the pillar.

Transmission spectrum was calculated for fixed wavelength resulting from the pillar resonance frequency of the p1 mode, $f$ - 562.3 MHz. The geometry parameters were the same as for band structure calculation ($r_p$ = 250 nm, $h_p$ = 750 nm, $h_{SiO2}$ = 1.5 µm and $a$ = 1 µm).

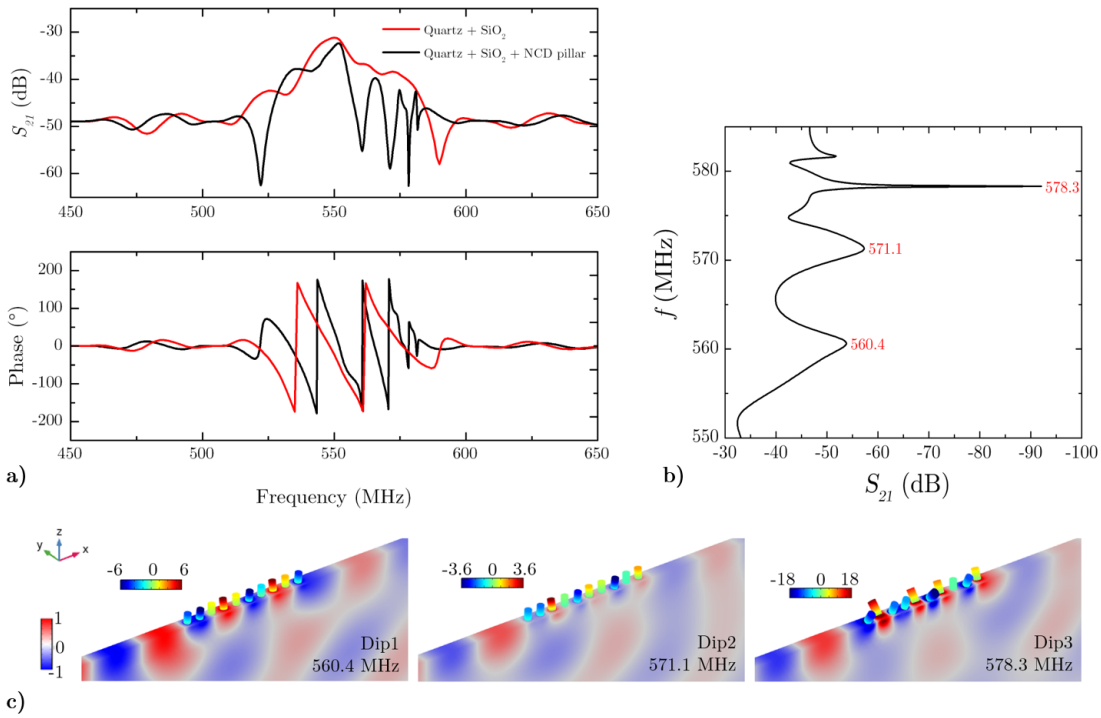


Figure 4.16: a) Transmission spectra ($S_{21}$ and phase) for 90ST-quartz + $SiO_2$ layer + diamond pillar for pillar resonance at 562.3 MHz (black) and transmission for 90ST-quartz + $SiO_2$ layer without PnMs (red) for comparison, b) enlargement of the $S_{21}$ flexion-mode-induced dips and c) $u_y$ displacement component at the dips. The amplitudes of the pillar displacement are normalized to the maximum amplitude in the $SiO_2$ guiding film.

Transmission spectra showed appereance of the dips after adding of 10 diamond pillars on top of the structure. The dip at 578.3 MHz refers to the local resonance of flexion pillar mode, the bending of pillars can be seen at the figure 4.19c), dip3. As the band structure was calculated using the unit cell, the resonance frequencies of the pillars were provided for an infinite system. However, during the transmission calculation, the system of finite size is considered. From this reason, the transmission spectrum includes not only the resonance modes of the pillars, but also the collective resonance modes arising from the finite size of the system. This refers to the dips at 560.4 and 571.1 MHz. To better understand the origin of all the peaks, it would be more appropriate to begin by examining the interaction of the wave with an individual pillar and gradually increasing the number of pillars. Another approach is to consider a multiple-cell configuration to calculate the

band structure. These considerations account for the differences in resonance frequencies obtained by the two calculation methods. However, within the scope of this study, we were unable to undertake such an analysis due to its computational time-intensive nature. Our primary focus was exclusively on investigating the sensitivity of first flexural resonance mode to mass load effect.

### Sensitivity as a function of filling factor $r/a$

As was mentioned before, sensitivity calculation was carried out for the slowest flexion pillar mode according to equation 4.5.

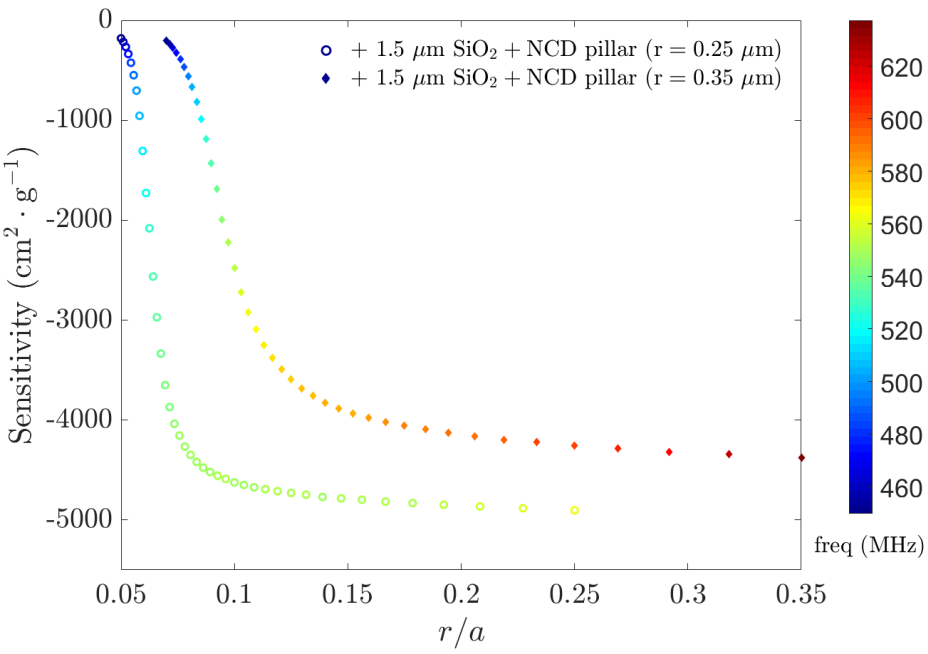


Figure 4.17: Sensitivity as a function of filling factor $r/a$ for diamond PnMs on 1.5 µm thick $SiO_2$ guiding layer, pillar radii $r = 0.25$ and 0.35 µm, $h_p = 750$ nm.

As can be seen from the graph 4.17, the sensitivity is steeply decreasing for very small values of $r/a$, for $r_p = 0.25$, $r/a < 0.075$, which is equal to $a = 3.3$ µm, for $r_p = 0.35$, $r/a < 0.125$, resulting in $a = 2.5$ µm. From these $r/a$ values and higher, the sensitivity remains constant, which means, that we don't need to decrease lattice parameter $a$ as much as possible to obtain better sensitivity. This result is interesting from the fabrication point of view, as fabrication of high density pillars is more complex. The 4.17 graph also shows, that sensitivity is lower for pillar with higher radius $r$ for fixed height $h$.

### 4.3.4 $SiO_2$ PnMs on $SiO_2$ guiding layer

For comparison with diamond pillars, the same work was done using $SiO_2$ pillar with the same geometry parameters ($r_p$ = 250 nm, $h_p$ = 750 nm, $h_{SiO2}$ = 1.5 µm and $a$ = 1 µm). At first, the band structure was calculated to see the acoustic modes and it can be seen on the figure 4.18a).

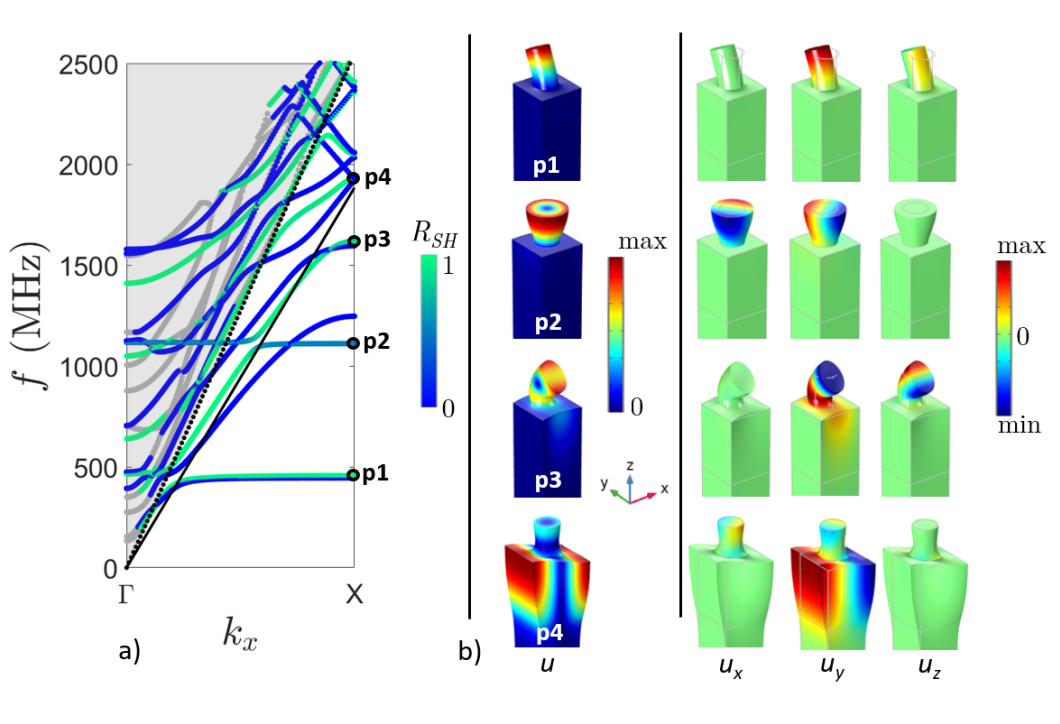


Figure 4.18: a) Band structure of PnMs based on pillar along Γ-X direction for 90ST-quartz + $SiO_2$ layer + $SiO_2$ pillar (blue denotes Rayleigh wave, green color means Love waves, gray lines are bulk waves) and b) mode shapes of SH surface modes with shown $u_x, u_y$ and $u_z$ deformation components

As for the diamond pillar, p1 mode ($f$ = 456 MHz) is localized flexion pillar mode and p3 ($f$ = 1618.6 MHz) is Love mode guided in the $SiO_2$ layer coupled with the pillar, p2 ($f$ = 1100.5 MHz) torsional mode also with $u_x$ displacement component. p4 mode is already above the dispersion curve for shear waves in silica layer (black line) and as can be seen from mode shapes, the acoustic energy is located in the guiding layer.

The properties of PnCs are highly dependent on contrast in physical properties (elasticity, acoustic velocity and density) of the matrix and inclusions material. The physical properties of diamond and $SiO_2$ are shown in the table 4.1. Due to a great Young's modulus and relatively low density, diamond has the highest acoustic velocity ($v = \sqrt{E/\rho}$). Higher eigenfrequencies of diamond pillars compare to silica ones are expected, as soft materials are expected to have lower eigenfrequencies. This is confirmed by our results.

Table 4.1: Relative physical properties of of diamond and silica, [159]

| | **Diamond** | **$SiO_2$** |
|---|---|---|
| **Acoustic velocity** $v$ (m/s) | 18 617 | 5640 |
| **Young's modulus** $E$ (GPa) | 1220 | 70 |
| **Density** $\rho$ **(kg/m$^3$)** | 3520 | 2200 |

Transmission spectrum was calculated for fixed wavelength corresponding to the pillar frequency of the p1 mode ($f$ = 456 MHz) with the same geometry parameters as for band structure calculation.

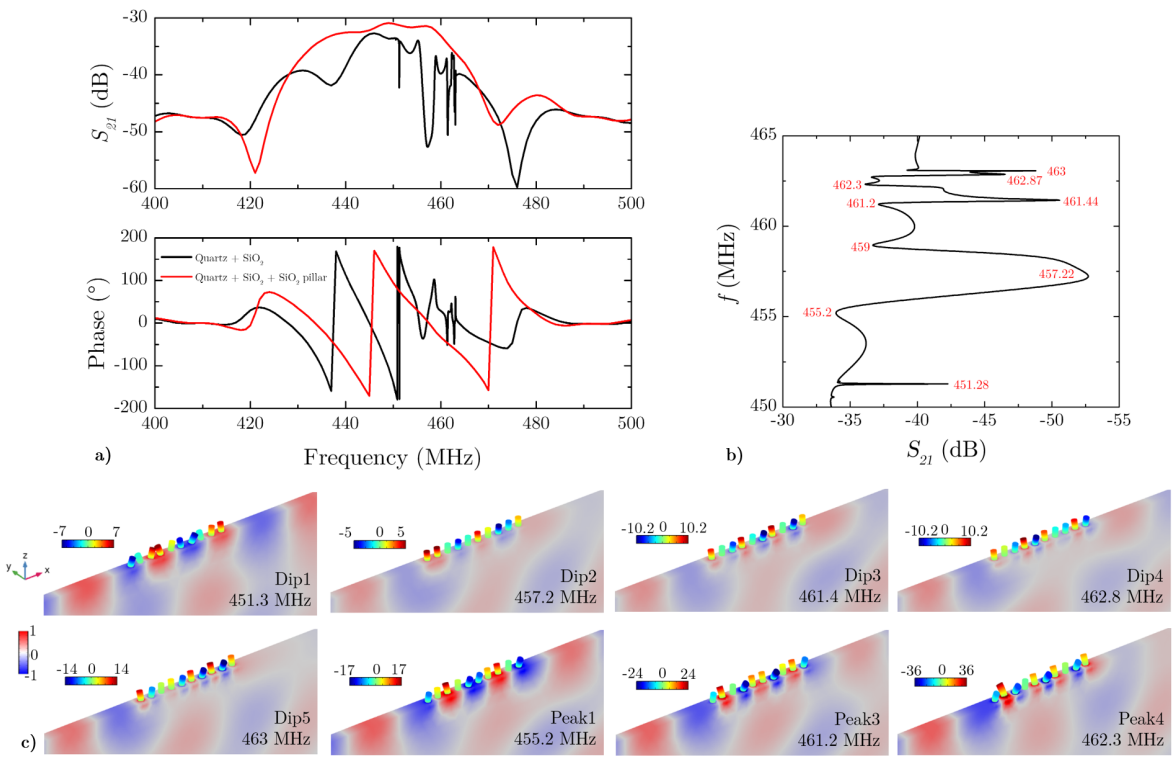


Figure 4.19: a) Transmission spectra ($S_{21}$ and phase) for 90ST-quartz + $SiO_2$ layer + $SiO_2$ pillar for pillar resonance at 456 MHz (black) and transmission for 90ST-quartz + $SiO_2$ layer without PnMs (red) for comparison, b) enlargement of the $S_{21}$ flexion-mode-induced dips and c) $u_y$ displacement component at the dips and peaks. The amplitudes of the pillar displacement are normalized to the maximum amplitude in the $SiO_2$ guiding film.

As for the transmission spectra with diamond pillars, we can observe appearance of the dips after adding $SiO_2$ pillar on top of the structure. The origin of all the dips in the spectra was not examined in the detail and it is hard to explain them as they arise also from the collective resonance modes. To confirm sensing abilities, transmission spectra were simulated without and with added mass on top of the pillars. From figure 4.20 can be clearly seen the frequency shift induced by added mass on top of the pillars. Sensitivity was roughly estimated (frequency spectra were calculated with the 10 kHz step) using

the equation 4.5. For the added mass per unit area of $m_A = 1 \cdot 10^{-8}$ g/cm$^2$, calculated sensitivity is $S_m = -8863$ cm$^2$/g, for $m_A = 5 \cdot 10^{-8}$ g/cm$^2$, sensitivity $S_m = -9306$ cm$^2$/g.

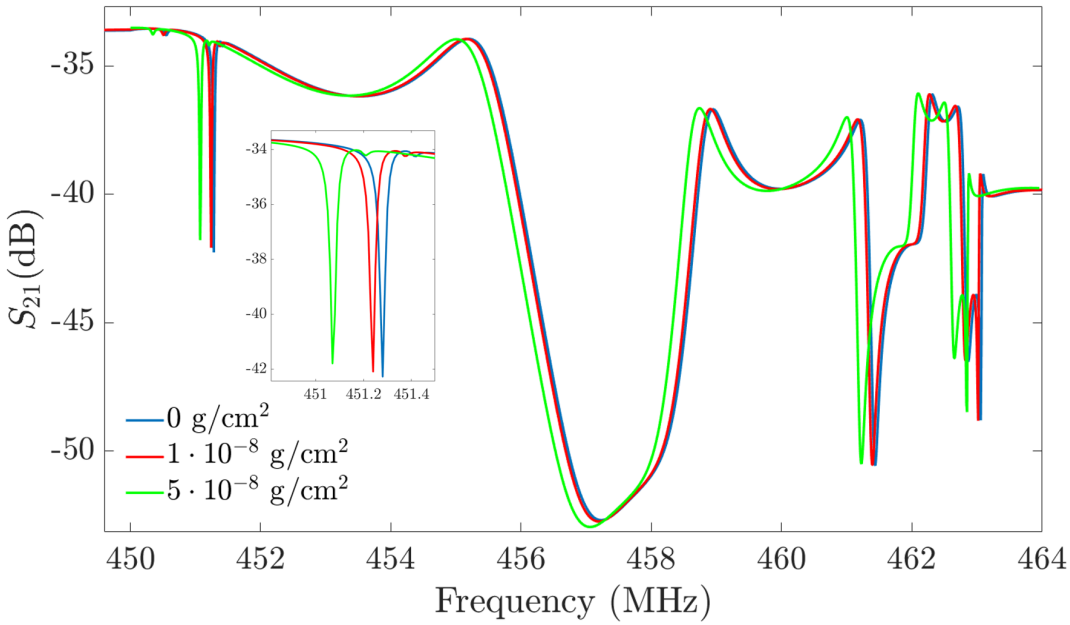


Figure 4.20: Transmission spectra ($S_{21}$ and phase) for 90ST-quartz + $SiO_2$ layer + $SiO_2$ pillar for pillar resonance at 456 MHz without and with added mass. Inset is the enlargement of the pillar resonance induced dip for better observation of the frequency shift

#### Sensitivity as a function of filling factor $r/a$

Effect of the filling factor $r/a$ was studied in the same way as for diamond PnMs for the same geometry parameters. From figure 4.21 can be seen, that the behavior is the same as for the diamond pillars, the sensitivity is steeply decreasing for very small values of $r/a$, otherwise it remains constant. As the calculation was performed for the same pillar geometry parameters as the transmission spectra, we can compare the sensitivity obtained from transmission calculation. For pillar with $r = 250$ nm and lattice parameter $a = 1$ µm, the filling factor $r/a$ equals to 0.25. From the graph 4.21, we can see, that the sensitivity is around -9000 cm$^2$/g, which is in good agreement with the values obtained from transmission spectra calculation.

### 4.3.5 Conclusions

This chapter focused on the FEM simulations of LW-SAW sensors with phononic metamaterials. This work builds on the results from the chapter 4.2, where we confirmed radiation

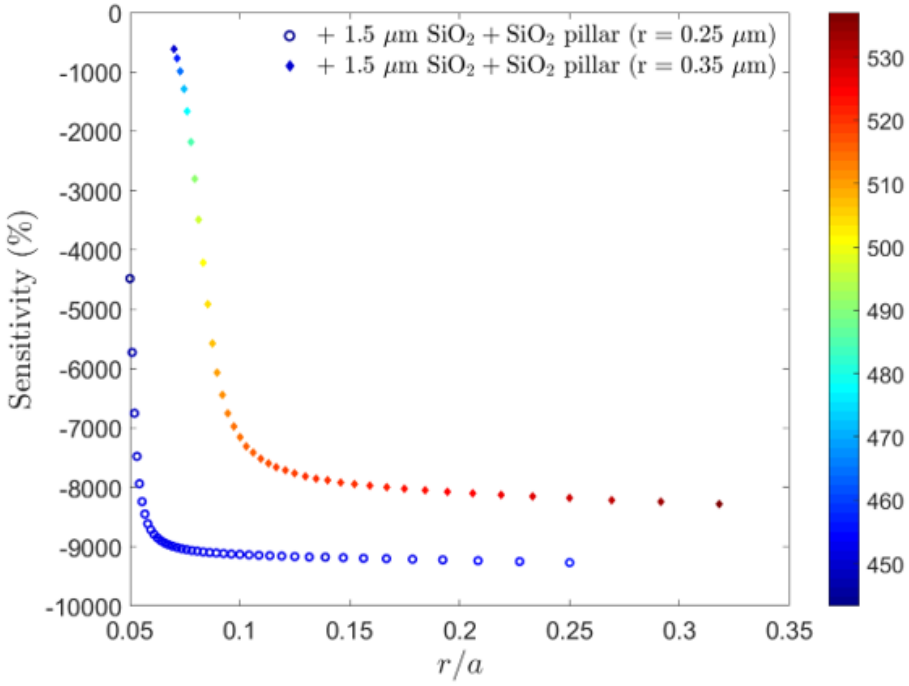


Figure 4.21: Sensitivity as a function of filling factor $r/a$ for $SiO_2$ PnMs on 1.5 µm thick $SiO_2$ guiding layer, pillar radii $r = 0.25$ and 0.35 µm, $h_p = 750$ nm.

of the Love mode into the bulk of the substrate for continuous diamond coatings and good confinement of the Love mode in the $SiO_2$ guiding layer, when the discrete diamond grains were used. The aim of this chapter was to study confinement of the acoustic waves in the PnMs and improvement of the sensitivity of such SAW sensors. In the band structure we observed coupled modes going below the dispersion curve for silica layer, that confirmed localization of the acoustic energy in the pillar for both studied materials (diamond and $SiO_2$) of pillars. Sensitivity was studied as a function of a filling factor $r/a$ giving the result, that the lattice parameter $a$ does not need to be decreased as much as possible to obtain better sensitivity of LW-SAW sensors with PnMs. Also the highest sensitivity obtained from these simulations for diamond PnMs is around 5000 $cm^2 \cdot g^{-1}$, which is much higher than the sensitivity obtained from the simulations for continuous diamond coating. Sensitivity for $SiO_2$ pillars is even higher around 9000 $cm^2 \cdot g^{-1}$. This theoretical study is promising for the fabrication of highly sensitive LW-SAW sensors with diamond PnMs for biosensing applications.

## 4.4 Diamond and silicon carbide as passivation layers for package less SAW sensors

This work has been presented on the international conference 2020 Virtual MRS Spring/Fall Meeting & Exhibit, November $27^{th}$ – December $4^{th}$ as the poster presentation.

### 4.4.1 Motivation

SAWs find applications in life sciences, in structural health monitoring, etc. Their surface is very sensitive to the changes of surrounding environment, which brings the need for the packaging of the SAW devices. Currently, SAW devices are usually packaged in the bulky hermetic enclosures, that are increasing both sensor's size and price [160]. SAW devices can also be operated in extremely confined environments such as implantable sensors to monitor or to provide real time treatment. In this case, it makes sense to protect the sensor surface and leave only the functionalized area visible for detection. This is true for implantable sensors where space is a major constraint and therefore they require the development of an intrinsically protected design. Also, this is true for biosensors where the surface is continuously exposed to the analysed biofluid [161]. One solution can be using of the package less structures, that are gaining popularity due to the need for reduction of sensor's dimension and complexity of the production [160, 162].

To achieve package less device, two concepts can be used: Isolated layer Acouctic Wave (ILAW) and Waveguiging Layer Acoustic Wave (WLAW) principle. ILAW principle is using combination of high and low acoustic impedance layers to form a Bragg mirror to confine the acoustic waves. WLAW principle is based on guiding of the shear surface wave in low acoustic velocity layer enclosed between semi-infinite substrate and high acoustic velocity thin film materials [160]. The upper high acoustic velocity layer works as an acoustically isolating layer, protecting the guided surface shear wave from undesired mechanical damping and eliminate the need for packaging, as is shown in the figure 4.22. With very high acoustic velocities, diamond ($v$ = 12 820 m/s [139]) and silicon carbide (SiC, $v$ = 12 600 m/s, polycrystal 3C-SiC [163]) are excellent candidates for package less SAW sensors applications. Both diamond and SiC also posses excellent mechanical properties, chemical inertness and SiC layers have a significantly higher adhesion and

wear resistance compared to the NCD layers [164, 165].

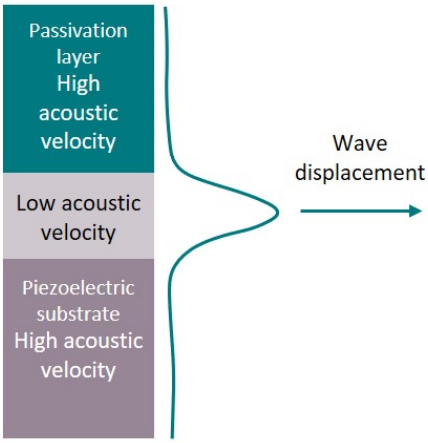


Figure 4.22: Illustration of the layered structure for WLAW devices

### 4.4.2 Methods

The theoretical investigation of the use of diamond and SiC as a passivation layer for SAW devices was carried out using COMSOL Multiphysics FEM simulation software. Two different piezoelectric materials were investigated, 90ST-cut quartz and 36°YX $LiTaO_3$ in combination with two common guiding layer materials – zinc oxide (ZnO) and silicone oxide ($SiO_2$). The calculations were carried out using the COMSOL model described in the section 3.1.2 and shown in the figure 3.2. The acoustic wavelength was arbitrary fixed to $\lambda = 10$ µm, thickness of guiding layers $h_{guid} = 2$ µm and 200 nm thick aluminum or gold electrodes were used on quartz or $LiTaO_3$ substrate respectively. Thickness of the passivation layers was changed in the range of 100 - 4000 nm.

### 4.4.3 Results

The figure 4.23 a) shows, that 2 µm thick diamond or SiC layers are sufficient to confine the acoustic wave in both guiding layers for the quartz substrate, as the sensitivity decrease almost to 0 %. The figure 4.23 clearly shows the wave propagating in the guiding layers with minimal displacement at the surface, which is confirmed by added mode shapes.

For the $LiTaO_3$ substrate, the results (see figure 4.24) show that the sensitivity decreases to 0 % around normalized thickness of passivation layer $h_{pass}/\lambda$ equal to 0.1, which is the half of the thickness necessary for the Quartz substrate. On the other hand, the wave confinment is more effective for the quartz substrate. This is due to the generation

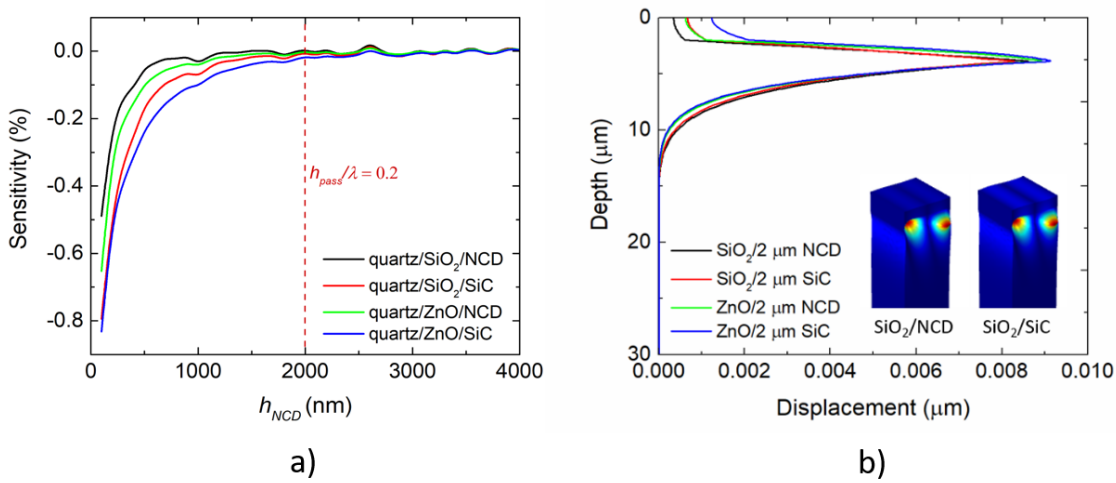


Figure 4.23: a) Sensitivity and b) wave displacement for the WLAW device with quartz substrate

of pure SH wave in quartz substrate in comparison to 36°YX $LiTaO_3$ substrate generating leaky waves. Also the velocity of SH waves in 90ST-cut quartz is higher than for the $LiTaO_3$ substrate.

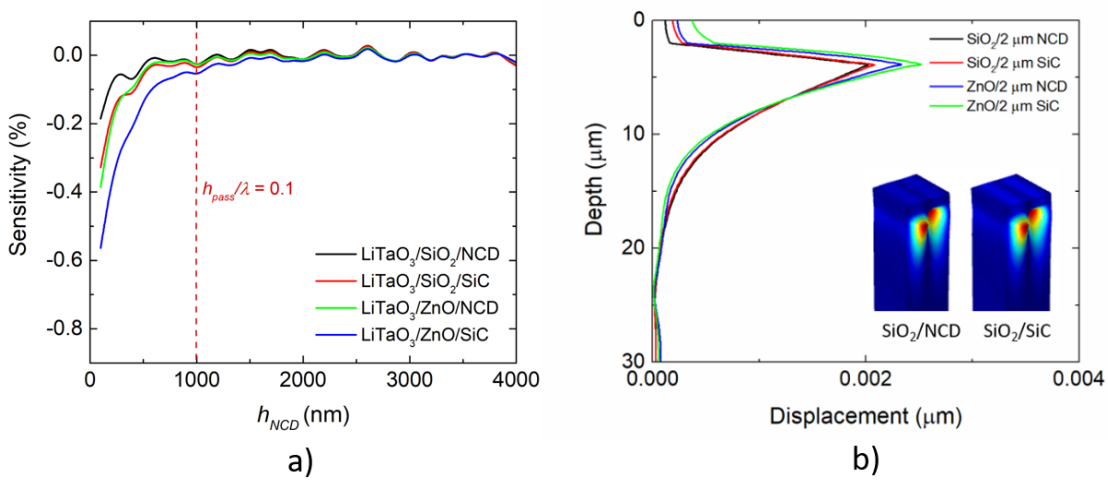


Figure 4.24: : a) Sensitivity and b) wave displacement for the WLAW device with $LiTaO_3$ substrate

From the theoretical results can be seen, that both tested guiding layer materials - $SiO_2$ and ZnO are suitable for WLAW devices without any significant difference. But the $SiO_2$ layer is clearly more advantageous from a practical point of view as diamond deposition on $SiO_2$ is not problematic on the contrary to ZnO which is etched away when exposed to hydrogen plasma. To address this problem, one can use an additional thin layer protecting zinc oxide during diamond deposition.

### 4.4.4 Conclusions

In conclusion of this study focused on biocensor applications, our research has primarily revolved around the use of protected surface acoustic waves (SAW). The incorporation of a protective diamond or silicone carbide layer offers a significant advantage as it allows for direct contact with the liquid without concerns about detrimental effects on the electrodes. This notable advancement is of paramount importance in the fields of biotechnology and biological detection, where the reliability and stability of sensors are crucial. By exploring the design of a protected wave structure, we have opened new avenues for the development of more robust and precise detection devices capable of addressing the challenges posed by complex biological environments. This innovative approach holds exciting prospects for medical, environmental, and industrial applications where reliable interaction with liquids and biological samples is imperative. In summary, our research unveils promising new perspectives for the future of biosensors and biological detection, with potentially profound implications across various sectors.

## 4.5 Experimental investigation of the properties of diamond coated LW-SAW sensors

To verify theoretical results obtained from FEM simulations, LW-SAW devices with different IDTs spatial periods were fabricated and characterized.

### 4.5.1 LW-SAW device fabrication

Sensors used in this chapter were fabricated in cooperation with Ing. Imrich Gablech, Ph.D. from CEITEC Brno according to procedure described in the chapter 3.2.2 SAW device fabrication at CEITEC. The photolithography mask for whole wafer fabrication was prepared using scripting tool Nanolithography Toolbox from Center for Nanoscale Science & technology (CNST) and National Institute of Standards and Technology (NIST). Frequency characterizations of fabricated LW-SAW sensors were carried out as described in chapter 3.2.3. All of the intrinsic nanocrystalline diamond layers depositions were done at low temperature using MW-LA-PECVD apparatus, details on the NCD deposition and characterization are discussed in the chapter 3.3.

### 4.5.2 ST-cut quartz LW-SAW sensors with $SiO_2$ guiding layer

Fabrication was carried out using 90 degrees rotated ST-cut quartz substrate to support excitation of SH waves, 200 nm thick aluminum electrodes and 2.5 µm thick amorphous $SiO_2$ guiding layer. Sensors with different IDTs spatial periods were prepared to obtain several silicon oxide normalized thicknesses $h_{SiO2}/\lambda$. The parameters of the IDTs (spatial period $\lambda$, acoustic aperture $W$, number of finger pairs $N$, propagation length $d$) and resulting silicon oxide normalized thickness $h_{SiO2}/\lambda$ are listed in the table 4.2. There were more IDTs pairs (4-6) with the same wavelength on each sensor and all of them were measured.

To study the effect of diamond coating on LW-SAW sensors, NCD layers with thicknesses of 57 nm, 100 nm and 133 nm were deposited on the $SiO_2$ guiding layers. AFM micrographs and Raman spectra of deposited NCD layers are shown in the figure 4.25. AFM micrographs shows closed NCD layer and from Raman spectra the diamond ($sp^3$) zone-center phonon peak at 1332 $cm^{-1}$ can be seen clearly for all NCD thicknesses with

Table 4.2: Parameters of IDTs used in diamond coated-LW-SAW sensor's properties study

| $\lambda$ (µm) | $W$ (µm) | $N$ | $d$ (µm) | $h_{SiO2}/\lambda$ |
|---|---|---|---|---|
| 32 | 820 | 88 | 3200 | 0.078 |
| 28 | 370 | 88 | 3360 | 0.089 |
| 24 | 620 | 88 | 2880 | 0.104 |
| 20 | 270 | 88 | 2400 | 0.125 |
| 16 | 420 | 88 | 1920 | 0.156 |
| 12 | 160 | 88 | 1440 | 0.208 |
| 10 | 133 | 88 | 1200 | 0.25 |

no significant $sp^2$ carbon fraction.

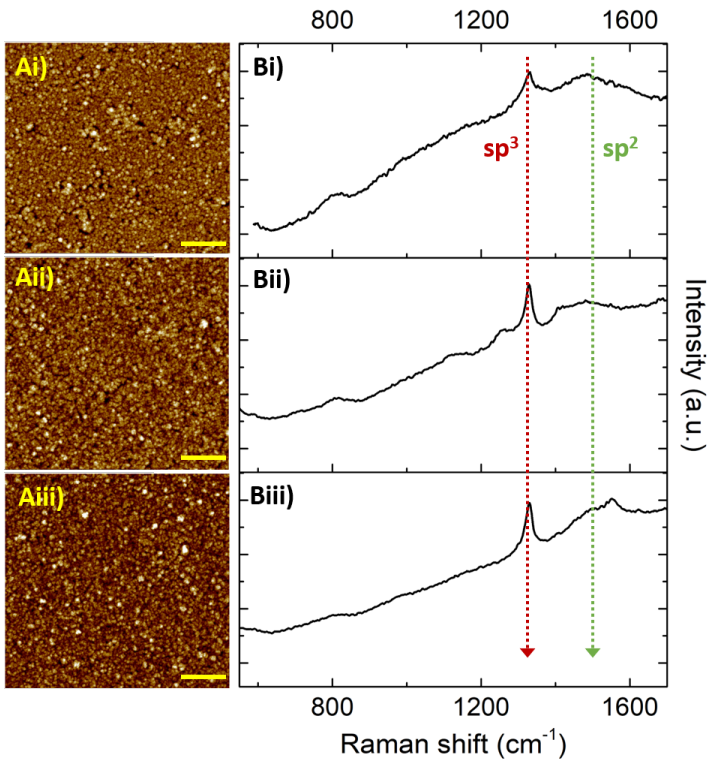


Figure 4.25: A) AFM micrographs and B) Raman spectra of the NCD layers deposited on LW-SAW sensors, where i) refers to 57 nm, ii) 100 nm and iii) 133 nm thin NCD layers, yellow bar indicates 1 µm

### Phase velocity dispersion - theory vs experiment

Sensors with all spatial periods were frequency characterized before and after deposition of thin NCD layers and phase velocity were calculated from resonant frequency using simple equation 4.1. Figure 4.26a) shows example of the transmission coefficient $S_{21}$ for sensor with spatial period $\lambda = 16$ µm. Increase of resonant frequency after deposition of 100 nm thick NCD layer can be clearly observed. Figure 4.26b) gives together the

phase velocity dispersion curves obtained by simulations with the experimental data. It can be seen, that the experimental and modeled phase velocity trends are very similar. But the phase velocity from the experiment is lower than the calculated one, mainly for the diamond-coated LW-SAW sensors. This shift is attributed to different mechanical properties used in simulations than are in the real sensors.

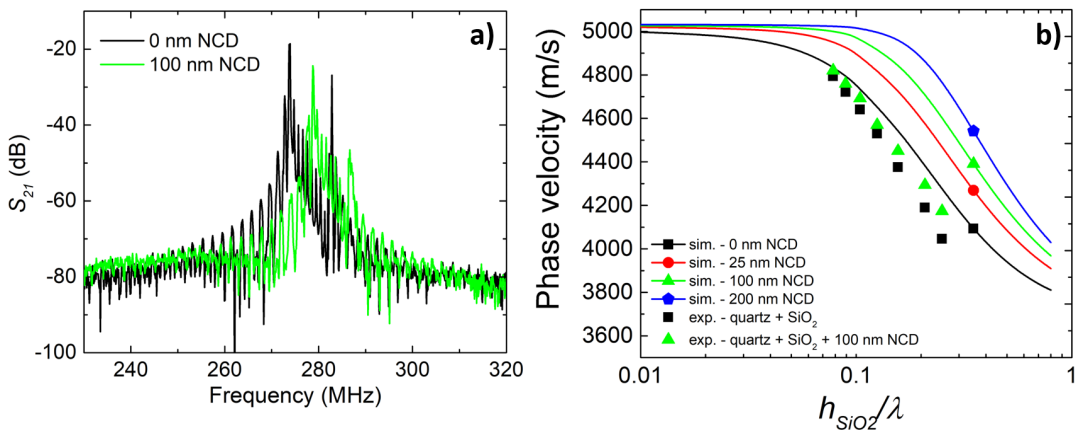


Figure 4.26: a) Spectra of transmission coefficient $S_{21}$ for LW-SAW sensor without and with NCD layer, $\lambda$ = 16 µm, $h_{SiO2}$ = 2.5 µm and b) phase velocity dispersion curves obtained experimentally and from simulations

After this experiment, simulations were repeated with changing Young's modulus $E$ of $SiO_2$ guiding layer and diamond layer to obtain a better agreement with the experimental data. At first, simulation for SAW structure without diamond was run with changing Young's modulus $E$ of $SiO_2$ guiding layer in the range of 10 - 70 GPa. Then the data were fitted in Matlab to find the exact value of $E_{SiO2}$ for given phase velocity and SAW wavelength from experiment. The same strategy was used to find the $E$ of diamond layer, just the corrected $E_{SiO2}$ was used. Figure 4.27 shows the phase velocity dispersion curves obtained from simulation with corrected Young's modulus in comparison with experimental data. Very good agreement of data can be seen for $E_{SiO2}$ = 60 GPa and $E_{NCD}$ = 240 GPa. The value of $E_{NCD}$ is much lower than previously used value of 1050 GPa of the single crystal diamond.

To support this result, the nanoindentation measurements were done on the nanocrystalline diamond layers in the cooperation with Mgr. Radim Čtvrtlík, Ph.D. from Joint Laboratory of Optics, Institute of Physics, CAS and Palacký University in Olomouc. Mechanical properties were measured at room temperature using a fully calibrated NanoTest

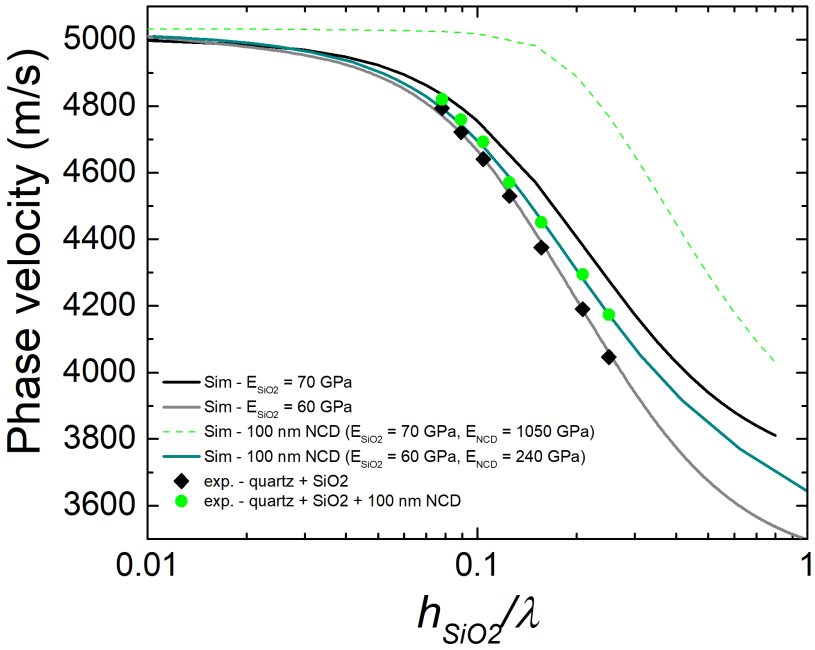


Figure 4.27: Phase velocity dispersion curves obtained experimentally and from simulations with corrected Young's modulus of $SiO_2$ guiding layer and thin NCD layer

instrument (MicroMaterials) equipped with diamond nanoindenter. Considering the very small thickness of the NCD layers, the nanoindentation hardness and reduced modulus were evaluated with a three sided pyramidal Berkovich indenter at a load of 0.6 mN. 57 nm, 100 nm and 133 nm thick NCD layers were measured on glass and silicone substrates. Obtained values of hardness and reduced modulus are shown in the graph 4.28 and listed in the table 4.3.

Table 4.3: Hardness and reduced elastic modulus of thin NCD layers with different thicknesses on two types of substrates

| NCD thickness (nm) | Substrate | Hardness (GPa) | Red. modulus (GPa) |
|---|---|---|---|
| 57 | Si | 10.3 ± 1.3 | 153 ± 12 |
| 57 | glass | 7.1 ± 0.7 | 90 ± 9 |
| 100 | Si | 9.5 ± 1.2 | 163 ± 16 |
| 100 | glass | 8.9 ± 1.2 | 101 ± 6 |
| 133 | Si | 11.7 ± 1.5 | 183 ± 35 |
| 133 | glass | 10.1 ± 0.6 | 118 ± 10 |

As the NCD layers are very thin and the indentation depth was around 20 µm, the influence of the substrate cannot be avoided. The reduced elastic modulus for NCD layers is lower than obtained from corrected simulations, which may reflect the influence of the

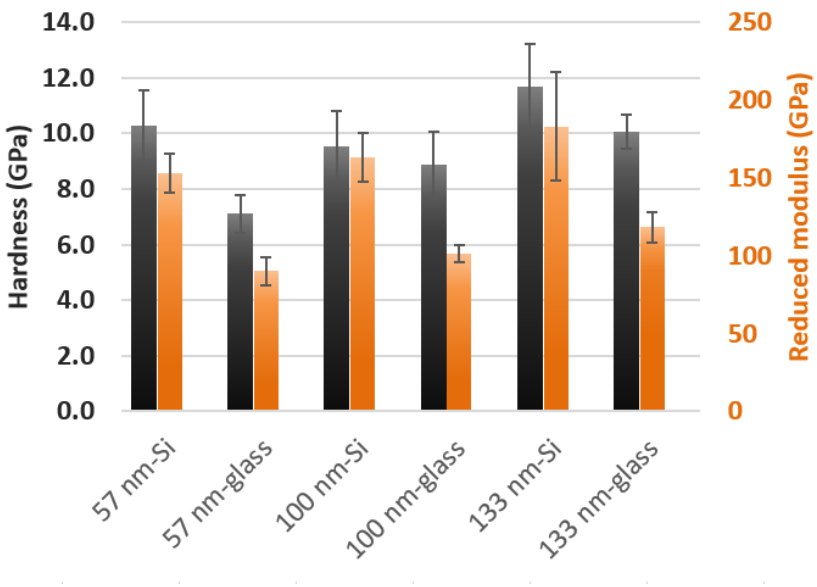


Figure 4.28: Hardness and reduced elastic modulus of thin NCD layers with different thicknesses on two types of substrates

substrate. Nanoindentation measurement done on the 310 nm thick NCD layers on silicon substrates gave value of reduced elastic modulus equal to 249 ± 20 GPa [166], which is close to the value obtained from simulation.

### Sensitivity study

According to simulations described in the chapter 4.1, sensitivity of LW-SAW sensors should decrease after the NCD coating for all types of substrates and guiding layers.

First pilot study was carried out using LW-SAW sensors fabricated at IoP. They consisted of 90ST-cut quartz substrate, 200 nm thick aluminum electrodes with two different spatial periods $\lambda = 16$ and 32 µm and 1.6 µm thick $SiO_2$ guiding layer. They were coated by 100 nm thin NCD layers. Sensor's sensitivity has been determined by measurement of the frequency response as a function of the thickness of a thin polymer deposited on its surface. The polymer consisted of a multi-layer of diluted lift-off resist (LOR) deposited by spin coating at 5000 rpm for 30 s and subsequently baked for 110 °C for 150 s on a hot plate. IDTs contact pads were also protected from LOR deposition by clean lab tape.

Figure 4.29 clearly shows a decrease in center resonant frequency with increasing LOR thickness caused by mass loading. The frequency shifts of the uncoated and NCD coated sensor are comparable for normalized thicknesses $h_{SiO2}/\lambda = 0.05$, which means that the sensitivity is not changed by deposition of a 100 nm thin NCD layer. But we can observe slight decrease in sensitivity for diamond coated sensors with $h_{SiO2}/\lambda = 0.1$ in comparison

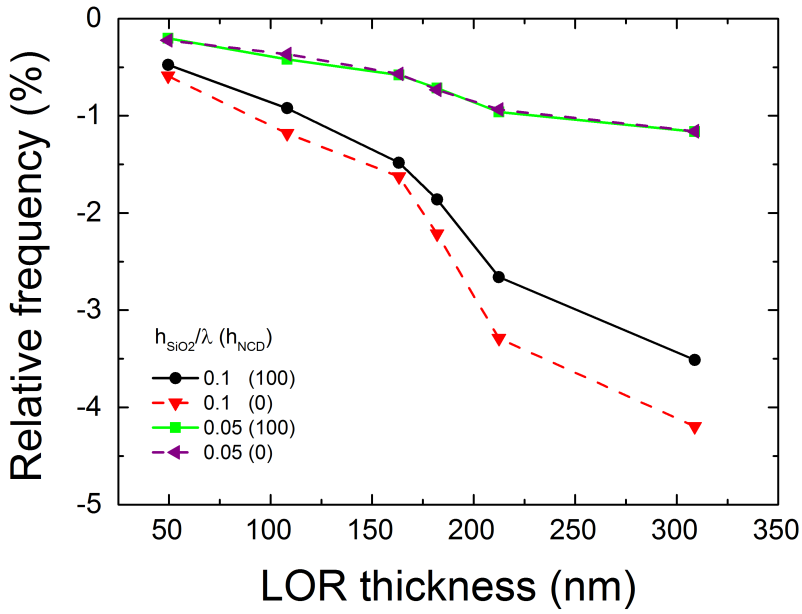


Figure 4.29: Relative center frequency shift as a function of the LOR thickness for ST-cut quartz/$SiO_2$ sensors with 100 nm NCD thickness for two different silicon normalized thicknesses $h_{SiO2} = 0.1$ and 0.05

with uncoated one. These results are not in agreement with theoretical calculations, as the high decrease in sensitivity after NCD coating has been expected. Expected result is, that the LW-SAW sensors with $h_{SiO2}/\lambda = 0.1$ exhibit higher sensitivity of 1170 $cm^2/g$ compared to 340 $cm^2/g$ of the sensor with $h_{SiO2}/\lambda = 0.05$.

To study the effect of the thickness of NCD layer on the sensor's sensitivity, the LW-SAW sensors described at the beginning of this chapter were used. 74 nm thick photoresist layer was deposited by spin coating on the sensing area of sensors and the frequency shift was measured. The mean values and standard deviations were calculated from all measured electrodes pairs with the same spatial period and the mean values are given in the graph 4.30. Relative frequency shift is increasing for the uncoated LW-SAW sensors with increasing value $h_{SiO2}/\lambda$. These measurements are consistent with expected results, as the IDTs with smaller spatial period, resulting in higher resonant frequency, are used to obtain higher $h_{SiO2}/\lambda$. From the same reason, we expected decreasing of the sensitivity of diamond coated sensors for increasing values of $h_{SiO2}/\lambda$, because the diamond normalized thickness $h_{NCD}/\lambda$ is increasing as well. This is fulfilled for 133 nm thick NCD layer. Sensitivity of sensor with 100 nm thick NCD layer is almost constant for the higher values of $h_{SiO2}/\lambda$.

To compare these results with theoretical simulations, new simulations were performed

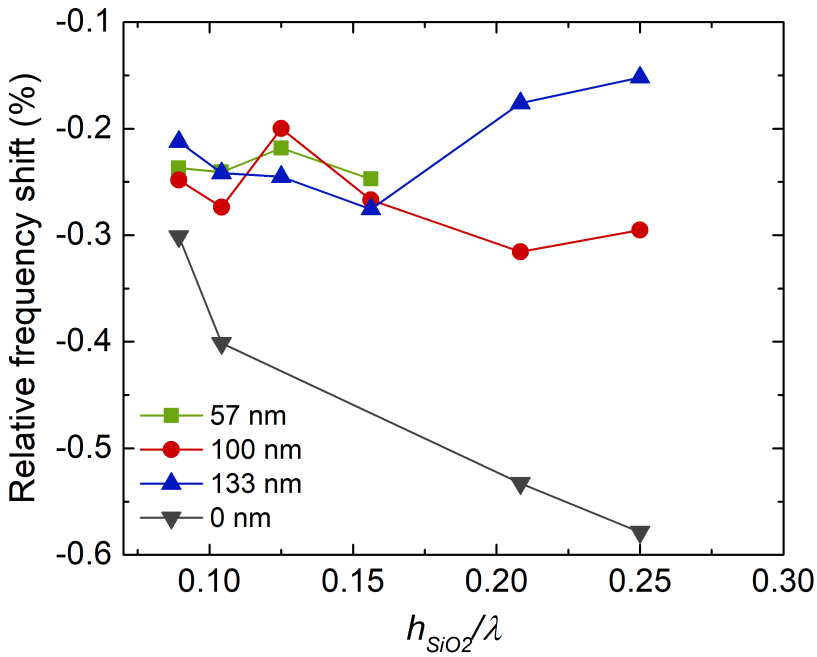


Figure 4.30: Relative center frequency shift as a function of the silicon normalized thickness for ST-cut quartz/$SiO_2$ sensors with different NCD thicknesses

that corresponds to the experimental approach. The thickness of silicon oxide guiding layer was fixed to 2.5 µm with Young's modulus $E_{SiO2} = 60$ and 70 GPa and the acoustic wavelength was changing in the range of 2 - 240 µm, which gives the $h_{NCD}/\lambda$ in the range 0.0104 - 1.25. Thickness of NCD layer was fixed to 100 and 133 nm with Young's modulus $E_{NCD} = 240$ GPa. To calculate the sensitivity, 74 nm thick PMMA layer ($\rho = 1.02$ g·cm$^{-3}$) was added on the model's surface. Graph 4.31 shows simulated relative frequency shift curves compared to the values obtained from the experiment. The diamond normalized thickness is changing for each wavelength. Hence for larger $\lambda$, there is not an impact of adding thin diamond layer on the sensitivity, as the $h_{NCD}/\lambda$ is very small, e.g. for $\lambda = 240$ µm, $h_{NCD}/\lambda = 0.000417$. The influence of diamond layer on the sensitivity can be seen for the values of $h_{SiO2}/\lambda$ 0.16 and higher, where the $\lambda = 15$ µm and $h_{NCD}/\lambda = 0.0067$. As the $h_{NCD}/\lambda$ becomes higher, the impact of diamond layer is getting more significant and reduces the sensitivity. Even though the frequency shift is smaller for higher values of $h_{SiO2}/\lambda$ for experimental data in comparison with simulations, the trends of simulated and experimental data are in a good agreement.

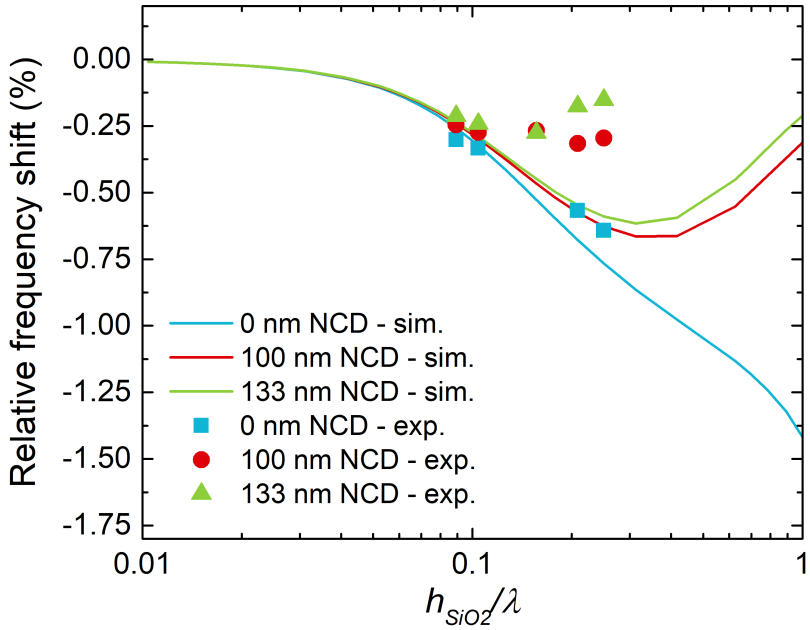


Figure 4.31: Comparison of relative center frequency shift obtained experimentally and from simulation as a function of the silicon normalized thickness for ST-cut quartz/$SiO_2$ sensors with different NCD thicknesses

### 4.5.3 36°YX $LiTaO_3$ LW-SAW sensors with $SiO_2$ guiding layer

LW-SAW sensors were fabricated on black 36°YX $LiTaO_3$ substrates with 200 nm thick aluminum electrodes and 2.5 µm thick amorphous $SiO_2$ guiding layer. Although black 36°YX $LiTaO_3$ substrate has ability to neutralize pyroelectric charges, the fabrication of LW-SAW sensors using whole 4" wafer is complex and several wafers were damaged during the fabrication process, as this substrate is very brittle. Parameters of the IDTs and resulting normalized silicon oxide thicknesses $h_{SiO2}/\lambda$ are listed in the table 4.4. Deposition of NCD layers and their characterization was carried out in the same way as was described in the chapter 4.5.2. NCD layers were deposited in three different thicknesses - 55, 65 and 98 nm.

#### Phase velocity dispersion - theory vs experiment

Example of the transmission coefficient $S_{21}$ for sensor with spatial period $\lambda = 16$ µm is shown in the figure 4.32a), where small resonant frequency shift after NCD layer deposition can be seen. Figure 4.32b) shows comparison of phase velocity dispersion as a function of $h_{SiO2}/\lambda$ obtained experimentally and from simulations. Experimentally obtained phase

Table 4.4: Parameters of IDTs used in diamond coated-LW-SAW sensors' properties study on 36°YX $LiTaO_3$ substrate

| $\lambda$ (µm) | $W$ (µm) | $N$ | $d$ (µm) | $h_{SiO2}/\lambda$ |
|---|---|---|---|---|
| 32 | 1400 | 20 | 3840 | 0.078 |
| 28 | 1100 | 20 | 3360 | 0.089 |
| 24 | 1100 | 20 | 2880 | 0.104 |
| 20 | 820 | 20 | 2400 | 0.125 |
| 16 | 700 | 20 | 1920 | 0.156 |
| 12 | 500 | 20 | 1440 | 0.208 |
| 10 | 410 | 20 | 1200 | 0.25 |

velocity is lower than the one from simulations. Also, the experimental data are scattered and does not follow one line clearly. This phase velocity drop in experimental data compared to simulation ones are possibly caused by different mechanical properties in real sensors than in simulations as was discussed for ST-cut quartz/$SiO_2$ sensors in previous section.

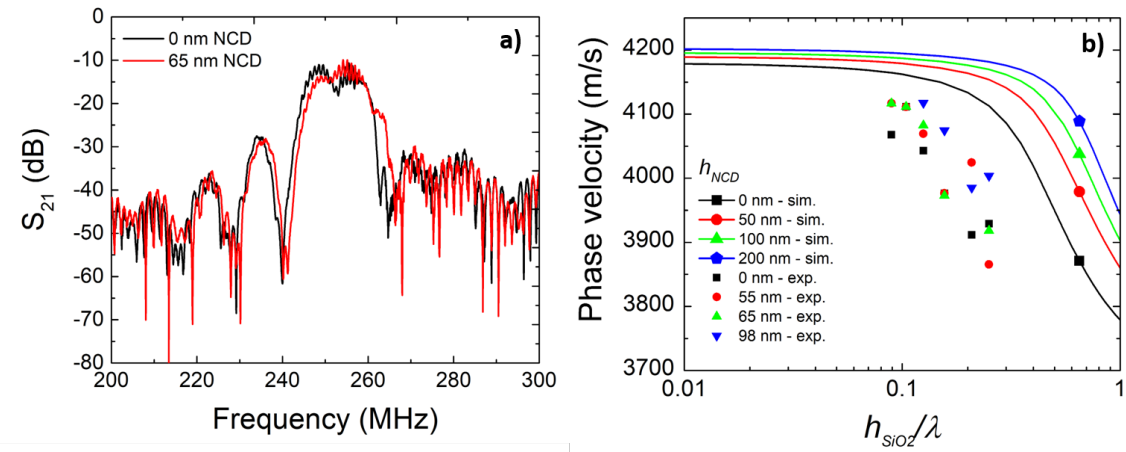


Figure 4.32: a) Spectra of transmission coefficient $S_{21}$ for LW-SAW sensor without and with NCD layer, $\lambda = 16$ µm, $h_{SiO2} = 2.5$ µm and b) phase velocity dispersion curves obtained experimentally and from simulations

Nanoindentation measurement was carried out on the diamond layers deposited on this set of samples and also on the $SiO_2$ layer deposited on $LiTaO_3$ samples. The nanoindentation hardness and reduced modulus were evaluated at a load of 0.6 mN for NCD layers and 10 mN for $SiO_2$ layers and results are shown in the figure 4.33 and table 4.5. The values for NCD layer with thicknesses 55 and 65 nm are comparable to the values obtained from nanoindentation measurement discussed in previous section, but for the 98 nm thick NCD layer were obtained unexpected low values even at several repeated measurements. On the contrary, measured reduced modulus 82 GPa for $SiO_2$ layer is

higher than the theoretical value 70 GPa. Low reduced modulus for NCD layer can explain small frequency shift observed on diamond-coated LW-SAW sensors in comparison with uncoated ones.

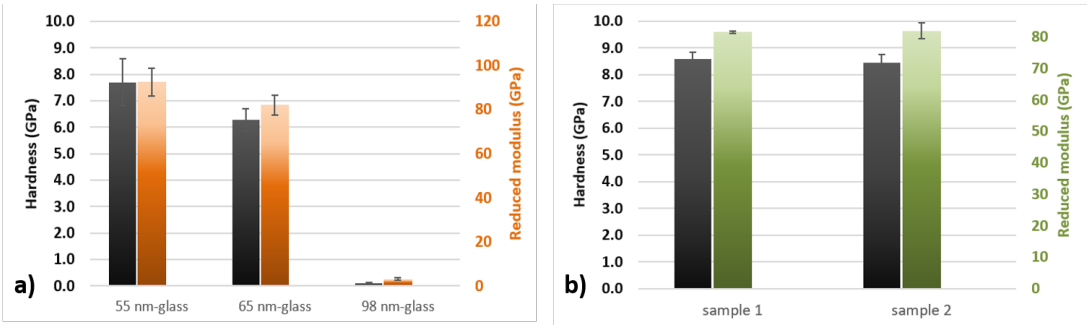


Figure 4.33: Hardness and reduced elastic modulus of a) thin NCD layers on glass substrates and b) $SiO_2$ layer on $LiTaO_3$ substrate

Table 4.5: Hardness and reduced elastic modulus of thin NCD layers on glass substrates and $SiO_2$ layer on $LiTaO_3$ substrate

| NCD thickness (nm) | Substrate | Hardness (GPa) | Red. modulus (GPa) |
|---|---|---|---|
| 55 | glass | 7.7 ± 0.9 | 93 ± 6 |
| 65 | glass | 6.3 ± 0.4 | 82 ± 5 |
| 98 | glass | **0.1 ± 0** | **3 ± 0** |
| $SiO_2$ | $LiTaO_3$ | 8.6 ± 0.2 | 82 ± 0 |
| $SiO_2$ | $LiTaO_3$ | 8.5 ± 0.3 | 82 ± 3 |

The samples were sent to IEMN to France for more precise frequency characterization, but those fragile samples were damaged during the transport and the planned sensitivity study unfortunately could not be implemented.

### 4.5.4 LW-SAW sensors with ZnO guiding layer

Deposition of the ZnO layers described in the chapter 3.2.1 was carried out on SAW sensors from 90ST-cut quartz and 36°YX $LiTaO_3$ substrates.

#### Diamond deposition on ZnO layers

Deposition of diamond layer on the ZnO layer is problematic, as ZnO layer can be etched during the deposition, therefore test samples were prepared at first. Three types of samples were prepared: 1) Si substrate, 380 nm thick ZnO layer, 2) Si substrate, 380 nm thick ZnO layer and 90 nm thin $Al_2O_3$ layer and 3) Si substrate, 380 nm thick ZnO layer and 50 nm thin $SiO_2$ layer. 150 nm thin NCD layers were deposited using standard conditions listed in

the chapter 3.3 and characterization was carried out by AFM and SEM techniques. The EDS measurement was carried out on the cross-section of samples to confirm presence of ZnO layer after NCD deposition. Figure 4.34 shows not fully closed NCD layer on Si/ZnO samples and EDS measurement revealed, that unprotected ZnO layer was etched during the NCD deposition process. On the Si/ZnO/$Al_2O_3$ sample can be seen, that only few diamond grains are present on the $Al_2O_3$ surface, but EDS measurement confirmed presence of ZnO under the $Al_2O_3$ layer. The best result was obtained for Si/ZnO/$SiO_2$ samples, where we can observe closed NCD layer and $SiO_2$ layer protected ZnO layer against etching during the NCD growth.

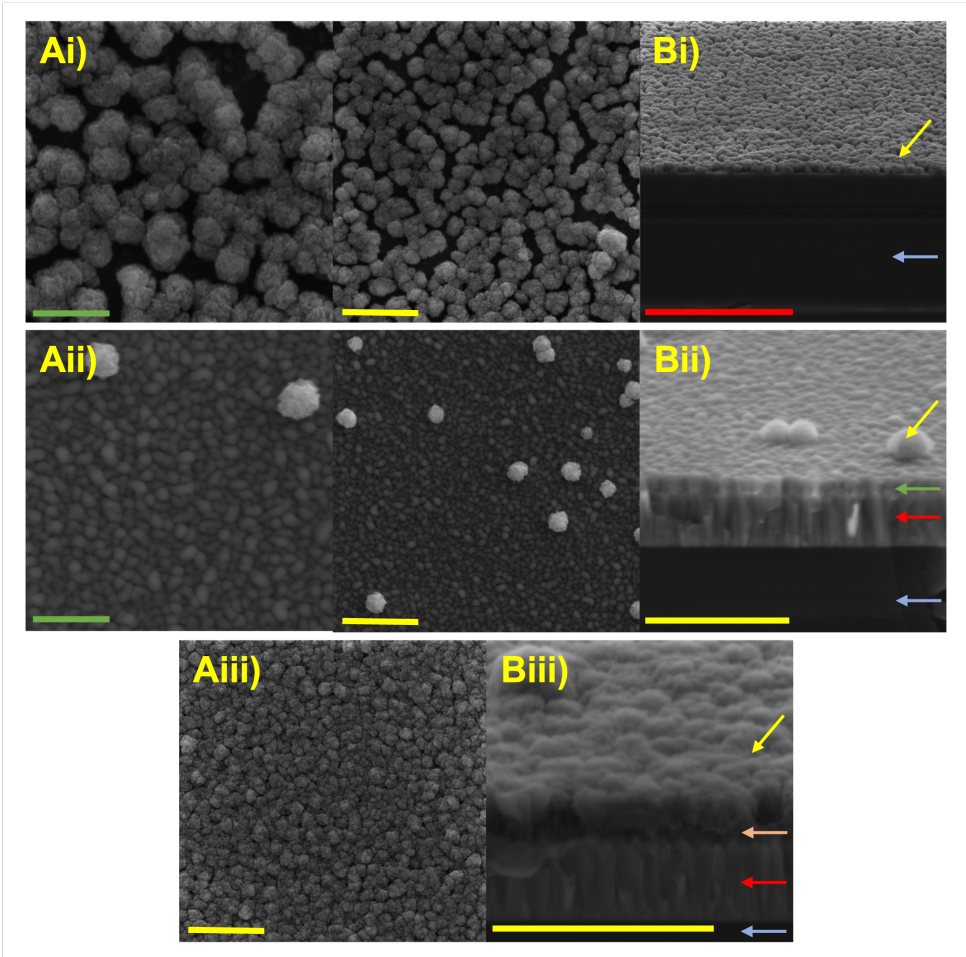


Figure 4.34: A) SEM micrographs of NCD layers deposited on ZnO layer and B) cross-section view, i) Si/ZnO, ii) Si/ZnO/$Al_2O_3$ and iii) Si/ZnO/$SiO_2$, green bar indicates 500 nm, yellow bar 1 µm and red bar is 5 µm, yellow arrow shows NCD layer, red arrow ZnO layer, green arrow $Al_2O_3$, orange arrow $SiO_2$ and blue arrow is the substrate

### Diamond coated-SAW sensors with ZnO guiding layer

1.9 µm thick ZnO guiding layer was deposited on the 90ST-cut quartz and 36°YX $LiTaO_3$ sensors with aluminum electrodes with spatial periods $\lambda = 32$, 24 and 16 µm.

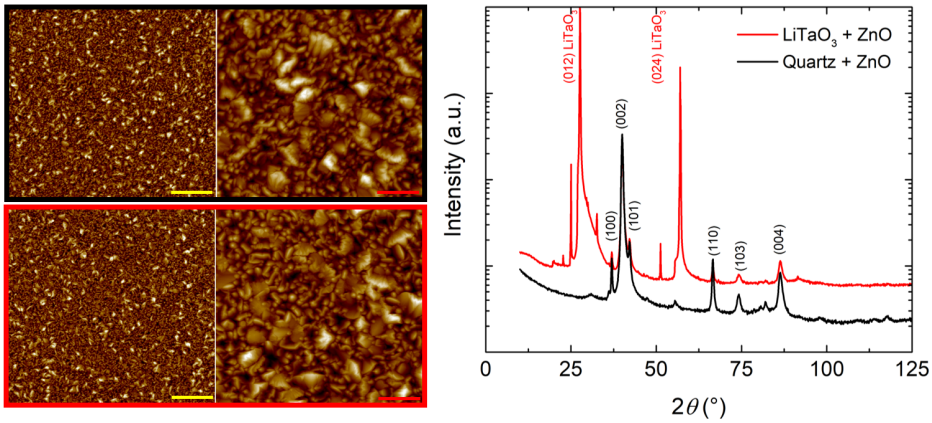


Figure 4.35: AFM micrographs and XRD spectra of ZnO layers deposited on ST-cut quartz and 36°YX $LiTaO_3$ SAW sensors

XRD patterns show crystalline structure with dominant reflections from the (002) plane, which confirms that the deposited ZnO layers are strongly textured along the c-axis of the hexagonal crystalline lattice [109]. AFM micrographs show homogeneous layers with a ZnO layer roughness rms = 49.2 nm for quartz substrate and rms = 53.1 nm for $LiTaO_3$ substrate. Prior the NCD growth, 50 nm thin $SiO_2$ protecting layer were deposited at the room temperature on the ZnO layer.

LW-SAW sensors with ZnO layers were frequency characterized before and after 50 nm thin $SiO_2$ protection layer and NCD layer depositions. Spectra of the transmission coefficient $S_{21}$ are shown in the graph 4.36 for sensors with IDTs spatial period $\lambda = 32$ µm. Resonant peak can be clearly seen for sensors without guiding layer and with ZnO layer. An increase in insertion loss is observed after the deposition of the thin $SiO_2$ layer. To our surprise the LW-SAW sensors were not working anymore after the deposition of NCD layer. The possible explanation is, that during the diamond deposition, the ZnO layers became conductive by elimination of oxygen disorders, that acts as acceptors and eliminates the free charge in the ZnO layers.

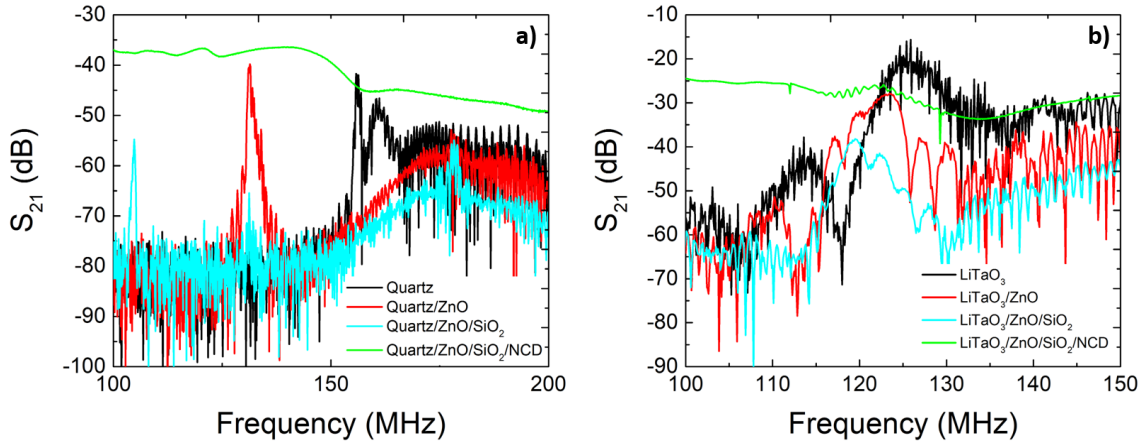


Figure 4.36: Spectra of transmission coefficient $S_{21}$ for LW-SAW sensors with ZnO layers deposited on a) ST-cut quartz and b) 36°YX $LiTaO_3$ substrates, $\lambda = 32$ µm

### 4.5.5 Conclusions

This chapter was focused on fabrication and characterization of LW-SAW sensors made from quartz and lithium tantalate piezoelectric substrates with $SiO_2$ or ZnO guiding layers. The aim of this chapter was to compare the experimental data with the one obtained from simulation to verify the simulation model. The phase velocity obtained experimentally was lower for 90ST-cut quartz/$SiO_2$ sensors and the difference between experimental and simulation data were even bigger for diamond coated sensors. This resulted from different mechanical properties of $SiO_2$ and diamond materials used in simulations and in real sensors. The simulations were corrected to fit the experimental data giving the Young modulus equal to 60 GPa and 240 GPa for $SiO_2$ and NCD layer respectively. To confirm this result, the nanoindentation measurement was carried out giving even lower Young modulus of NCD layer in the range of 90 - 120 GPa on glass substrate. As the NCD layers are very thin, the influence of the glass ($E = 70$ GPa) and silicon ($E = 168$ GPa) cannot be avoided, which is compared by higher reduced modulus values obtained on samples with silicon substrates. This result is important as it shows that the obtained simulation results for diamond coated sensors does not completely reflect their real behavior. This was confirmed during the sensitivity study, as the expected big drop in sensitivity for diamond coated LW-SAW sensors was not observed. We also observed a decrease in the sensitivity after NCD deposition on top of ST-cut quartz/$SiO_2$ sensors for higher values of $h_{SiO2}/\lambda$.

We observed the same result on sensors fabricated on 36°YX $LiTaO_3$ substrate with

$SiO_2$ layer. Phase velocity obtained experimentally was lower in comparison with the simulation. Nanoindentation measurement revealed even lower Young modulus of NCD layers equal to 80 - 90 GPa. As this values were measured on glass substrate, the real values will be slightly higher. The sensitivity could not be carried out as the samples were damaged during the transport to IEMN in France.

We also studied the LW-SAW sensors with ZnO as guiding layer on both piezoelectric substrates. Deposition of thin NCD layers were successfully achieved using 50 nm thin $SiO_2$ protecting layer. Unprotected ZnO layer is etched away during the diamond deposition process. Diamond deposition of NCD layers were successful on LW-SAW sensors with ZnO layer, but unfortunately the sensors were not working after this deposition. The possible explanation is the elimination of oxygen disorders from ZnO layer during the diamond deposition that caused conductivity of ZnO layer.

Important part of biosensor development is the proper choose of the biosensing elements. In this Thesis the bacteriophage's tail fibers were chosen. The next chapter is devoted to the description of their production, purification and also the specificity of their binding to the host bacteria is studied.

## 4.6 Bacteriophage's tail fibers production

The six bacteriophage T7 tail fibers are homo-trimers of the gp17 protein. They are responsible for the first specific, reversible attachment to its host *E. coli* lipopolysacharide (LPS) using the C-terminal domains [167]. Gp12 proteins are short tail fibers of bacteriophage T4 and bind irreversibly to the host cell LPS core region [168] and ORF26 is the tail fiber of bacteriophage T1 [169]. TEM pictures of T4 and T7 phages are shown in the figure 4.37. His-tag is a affinity tag consisting of six polyhistidine residues and this tag has strong interaction with immobilized metal ion matrices, transition metal ions such as $Co^{2+}$, $Ni^{2+}$, $Cu^{2+}$ or $Zn^{2+}$. This is advantageously used for the purification of peptides, as they are efficiently retained on the metal ion matrices and can be easily eluted by either adjusting pH of the column buffer or by adding free imidazole to the washing buffer [170]. Apart from its use in purification, his-tags can be used for protein immobilization to the various surfaces with attached transition metal ions, which will be used in this Thesis.

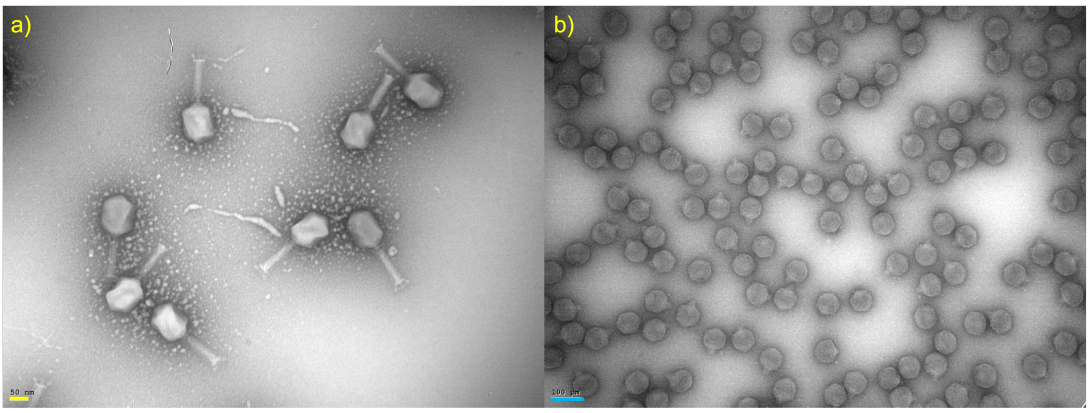


Figure 4.37: TEM pictures of a) T4 and b) T7 bacteriophages, yellow bar refers to 50 nm and blue bar refers to 100 µm

All of the proteins were obtained during a six months stay at the National Centre of Biotechnology (CNB-CSIC) in Madrid, Spain within the research group Structural Biology of Viral Fibers under the leadership of Mark J. van Raaij.

Production and purification of his-tagged proteins can be divided into four main steps: 1) transformation of the plasmid carrying the gens for the desired protein and also the gens for antibiotic resistance in the suitable bacteria cells, 2) growth of the transformed bacteria cells and protein expression, 3) harvesting of cells, their lysis and collecting the protein and 4) protein purification. Simplified schematic of protein production and purification process is shown in the figure 4.38.

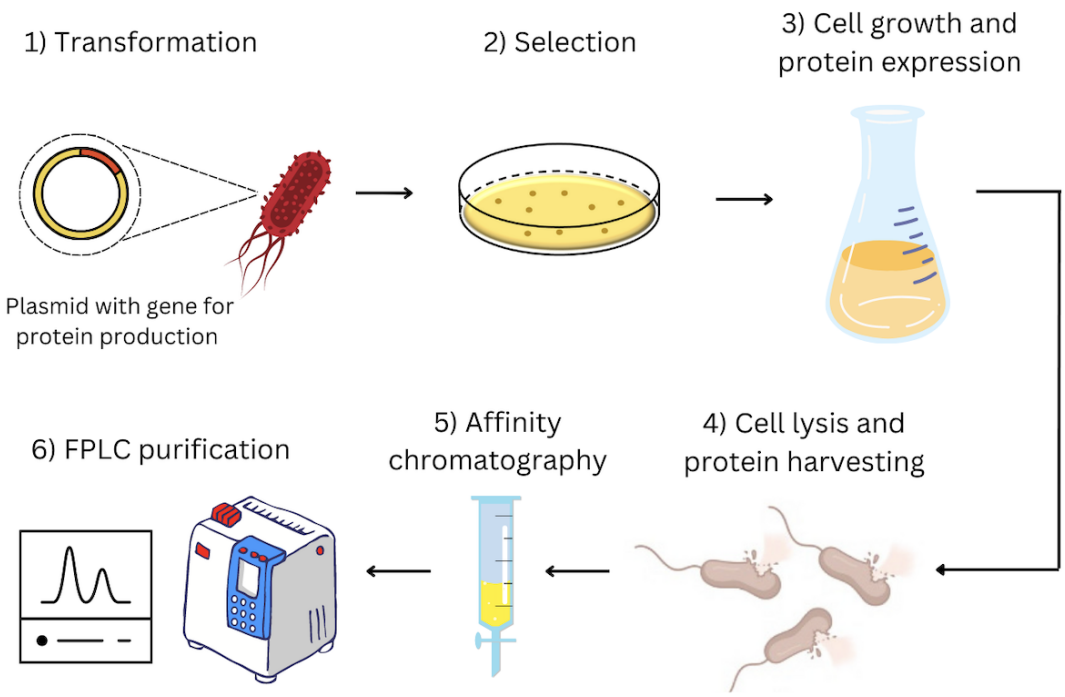


Figure 4.38: Schematic of protein production and purification

### 4.6.1 Production and purification of His-tagged gp17 protein

For expression of the gp17 protein, *E. coli* strain BL21(DE3-) was freshly transformed with the plasmid pET30a(+), containing gene for gp17 expression, by thermic shock. 50 µl of bacteria cells were mixed with 3 µl of plasmids and putted to 42 °C for 45 seconds followed by 2 minutes on ice. 250 µl of LB media was added and left shaking at 37 °C for 1 hour. The culture was spread onto a plate with LB media containing kanamycin and left at 37 °C overnight to let the transformed cells grown. Four 0.9 l cultures (LB medium with kanamycin) with transformed cells were grown aerobically at 37 °C to an optical density of 0.6 - 0.8 measured at 600 nm. Cultures were then cooled to 16 °C and the protein expression was induced by adding 900 µl of 1 mM isopropyl-$\beta$-D-1-thiogalactopyranoside (IPTG). Protein expression was carried out at 16 °C shaking (120 rpm) overnight to achieve good protein folding. Cells were harvested by centrifugation (6000 g, 5 °C, 10 minutes), resuspended in 40 ml of lysis buffer (50mM Tris-HCl pH 8.0, 4% glycerol, 50mM ammonium chloride, 2mM EDTA, 150mM sodium chloride) and lysed by sonication. Insoluble material was removed by centrifugation (15000 g, 4 °C, 30 minutes) and supernatant containing expressed protein was collected.

Purification of gp17 protein was carried out by immobilized metal chromatography

and anion exchange chromatography. 2 ml of nickel-nitriloacetic acid resin (NiNTA, Jena Bioscience, Jena, Germany) was added to the supernatant and incubated for 30 min on ice to let the His-tag bind to the $Ni^{2+}$ ions in resin. The suspension was poured into a column and washed with 50mM Tris-HCl pH 8.5, 0.3M NaCl buffer. Elution of protein was performed with a step gradient of imidazole in the same buffer (0.1, 0.15, 0.2, 0.25, 0.3, 0.4 and 1.0M imidazole) and all collected fractions were checked on SDS-PAGE electrophoresis, as is shown on figure 4.39.

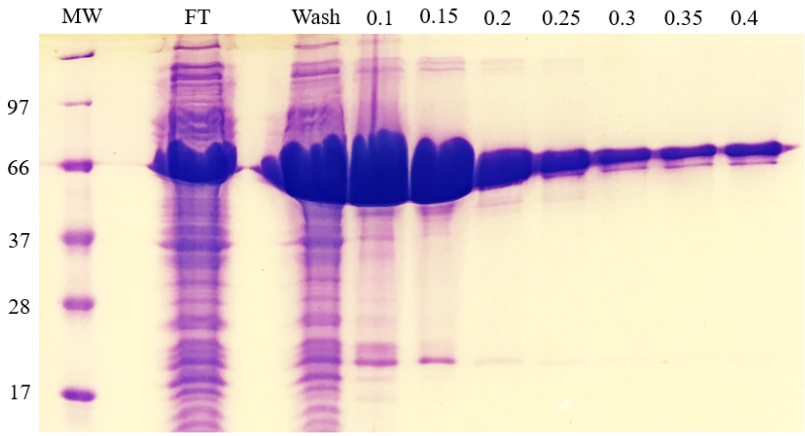


Figure 4.39: SDS-PAGE after Ni purification, lane MW is a mixture of molecular-weight marker proteins (in kDa), lane FT (flow through), lane Wash(0.05mM imidazole) and lanes 0.1 - 0.4 indicate step gradient of imidazole. Size of trimer of gp17 is 66 kDa.

The eluted protein was dialyzed against 10mM Tris-HCl pH 8.5 overnight. Final purification was carried out by using fast protein liquid chromatography (FPCL) by loading onto an UnoQ12 quaternary ammonium strong anion-exchange column (BioRad, Madrid, Spain). The protein was eluted with a linear gradient of 0-1M NaCl in 10mM Tris-HCl pH 8.5. The purified gp17 protein was eluted around 0.25M NaCl and its purity was checked by using SDS-PAGE, see figure 4.40. The washing of protein from NaCl was done using concentration flask by centrifugation (5000 g, 15 °C, 20 min). Second washing step was done using the washing buffer (10 mM Tris-HCl, pH 8.5) and centrifugation (15 °C, 6000 g, 40 min) and repeated three times. The final concentration of gp17 protein was checked using a Nanodrop spectrophotometer.

### 4.6.2 Production and purification of His-tagged gp12 protein

For production of gp12 protein, the *E. coli* strain JM109(DE3) was freshly transformed with the pCDFduet-gp12gp57 plasmid by using thermic shock method. Transformed

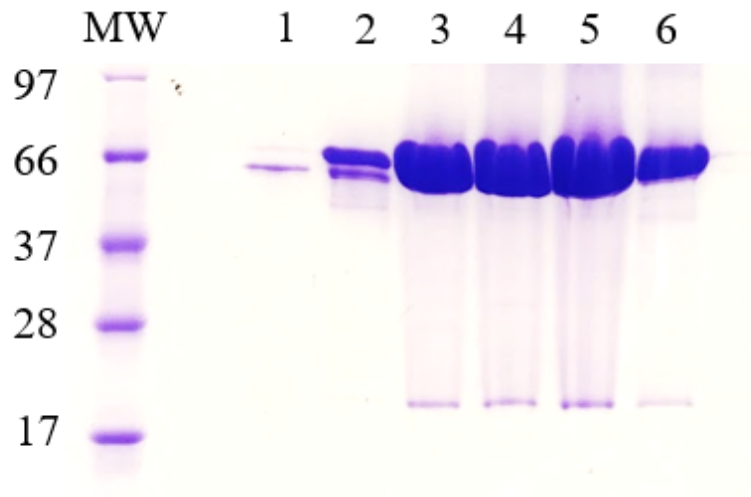


Figure 4.40: SDS-PAGE of purified gp17 protein. Lane MW is a mixture of molecular-weight marker (in kDa) and lanes 1-6 are fractions containing gp17

cells were putted on plate containing streptomycin antibiotics and grown overnight at 37 °C. Three 0.9 l cultures (LB medium with streptomycin) were grown at 37 °C until $OD_{600}$ reached 0.6. Then, the bacterial culture was cooled down on ice to 18 °C, protein expression was induced by adding 900 µl of 0.1mM IPTG and incubated overnight at 18 °C. Cells were harvested by centrifugation (6000 g, 5 °C, 10 min), supernatant was discarded and pellet was resuspended in lysis buffer (50mM $Na_2HPO_4$, 300mM NaCl, pH 8) and lysed by sonication. Lysed bacteria were treated by 1 mM PMSF and incubated on ice for 15 minutes. Fractions were separated by several centrifugation (15 000 g, 15 °C, 45 min). As gp12 strongly bind to the bacteria cells residues, soluble fractions were discarded and pellet was resuspended in Tris buffer and gently mixed for 30 min. This process was repeated three times. Last pellet was resuspended in phosphate buffer (50mM $Na_2HPO_4$, 300mM NaCl, pH 8) and centrifuged (15 000 g, 15 °C, 45 min). The soluble fraction was kept and filtered through 0.45 µm PVDF filter and incubated overnight at 10 °C with 1% w/v glycerol.

For gp12 purification, the preparation was incubated with NiNTA agarose for 30 minutes on ice. The suspension was poured on the column and washed with three wash buffers: WASH I (50mM $NaH_2PO_4{\cdot}H_2O$, 300mM NaCl, 25mM imidazole, 1% glycerol (w/v), 0.05% TWEEN20 (v/v), pH 8, 15 ml), WASH II (50mM $NaH_2PO_4{\cdot}H_2O$, 300mM NaCl, 25mM imidazole, 1% glycerol (w/v), 15 ml) and WASH III (50mM $NaH_2PO_4{\cdot}H_2O$, 300mM NaCl, 100mM imidazole, 1% glycerol (w/v), 10 ml). The protein was eluted using 5x5 ml of elution buffer (50mM $NaH_2PO_4{\cdot}H_2O$, 300mM NaCl, 500mM imidazole,

4% glycerol (w/v), pH 8). All of the collected fractions were checked on SDS-PAGE, shown on figure 4.41. Prior loading to SDS-PAGE, protein samples were heated at 95 °C for 5 minutes to obtain denaturated monomeric form. The buffer of chosen eluted fractions (E1, E2 and E3) was exchanged to phosphate buffer using centrifuge concentrators (5000 g, 5 °C) and final gp12 concentration was checked spectrophotometrically (using Nanodrop).

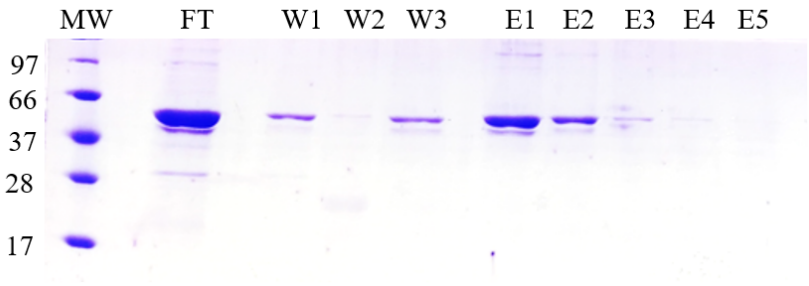


Figure 4.41: SDS-PAGE of purified gp12 protein. Lane MW is a mixture of molecular-weight marker (in kDa), lane FT is flow through, W1 - W3 are washes and lanes E1 - E5 corresponds to 5 elution fractions, heated gp12 (denaturated protein) as monomeric has size 57.5 kDa.

### 4.6.3 Production and purification of His-tagged ORF26 protein

For ORF26 protein production, the *E. coli* bacteria JM109 strain was freshly transformed by plasmid pet28F1p26.296S578A by thermic shock. Transformed cells were placed on plate (LB with kanamycin) and grown overnight at 37 °C. Four 0.9l cultures (LB with kanamycin) were grown at 37 °C shaking till $OD_{600}$ reached 0.7. Cultures were cooled down on ice for 30 minutes and the protein expression was induced by adding 500 µl 1M IPTG to each and let shaking overnight at 16 °C. Cells were harvested by centrifugation (6000 g, 5 °C, 10 min), resuspended in lysis buffer (500mM NaCl, 20mM Tris-HCl, 10% glycerol, pH 8.5) and lysed by sonication. The released protein and bacterial cells residues were separated by centrifugation (15 000 g, 4 °C, 30 min). Supernatant was incubated with 2 ml of NiNTA resin (for each 25 ml of supernatant) and shaked for 30 min on ice. The suspension was poured into a column and washed with washing buffer (20mM imidazole, 500mM NaCl, 10mM Tris-HCl pH 8.5). Elution of protein was performed with a step gradient of imidazole in the same buffer (0.1, 0.15, 0.2, 0.25, 0.3, 0.4 and 1.0M imidazole) and all collected fractions were checked on SDS-PAGE electrophoresis.

The eluted protein was dialyzed against 200nM NaCl, 10mM Tris-HCl pH 8.5 for 1 hour

followed by dialization against 10mM Tris-HCl pH 8.5 overnight. Final purification was carried out using FPLC method by loading onto an ResQ anionic column and the protein was eluted with a linear gradient of 0-1 M NaCl in 10mM Tris-HCl pH 8.5. The washing of protein from NaCl was done using the concentration flask by centrifugation (5000 g, 15 °C, 20 min) followed by washing using the 10mM Tris-HCl, pH 8.5 and centrifugation (6000 g, 15 °C, 40 min) and repeated three times. The final concentration of obtained ORF26 protein was checked using Nanodrop.

### 4.6.4 Immunofluorescence assay

Immunofluorescence assays were used to study produced protein's binding to three different bacteria strains - *Escherichia coli* BL21(DE3-), *Salmonella enterica* subsp. enterica serovar Anatum A1 and *Staphylococcus aureus* RN9220 ΔSpA. Schematic of the immunofluorescence assay principle is shown in the figure 4.42.

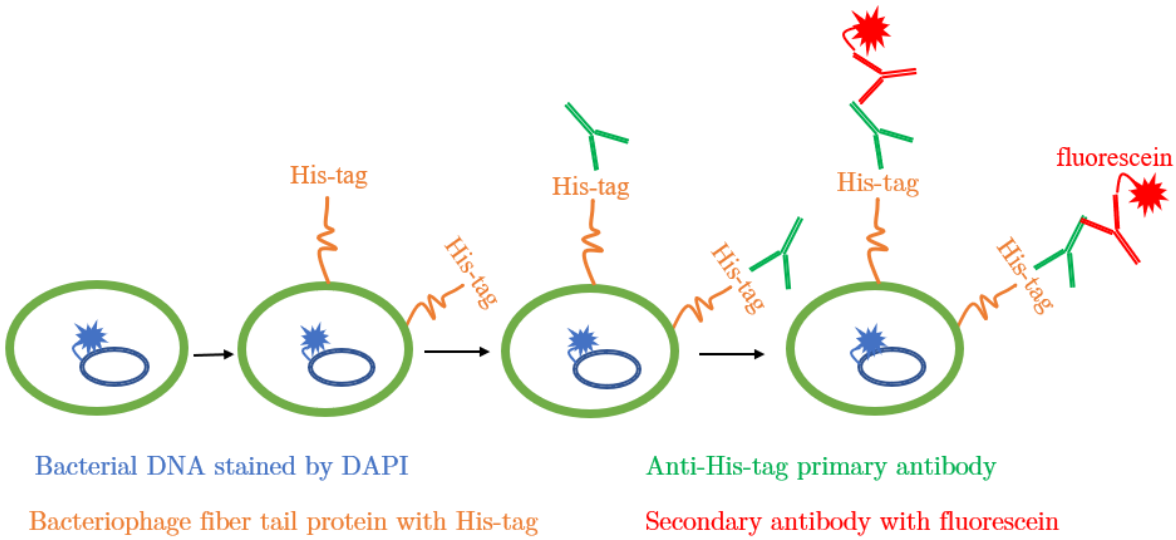


Figure 4.42: Schematic of the immunofluorescence assay

#### Materials

**Chemicals.** For the immunofluorescence assay the following chemicals were used: phosphate buffer saline (PBS) was prepared in laboratory of CNB, Paraformaldehyde (PFA, 16% in water) was used for cells fixation, ProLong Gold (Thermo Fisher) was used to protect fluorescent dyes from photobleaching during fluorescence microscopy and Fetal calf serum (FCS) was used for blocking to prevent non-specific adhesion of fluorescent

dyes. DAPI (4′,6-diamidino-2-phenylindole) is blue-fluorescent DNA stain used for bacteria cells staining. Anti-His-tag rabbit antibody (Thermo Fisher) as primary antibody and secondary fluorescent-labeled AlexaFluor546 goat anti-rabbit antibody (Thermo Fisher) were used.

**Bacterial strains.** All strains used in this work were grown in LB medium at 37 °C shaking overnight. $OD_{600}$ was measured and the number of cells/ml was calculated, desired number of cells for each bacteria strain is shown in the table 4.6.

**Proteins** All used proteins were prepared according to the protocols mentioned above. Concentration of proteins was measured by Nanodrop in mg/ml and recalculated using the theoretical extinction coefficient of each protein. The volume of protein solution added to the sample was adjusted to obtain concentration of $6 \cdot 10^{-8}$ mol. All used proteins are tail fibers of bacteriophages that bind to the *Escherichia coli* cells.

Table 4.6: Bacteria strains with needed number of cells/ml and used proteins

| **Bacteria strain** | |
|---|---|
| *Escherichia coli* BL21(DE3-) | $1.6 \cdot 10^9$ cells/ml |
| *Salmonella enterica* subsp. enterica serovar Anatum A1 | $1.6 \cdot 10^9$ cells/ml |
| *Staphylococcus aureus*RN9220 ΔSpA | $3.2 \cdot 10^9$ cells/ml |
| **Protein** | **Extinction coefficient** |
| gp17 | $\epsilon = 52940\ \mathrm{M}^{-1} \cdot \mathrm{cm}^{-1}$ |
| gp12 | $\epsilon = 54445\ \mathrm{M}^{-1} \cdot \mathrm{cm}^{-1}$ |
| ORF26 | $\epsilon = 66600\ \mathrm{M}^{-1} \cdot \mathrm{cm}^{-1}$ |

### Protocol

Fresh bacterial cultures were grown overnight at 37 °C shaking. The volume of bacterial cultures containing desired number of cells were calculated from $OD_{600}$. Cells were harvested by centrifugation at 6000 g for 5 minutes and washed in PBS buffer once. 50 µl of cells (for one glass slide sample) were incubated with DAPI ($c$=15 µg/ml) for 30 minutes at room temperature. From this step, all further work was carried out in dark to protect fluorescent dye from light. Cells were washed twice in 200 µl of PBS buffer by centrifugation (6000 g, 5 min), finally resuspended in 50 µl of PBS buffer and incubated with the

calculated amount of solution containing protein for 1 hour at room temperature. For negative control, only PBS buffer without protein was added to the cells. Cells were then washed in PBS buffer by centrifugation (8000 g, 5 min). 240 µl of 4% PFA was added to each sample and incubated for 7 minutes. Cells were washed twice in PBS buffer by centrifugation (8000 g, 5 min) and finally resuspended in 200 µl of PBS buffer. Sample was put on the coverslip and left for 40 minutes to attach cells to the coverslip. Then each sample was washed with 400 µl of PBS buffer. 200 µl of FCS (20% in PBS buffer) was added to each sample to block coverslip surface to avoid non-specific absorption of antibodies. After 30 minutes, FCS was removed and 200 µl of primary antibody (1:500, 2% FCS in PBS) was added for 2 hours. Primary antibody solution was removed and samples were washed five times with 400 µl of PBS buffer. 200 µl of secondary antibody (1:500 in PBS) was added and incubated for 2 hours. Then the secondary antibody solution was removed and samples were washed five times with 400 µl of PBS buffer. 3 µl of ProLong Gold was added to the glass slide and the coverslip with cells was flipped onto it and let dry overnight at dark.

### Results

All of the three proteins - gp17, gp12 and ORF26 were tested for binding to all three different bacteria strains, as is shown in table 4.7.

Table 4.7: Expectation and results of protein binding to bacteria cells

| | **gp17** | | **gp12** | | **ORF26** | |
|---|---|---|---|---|---|---|
| | expected | result | expected | result | expected | result |
| *E. coli* | ✓ | ✓ | ✓ | ✓ | ✓ | ✓ |
| *Salmonella* | × | × | × | ✓ | × | × |
| *Staphylococcus* | × | × | × | × | × | × |

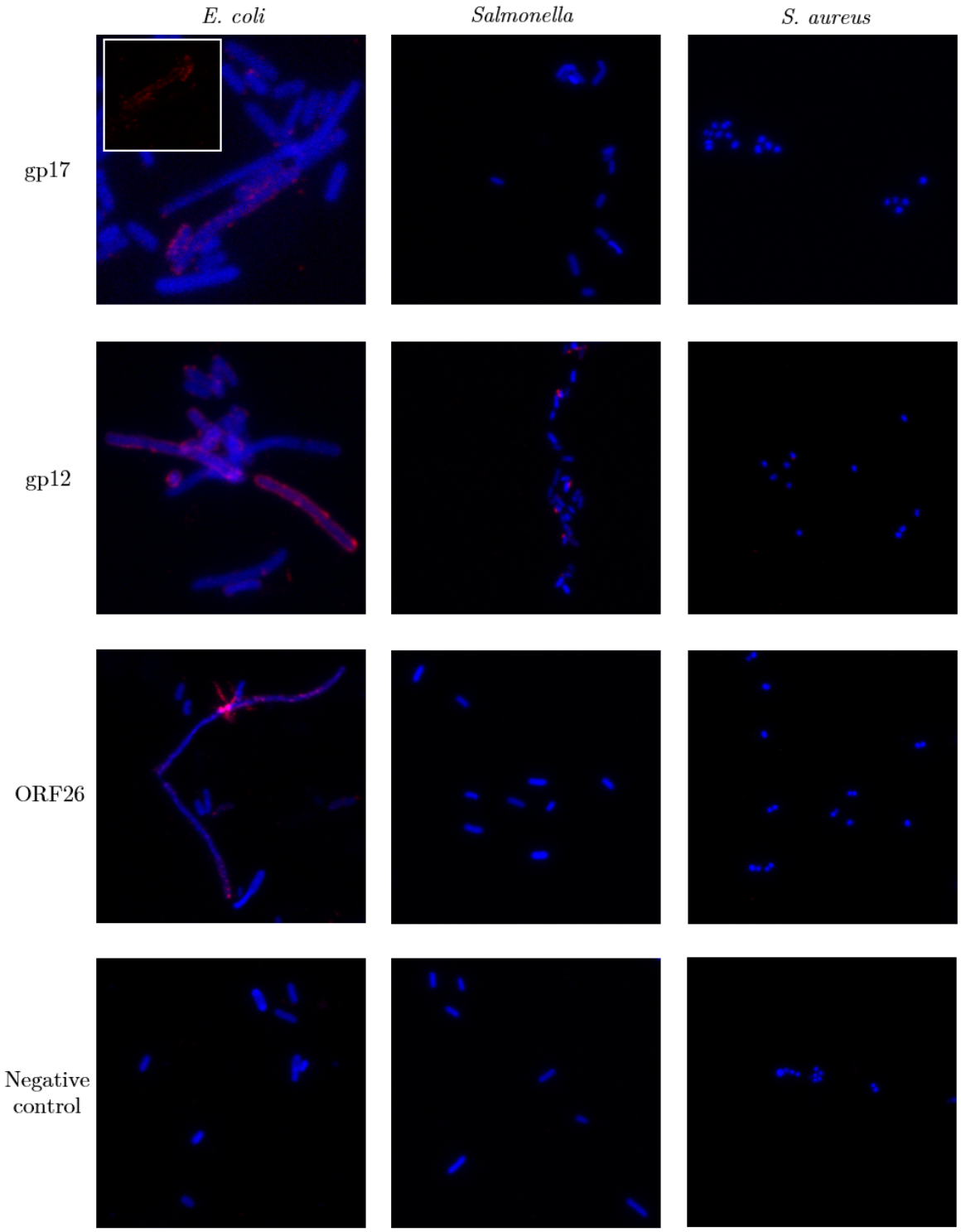


Figure 4.43: Results from bacteria binding study using fluorescent microscopy. Three different strains of bacteria were tested for protein binding. Blue are the bacterial cells stained by DAPI and red are the attached proteins to the bacteria cells.

### 4.6.5 Conclusions

This chapter summarizes the work, that was carried out within the internship at the National Center of Biotechnology (CNB-CSIC). Three different N-terminally his-tagged

bacteriophage's tail fibers proteins binding to *E. coli* cells were successfully produced. Immunofluorescence assay was carried out to investigate the ability of produced tail fibers to bind to different bacterial cells. Gp17 protein as well as ORF26 bind to *E. coli* cells as was expected, gp12 also binds a little bit to *Salmonella* cells, which can lead to non-specific interactions when used in biosensors.

## 4.7 Functionalization of the diamond layers

To obtain a biosensor, it is necessary to attach bioreceptors on the sensor's surface. In this work, the bacteriophage's tail fibers with his-tag are used to functionalize the diamond surface, their production is described in previous chapter 4.6.

For the immobilization of the (His)6-tagged proteins, it is necessary to introduce metal cations on the surface. In this work, two different approaches were used to obtain $Ni^{2+}$ ions on the BDD surface: 1/ attachment of nitriloacetic acid (NTA), which is one of the most common chelating agent used for immobilization of metal cations and 2/ introduction of nickel nanoparticles (NiNPs) on diamond surface.

Both of the functionalization approaches were carried out using electrochemical methods, so the boron-doped diamond (BDD) layers were used. BDD is an excellent chemically and mechanically stable electrode with a wide potential window in both aqueous and non-aqueous solvents, very low double layer capacitance and background currents [171, 172]. Electrochemical characterizations were carried out by my colleague Mgr. Simona Baluchová, Ph.D.

### 4.7.1 Electrochemical characterization of the BDD electrodes

Prior to the immobilization protocol, all of the samples were electrochemically (E/C) characterized to determine the quality of the layer from the E/C point of view.

To investigate the electrochemical performance of fabricated BDD layers, cyclic voltammetry (CV) was recorded in a supporting electrolyte 1 mol·L$^{-1}$ KCl and two different redox probes, namely: $[Ru(NH_3)_6]^{3+/2+}$ (surface insensitive probe) and $[Fe(CN)_6]^{3-/4-}$ (surface sensitive probe) and electrochemical impedance spectroscopy (EIS). Cyclic voltammograms were recorded with a scan rate of $v$ = 100 mV·s$^{-1}$ (5x) in the 1 mmol·L$^{-1}$ $[Ru(NH_3)_6]^{3+/2+}$ in 1 mol·L$^{-1}$ KCl and 1 mmol·L$^{-1}$ $[Fe(CN)_6]^{3-/4-}$ in 1 mol·L$^{-1}$ KCl solutions. The most valuable parameter obtained from these measurements is anodic and cathodic peak potential separation ($\Delta E_p$), which is inherently related to the heterogeneous electron transfer rate. The value for the fully reversible system exchanging only one electron is 59 mV [138]. EIS spectra were recorded in the frequency range $f$ from 100 kHz to 0.1 Hz in the 1 mmol·L$^{-1}$ $[Fe(CN)_6]^{3-/4-}$ in 1 mol·L$^{-1}$ KCl solution. All experiments were carried out at room temperature.

### Low temperature BDD electrodes

The BDD layers were grown on the conductive (100)-oriented 10x10 mm silicon (cSi) substrates (ON Semiconductor, Czech Republic). Prior the diamond seeding, samples were cleaned using sonication in acetone, isopropylalcohol and hot distilled water for 5 minutes in each followed by 10 minutes in $H_2SO_4$ + $H_2O_2$ mixture (1:1) and sonicated twice in hot water for 5 minutes. As thin $SiO_2$ layer form naturally on Si surface, all samples were etched for 30 seconds in hydrofluoric acid (HF) and rinsed twice in hot water in ultrasonic bath for 5 minutes. After the cleaning procedure, samples were seeded with nanodiamond particle colloid by spin coating (30 s at 3000 rpm). Two different series - S1 and S2 of BDD layers were grown using MW-LA-PECVD apparatus at low temperatures, as the immobilization of the proteins is intended to be carried out on the acoustic sensors (LW-SAW device or QCM). The conditions used for the BDD layers deposition are shown in table 4.8. AFM was used to observe the morphology of the layers and Raman spectroscopy was measured to give a qualitative indication of the purity (diamond vs. non-diamond carbon content) of BDD layers. Raman spectra confirmed incorporation of boron atoms into the diamond lattice as the B related peaks at *ca* 470 $cm^{-1}$ and 1217 $cm^{-1}$ are present and diamond Raman line is red shifted to 1299 $cm^{-1}$ (S1) and 1305 $cm^{-1}$ (S2) respectively [138], see picture 4.44a). Boron concentration obtained from Raman spectra was $\sim 4 \cdot 10^{21}$ atoms·$cm^{-3}$ for Serie 1 and $\sim 1.58 \cdot 10^{21}$ atoms·$cm^{-3}$ , which is above the accepted value for metal-insulator transition [138]. AFM picture showed fully closed layer with cauliflower structure and roughness RMS = 14.7 nm (S1) and crystalline layer with roughness RMS = 12.4 nm (S2), see picture 4.44b) and c).

Table 4.8: BDD layers deposition conditions at low temperature

| | **Serie 1** | **Serie 2** |
|---|---|---|
| **Process gas flow (sccm)** | 8 $CH_4$, 40 $H_2$,150 $B_2H_6$, 1.75 $CO_2$ | |
| **MW power (kW)** | $2 \cdot 2.7$ | |
| **Process pressure (mBar)** | 0.25 | |
| **Substrate temperature (°C)** | $\sim$ 450 | $\sim$ 600 |

*Electrochemical characterization using redox markers*

Electrochemical characterization of fabricated BDD electrodes was conducted by CV and EIS as described above. The measured values of $\Delta E_p$ for studied electrodes in two different redox probes are tabulated in the table 4.9.

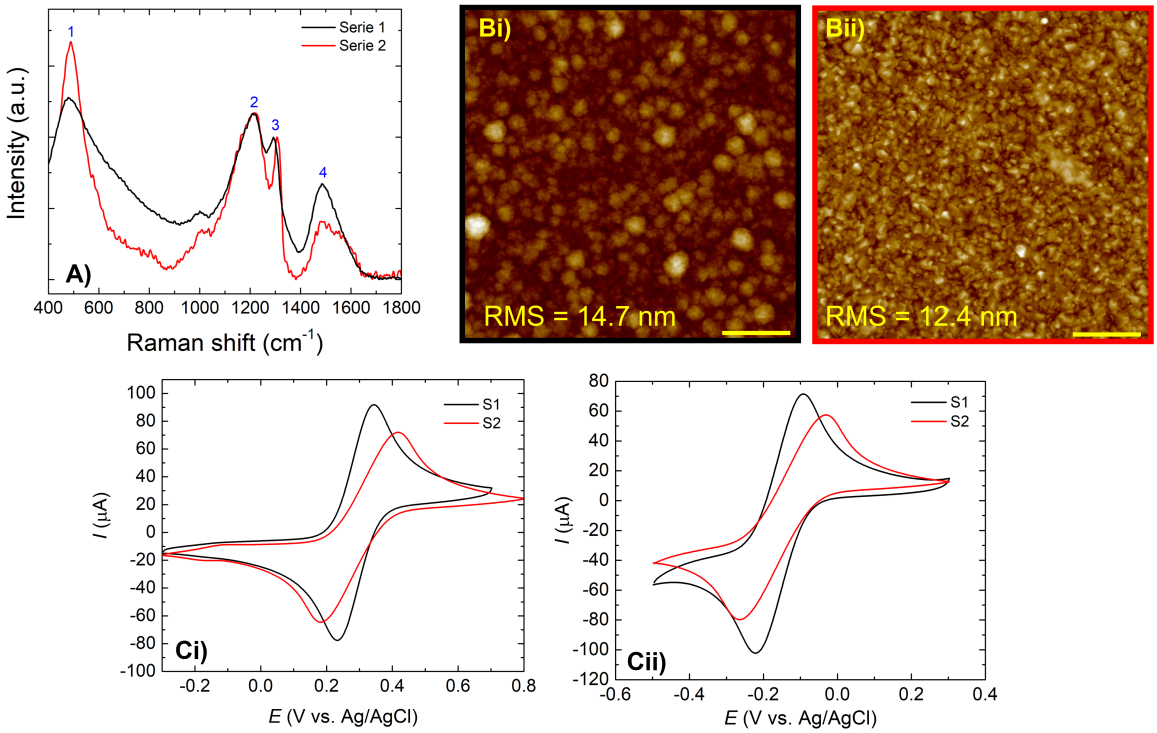


Figure 4.44: A) 488 nm Raman spectra showing standard B related features at *ca* 470 $cm^{-1}$ (1) and 1217 $cm^{-1}$ (2), red shifted diamond Raman line at 1299 $cm^{-1}$ (S1), 1305 $cm^{-1}$ (S2) (3) and contribution from non-diamond carbon phase with a band at ca. 1490 $cm^{-1}$ (4), Bi) showing AFM picture of deposited BDD layer (with thickness of 272 nm) with a cauliflower structure (S1), Bii) AFM picture of BDD layer with crystalline structure (S2), yellow bar indicates 1 µm, Ci) Cyclic voltammograms of 1 mmol·$L^{-1}$ $[Fe(CN)_6]^{3-/4-}$ redox marker in 1 mol·$L^{-1}$ KCl electrolyte, Cii) cyclic voltammograms with 1 mmol·$L^{-1}$ $[Ru(NH_3)_6]^{3+/2+}$ redox marker in 1 mol·$L^{-1}$ KCl electrolyte.

Table 4.9: $\Delta E_p$ obtained from CV experiments with redox markers (all 1 mmol·$L^{-1}$ in 1 mol·$L^{-1}$ KCl) for low temperature BDD electrodes

| **Electrode number** | $\Delta E_p$ **- $[Ru(NH_3)_6]^{3+/2+}$ (mV)** | $\Delta E_p$ **- $[Fe(CN)_6]^{3-/4-}$ (mV)** |
|---|---|---|
| **Serie 1** | | |
| 1 | 131 | 113 |
| 2 | 120 | 192 |
| 3 | 126 | 234 |
| 4 | 128 | 158 |
| **Serie 2** | | |
| 1 | 264 | 262 |
| 2 | 195 | 190 |
| 3 | 255 | 251 |
| 4 | 240 | 238 |
| 5 | 200 | 200 |

All studied electrodes provided well-defined pairs of redox peaks for both markers. However, extracted $\Delta E_p$ values, being averagely 2 - 4 times larger than 'ideal' value of 59 mV, signalizes hindered heterogeneous electron transfer kinetics. Even though [B]

values estimated from Raman spectra implies heavily doped, and thus presumably highly conductive BDD films, this does not reflect in observed electrochemical behavior.

Using higher deposition temperature for Serie 2 changed the diamond layer morphology, bud did not help to obtain better E/C behavior of BDD electrodes. This E/C characterization showed inhibited electron transfer kinetics, hampered conductivity, and thus insufficient quality of BDD electrodes, so we did not continue with functionalization protocol on them.

### High temperature BDD electrodes

The samples were cleaned and seeded in the same way as samples used for low temperature BDD growth. 344 nm thin BDD layers with boron to carbon ratio (B/C) 4000 ppm were deposited using an ASTeX 5010 (Seki Technotron, Japan) deposition system, deposition conditions are listed in table 4.10. Raman spectra confirmed incorporation of boron atoms in the diamond lattice (picture 4.45a)) and a small contribution from non-diamond carbon phase. AFM measurement showed crystalline structure of BDD layers (picture 4.45b)) with roughness RMS = 23.5 nm. Boron concentration obtained from Raman spectra was $\sim 2.4{\cdot}10^{21}$ atoms $\cdot$ cm$^{-3}$. Electrochemical behavior was investigated in the same way as for low temperature BDD electrodes, $\Delta E_p$ values are listed in the table 4.11. $\Delta E_p$ values for both redox markers were very close to the ideal value of 59 mV for all measured electrodes, which indicates good electrochemical properties of BDD electrodes (fast electron transfer kinetics). Recorded EIS spectra were fitted using Randles equivalent circuit and obtained values of double layer capacitance $C_{dl}$, that is typically $<$ 10 µF·cm$^{-2}$ for high-quality BDD electrode [173] , and charge transfer resistance $R_{CT}$ are tabulated in the table 4.12.

Table 4.10: BDD layers deposition conditions at high temperature

| | |
|---|---|
| **Process gas flow (sccm)** | 2.5 $CH_4$, 492 $H_2$,5 $B_2H_6$ |
| **MW power (kW)** | 1.15 |
| **Process pressure (mBar)** | 50 |
| **Substrate temperature (°C)** | 1000 |

All of the measurements of high temperature BDD electrodes showed great electrochemical behavior, therefore they were used in further experiments of diamond functionalization. In order to attach bacteriophage's tail fibers to the diamond surface, two different approaches were studied: 1/ electrodeposition of Ni nanoparticles (NiNPs) directly fol-

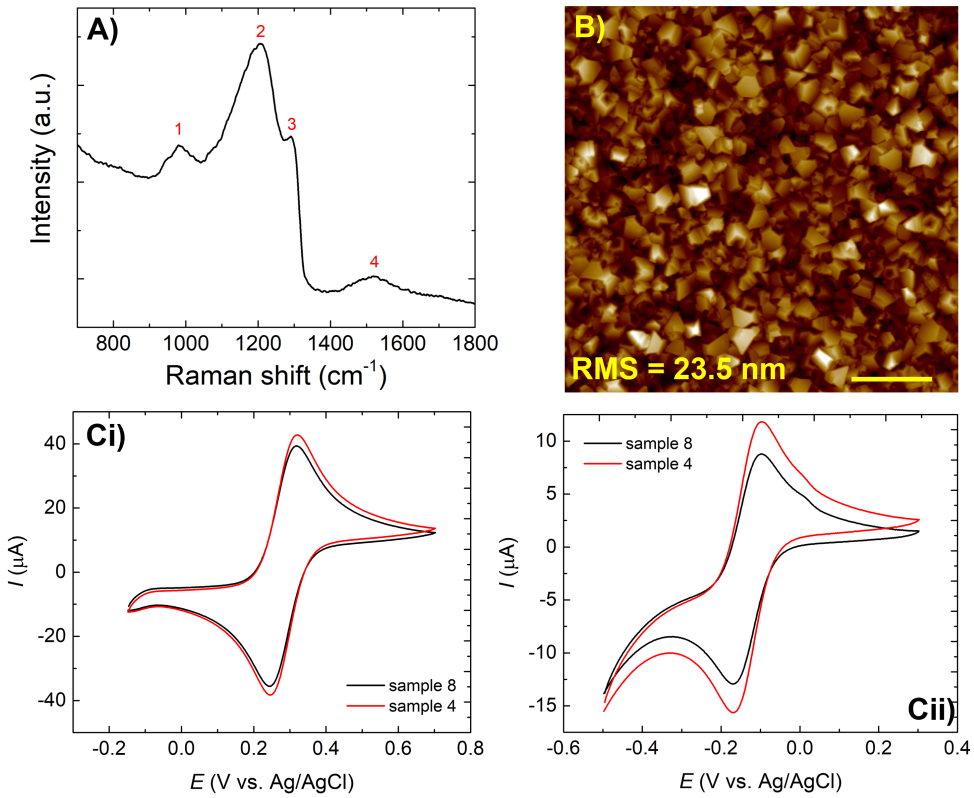


Figure 4.45: A) 488 nm Raman spectra showing standard B related features 1210 $cm^{-1}$ (2), red shifted diamond Raman line at 1292 $cm^{-1}$ (3) and a small contribution from non-diamond carbon phase with a band at ca. 1520 $cm^{-1}$ (4), and B) showing AFM picture of deposited BDD layer (with thickness of 344 nm) with a crystalline structure, yellow bar indicates 1 µm, Ci) Cyclic voltammograms of 1 mmol·$L^{-1}$ $[Fe(CN)_6]^{3-/4-}$ redox marker in 1 mol·$L^{-1}$ KCl electrolyte, Cii) cyclic voltammograms with 1 mmol·$L^{-1}$ $[Ru(NH_3)_6]^{3+/2+}$ redox marker in 1 mol·$L^{-1}$ KCl electrolyte.

Table 4.11: $\Delta E_p$ obtained from CV experiments with redox markers (all 1 mmol·$L^{-1}$ in 1 mol·$L^{-1}$ KCl) for high temperature BDD electrodes

| **Electrode number** | $\Delta E_p$ **- $[Ru(NH_3)_6]^{3+/2+}$ (mV)** | $\Delta E_p$ **- $[Fe(CN)_6]^{3-/4-}$ (mV)** |
|---|---|---|
| 1 | 72 | 76 |
| 2 | 72 | 72 |
| 3 | 70 | 74 |
| 4 | 72 | 74 |
| 5 | 68 | 76 |
| 6 | 72 | 74 |
| 7 | 74 | 74 |
| 8 | 70 | 74 |

lowed by attachment of N-terminally (His)6-tagged tail fibers and 2/ electrografting of nitriloacetic acid (NTA) followed by entrapment of nickel ions and N-terminally (His)6-tagged tail fibers attachment. Electrodes with numbers 1, 5 and 8 were used for electrodeposition of NiNPs and electrodes with numbers 2, 3, 4 and 6 were used for the second

Table 4.12: $C_{dl}$ and $R_{CT}$ obtained from EIS experiments with redox marker (1 mmol·L$^{-1}$ $[Fe(CN)_6]^{3-/4-}$ in 1 mol·L$^{-1}$ KCl) for high temperature BDD electrodes

| **Electrode number** | $C_{dl}$ (µF · cm$^{-2}$) | $R_{CT}$ Ω · cm$^2$ |
|---|---|---|
| 1 | 1.2 | 157 |
| 2 | 1.35 | 119 |
| 3 | 1.2 | 108 |
| 4 | 1.2 | 171 |
| 5 | 1.2 | 110 |
| 6 | 1.3 | 135 |
| 7 | 1.2 | 134 |
| 8 | 1.2 | 159 |

approach involving NTA.

### 4.7.2 Electrodeposition of nickel nanoparticles

Preparation of BDD electrodes decorated with NiNPs and further (His)6-tagged protein attachment was carried out in following steps:

1. A 5mM $NiSO_4$ solution in 10mM PBS buffer (pH 6.5) was purged with nitrogen for 10 minutes to eliminate the oxygen prior the electrodeposition.

2. Cyclic voltammogram was measured in the potential range from +0.2 V to -1.5 V to find the potential of the reduction peak $E_{pc}$. The reduction of nickel ions to metallic Ni occurred at this potential. Values of $E_{pc}$ for different samples are listed in the table 4.13.

Table 4.13: $E_{pc}$ used for NiNPs electrodeposition

| **Electrode number** | 1 | 5 | 8 |
|---|---|---|---|
| $E_{pc}$ (V) | -1.4 | -1.5 | -1.5 |

3. Electrodeposition of NiNPs was carried out by reduction of a 5mM $NiSO_4$ solution in 10mM PBS buffer (pH 6.5) by pulse at $E_{pc}$ for 200 s, at 0 V for 1 minute followed by another pulse at $E_{pc}$ for 200 s. This cycle was repeated 10 times (sample 1) and 5 times (samples 5 and 8) [174].

4. Formation of an nickel oxide on NiNPs' surface is important for further (His)6-tagged protein (HTP) attachment. Oxidation of NiNPs was achieved in 10mM PBS

buffer (pH 7.4) by scanning the potential between 0 and +0.9 V at a scan rate 50 mV $\cdot$ s$^{-1}$ (50 cycles) [175].

5. Incubation with the N-terminally his-tagged gp17 protein. Proteins stored at -80 °C were slowly thawed and centrifuged at 15000 g at 4 °C for 10 minutes to remove degraded protein. Concentration was checked using Nanodrop spectrophotometer and adjusted to final concentration c = 200 µg/ml in 10mM Tris-HCl buffer, pH 8.5. Volumes and times of incubation for different samples are listed in the table 4.14.

Table 4.14: $V$ of gp17 protein solution and $t$ used for incubation on NiNPs/BDD electrodes

| **Electrode number** | 1 | 5 | 8 |
|---|---|---|---|
| $V$ (µl) | 130 | 150 | 150 |
| $t$ (h) | 2 | 1.5 | 1.5 |

6. Incubation with bacteria *E. coli* was done on samples 5 ($t$ = 1.5 h) and 8 ($t$ = 2 h) by adding 150 µl of bacteria on NiNPs/BDD electrode and then thoroughly washed by PBS buffer. The bacterial culture of *E. coli* strain BL21(DE3-) was grown overnight in LB media at 37 °C shaking, cells were harvested by centrifugation (6000 g, 5 °C, 10 min), resuspended and diluted in PBS buffer to achieve $OD_{600}$ = 1.

### Characterization

To confirm the changes on the BDD electrodes' surface, E/C characterization by CV and EIS was performed after steps 4, 5 and 6. CVs were recorded in solution of 1 mmol $\cdot$ L $[Fe(CN)_6]^{3-/4-}$ in 10 mmol$\cdot$L$^{-1}$ PBS (pH 7.4) and 1 mmol$\cdot$L$^{-1}$ $[Fe(CN)_6]^{3-/4-}$ in 1 mol$\cdot$L$^{-1}$ KCl with a scan rate $v$ = 100 mV$\cdot$s$^{-1}$. The presence of NiNPs was also probed by scanning electron microscopy.

CV measurement in 1 mmol $\cdot$ L$^{-1}$ $[Fe(CN)_6]^{3-/4-}$ in 10 mmol $\cdot$ L$^{-1}$ PBS (pH 7.4) of sample 1 reveals the reversible redox couple at cca 180 mV/300 mV corresponding to the surface confined Ni(II)/oxyhydroxide species (see graph 4.46). The anodic peak at 300 mV corresponds to the oxidation of $Ni(OH)_2$ to NiO(OH) and cathodic peak at 180 mV reduction of NiO(OH) back to $Ni(OH)_2$ [175]. These peaks disappeared after (His)6-tagged gp17 protein binding, which confirmed that Ni(II)/oxyhydroxide species are involved in the protein's attachment. The characteristic reversible redox peaks of the $[Fe(CN)_6]^{3-/4-}$ decreased after incubation with gp17 protein, that indicates a partial

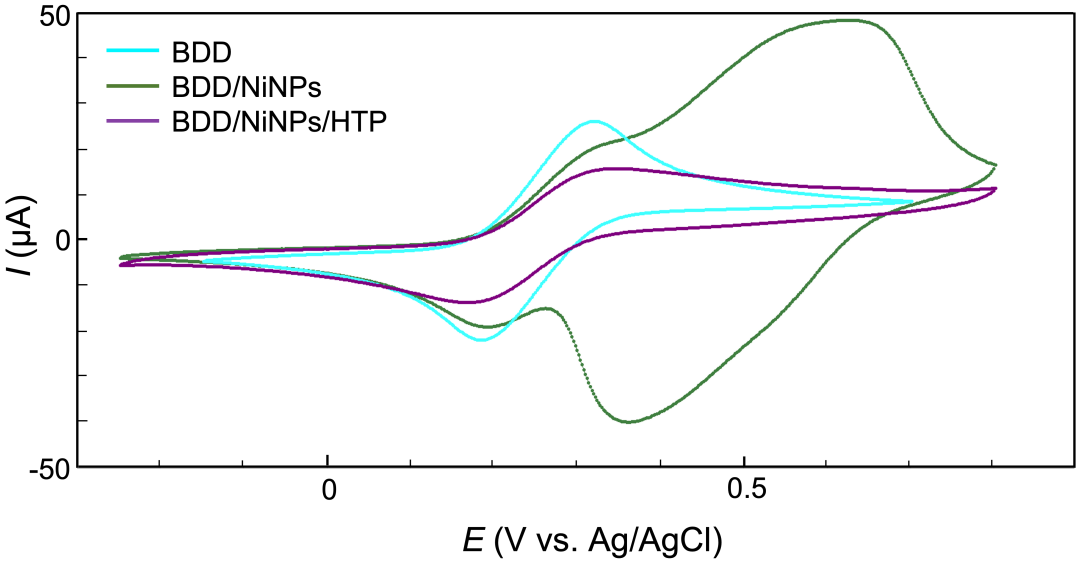


Figure 4.46: Cyclic voltammograms of 1 mmol · $L^{-1}$ $[Fe(CN)_6]^{3-/4-}$ in 10 mmol · $L^{-1}$ PBS (pH 7.4) recorded on bare BDD electrode, BDD/NiNPs and BDD/NiNPs/HTP modified electrodes

inactivation of the electrode surface resulting from protein binding. CV measurement in 1 mmol · $L^{-1}$ $[Fe(CN)_6]^{3-/4-}$ in 1 mol · $L^{-1}$ KCl revealed increase of the redox peaks indicating electrocatalytic effect of NiNPs. SEM measurement revealed uniform deposition of spherical NiNPs with an approximate diameter of 200 nm covering the entire working electrode surface, see picture 4.47.

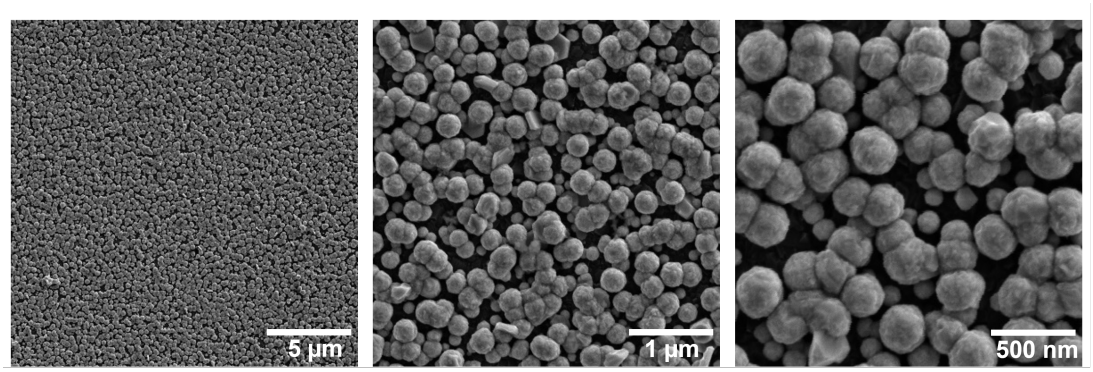


Figure 4.47: Low and high magnification scanning electron micrographs of NiNPs deposited on BDD electrode

As the electrodeposition of the NiNPs and immobilization of (His)6-tagged gp17 protein was confirmed, whole protocol was repeated on the samples 5 and 8 including bacteria attachment step. CV performed in both electrolytes showed the same behavior as for sample 1 (see graph 4.48a)), and $\Delta E_p$ was increasing after each step, which indicates changes on the electrode's surface causing inhibition of the electron transfer due to NiNPs, protein and bacteria attachment. $\Delta E_p$ values are tabulated in the table 4.15. Protein and

bacteria binding was further confirmed by EIS measured in the presence of redox probe $[Fe(CN_6)]^{3-/4-}$ in KCl. The measurement demonstrated increase in the electron transfer resistance on the protein and bacteria modified BDD/NiNPs electrodes in the comparison with unmodified BDD/NiNPs electrode, see graph 4.48b). This indicated deposition of the protein/bacteria insulating layer on the working electrode surface, that resulted in blocking of electrochemical active sites and thus decreasing electron transfer rate.

Table 4.15: $\Delta E_p$ obtained from CV experiments in 1 mmol $\cdot$ L$^{-1}$ $[Fe(CN)_6]^{3-/4-}$ in 10 mmol $\cdot$ L$^{-1}$ PBS (pH 7.4) and 1 mmol $\cdot$ L$^{-1}$ $[Fe(CN)_6]^{3-/4-}$ in 1 mol $\cdot$ L$^{-1}$ KCl recorded on bare BDD electrode, BDD/NiNPs, BDD/NiNPs/HTP and BDD/NiNPs/HTP/*E.coli*

| **Electrode** | **BDD** | **BDD/NiNPs** | **BDD/NiNPs/HTP** | **BDD/NiNPs/HTP/*E.coli*** |
|---|---|---|---|---|
| $\Delta E_p$ (mV) in 1 mmol $\cdot$ L$^{-1}$ $[Fe(CN)_6]^{3-/4-}$ in 10 mmol $\cdot$ L$^{-1}$ PBS | | | | |
| Sample 5 | 170 | * | 286 | 324 |
| Sample 8 | 160 | 146 | 266 | 344 |
| $\Delta E_p$ (mV) in 1 mmol $\cdot$ L$^{-1}$ $[Fe(CN)_6]^{3-/4-}$ in 1 mol $\cdot$ L$^{-1}$ KCl | | | | |
| Sample 5 | 74 | 94 | 182 | 210 |
| Sample 8 | 74 | 78 | 92 | 94 |

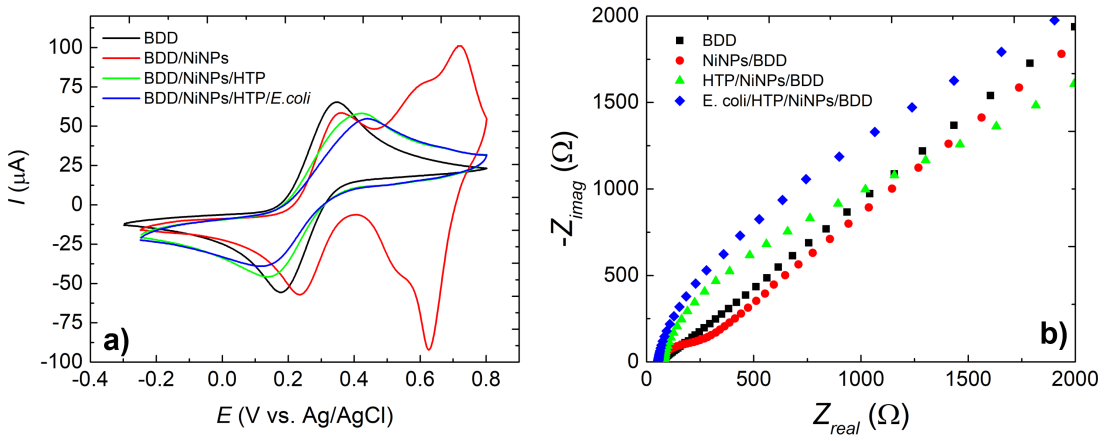


Figure 4.48: a) Cyclic voltammograms of 1 mmol $\cdot$ L$^{-1}$ $[Fe(CN)_6]^{3-/4-}$ in 10 mmol $\cdot$ L$^{-1}$ PBS (pH 7.4) and b) Nyquist plot of 1 mmol $\cdot$ L$^{-1}$ $[Fe(CN)_6]^{3-/4-}$ in 1 mol $\cdot$ L$^{-1}$ KCl recorded on bare BDD electrode, BDD/NiNPs, BDD/NiNPs/HTP and BDD/NiNPs/HTP/E.coli, HTP - his-tagged gp17 protein

### 4.7.3 Protein attachment via covalent grafting of NTA acid

Functionalization of BDD electrodes by NTA acid was carried out according to procedure described in [176]. Functionalization was done in two steps (electrochemical activation

of the surface and attachment of NTA acid) followed by (His)6-tagged gp17 protein and *E.coli* bacteria attachment, the individual steps are described below.

1. Electrochemical grafting of 5 mmol·$L^{-1}$ aminobenzoic acid $H_2NPhCOOH$ (AB acid) was achieved by cyclic voltammetry in 0.5 mol·$L^{-1}$ $NaClO_4$ aqueous solution.

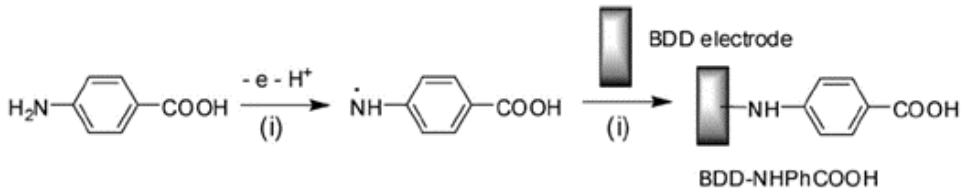


Figure 4.49: Electrochemical grafting of $H_2NPhCOOH$ on BDD electrode, reproduced from [176]

2. Prior to the NTA acid attachment, the carboxylic groups on BDD-COOH electrode were activated by EDC/NHS protocol, that is used for amide bonding formation. BDD-$H_2NPhCOOH$ surface was activated in 5 mmol·$L^{-1}$ EDC and 10 mmol·$L^{-1}$ NHS-sulfo in PBS buffer (pH 7.4) for 2 hours. Subsequently, the activated BDD-COOH electrodes were incubated in PBS buffer (pH 7.4) containing 5 mmol·$L^{-1}$ aminobutyl-nitrilotriacetic acid (AB-NTA) for 3 hours.

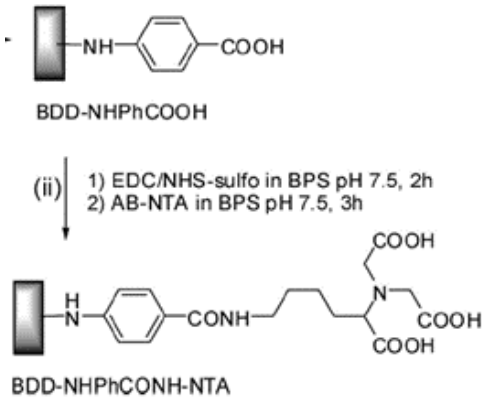


Figure 4.50: Immobilization of NTA acid onto COOH-terminated BDD electrode's surface using EDC/NHS protocol, reproduced from [176]

3. Prior to the nickel ions attachment, the samples were incubated with 0.1 mol·$L^{-1}$ KOH for 5-10 min to achieve deprotonation of the -COOH groups. Ni ions attachment to NTA acid was carried out at 5 mmol ·$L^{-1}$ $NiSO_4$ in PBS buffer (pH 6.5) for 2 hours.

4. Incubation with the N-terminally his-tagged gp17 protein was carried out according to the same protocol as described in the chapter 4.7.2 Electrodeposition of nickel

nanoparticles, paragraph 5. To exclude the non-specific interactions, sample 4 was incubated with the fetal calf serum (FCS) for 2 hours.

5. Incubation with the bacteria *E. coli* was carried out according to the same protocol as described in the chapter 4.7.2 Electrodeposition of nickel nanoparticles, paragraph 6.

### Characterization

Changes on the BDD electrodes' surfaces were confirmed by measuring CV and EIS with $[Fe(CN)_6]^{3-/4-}$ redox probe in two different electrolytes (0.5M HCl pH 0.3 and 10mM PBS pH 7.4) after steps 1, 2, 4 and 5, the $\Delta E_p$ values are listed in the table 4.16.

Table 4.16: $\Delta E_p$ obtained from CV experiments with $[Fe(CN)_6]^{3-/4-}$ redox marker after different modification steps

| **El. number** | **bare** | **AB-modified** | **AB-NTA modified** | **His-AB-NTA mod.** |
|---|---|---|---|---|
| **$\Delta E_p$ - $[Fe(CN)_6]^{3-/4-}$ in HCl (mV)** | | | | |
| 2 | 72 | 136 | 158 | -* |
| 3 | 74 | 104 | 116 | - |
| 4 | 72 | 130 | 98 | - |
| 6 | 76 | 80 | 80 | - |
| **$\Delta E_p$ - $[Fe(CN)_6]^{3-/4-}$ in PBS pH 7.4 (mV)** | | | | |
| 2 | 158 | >500 | no peaks | |
| 3 | 154 | >500 | no peaks | peaks |
| 4 | 152 | >500 | no peaks | - |
| 6 | 156 | >500 | >400 | 268 |

* measurement in HCl was not carried out after modification with protein to avoid hydrolyzation of protein in strongly acidic environment

As carboxylic groups are protonated in acidic environment, there should be barely no interaction between redox marker and surface electrode in HCl after all modification steps. This is confirmed by CV measurements (see table 4.16 and figure 4.51a)), when there is small increase in $\Delta E_p$ values after AB acid and NTA acid attachment steps. In neutral environment (PBS pH 7.4) carboxylic groups are dissociated (negatively charged -$COO^-$ groups) which results in electrostatic repulsion of modified electrode's surface and $[Fe(CN)_6]^{3-/4-}$ anions. This can be observed as a significant increase in $\Delta E_p$ values, which was also confirmed, see table 4.16 and figure 4.51b).

The electrochemical measurements confirmed the attachment of NTA acid to the BDD electrode's surface, so we proceed to the $Ni^{2+}$ incubation followed by 6-his-tagged gp17

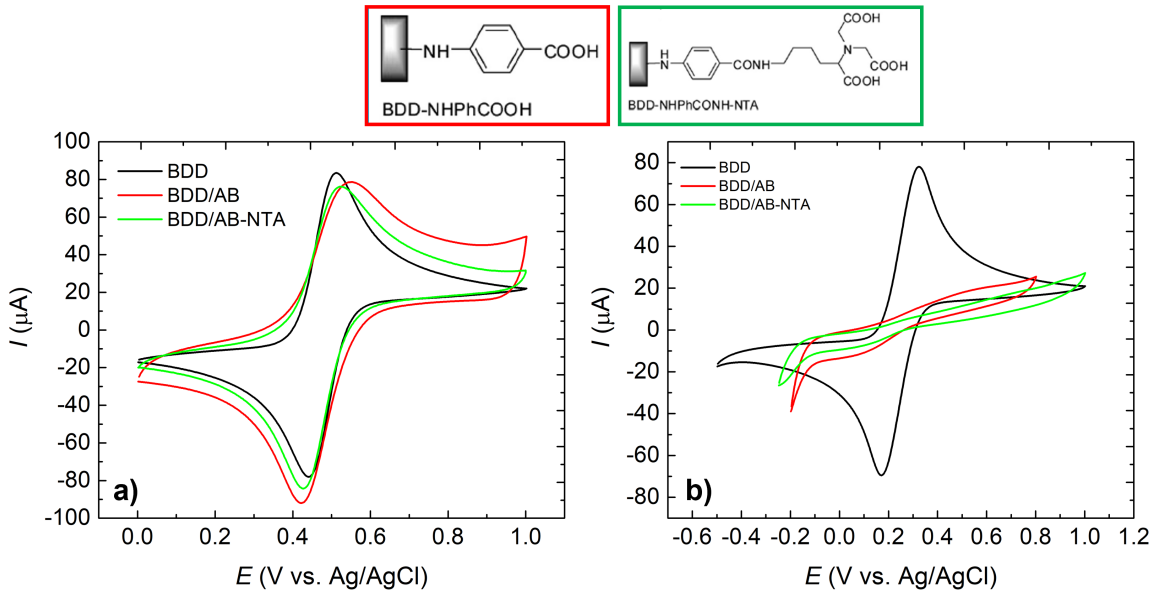


Figure 4.51: Cyclic voltammograms of a) 1 mmol · $L^{-1}$ $[Fe(CN)_6]^{3-/4-}$ in 0.5 mol · $L^{-1}$ HCl (pH 0.3) and b) 1 mmol · $L^{-1}$ $[Fe(CN)_6]^{3-/4-}$ in 10 mmol · $L^{-1}$ PBS (pH 7.4) recorded on bare BDD electrode, BDD/AB-acid, BDD/AB-NTA acid

protein attachment. To exclude non-specific interactions, we incubated sample 4 with FSB protein without his-tag and sample 3 with his-tagged gp17. Figure 4.52a) clearly shows that there is no significant change in $\Delta E_p$ after incubation with FBS protein, which indicates that there is not a non-specific interaction as the FBS protein did not attach to the BDD surface. After incubation with his-tagged gp17 protein, we can observe appearance of the peaks, which could indicate attachment of the his-tagged protein via $Ni^{2+}$ ions to the NTA acid on the BDD surface, see graph 4.52b). The last step was the incubation of the sample with his-tagged gp17 protein with the bacteria cells. We could observe appearance of the peaks in the CV spectra after *E. coli* attachment, which indicates that the attachment was not successful, see graph 4.53a).

To confirm the results of CV measurement, sample 6 was kept in 10% formaldehyde in DI water overnight at 4 °C to fix the bacteria and AFM was measured. As a control, *E.coli* culture was dropped also on the bare glass substrate and fixed in the same way as on BDD electrode. The bacteria were not find on the surface of modified BDD electrode (sample 6), but were clearly visible on the glass substrate, see picture 4.54. To exclude non-specific interaction of the bacteria, we also incubated bare BDD electrode with the bacteria culture. CV measurement indicated, that there is no attachment of bacteria cells to the non-modified BDD electrode, see graph 4.53b).

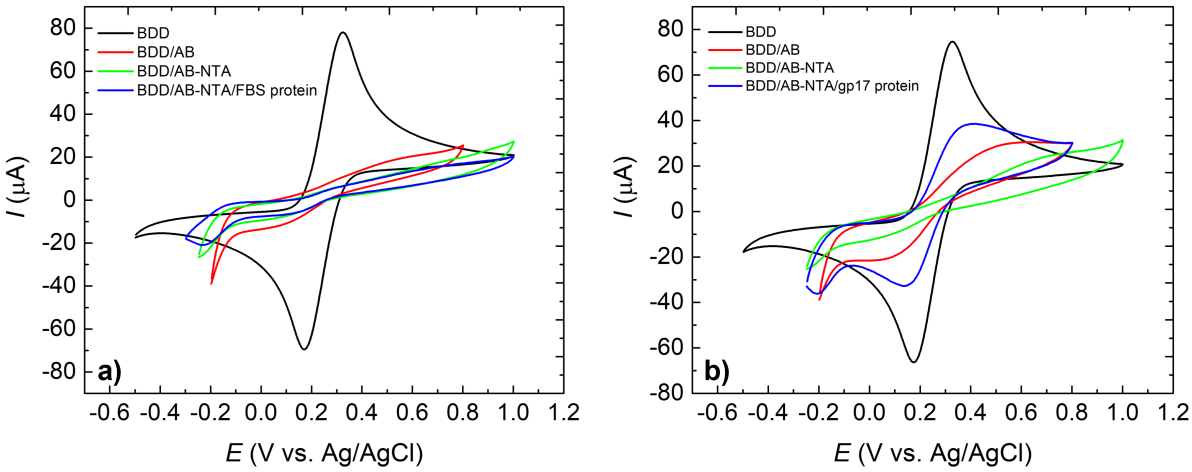


Figure 4.52: Cyclic voltammograms of 1 mmol · $L^{-1}$ $[Fe(CN)_6]^{3-/4-}$ in 10 mmol · $L^{-1}$ PBS (pH 7.4) recorded on bare BDD electrode, BDD/AB-acid, BDD/AB-NTA acid and A) BDD/AB-NTA/FSB protein or B) BDD/AB-NTA/gp17 protein

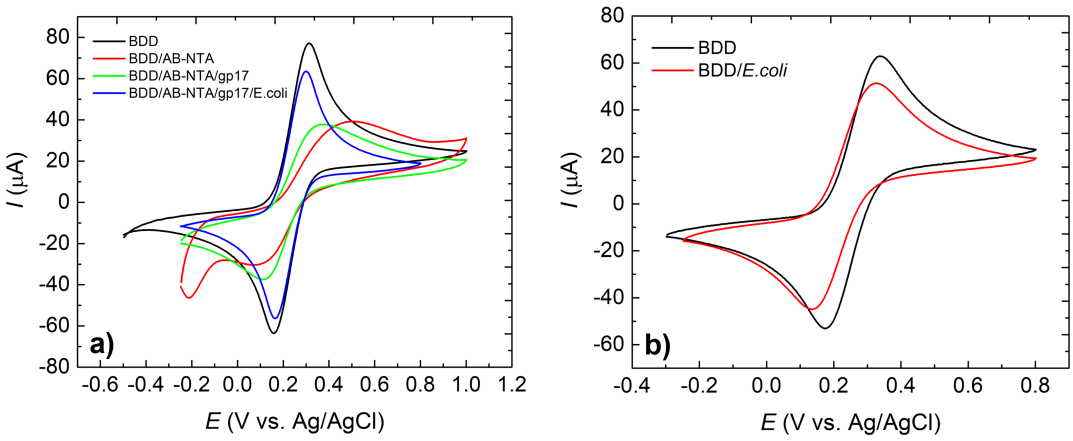


Figure 4.53: Cyclic voltammograms of 1 mmol · $L^{-1}$ $[Fe(CN)_6]^{3-/4-}$ in 10 mmol · $L^{-1}$ PBS (pH 7.4) recorded a) on bare BDD electrode, BDD/AB-NTA acid, BDD/AB-NTA/his-tagged gp17 protein and BDD/AB-NTA/gp17/*E.coli* and b) on bare BDD electrode and BDD/*E.coli* electrode

### 4.7.4 Conclusions

Within this chapter I focused on the electrochemical characterization of BDD electrodes in order to attach his-tagged gp17 protein to the electrode's surface as a bioreceptor for the bacteria detection. At first, we investigated electrochemical properties of BDD electrodes deposited at low temperature, but they showed insufficient E/C quality (slow electron transfer kinetics). High temperature BDD electrodes showed excellent E/C quality, so they were used for functionalization protocols. We investigated two different approaches -

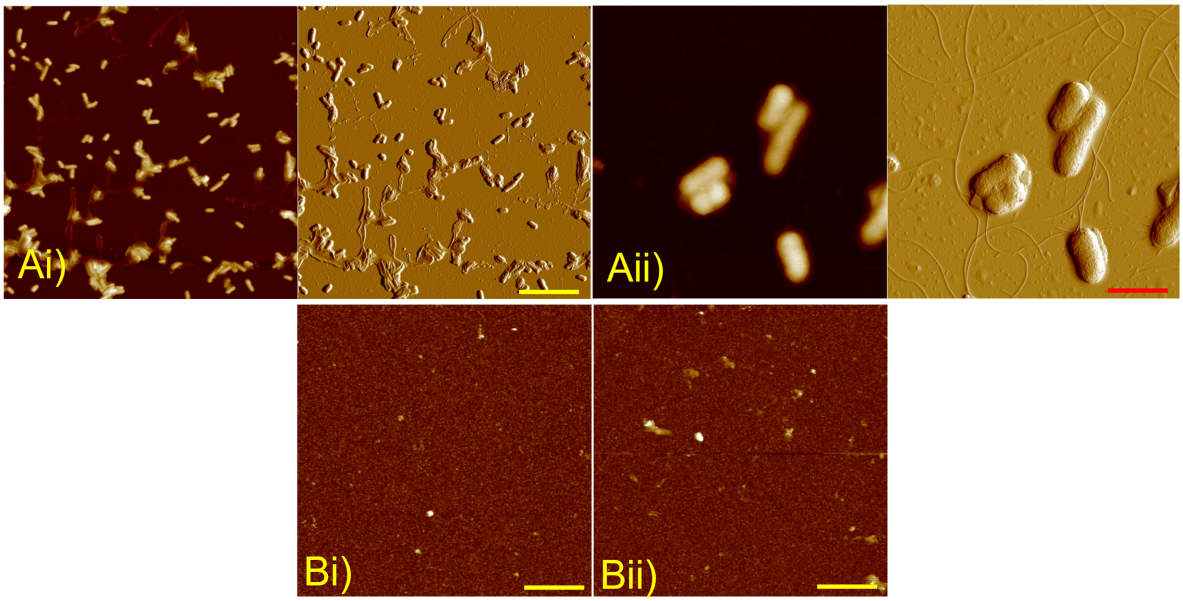


Figure 4.54: AFM micrographs of *E.coli* cells on the A) glass substrate and B) functionalized BDD electrode, yellow bar indicates 8 µm and red bar 1 µm

electrodeposition of Ni nanoparticles and attachment of NTA acid to the surface. The first mentioned approach is easier and quicker to prepare as the electrodeposition of NiNPs needs only one E/C step and can be directly followed by quick oxidation of NiNPs and incubation with the protein. We also confirmed that this protocol was working well and according to E/C measurement we successfully attached proteins as well as bacteria. The second approach involving covalent grafting of NTA acid to the BDD surface is more complicated as it needs more incubation steps before the surface is ready for the his-tagged protein attachment. Anyway the E/C measurement confirmed, that we were able to attach NTA acid as well as his-tagged protein to the BDD surface. But we were not able to confirm attachment of bacteria cells. It would be also beneficial to support the E/C measurements by another characterization technique, such as XPS, that was unfortunately not performed due to lack of time.

## 4.8 BDD-coated QCM sensors for biosensing

Piezoelectric Quartz Crystal Microbalance (QCM) sensors are cheap, mass-produced bulk acoustic sensors. Their mass sensing capabilities can be combined with electrochemical detection in so-called electrochemical quartz crystal microbalance (EQCM). Boron doped diamond (BDD) possesses excellent electrochemical properties. For these reasons the deposition of BDD layers on QCM sensors has been investigated.

### 4.8.1 BDD layers deposition

QCM crystals with working frequency at 10 MHz were purchased from two different companies (Krystaly, Hradec Králové a.s. and Novaetech Srl). They varied in the roughness of gold electrode – for QCM from Krystaly we measured roughness RMS = 274 nm, and for QCM from Novaetech RMS = 2.7 nm.

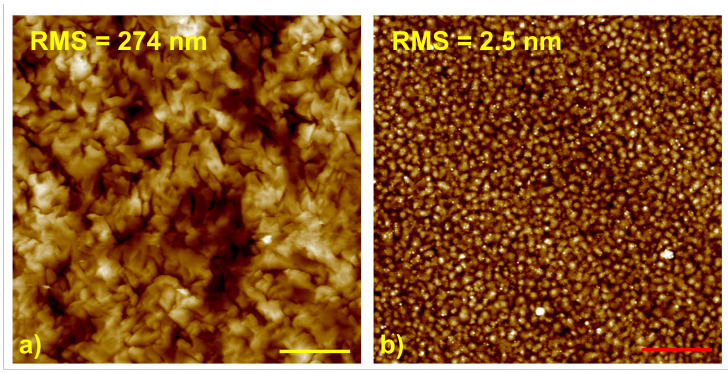


Figure 4.55: AFM micrographs of the gold electrode surface of QCM sensors with different roughness, a) QCM from Krystaly, Hradec Králové, b) QCM from Novaetech Srl., yellow bar indicates 10 µm, red bar is 1 µm

As the gold electrode is the most common in QCM technology and deposition of diamond on gold is not so straightforward, diamond seeding study on gold was carried out to obtain the best BDD layers.

#### Diamond seeding study on gold

At first, the seeding and diamond growth was tested on glass substrates (10x10 mm) with 10 nm titanium adhesion layer and 90 nm gold layer on top. All BDD layers were deposited using LA-MW-PECVD apparatus at low temperature, used conditions are listed in the table 4.17 with different diamond seeding procedure, see table 4.18. Nanodiamond particle

water based colloid NanoAmando®B from NanoCarbon Research Institute Ltd. was used for all depositions. Spin coating was carried out for 5 s at 1500 rpm followed by 35 s at 3800 rpm. Quality of deposited BDD layers was characterized by Renishaw InVia Raman microscope with a 488 nm excitation laser at a power of 25 mW at 20 °C. Morphology of BDD layers was investigated using Tescan FERA3 scanning electron microscope.

Table 4.17: Conditions for deposition of BDD layers on gold at LA-MW-PECVD apparatus

| **Process gas flow (sccm)** | | | | **Pressure (mBar)** | **Power (kW)** | **Substrate temp. (°C)** |
|---|---|---|---|---|---|---|
| $CH_4$ | $H_2$ | $B_2H_6$ | $CO_2$ | | | |
| 8 | 40 | 150 | 1.75 | 0.25 | 2x2.7 | ∼ 350 |

Table 4.18: Different seeding conditions used in seeding study on gold layers for BDD layers growth

| **Sample** | **Annealing** | **Seeding conditions** |
|---|---|---|
| 1 | 250°C in $N_2$, 1 h | colloidal ND susp. in DI., 30 min in US bath → dried without compressed air |
| 2 | 250°C in $N_2$, 1 h | colloidal ND susp. in DI, 30 min in US bath → rinsing in DI and dried with compressed air |
| 3 | 250°C in $N_2$, 1 h | colloidal susp. of nanodiam. in ethylenglycol, 30 min in US bath → dried with compr. air |
| 4 | 250°C in $N_2$, 1 h | PDDAC polymer (1/10 v/v in DI) 10 min in US bath, 1 g/l colloidal ND susp. in DI 10 min in US bath |
| 5 | 250°C in $N_2$, 1 h | PDDAC polymer (1/10 v/v in DI) 10 min in US bath, 1 g/l ND susp. in DI spin coating |
| 6 | 250°C in $N_2$,1 h | PDDAC as received 10 min in US bath, 1 g/l ND susp. in DI spin coating |
| 7 | 250°C in $N_2$, 1 h | 1 g/l ND susp. in DI, spin coating |

Figure 4.56A) shows, that closed BDD layer with cauliflower structure was obtained after seeding procedure on sample 1, 2, 3 and 7. Seeding using PDDAC polymer (samples 4, 5, 6) did not ensure the necessary density of diamond nucleation sites on the gold layer. Raman spectra (figure 4.56B)) confirmed presence of BDD layer on samples 1, 2, 3 and 7 as the diamond peak and boron related features can be clearly seen. On the other hand, spectra of samples 4, 5 and 6 lacks the diamond and boron related peaks confirming, that only few diamond grains are present on the samples.

Seeding procedures were repeated also on QCM sensors with rough gold electrode to confirm, which one will work best for this type of substrate. Seeding conditions are listed in the table 4.19. SEM micrographs of deposited BDD layers are shown in the picture 4.57. The best BDD layer was obtained on QCM-1 and QCM-2 and seeding procedure

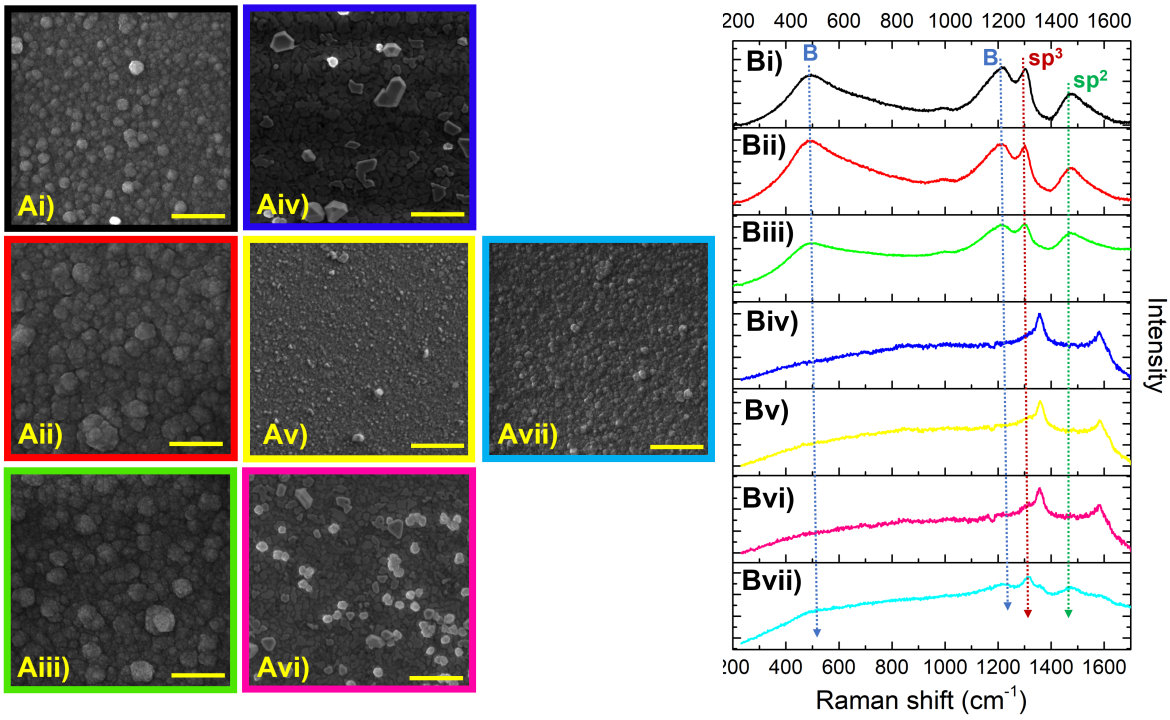


Figure 4.56: A) SEM micrographs and B) Raman spectra of the BDD layers deposited on the gold electrode surface, number of picture refers to the sample listed in the table 4.18, yellow bar refers to 1 µm

on QCM-2 was used for further work in this chapter. QCM sensors from Novaetech Srl. company with very smooth gold electrodes were not coated successfully as they suffered from delamination of the gold electrode during the BDD deposition regardless the used seeding conditions.

Table 4.19: Different seeding conditions used in seeding study on gold electrodes of QCMs for BDD layers growth

| Sample | Seeding conditions |
|---|---|
| QCM-1 | 1 g/l ND susp. in DI, 1 h in US bath, dried with compr. air |
| QCM-2 | 1 g/l ND susp. in DI, spin coating |
| QCM-3 | PDDAC polymer (1/10 v/v in DI) 10 min in US bath, 1 g/l colloidal ND susp.in DI 10 min in US bath |
| QCM-4 | PDDAC polymer (1/10 v/v in DI) 10 min in US bath, 1 g/l ND susp. in DI spin coating |

### 4.8.2 QCM's sensitivity and performance in liquid

The sensitivity and behavior of BDD coated QCMs in liquids with different density were investigated and compared with uncoated QCMs. All of the measurements were per-

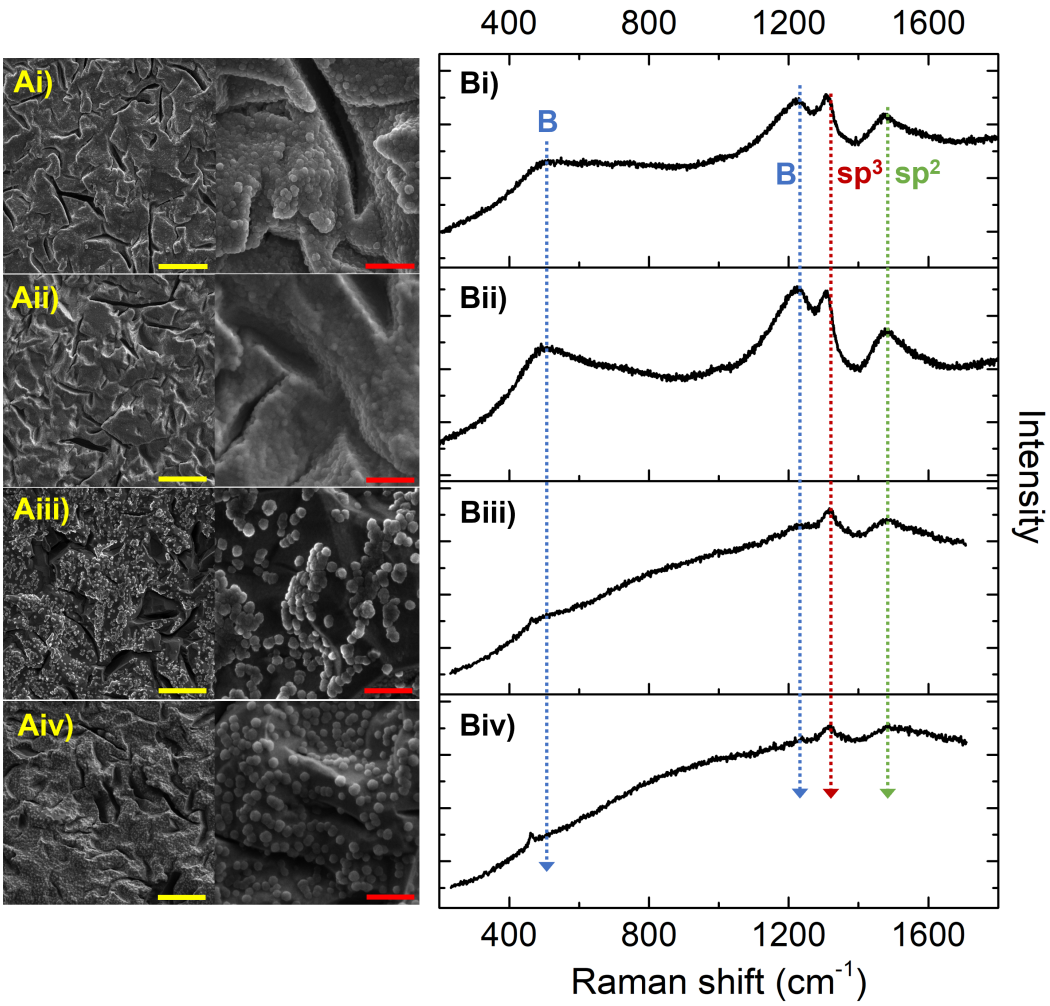


Figure 4.57: A) SEM micrographs and B) Raman spectra of the BDD layers deposited on the gold electrode of the QCMs sensors from Krystaly company, samples (i) QCM-1, (ii) QCM-2, (iii) QCM-3 and (iv) QCM-4, seeding conditions are listed in the table 4.19, yellow bar refers to 5 µm, red bar is 1 µm

formed using OpenQCM $Q^{-1}$ module and its open source software. To compare the BDD layer influence on the QCMs properties, sensors with two different BDD layer thicknesses (130 and 320 nm) were used. BDD layers were prepared using the same seeding conditions as for the QCM-2 listed above in the table 4.19. Boron concentration of used layers was estimated to be around $4{\cdot}10^{21}$ cm$^{-3}$ for 320 nm layer and $2{\cdot}10^{21}$ cm$^{-3}$ for 130 nm thin layer.

To investigate QCMs performance in liquid, solutions with 3 different sucrose weight percent 7.5 %, 15 % and 30 % were prepared. Peristaltic pump was used to insert liquid in the measurement chamber, pump was stopped and the frequency variation was measured at the equilibrium in a static liquid conditions, measurement setup can be seen in the

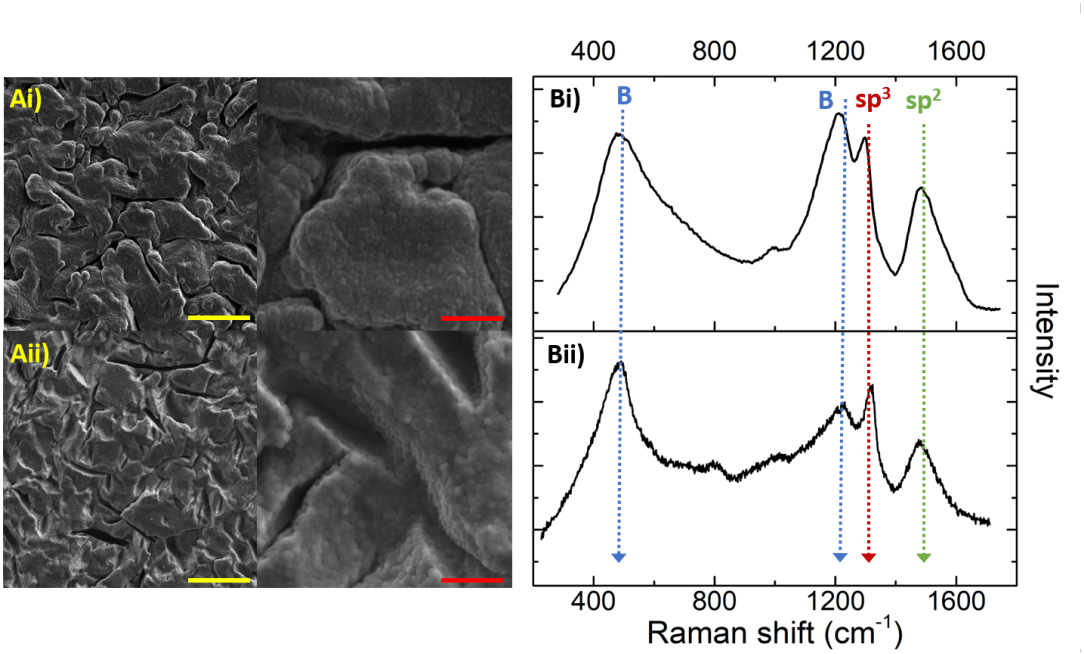


Figure 4.58: A) SEM micrographs and B) Raman spectra of the BDD layers, (i) 320 nm and (ii) 130 nm thin BDD layer, yellow bar refers to 5 µm, red bar is 1 µm

figure 4.59. Between insertion of solution with another sucrose concentration, chamber was washed with pure DI water in order to wash away sucrose molecules from previous solution. This simple experiment showed, that QCMs sensors behavior in liquid with different viscosity and density is not affected by adding the BDD coating, as the frequency shift was linearly proportional to the sucrose weight concentration and comparable for all BDD-coated QCMs and uncoated QCM sensor, see graph 4.60a).

Figure 4.59: Measurement setup: OpenQCM $Q^{-1}$ module with mounted QCM sensor connected to peristaltic pump

The sensor's sensitivity was investigated using gold nanoparticles (AuNPs) solutions.

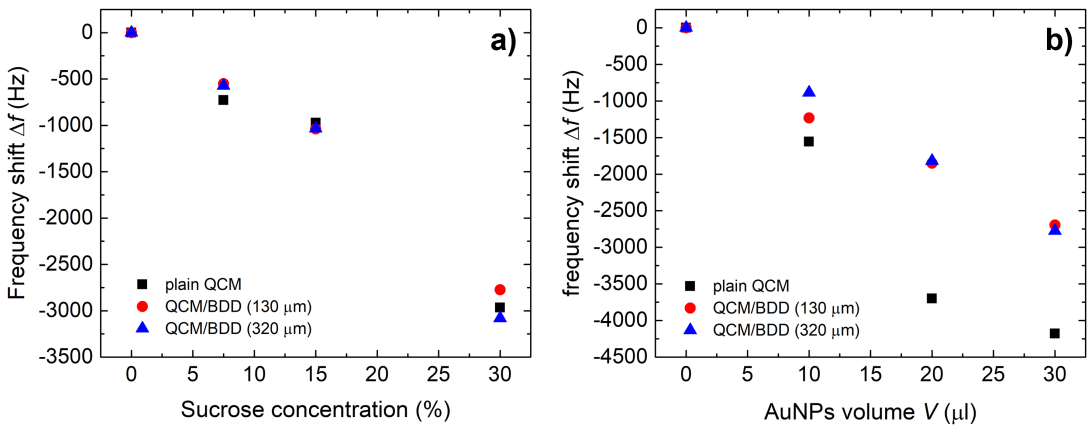


Figure 4.60: Frequency shift of plain and BDD-coated QCM sensor in a) solutions with different sucrose concentrations and b) different volume of AuNPs solutions

3 consecutive measurements were done by dropping 10 µl of AuNPs solution on the QCM sensor surface, letting the liquid dry and the frequency variation was then measured. Plain QCM sensor showed higher relative frequency shift (-0.04 % for 30 µl of AuNPs) in comparison to BDD-coated QCM sensors (-0.027 %) for both BDD layer thicknesses (130 and 320 nm), see graph 4.60b). This experiment showed decrease in sensitivity after adding BDD layer on QCM sensor, but the sensitivity is not affected by thickness of the added BDD layer. This result needs to be further investigated.

### 4.8.3 Electrochemical behavior

Basic electrochemical characterization of BDD-coated QCM samples was performed by recording cyclic voltammetry (CV) of two redox probes, namely: $[Ru(NH_3)_6]^{3+/2+}$ (surface insensitive probe) and $[Fe(CN)_6]^{3-/4-}$ (surface sensitive probe). Two set of samples were characterized, 1) with 272 nm thick BDD layer with boron concentration of $4{\cdot}10^{21}$ cm$^{-3}$ and 2) with 170 nm thick BDD layer with boron concentration of 1.14 $\cdot 10^{21}$ cm$^{-3}$. Raman spectra and SEM micrographs are shown in the figure 4.61. Cyclic voltammograms were recorded with a scan rate of $v$ = 100 mV$\cdot$ s$^{-1}$ (5x) in the 1 mmol$\cdot$L$^{-1}$ $[Ru(NH_3)_6]^{3+/2+}$ in 1 mol$\cdot$L$^{-1}$ KCl and 1 mmol$\cdot$L$^{-1}$ $[Fe(CN)_6]^{3-/4-}$ in 1 mol$\cdot$L$^{-1}$ KCl solutions. The measured values of peak-to-peak separation are listed in the table 4.20. Near-reversible redox behavior manifesting fast electron transfer kinetics was observed, which also confirms a very good quality of the prepared BDD layers.

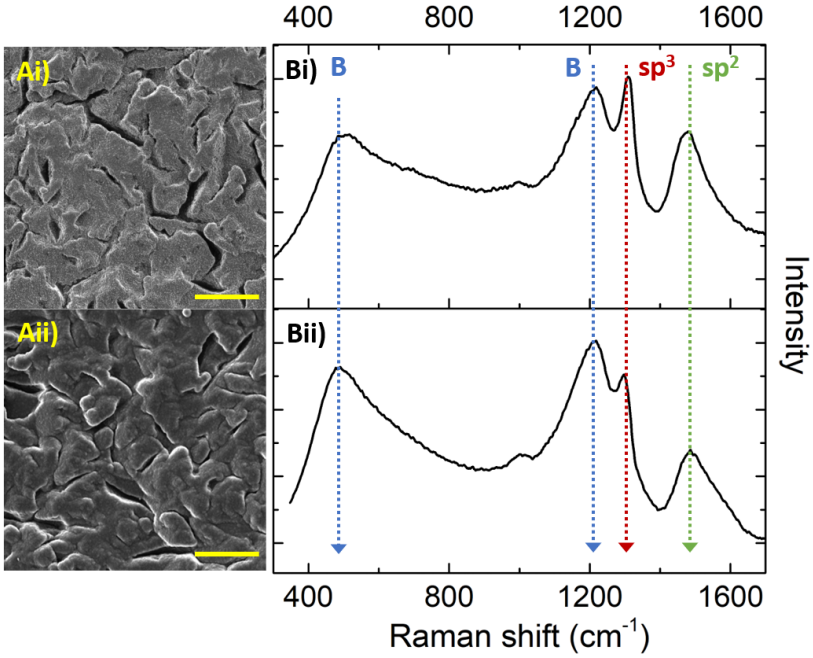


Figure 4.61: A) SEM micrographs and B) Raman spectra of the BDD layers, (i) 170 nm and (ii) 272 nm thin BDD layer, yellow bar refers to 5 µm

Table 4.20: $\Delta E_p$ obtained from CV experiments with redox markers (all 1 mmol·L$^{-1}$ in 1 mol·L$^{-1}$ KCl) for BDD-coated QCM sensors

| **Electrode number** | $\Delta E_p$ **- [Ru(NH$_3$)$_6$]$^{3+/2+}$ (mV)** | $\Delta E_p$ **- [Fe(CN)$_6$]$^{3-/4-}$ (mV)** |
|---|---|---|
| Series 1 | | |
| 1 | 77 | 84 |
| 2 | 73 | 79 |
| 3 | 74 | 83 |
| Series 2 | | |
| 1 | 74 | 74 |
| 2 | 76 | 78 |
| 3 | 78 | 82 |
| 4 | 82 | 88 |

### 4.8.4 Diamond surface functionalization

In order to attach his-tagged proteins to the BDD surface, we used the same two procedures as were described in the section 4.7: 1) electrodeposition of NiNPs and 2) electrografting of NTA acid. Figure 4.62 shows a home-made electrochemical sample holder to make electric contact from the top of the QCM sample.

Figure 4.62: Home-made electrochemical QCM holder to contact BDD layer on top of QCM sensor

### Protein attachment via electrodeposition of nickel nanoparticles

Electrodeposition of NiNPs was carried out using the same protocol as described in the chapter 4.7.2. The CV measurement in 1 mmol $\cdot L^{-1}$ $[Fe(CN)_6]^{3-/4-}$ in 10 mmol $\cdot$ $L^{-1}$ PBS (pH 7.4) electrolyte reveals the reversible redox couple corresponding to the surface confined Ni(II)/oxyhydroxide species, that confirms successful electrodeposition of NiNPs, see graph 4.63a). To test non-specific protein attachment to the functionalized BDD surface, the NiNPs modified-QCM sensor was incubated with FBS protein for 2 hours. We can observe increase of the peaks measured in the PBS electrolyte after the FBS incubation. As the FBS has very complex composition, such as proteins, carbohydrates, growth factors, cytokines, fats, vitamins, minerals, hormones, non-protein nitrogen, and inorganic compounds [177], any non-specific interaction could occur that provides better signal from ferro-/ferri-cyanid surface sensitive probe. For this reason, the CVs were also measured in the 1 M KCl that provides signal directly from deposited NiNPs, where we can observe significant reduction of the signal from NiNPs after incubation with his-tagged protein, which indicates attachment of the protein to the NiNPs, see graph 4.63b).

QCM sensors were also frequency characterized before and after deposition of NiNPs. As the functionalized QCM sensors are intended to be used in biosensing, they were also characterized in PBS buffer. Characterization was carried out using OpenQCM $Q^{-1}$ device. Fundamental frequency of QCMs was measured on air or by adding of 200 µl of

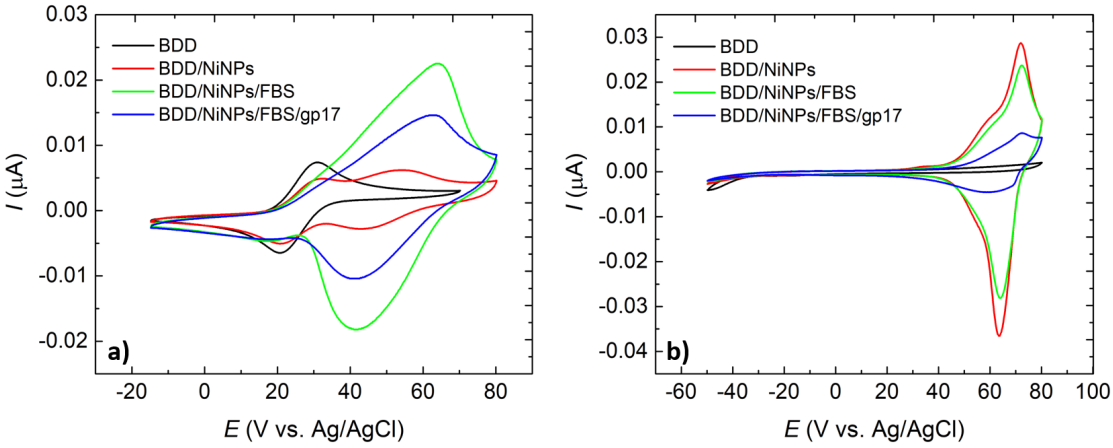


Figure 4.63: Cyclic voltammograms of a) 1 mmol · $L^{-1}$ $[Fe(CN)_6]^{3-/4-}$ in 10 mmol · $L^{-1}$ PBS (pH 7.4) and b) 1 M KCl recorded on bare BDD electrode, BDD/NiNPs and BDD/NiNPs/FBS and BDD/NiNPs/FBS/HTP

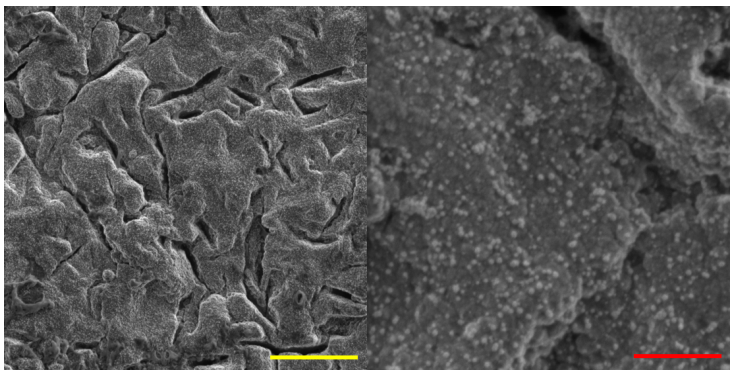

Figure 4.64: SEM micrographs of QCM/BDD surface after NiNPs deposition, yellow bar refers to 5 µm, red bar is 1 µm

PBS buffer on the surface using the open pippeting module of OpenQCM $Q^{-1}$ device. Three different samples were characterized and the relative frequency shifts are listed in the table 4.21. Resonance frequency of bare QCM/BDD sensor on air was taken as $f_0$ for all of the relative frequency shift $\Delta f$ calculations.

Table 4.21: Relative frequency shift of QCMs before and after NiNPs deposition on air and in PBS buffer

| **Electrode number** | **1** | **2** | **3** |
|---|---|---|---|
| $f_0$ (Hz) | 9998000 | 9975274 | 9973912 |
| **$\Delta f$ in PBS (%)** | -0.0592 | -0.0566 | -0.06018 |
| **$\Delta f$ NiNPs on air (%)** | -0.0328 | -0.0463 | -0.0282 |
| **$\Delta f$ NiNPs in PBS (%)** | -0.0419 | -0.0521 | -0.0548 |
| **$\Delta f$ NiNPs on air after PBS (%)** | **0.0259** | -0.0194 | **0.0205** |

It is expected, that frequency shift in PBS will be higher than in the air. Also is expected negative frequency shift after deposition of NiNPs due to mass loading on the

surface. This is fulfilled for both measurements in PBS (before and after NiNPs deposition) and for QCM's with NiNPs on air. But we can observe positive frequency increment after measurement of QCM's with NiNPs in PBS buffer, in table 4.21 are highlighted in red color, which means, that NiNPs are not attached well to the sensor's surface and they are detached during the frequency measurement, probably due to the vibrations of the sensor. After this measurement we did not continue with the experiment using the his-tagged protein as washing the NiNPs away during the measurement is a crucial problem and therefore this functionalization approach cannot be used for the biosensor fabrication.

**Protein attachment via electrografting of NTA acid**

For the attachment of the NTA acid to the BDD surface, we followed the protocol described in the chapter 4.7.3. Confirmation of the attachment of NTA acid was performed by measurement of the CVs in the solutions of $[Fe(CN)_6]^{3-/4-}$ in 0.5 M HCl (acidic medium, pH 0.3) and $[Fe(CN)_6]^{3-/4-}$ in 10 mM PBS buffer (neutral medium, pH 7.4), $\Delta E_p$ are listed in the table 4.22. From this measurement we can confirm successful attachment of aminobenzoic acid to the BDD surface, as we observed constant $\Delta E_p$ value for $[Fe(CN)_6]^{3-/4-}$ in HCl and an increase in $\Delta E_p$ for$[Fe(CN)_6]^{3-/4-}$ in PBS. However for the second modification step (attachment of NTA acid) we observed an increase in $\Delta E_p$ for $[Fe(CN)_6]^{3-/4-}$ in HCl and a decrease in $\Delta E_p$ for $[Fe(CN)_6]^{3-/4-}$ in PBS. These results indicate that the attachment of AB-NTA on the surface was not achieved.

Table 4.22: $\Delta E_p$ obtained from CV experiments with redox markers in different electrolytes

| **QCM/BDD** | **bare** | **AB-modified** | **AB-NTA modified** |
|---|---|---|---|
| **$\Delta E_p$ - $[Fe(CN)_6]^{3-/4-}$ (mV) in HCl pH 0.3** | | | |
| | 84 | 86 | **178** |
| **$\Delta E_p$ - $[Fe(CN)_6]^{3-/4-}$ (mV) in PBS pH 7.4** | | | |
| | 152 | 258 | **230** |

## 4.8.5 Conclusions and remarks for future work

This chapter brings the preliminary results on BDD coated QCMs for use as a biosensing element. Deposition of BDD layers on gold layers were studied and followed by coating of QCM sensors. Several seeding procedures were tried to obtain the best BDD layer on gold substrate. Deposition of BDD layers on QCM sensors was successfully achieved on

sensors with rough surface. Sensors with very smooth gold electrodes were not coated successfully as delamination of gold electrode occurred during the BDD depositions. The study of the influence of adding the BDD layer did not show any significant change in the behavior of QCM sensors in liquid with different density and viscosity. QCM's sensitivity slightly decreased after adding BDD layer in comparison with plain QCM sensor.
Two different E/C functionalization protocols were studied in order to attach his-tagged gp17 protein to BDD layers. According to CV results, the deposition of NiNPs followed by attachment of gp17 protein was successfully achieved. But we were not able to confirm attachment of bacteria *E. coli* cells to the functionalized sensors. The second approach, electrografting of NTA acid to BDD layer, were not achieved so far on QCM sensors.
However several problems appeared and need to be addressed for successful development of BDD-coated QCM biosensor:

1. Deposition of BDD layer on QCM with rough electrodes were successful. However the high roughness of QCM surface brings a challenging task of deposition really fully closed BDD layer. Seeding procedure needs to be improved, that the diamond seeds will reach even the deep narrow places on the rough gold electrode. Second option is master the deposition on the very smooth gold electrode, where we were not successful so far.

2. Functionalization of the BDD layer using NiNPs is not usable option so far as they detached during frequency measurement. It is easy and straightforward protocol, but adhesion of deposited NiNPs needs to be optimized directly for this type of BDD electrode.

# 5 | Summary and future perspectives

The work presented here is the first step towards the development of Love-wave biosensors with integrated diamond layer. At first, FEM simulations of diamond coated LW-SAW sensors were performed to study the effect of diamond layer on the behavior of the sensors made from different piezoelectric materials and guiding layers. We found out, that the phase velocity increases with adding of diamond layer, that is caused by increased rigidity of the surface. Adding of thin diamond layer also caused decrease of electromechanical coupling coefficient and the sensitivity as well. The sensitivity decrease was a building stone for further chapters focused on the experimental comparison of LW-SAW sensors with continuous diamond layer or discrete diamond coating or integration of LW-SAW sensors with phononic metamaterials.

In chapter 4.2, we successfully deposited isolated diamond grains and coalesced diamond layers on $SiO_2$/ST-cut quartz LW-SAW devices by LA-MW-PECVD method at low temperature and the devices maintained their piezoelectric properties. We confirmed good confinement of Love mode in the $SiO_2$ guiding layer for discrete NCD coating, but for the continuous layer the Love mode radiates into the bulk, which will decrease the sensitivity.

Chapter 4.3 is focused on the enhancing the sensitivity of SAW sensors by using the surface phononic metamaterials. At first, the band gap formation is explained briefly. The effect of PnMS on sensitivity was studied theoretically by FEM simulations and the effect of pillar geometry was discussed. We confirmed localization of the acoustic energy in the pillar for diamond and $SiO_2$ pillars and great improvement in the sensitivity, for diamond PnMS was achieved sensitivity around 5000 $cm^2 \cdot g^{-1}$ and for $SiO_2$ was 9000 $cm^2 \cdot g^{-1}$.

Chapter 4.4 is short chapter discussing the suitability of diamond and silicon carbide layers as passivation layers for package less SAW sensors. We found out that for ST-cut quartz/$SiO_2$ or ZnO sensors the thickness of passivation layer $h_{pass}/\lambda$ equal to 0.2 and for

36°YX $LiTaO_3/SiO_2$ or ZnO 0.1 is sufficient to reduce the sensitivity for both diamond and silicon carbide.

Chapter 4.5 describes the experimental investigation of diamond-coated LW-SAW sensors and comparison with the theoretical results. The main conclusion of this chapter is, that the sensitivity of diamond coated sensors does not decreases as much as expected from simulations. We investigated this result and it was found out, that the mechanical properties of NCD layer are different than we used in simulations. Mainly Young's modulus has much lower values ($\sim$) 240 GPa in comparison with 1050 GPa used in simulations. This is an important result, that unfortunately sends the results of the previous theoretical simulation only to the theoretical level, as the mechanical properties of real thin NCD layers are far different from the ones used there. We also studied the SAW devices with ZnO layer, but deposition of NCD layer on ZnO was not successful as the devices stopped working after diamond depositions. One possible explanation is the elimination of oxygen disorders from ZnO layer during diamond deposition making the ZnO layer conductive.

Chapter 4.6 is biological one that describes production of three different his-tagged bacteriophage's tail fibers. Another important part is investigation of the protein binding to the bacteria host cells, that was carried out using immunofluorescence assay. We found out, that gp17 and ORF26 specifically binds to *E.coli* cells, and gp12 also unexpectedly bonded to the *Salmonella* cells. These produced proteins were further used for functionalization of diamond layers.

Chapter 4.7 describes electrochemical functionalization of BDD layer in order to attach his-tagged proteins. We found out that BDD electrodes deposited at low temperature does not have required electrochemical properties, hence high temperature BDD electrodes were used. Two different functionalization protocols were successfully developed to attach his-tagged proteins. Binding of the *E.coli* cells was confirmed on the BDD surface functionalized with NiNPs, but unfortunately not for the second protocol using NTA acid.

Last chapter 4.8 describes the possibility of BDD-coated QCM sensors for biosensing. The same protocols for diamond layer functionalization were used as described in the previous chapter. We successfully deposited nickel nanoparticles on the QCM/BDD sensors, but during the frequency characterization in liquids the NiNPs detached from the diamond possibly due to crystal vibrations. The second approach, electrografting of

NTA acid to BDD layer, was not achieved on QCM/BDD layer so far.

The large amount of work carried out in this Thesis demonstrates that the development of diamond-based acoustic biosensor is complex, especially within a period of pandemic. When COVID-19 pandemic hit the world and interrupted lab work, I focused on the theoretical simulations during the lock-downs. In contrary to previous publication [178], we found out late that the mechanical properties of simulated NCD layers and the layers deposited at low temperature are different. This result drastically changes the perspectives of diamond use in acoustic devices. For instance, the sensitivity of LW-SAW devices is not reduced as much as one could expected and diamond-coated LW-SAW sensors are still good candidates to develop sensitive real-time device for bacteria detection in liquids. As the BDD layers are very good electrochemical electrodes with excellent properties and the routes for their electrochemical functionalization are known, it will be advantageous to connect two different signal read-outs at one device - electrochemical and acoustic characterization, either in LW-SAW sensors or QCM devices respectively. This Thesis, with its unexpected negative results but also its successes, confirms the potential use of diamond coated LW-SAW and QCM devices for selective bacterial detection in liquid using bacteriophages' tail fibers.

# 6 | List of publications

**Publications related to the doctoral thesis topic**

- Talbi A., Soltani A., Rumeau A., Taylor A., **Drbohlavova L.**, Klimsa L., Kopecek J., Fekete L., Krecmarova M., Mortet V.: Simulations, fabrication and characterization of diamond-coated Love wave-type surface acoustic wave sensors. Physica status solidi (a) 2015, **212(11)**, 2606-2610, IF = 2.17

- **Drbohlavova L.**, Bulir J., Vales V., Krecmarova M., Taylor A., Talbi A., Soltani A., Mortet V.: Fabrication methods of diamond coated Love wave SAW biosensors for bacterial detection applications. In Instruments and Methods for Biology and Medicine 2015. Kladno: Czech Technical University in Prague, 2015, p. 18-23. ISBN 978-80-01-05851-0

- **Drbohlavova L.**, Gerbedoen J.C., Taylor A., Talbi A., Fekete L., Ashcheulov P., Soltani A., Bovtun V., Kempa M., Bartoň J., Cigler P., Mortet V.: Diamond Coated LW-SAW Sensors-Study of Diamond Thickness Effect. Proceedings **2017**, 1, 540

- Liu Y., Talbi A., Djafari-Rouhani B., El Boudoti E. H., **Drbohlavová L.**, Mortet V., Bou Matar O., Pernod P. Interaction of Love waves with coupled cavity modes in a 2D holey phononic crystal. Physics Letters A 2019, **383**(13), 1502-1505 DOI: 10.1016/j.physleta.2019.01.053. ISSN 03759601, IF = 2.707

- **Drbohlavová L.**, Fekete L., Bovtun V., Kempa M., Taylor A., Liu Y., Bou Matar O., Talbi A., Mortet V. Love-wave devices with continuous and discrete nanocrystalline diamond coating for biosensing applications. Sensors and Actuators A: Physical. 2019, 298. DOI: 10.1016/j.sna.2019.111584. ISSN 09244247, IF = 4.291

**Publications not related to the doctoral thesis topic**

- Mortet V., **Drbohlavová L.**, Lambert N., Taylor A., Ashcheulov P., Davydova M., Lorincik J., Aleshin M., Hubik P., Conductivity of boron-doped diamond at high electrical field. Diamond and Related Materials 2019, **98** DOI: 10.1016/j.diamond.2019.107476. ISSN 09259635

**Participation to international conferences**

**Oral presentation**

- "Fabrication methods of diamond coated Love wave SAW biosensors for bacterial detection applications", Instruments & Methods for Biology and Medicine 2015 (IMBM 2015) student conference, FBME CTU in Prague,Sitna Sq. 3105, Kladno Czech Republic May 28th, 2015

**Poster presentation**

- "Simulations, fabrication and characterizations of diamond coated Love wave surface acoustic wave sensors" at Hasselt Diamond workshop 2015 - SBDD XX, Cultureel centrum Hasselt, Hasselt, Belgium, February 25th - 27th, 2015

- "Love-wave type surface acoustic wave sensors: effect of diamond thin film coating thickness" at Hasselt Diamond workshop 2017 – SBDD XXII, Cultureel centrum Hasselt, Hasselt, Belgium, March 8th-10th, 2017

- "Diamond Coated LW-SAW Sensors-Study of Diamond Thickness Effect" at Eurosensors 2017, Paris, France, September 3th - 6th, 2017

- "Theoretical investigation of diamond coated SiO2/ST-quartz and SiO2/36°YX LiNbO3 structures for biosensing applications" at E-MRS Fall meeting 2018, Warsaw, Poland, September 17th – 20th, 2018

- "Diamond and silicon carbide as passivation layers for packageless SAW sensors" at MRS Virtual Spring/Fall meeting Boston 2020, November 27 - December 4, 2020

- "Enhancing the sensitivity of SAW sensors using the diamond surface phononic metamaterials" at MRS Virtual Spring/Fall meeting Boston 2020, November 27 - December 4, 2020

# Bibliography


[1] Asif Ahmed, Jo V. Rushworth, Natalie A. Hirst, and Paul A. Millner. Biosensors for whole-cell bacterial detection. *Clinical Microbiology Reviews*, 27:631–646, 2014.

[2] Robert S. Burlage and Joshua Tillmann. Biosensors of bacterial cells. *Journal of Microbiological Methods*, 138:2–11, 2017.

[3] Hüseyin Oğuzhan Kaya, Arif E. Cetin, Mostafa Azimzadeh, and Seda Nur Topkaya. Pathogen detection with electrochemical biosensors: Advantages, challenges and future perspectives, 2 2021.

[4] Jordi Riu and Barbara Giussani. Electrochemical biosensors for the detection of pathogenic bacteria in food, 5 2020.

[5] Nishant Kumar, Yuan Hu, Suman Singh, and Boris Mizaikoff. Emerging biosensor platforms for the assessment of water-borne pathogens. *The Analyst*, 143:359–373, 2018.

[6] Dmitri Ivnitski, Ihab Abdel-Hamid, Plamen Atanasov, Ebtisam Wilkins, and Stephen Stricker. Application of electrochemical biosensors for detection of food pathogenic bacteria. *Electroanalysis*, 12:317–325, 3 2000.

[7] M. B. Maas, W. J. Perold, and L. M.T. Dicks. Biosensors for the detection of escherichia coli, 10 2017.

[8] J Du, G.L Harding, A.F Collings, and P.R Dencher. An experimental study of love-wave acoustic sensors operating in liquids. *Sensors and Actuators A: Physical*, 60:54–61, 5 1997.

[9] V. Vaijayanthimala, Po Yun Cheng, Shih Hua Yeh, Kuang Kai Liu, Cheng Hsiang Hsiao, Jui I. Chao, and Huan Cheng Chang. The long-term stability and biocompatibility of fluorescent nanodiamond as an in vivo contrast agent. *Biomaterials*, 33:7794–7802, 2012.

[10] Anke Krueger and Daniel Lang. Functionality is key: Recent progress in the surface modification of nanodiamond. *Advanced Functional Materials*, 22:890–906, 3 2012.

[11] Vadym N. Mochalin, Olga Shenderova, Dean Ho, and Yury Gogotsi. The properties and applications of nanodiamonds, 2012.

[12] David Rifkind and Geraldine L. Freeman. Introduction to part c: Bacteria, 2005.

[13] Lucie Drbohlavova. Development of a saw sensor platform for pathogen detection, 2016.

[14] Stanislav Rozsypal. *Nový přehled biologie*. Scientia, 2003.

[15] Guntram Seltmann and Otto Holst. *The Bacterial Cell Wall.* Springer Berlin Heidelberg, 2002.

[16] Donnenberg. *Escherichia coli: Pathotypes and Principles of Pathogenesis.* Academic Press, 2013.

[17] Arghavan Shabani, Christophe A. Marquette, Rosemonde Mandeville, and Marcus F. Lawrence. Modern probe-assisted methods for the specific detection of bacteria. *Journal of Biomedical Science and Engineering*, 08:104–121, 2015.

[18] Kiev S. Gracias and John L. McKillip. A review of conventional detection and enumeration methods for pathogenic bacteria in food. *Canadian Journal of Microbiology*, 50:883–890, 11 2004.

[19] Momna Rubab, Hafiz Muhammad Shahbaz, Amin N. Olaimat, and Deog Hwan Oh. Biosensors for rapid and sensitive detection of staphylococcus aureus in food. *Biosensors and Bioelectronics*, 105:49–57, 2018.

[20] Allen D. Taylor, Qiuming Yu, Shengfu Chen, Jiří Homola, and Shaoyi Jiang. Comparison of e. coli o157:h7 preparation methods used for detection with surface plasmon resonance sensor. *Sensors and Actuators B: Chemical*, 107:202–208, 5 2005.

[21] Özlem Torun, İsmail Hakkı Boyacı, Erhan Temür, and Uğur Tamer. Comparison of sensing strategies in spr biosensor for rapid and sensitive enumeration of bacteria. *Biosensors and Bioelectronics*, 37:53–60, 8 2012.

[22] Seung Min Yoo and Sang Yup Lee. Optical biosensors for the detection of pathogenic microorganisms. *Trends in Biotechnology*, 34:7–25, 1 2016.

[23] Borja Sepúlveda, Paula C. Angelomé, Laura M. Lechuga, and Luis M. Liz-Marzán. Lspr-based nanobiosensors. *Nano Today*, 4:244–251, 6 2009.

[24] Peng Zhang, You-Peng Chen, Wei Wang, Yu Shen, and Jin-Song Guo. Surface plasmon resonance for water pollutant detection and water process analysis. *TrAC Trends in Analytical Chemistry*, 85:153–165, 12 2016.

[25] Reshma Bharadwaj, V.V.R. Sai, Kamini Thakare, Arvind Dhawangale, Tapanendu Kundu, Susan Titus, Pradeep Kumar Verma, and Soumyo Mukherji. Evanescent wave absorbance based fiber optic biosensor for label-free detection of e. coli at 280nm wavelength. *Biosensors and Bioelectronics*, 26:3367–3370, 3 2011.

[26] Hana Vaisocherová-Lísalová, Ivana Víšová, Maria Laura Ermini, Tomáš Špringer, Xue Chadtová Song, Jan Mrázek, Josefína Lamačová, N. Scott Lynn, Petr Šedivák, and Jiří Homola. Low-fouling surface plasmon resonance biosensor for multi-step detection of foodborne bacterial pathogens in complex food samples. *Biosensors and Bioelectronics*, 80:84–90, 6 2016.

[27] Seung-Ho Ohk and Arun K. Bhunia. Multiplex fiber optic biosensor for detection of listeria monocytogenes, escherichia coli o157:h7 and salmonella enterica from ready-to-eat meat samples. *Food Microbiology*, 33:166–171, 4 2013.

[28] Yasi Li, Jiawei Zhu, Hongyan Zhang, Weimin Liu, Jiechao Ge, Jiasheng Wu, and Pengfei Wang. High sensitivity gram-negative bacteria biosensor based on a small-molecule modified surface plasmon resonance chip studied using a laser scanning confocal imaging-surface plasmon resonance system. *Sensors and Actuators B: Chemical*, 259:492–497, 4 2018.

[29] H. Baccar, M. B. Mejri, I. Hafaiedh, T. Ktari, M. Aouni, and A. Abdelghani. Surface plasmon resonance immunosensor for bacteria detection. *Talanta*, 82:810–814, 2010.

[30] Yixian Wang, Zunzhong Ye, Chengyan Si, and Yibin Ying. Monitoring of escherichia coli o157:h7 in food samples using lectin based surface plasmon resonance biosensor. *Food Chemistry*, 136:1303–1308, 2013.

[31] Seung Min Yoo, Do Kyun Kim, and Sang Yup Lee. Aptamer-functionalized localized surface plasmon resonance sensor for the multiplexed detection of different bacterial species. *Talanta*, 132:112–117, 2015.

[32] Li Xue, Lingyan Zheng, Huilin Zhang, Xiu Jin, and Jianhan Lin. An ultrasensitive fluorescent biosensor using high gradient magnetic separation and quantum dots for fast detection of foodborne pathogenic bacteria. *Sensors and Actuators, B: Chemical*, 265:318–325, 2018.

[33] Rafaela N. Lopes, Domingos M.C. Rodrigues, Regina C.S.B. Allil, and Marcelo M. Werneck. Plastic optical fiber immunosensor for fast detection of sulfate-reducing bacteria. *Measurement*, 125:377–385, 9 2018.

[34] Christopher F. Fronczek, David J. You, and Jeong Yeol Yoon. Single-pipetting microfluidic assay device for rapid detection of salmonella from poultry package. *Biosensors and Bioelectronics*, 40:342–349, 2013.

[35] Jiao Hu, Yong Zhong Jiang, Man Tang, Ling Ling Wu, Hai Yan Xie, Zhi Ling Zhang, and Dai Wen Pang. Colorimetric-fluorescent-magnetic nanosphere-based multimodal assay platform for salmonella detection. *Analytical Chemistry*, 91:1178–1184, 1 2019.

[36] Dániel Petrovszki, Sándor Valkai, Evelin Gora, Martin Tanner, Anita Bányai, Péter Fürjes, and András Dér. An integrated electro-optical biosensor system for rapid, low-cost detection of bacteria. *Microelectronic Engineering*, 239-240, 2 2021.

[37] Shuaishuai Yan, Cheng Liu, Shuiqin Fang, Junfei Ma, Jingxuan Qiu, Dongpo Xu, Li Li, Jiaping Yu, Daixi Li, and Qing Liu. Sers-based lateral flow assay combined with machine learning for highly sensitive quantitative analysis of escherichia coli o157:h7. *Analytical and Bioanalytical Chemistry*, 412:7881–7890, 2020.

[38] Meng Xu, Ronghui Wang, and Yanbin Li. Electrochemical biosensors for rapid detection of escherichia coli o157:h7. *Talanta*, 162:511–522, 2017.

[39] Ankan Dutta Chowdhury, Amitabha De, Chirosree Roy Chaudhuri, Krishnan Bandyopadhyay, and Pintu Sen. Label free polyaniline based impedimetric biosensor for detection of e. coli o157:h7 bacteria. *Sensors and Actuators, B: Chemical*, 171-172:916–923, 2012.

[40] Zeynep Altintas, Mete Akgun, Guzin Kokturk, and Yildiz Uludag. A fully automated microfluidic-based electrochemical sensor for real-time bacteria detection. *Biosensors and Bioelectronics*, 100:541–548, 2018.

[41] Lan Yao, Lei Wang, Fengchun Huang, Gaozhe Cai, Xinge Xi, and Jianhan Lin. A microfluidic impedance biosensor based on immunomagnetic separation and urease catalysis for continuous-flow detection of e. coli o157:h7. *Sensors and Actuators, B: Chemical*, 259:1013–1021, 2018.

[42] Gustavo A. Zelada-Guillén, José Luis Sebastián-Avila, Pascal Blondeau, Jordi Riu, and F. Xavier Rius. Label-free detection of staphylococcus aureus in skin using real-time potentiometric biosensors based on carbon nanotubes and aptamers. *Biosensors and Bioelectronics*, 31:226–232, 2012.

[43] E. Sheikhzadeh, M. Chamsaz, A.P.F. Turner, E.W.H. Jager, and V. Beni. Label-free impedimetric biosensor for salmonella typhimurium detection based on poly [pyrrole-co-3-carboxyl-pyrrole] copolymer supported aptamer. *Biosensors and Bioelectronics*, 80:194–200, 6 2016.

[44] Jyoti Bhardwaj, Sivaranjani Devarakonda, Suveen Kumar, and Jaesung Jang. Development of a paper-based electrochemical immunosensor using an antibody-single walled carbon nanotubes bio-conjugate modified electrode for label-free detection of foodborne pathogens. *Sensors and Actuators, B: Chemical*, 253:115–123, 2017.

[45] Yongjin Zou, Jing Liang, Zhe She, and Heinz Bernhard Kraatz. Gold nanoparticles-based multifunctional nanoconjugates for highly sensitive and enzyme-free detection of e.coli k12. *Talanta*, 193:15–22, 2 2019.

[46] Nidhi Dhull, Gurpreet Kaur, Prateek Jain, Priyanka Mishra, Divya Singh, Lilly Ganju, Vinay Gupta, and Monika Tomar. Label-free amperometric biosensor for escherichia coli o157:h7 detection. *Applied Surface Science*, 495, 11 2019.

[47] Saravanan Rengaraj, Álvaro Cruz-Izquierdo, Janet L. Scott, and Mirella Di Lorenzo. Impedimetric paper-based biosensor for the detection of bacterial contamination in water. *Sensors and Actuators B: Chemical*, 265:50–58, 7 2018.

[48] Azam Yaghoobi, Ramin Abiri, Amirhoushang Alvandi, Elham Arkan, Ghobad Mohammadi, Tooraj Farshadnia, and Ali R. Jalalvand. An efficiently engineered electrochemical biosensor as a novel and user-friendly electronic device for biosensing of streptococcus pneumoniae bacteria. *Sensing and Bio-Sensing Research*, 36, 6 2022.

[49] D. S. Ballantine, R. M. White, S. J. Martin, A. J. Ricco, G. C. Frye, H. Wohltjen, and E. T. Zellers. *Acoustic wave sensors. Theory, design and physicochemical applications.* ACADEMIC PRESS, San Diego, CA, 1997.

[50] Kerstin Länge, Bastian E. Rapp, and Michael Rapp. Surface acoustic wave biosensors: A review. *Analytical and Bioanalytical Chemistry*, 391:1509–1519, 2008.

[51] Faridah Salam, Yildiz Uludag, and Ibtisam E. Tothill. Real-time and sensitive detection of salmonella typhimurium using an automated quartz crystal microbalance (qcm) instrument with nanoparticles amplification. *Talanta*, 115:761–767, 2013.

[52] E. Howe and G. Harding. A comparison of protocols for the optimisation of detection of bacteria using a surface acoustic wave (saw) biosensor. *Biosensors and Bioelectronics*, 15:641–649, 2000.

[53] Xuesong Jiang, Ronghui Wang, Yun Wang, Xiaoli Su, Yibin Ying, Jianping Wang, and Yanbin Li. Evaluation of different micro/nanobeads used as amplifiers in qcm immunosensor for more sensitive detection of e. coli o157:h7. *Biosensors and Bioelectronics*, 29:23–28, 2011.

[54] Noor Azlina Masdor, Zeynep Altintas, and Ibtisam E. Tothill. Sensitive detection of campylobacter jejuni using nanoparticles enhanced qcm sensor. *Biosensors and Bioelectronics*, 78:328–336, 2016.

[55] Leonardo Lamanna, Francesco Rizzi, Venkat R. Bhethanabotla, and Massimo De Vittorio. Conformable surface acoustic wave biosensor for e-coli fabricated on pen plastic film. *Biosensors and Bioelectronics*, 163:112164, 2020.

[56] Sandro Spagnolo, Brian De La Franier, Katharina Davoudian, Tibor Hianik, and Michael Thompson. Detection of e. coli bacteria in milk by an acoustic wave aptasensor with an anti-fouling coating. *Sensors*, 22, 3 2022.

[57] Juliana Chawich, Walid M. Hassen, Céline Elie-Caille, Thérèse Leblois, and Jan J. Dubowski. Regenerable zno/gaas bulk acousticwave biosensor for detection of escherichia coli in "complex" biological medium. *Biosensors*, 11, 5 2021.

[58] Mariacristina Gagliardi, Matteo Agostini, Francesco Lunardelli, Leonardo Lamanna, Alessio Miranda, Agostino Bazzichi, Antonella Giuliana Luminare, Fabrizio Cervelli, Francesca Gambineri, Michele Totaro, Michele Lai, Giuseppantonio Maisetta, Giovanna Batoni, Mauro Pistello, and Marco Cecchini. Surface acoustic wave-based lab-on-a-chip for the fast detection of legionella pneumophila in water. *Sensors and Actuators B: Chemical*, 379, 3 2023.

[59] H. W. Ackermann. 5500 phages examined in the electron microscope. *Archives of Virology*, 152:227–243, 2007.

[60] David R Harper, Benjamin H Burrowes, and Elizabeth M Kutter. Bacteriophage: Therapeutic uses, 8 2014.

[61] Łukasz Richter, Marta Janczuk-Richter, Joanna Niedziółka-Jönsson, Jan Paczesny, and Robert Hołyst. Recent advances in bacteriophage-based methods for bacteria detection. *Drug Discovery Today*, 23:448–455, 2018.

[62] Marta Janczuk, Joanna Niedziółka-Jönsson, and Katarzyna Szot-Karpińska. Bacteriophages in electrochemistry: A review. *Journal of Electroanalytical Chemistry*, 779:207–219, 10 2016.

[63] Zeinab Hosseinidoust, Adam L.J. Olsson, and Nathalie Tufenkji. Going viral: Designing bioactive surfaces with bacteriophage. *Colloids and Surfaces B: Biointerfaces*, 124:2–16, 12 2014.

[64] H. Anany, W. Chen, R. Pelton, and M. W. Griffiths. Biocontrol of listeria monocytogenes and escherichia coli o157:h7 in meat by using phages immobilized on modified cellulose membranes. *Applied and Environmental Microbiology*, 77:6379–6387, 9 2011.

[65] Saroh Niyomdecha, Warakorn Limbut, Apon Numnuam, Proespichaya Kanatharana, Ratthaphol Charlermroj, Nitsara Karoonuthaisiri, and Panote Thavarungkul. Phage-based capacitive biosensor for salmonella detection. *Talanta*, 188:658–664, 2018.

[66] Arghavan Shabani, Christophe A. Marquette, Rosemonde Mandeville, and Marcus F. Lawrence. Magnetically-assisted impedimetric detection of bacteria using phage-modified carbon microarrays. *Talanta*, 116:1047–1053, 2013.

[67] Huan Yue, Yong He, Enci Fan, Lin Wang, Shuguang Lu, and Zhifeng Fu. Label-free electrochemiluminescent biosensor for rapid and sensitive detection of pseudomonas aeruginosa using phage as highly specific recognition agent. *Biosensors and Bioelectronics*, 94:429–432, 2017.

[68] Fengjiao He, Meiyu Xiang, and Xianwen Mi. A new bacteriophage-modified piezoelectric sensor for rapid and specific detection of mycobacterium. *Analytical Letters*, 45:1242–1253, 2012.

[69] Rajesh Guntupalli, Iryna Sorokulova, Eric Olsen, Ludmila Globa, Oleg Pustovyy, Timothy Moore, Bryan Chin, James Barbaree, and Vitaly Vodyanoy. Detection and identification of methicillin resistant and sensitive strains of staphylococcus aureus using tandem measurements. *Journal of Microbiological Methods*, 90:182–191, 2012.

[70] Nitilaksha Hiremath, Rajesh Guntupalli, Vitaly Vodyanoy, Bryan A. Chin, and Mi Kyung Park. Detection of methicillin-resistant staphylococcus aureus using novel lytic phage-based magnetoelastic biosensors. *Sensors and Actuators, B: Chemical*, 210:129–136, 2015.

[71] Nancy Tawil, Edward Sacher, Rosemonde Mandeville, and Michel Meunier. Surface plasmon resonance detection of e. coli and methicillin-resistant s. aureus using bacteriophages. *Biosensors and Bioelectronics*, 37:24–29, 2012.

[72] Ji Wang, Huihui Li, Changbin Li, Yifeng Ding, Yuanshang Wang, Wenjuan Zhu, Jia Wang, Yanchun Shao, Hui Pan, and Xiaohong Wang. Eis biosensor based on a novel myoviridae bacteriophage sep37 for rapid and specific detection of salmonella in food matrixes. *Food Research International*, 158, 8 2022.

[73] Dhara Patel, Yan Zhou, and Ramaraja P. Ramasamy. A bacteriophage-based electrochemical biosensor for detection of methicillin-resistant staphylococcus aureus. *Journal of The Electrochemical Society*, 168:057523, 5 2021.

[74] Nader Abdelhamied, Fatma Abdelrahman, Ayman El-Shibiny, and Rabeay Y.A. Hassan. Bacteriophage-based nano-biosensors for the fast impedimetric determination of pathogens in food samples. *Scientific Reports*, 13, 12 2023.

[75] Kenta Nakama, Mohammed Sedki, and Ashok Mulchandani. Label-free chemiresistor biosensor based on reduced graphene oxide and m13 bacteriophage for detection of coliforms. *Analytica Chimica Acta*, 1150, 3 2021.

[76] Amit Singh, Denis Arutyunov, Mark T. McDermott, Christine M. Szymanski, and Stephane Evoy. Specific detection of campylobacter jejuni using the bacteriophage nctc 12673 receptor binding protein as a probe. *Analyst*, 136:4780–4786, 2011.

[77] Somayyeh Poshtiban, Muhammad Afzal Javed, Denis Arutyunov, Amit Singh, Graham Banting, Christine M. Szymanski, and Stephane Evoy. Phage receptor binding protein-based magnetic enrichment method as an aid for real time pcr detection of foodborne bacteria. *Analyst*, 138:5619–5626, 2013.

[78] Muhammad A. Javed, Somayyeh Poshtiban, Denis Arutyunov, Stephane Evoy, and Christine M. Szymanski. Bacteriophage receptor binding protein based assays for the simultaneous detection of campylobacter jejuni and campylobacter coli. *PLoS ONE*, 8, 2013.

[79] Hae Ja Shin and Woon Ki Lim. Rapid label-free detection of e. coli using a novel spr biosensor containing a fragment of tail protein from phage lambda. *Preparative Biochemistry and Biotechnology*, 48:498–505, 2018.

[80] Seok Hywan Hyeon, Woon Ki Lim, and Hae Ja Shin. Novel surface plasmon resonance biosensor that uses full-length det7 phage tail protein for rapid and selective detection of salmonella enterica serovar typhimurium. *Biotechnology and Applied Biochemistry*, 68:5–12, 2 2021.

[81] Zhaozhao Tang, Wenyan Wu, and Jinliang Gao. Water pressure sensing based on wireless passive saw technology. *Procedia Engineering*, 119:892–900, 2015.

[82] María Isabel Rocha Gaso. Analysis, implementation and validation of a love mode surface acoustic wave device for its application as sensor of biological processes in liquid media., 2013.

[83] Y. Q. Fu, J. K. Luo, N. T. Nguyen, A. J. Walton, A. J. Flewitt, X. T. Zu, Y. Li, G. McHale, A. Matthews, E. Iborra, H. Du, and W. I. Milne. Advances in piezoelectric thin films for acoustic biosensors, acoustofluidics and lab-on-chip applications. *Progress in Materials Science*, 89:31–91, 2017.

[84] Antonio Arnau. *Piezoelectric Transducers and Applications*. Springer Berlin Heidelberg, 2008.

[85] Inke Pitz, Leonard Hall, Hedley Hansen, Vijay Varadan, and Chris Bertram. Trade-offs for wireless transcutaneous rf communication in biotelemetric applications. *Proceedings of SPIE*, 4937:307–318, 2002.

[86] María-Isabel Rocha-Gaso, Carmen March-Iborra, Ángel Montoya-Baides, and Antonio Arnau-Vives. Surface generated acoustic wave biosensors for the detection of pathogens: A review. *Sensors*, 9:5740–5769, 2009.

[87] J K Luo, Y Q Fu, and W I Milne. Acoustic wave based microfluidics and lab-on-a-chip, 2013.

[88] Tomasz G. Zielinski. Bulk and surface acoustic waves in piezoelectric media.

[89] Trang Hoang. Design and realization of saw pressure sensor using aluminum nitride, 1 2009.

[90] Igor Laposa. Simulace piezoelektrických rezonančních senzorů, 2013.

[91] Colin Campbell. *Surface Acoustic Wave Devices and Their Signal Processing Applications*. Academic Press, INC., 1989.

[92] Eugene Dieulesaint and Daniel Royer. Propagation et génération des ondes élastiques, 2001.

[93] Yi Zhang, Jikui Luo, Andrew J. Flewitt, Zhiqiang Cai, and Xiubo Zhao. Film bulk acoustic resonators (fbars) as biosensors: A review. *Biosensors and Bioelectronics*, 116:1–15, 9 2018.

[94] S. T. Ten, U. Hashim, S. C.B. Gopinath, W. W. Liu, K. L. Foo, S. T. Sam, S. F.A. Rahman, C. H. Voon, and A. N. Nordin. Highly sensitive escherichia coli shear horizontal surface acoustic wave biosensor with silicon dioxide nanostructures. *Biosensors and Bioelectronics*, 93:146–154, 2017.

[95] G. Kovacs, M.J. Vellekoop, R. Haueis, G.W. Lubking, and A. Venema. A love wave sensor for (bio)chemical sensing in liquids. *Sensors and Actuators A: Physical*, 43:38–43, 5 1994.

[96] Thomas M.A. Gronewold. Surface acoustic wave sensors in the bioanalytical field: Recent trends and challenges. *Analytica Chimica Acta*, 603:119–128, 2007.

[97] Nicolas Moll, Emilie Pascal, Duy Haï Dinh, Jean Paul Pillot, Bernard Bennetau, Dominique Rebière, Daniel Moynet, Yan Mas, Djavad Mossalayi, Jacques Pistré, and Corinne Déjous. A love wave immunosensor for whole e. coli bacteria detection using an innovative two-step immobilisation approach. *Biosensors and Bioelectronics*, 22:2145–2150, 2007.

[98] R. M. White and F. W. Voltmer. Direct piezoelectric coupling to surface elastic waves. *Applied Physics Letters*, 7:314–316, 1965.

[99] Anurupa Shaw. La génération d'impulsions courtes d'ondes acoustiques de surface sur un matériau piézo-électrique, 2017.

[100] Bernhard Jakoby, Jeroen Bastemeijer, and Michael J. Vellekoop. Temperature-compensated love-wave sensors on quartz substrates. *Sensors and Actuators, A: Physical*, 82:83–88, 2000.

[101] K. Nakamura, M. Kazumi, and H. Shimizu. Sh-type and rayleigh-type surface waves on rotated y-cut litao3. pages 819–822. IEEE, 1977.

[102] G. A. Smolenskii, N. N. Krainik, N. P. Khuchua, V. V. Zhdanova, and I. E. Mylnikova. The curie temperature of linbo3. *Physica status solidi b*, 13:309–314, 1966.

[103] Zhenwei Peng and Simon A.T. Redfern. Mechanical properties of quartz at the alfa-beta phase transition: Implications for tectonic and seismic anomalies. *Geochemistry, Geophysics, Geosystems*, 14:18–28, 1 2013.

[104] H. J. Levinstein, A. A. Ballman, and C. D. Capio. Domain structure and curie temperature of single-crystal lithium tantalate. *Journal of Applied Physics*, 37:4585–4586, 11 1966.

[105] Jin Qian, Cuiping Li, Lirong Qian, Mingji Li, Hongji Li, and Baohe Yang. Three-dimensional finite element simulation of love mode surface acoustic wave in layered structures including zno piezoelectric film and diamond substrate. *Diamond and Related Materials*, 88:123–128, 2018.

[106] Juan Gabriel and Rodríguez Madrid. Ultra high frequency thin film saw devices, 2013.

[107] Huiyan Wu, Xiangming Xiong, Hongfei Zu, James H.-C. Wang, and Qing-Ming Wang. Theoretical analysis of a love wave biosensor in liquid with a viscoelastic wave guiding layer. *Journal of Applied Physics*, 121:054501, 2 2017.

[108] Lokesh Rana, Reema Gupta, Monika Tomar, and Vinay Gupta. Highly sensitive love wave acoustic biosensor for uric acid. *Sensors and Actuators, B: Chemical*, 261:169–177, 2018.

[109] Juliana Chawich, Sabina Kuprenaite, Samuel Margueron, Pascal Boulet, Jan J. Dubowski, Céline Elie-Caille, and Thérèse Leblois. Deposition and characterization of zno thin films on gaas and pt/gaas substrates. *Materials Chemistry and Physics*, 247, 2020.

[110] F. Herrmann, M. Weihnacht, and S. Büttgenbach. Properties of shear-horizontal surface acoustic waves in different layered quartz–sio2 structures. *Ultrasonics*, 37:335–341, 6 1999.

[111] K. Kalantar-zadeh, W. Wlodarski, A. Holland, M. Austin, and H. Mendis. Design and fabrication of a sio2/st-cut quartz love mode surface acoustic wave transducer for operation in liquid media. pages 308–311. IEEE, 2000.

[112] John C. Kotz, Paul M. Treichel, and Gabriela C. Weaver. *Chemistry and chemical reactivity.* Thomson Brooks/Cole, 6th edition, 2006.

[113] Ei ichi Yasuda, Michio Inagaki, Katsumi Kaneko, Morinobu Endo, Asao Oya, and Yasuhiro Tanabe. *Carbon Alloys: Novel Concepts to Develop Carbon Science and Technology.* Elsevier, 2003.

[114] Aparna Das and Bimal Krishna Banik. Microwave-assisted cvd processes for diamond synthesis, 2021.

[115] Michal Gulka. Bio-molecular sensors for molecular diagnostics in nanomedicine based on color centres in diamond, 2017.

[116] Paul W. May. Diamond thin films: A 21st-century material. *Philosophical Transactions of the Royal Society A: Mathematical, Physical and Engineering Sciences*, 358:473–495, 2000.

[117] Christopher M Breeding and James E Shigley. The "type" classification system of diamonds and its importance in gemology, 2009.

[118] Norio Tokuda. Homoepitaxial diamond growth by plasma-enhanced chemical vapor deposition, 2019.

[119] Sylvia Wenmackers. Morphology, functionality and molecular conformation study of cvd diamond surfaces functionalised with organic linkers and dna, 2008.

[120] Sylvia Wenmackers, Veronique Vermeeren, Martin VandeVen, Marcel Ameloot, Nathalie Bijnens, Ken Haenen, Luc Michiels, and Patrick Wagner. Diamond-based dna sensors: Surface functionalization and read-out strategies. *Physica Status Solidi (A) Applications and Materials Science*, 206:391–408, 3 2009.

[121] Sabine Szunerits, Christoph E. Nebel, and Robert J. Hamers. Surface functionalization and biological applications of cvd diamond. *MRS Bulletin*, 39:517–524, 2014.

[122] Amanda M. Schrand, Suzanne A.Ciftan Hens, and Olga A. Shenderova. Nanodiamond particles: Properties and perspectives for bioapplications. *Critical Reviews in Solid State and Materials Sciences*, 34:18–74, 1 2009.

[123] Robert J. Hamers, Wensha Yang, Orlando Auciello, and James E. Butler. Dna-modified ncd thin films as stable, biologically active substrates. *Nature materials*, 1:253–258, 2002.

[124] Guo Jun Zhang, Kwang Soup Song, Yusuke Nakamura, Taro Ueno, Takashi Funatsu, Iwao Ohdomari, and Hiroshi Kawarada. Dna micropatterning on polycrystalline diamond via one-step direct amination. *Langmuir*, 22:3728–3734, 2006.

[125] Christoph E. Nebel, Dongchan Shin, Bohuslav Rezek, Norio Tokuda, Hiroshi Uetsuka, and Hideyuki Watanabe. Diamond and biology, 6 2007.

[126] Wensha Yang, James E. Butler, John N. Russell, and Robert J. Hamers. Interfacial electrical properties of dna-modified diamond thin films: Intrinsic response and hybridization-induced field effects. *Langmuir*, 20:6778–6787, 8 2004.

[127] A. Rahim Ruslinda, Shinya Tajima, Yoko Ishii, Yuichiro Ishiyama, Robert Edgington, and Hiroshi Kawarada. Aptamer-based biosensor for sensitive pdgf detection using diamond transistor. *Biosensors and Bioelectronics*, 26:1599–1604, 12 2010.

[128] A. Rahim Ruslinda, Y. Ishiyama, V. Penmatsa, S. Ibori, and H. Kawarada. Repulsive effects of hydrophobic diamond thin films on biomolecule detection. *Applied Surface Science*, 328:314–318, 2015.

[129] Adarsh D. Radadia, Courtney J. Stavis, Rogan Carr, Hongjun Zeng, William P. King, John A. Carlisle, Aleksei Aksimentiev, Robert J. Hamers, and Rashid Bashir. Control of nanoscale environment to improve stability of immobilized proteins on diamond surfaces. *Advanced Functional Materials*, 21:1040–1050, 3 2011.

[130] Qianwen Zhang, Minghui Zhang, Yuxiang Du, Bangqiang Xu, Genqiang Chen, Shi He, Dan Zhang, Qi Li, and Hong Xing Wang. Trace detection of sars-cov-2 n-protein by diamond solution-gate field-effect transistor. *Diamond and Related Materials*, 134, 4 2023.

[131] Siyu Yu, Shetian Liu, Xin Jiang, and Nianjun Yang. Recent advances on electrochemistry of diamond related materials. *Carbon*, 200:517–542, 11 2022.

[132] Zejun Deng, Ruitong Zhu, Li Ma, Kechao Zhou, Zhiming Yu, and Qiuping Wei. Diamond for antifouling applications: A review, 8 2022.

[133] Nathalie Bijnens, Veronique Vermeeren, Michael Daenen, Lars Grieten, Ken Haenen, Sylvia Wenmackers, Oliver A. Williams, Marcel Ameloot, Martin Vandeven, Luc Michiels, and Patrick Wagner. Synthetic diamond films as a platform material for label-free protein sensors. *Physica Status Solidi (A) Applications and Materials Science*, 206:520–526, 3 2009.

[134] Tomáš Mackuľak, Erika Medvecká, Andrea Vojs Staňová, Paula Brandeburová, Roman Grabic, Oksana Golovko, Marián Marton, Igor Bodík, Alžbeta Medveďová, Miroslav Gál, Matej Planý, Alexander Kromka, Viera Špalková, Andrea Škulcová, Ivana Horáková, and Marian Vojs. Boron doped diamond electrode – the elimination of psychoactive drugs and resistant bacteria from wastewater. *Vacuum*, 171, 1 2020.

[135] Carlos A. Martínez-Huitle and Enric Brillas. A critical review over the electrochemical disinfection of bacteria in synthetic and real wastewaters using a boron-doped diamond anode. *Current Opinion in Solid State and Materials Science*, 25, 8 2021.

[136] Wioleta Białobrzeska, Mateusz Ficek, Bartłomiej Dec, Silvio Osella, Bartosz Trzaskowski, Andres Jaramillo-Botero, Mattia Pierpaoli, Michał Rycewicz, Yanina Dashkevich, Tomasz Łęga, Natalia Malinowska, Zofia Cebula, Daniel Bigus, Daniel Firganek, Ewelina Bięga, Karolina Dziąbowska, Mateusz Brodowski, Marcin Kowalski, Mirosława Panasiuk, Beata Gromadzka, Sabina Żołędowska, Dawid Nidzworski, Krzysztof Pyrć, William A. Goddard, and Robert Bogdanowicz. Performance of electrochemical immunoassays for clinical diagnostics of sars-cov-2 based on selective nucleocapsid n protein detection: Boron-doped diamond, gold and glassy carbon evaluation. *Biosensors and Bioelectronics*, 209, 8 2022.

[137] Zhen Yang, Mingji Li, Hongji Li, Huayi Li, Cuiping Li, and Baohe Yang. Polycrystalline boron-doped diamond-based electrochemical biosensor for simultaneous detection of dopamine and melatonin. *Analytica Chimica Acta*, 1135:73–82, 10 2020.

[138] Simona Baluchová, Mariola Brycht, Andrew Taylor, Vincent Mortet, Jan Krůšek, Ivan Dittert, Silvia Sedláková, Ladislav Klimša, Jaromír Kopeček, and Karolina Schwarzová-Pecková. Enhancing electroanalytical performance of porous boron-doped diamond electrodes by increasing thickness for dopamine detection. *Analytica Chimica Acta*, 1182, 2021.

[139] V. Mortet, O. A. Williams, and K. Haenen. Diamond: A material for acoustic devices. *Physica Status Solidi (A) Applications and Materials Science*, 205:1009–1020, 2008.

[140] V. Procházka, P. Kulha, T. Izsák, E. Ukraintsev, M. Varga, V. Jirásek, and A. Kromka. Detection of globular and fibrillar proteins by quartz crystal microbalance sensor coated with a functionalized diamond thin film. *Applied Surface Science*, 589, 7 2022.

[141] R. Manai, M. Habchi, D. Kamouni-Belghiti, M. A. Persuy, L. Rousseau, M. Possas Abreu, D. Grebert, K. Badonnel, P. Bergonzo, E. Pajot-Augy, G. Sanz, and E. Scorsone. Diamond microcantilevers as transducers for olfactory receptors - based biosensors: Application to the receptors m71 and or7d4. *Sensors and Actuators, B: Chemical*, 238:1199–1206, 1 2017.

[142] Emmanuel Scorsone, Raafa Manai, Maria J. Ricatti, Marco Redaelli, Philippe Bergonzo, Krishna C. Persaud, and Carla Mucignat. Major urinary proteins on nanodiamond-based resonators toward artificial olfaction. *IEEE Sensors Journal*, 16:6543–6550, 9 2016.

[143] Ting Wei Liu, Yao Chuan Tsai, Yu Ching Lin, Takahito Ono, Shuji Tanaka, and Tsung Tsong Wu. Design and fabrication of a phononic-crystal-based love wave resonator in ghz range. *AIP Advances*, 4:0–11, 2014.

[144] A. C. Ferrari and J. Robertson. Origin of the 1150 cm$^{\{-1\}}$ raman mode in nanocrystalline diamond. *Physical Review B - Condensed Matter and Materials Physics*, 63:2–5, 2001.

[145] Andrea Carlo Ferrari and John Robertson. Raman spectroscopy of amorphous, nanostructured, diamond-like carbon, and nanodiamond. *Philosophical Transactions of the Royal Society A: Mathematical, Physical and Engineering Sciences*, 362:2477–2512, 2004.

[146] Steven Prawer and Robert J. Nemanich. Raman spectroscopy of diamond and doped diamond, 11 2004.

[147] Kourosh Kalantar-Zadeh, Wojtek Woldarski, Yuen Y. Chen, Benjamin N. Fry, and Kosmas Galatsis. Novel love mode surface acoustic wave based immunosensors. *Sensors and Actuators, B: Chemical*, 91:143–147, 2003.

[148] L. Drbohlavová, L. Fekete, V. Bovtun, M. Kempa, A. Taylor, Y. Liu, O. Bou Matar, A. Talbi, and V. Mortet. Love-wave devices with continuous and discrete nanocrystalline diamond coating for biosensing applications. *Sensors and Actuators, A: Physical*, 298, 2019.

[149] Andrew Taylor, František Fendrych, Ladislav Fekete, Jan Vlček, Vladimíra Řezáčová, Václav Petrák, Jaroslav Krucký, Miloš Nesládek, and Michael Liehr. Novel high frequency pulsed mw-linear antenna plasma-chemistry: Routes towards large area, low pressure nanodiamond growth. *Diamond and Related Materials*, 20:613–615, 2011.

[150] R. Lucklum and J. Li. Phononic crystals for liquid sensor applications. *Measurement Science and Technology*, 20, 2009.

[151] H. Alva Medrano, C. Guillén Gallegos, A. Mendoza Suárez, and H. Pérez Aguilar. Calculation of band structures of a phononic crystal within a waveguide in 3d with cubic inclusions using a periodic green's function method. *Journal of Physics: Conference Series*, 1221, 2019.

[152] Yung Yu Chen, Yan Ruei Lin, Tsung Tsong Wu, and Shih Yung Pao. Anchor loss reduction of quartz resonators utilizing phononic crystals. *2015 IEEE International Ultrasonics Symposium, IUS 2015*, pages 10–13, 2015.

[153] Roy H. Olsson, Maryam Ziaei-Moayyed, Bongsang Kim, Charles Reinke, Mehmet F. Su, Patrick Hopkins, Yasser M. Soliman, Drew F. Goettler, Zayd C. Leseman, and Ihab El-Kady. Micro and nano fabricated phononic crystals: Technology and applications. *IEEE International Ultrasonics Symposium, IUS*, pages 983–988, 2011.

[154] Y. Liu, A. Talbi, B. Djafari-Rouhani, E.H. El Boudouti, L. Drbohlavová, V. Mortet, O. Bou Matar, and P. Pernod. Interaction of love waves with coupled cavity modes in a 2d holey phononic crystal. *Physics Letters, Section A: General, Atomic and Solid State Physics*, 383, 2019.

[155] Yuxin Liu, Abdelkrim Talbi, Philippe Pernod, and Olivier Bou Matar. Highly confined love waves modes by defect states in a holey sio 2 /quartz phononic crystal. *Journal of Applied Physics*, 124, 2018.

[156] R. H. Olsson and I. El-Kady. Microfabricated phononic crystal devices and applications. *Measurement Science and Technology*, 20, 2009.

[157] S. Yankin, A. Talbi, Y. Du, J. C. Gerbedoen, V. Preobrazhensky, P. Pernod, and O. Bou Matar. Finite element analysis and experimental study of surface acoustic wave propagation through two-dimensional pillar-based surface phononic crystal. *Journal of Applied Physics*, 115, 2014.

[158] Yu Du. Investigation of micro and nano structured materials for acoustic band gaps engineering in electro-acoustic devices, 2015.

[159] Yuxin Liu. Artificial micro-nano structured materials based phononic crystals for love waves manipulation, 2019.

[160] Ouarda Legrani, Omar Elmazria, Sergei Zhgoon, Philippe Pigeat, and Ausrine Bartasyte. Packageless aln/zno/si structure for saw devices applications. *IEEE Sensors Journal*, 13:487–491, 2013.

[161] Sami Hage-Ali, Omar Elmazria, Gael Pierson, Richard Kouitat, Moise Deroh, Florian Bartoli, Thierry Aubert, and Abdelkrim Talbi. Packageless acoustic wave sensors for wireless body-centric applications. *Proceedings of IEEE Sensors*, 3:18–20, 2017.

[162] K. Bhattacharjee, A. Shvetsov, and S. Zhgoon. Packageless saw devices with isolated layer acoustic waves (ilaw) and waveguiding layer acoustic waves (wlaw). *Proceedings of the IEEE International Frequency Control Symposium and Exposition*, pages 135–140, 2007.

[163] Y. Chinone, S. Ezaki, F. Fujita, and K. Matsumoto. Applications of high purity sic prepared by chemical vapor deposition. pages 198–206. Springer Berlin Heidelberg, 1988.

[164] Andrew Taylor, Jan Drahokoupil, Ladislav Fekete, Ladislav Klimša, Jaromír Kopeček, Adam Purkrt, Zdeněk Remeš, Radim Čtvrtlík, Jan Tomáštík, Otakar Frank, Petr Janíček, Jan Mistrík, and Vincent Mortet. Structural, optical and mechanical properties of thin diamond and silicon carbide layers grown by low pressure microwave linear antenna plasma enhanced chemical vapour deposition. *Diamond and Related Materials*, 69:13–18, 2016.

[165] A. Taylor, L. Klimša, J. Kopeček, Z. Remeš, M. Vronka, R. Čtvrtlík, J. Tomáštík, and V. Mortet. Synthesis and properties of diamond - silicon carbide composite layers. *Journal of Alloys and Compounds*, 800:327–333, 2019.

[166] A. Taylor, L. Klimša, J. Kopeček, Z. Remeš, M. Vronka, R. Čtvrtlík, J. Tomáštík, and V. Mortet. Synthesis and properties of diamond - silicon carbide composite layers. *Journal of Alloys and Compounds*, 800:327–333, 2019.

[167] Carmela Garcia-Doval and Mark J. van Raaij. Structure of the receptor-binding carboxy-terminal domain of bacteriophage t7 tail fibers. *Proceedings of the National Academy of Sciences*, 109:9390–9395, 6 2012.

[168] Mark J. van Raaij, Guy Schoehn, Michel Jaquinod, Keith Ashman, Martin R. Burda, and Stefan Miller. Identification and crystallisation of a heat-and protease-stable fragment of the bacteriophage t4 short tail fibre. *Biological Chemistry*, 382:1049–1055, 7 2001.

[169] Mary D. Roberts, Nancy L. Martin, and Andrew M. Kropinski. The genome and proteome of coliphage t1. *Virology*, 318:245–266, 1 2004.

[170] Joshua A. Bornhorst and Joseph J. Falke. [16] purification of proteins using polyhistidine affinity tags, 2000.

[171] Z. Vlčková Živcová, V. Mortet, A. Taylor, A. Zukal, O. Frank, and L. Kavan. Electrochemical characterization of porous boron-doped diamond prepared using sio2 fiber template. *Diamond and Related Materials*, 87:61–69, 2018.

[172] Mariola Brycht, Simona Baluchová, Andrew Taylor, Vincent Mortet, Silvia Sedláková, Ladislav Klimša, Jaromír Kopeček, and Karolina Schwarzová-Pecková. Comparison of electrochemical performance of various boron-doped diamond electrodes: Dopamine sensing in biomimicking media used for cell cultivation. *Bioelectrochemistry*, 137, 2021.

[173] Julie V. Macpherson. A practical guide to using boron doped diamond in electrochemical research. *Physical Chemistry Chemical Physics*, 17:2935–2949, 2015.

[174] Palaniappan Subramanian, Yannick Coffinier, Doris Steinmüller-Nethl, John Foord, Rabah Boukherroub, and Sabine Szunerits. Diamond nanowires decorated with metallic nanoparticles: A novel electrical interface for the immobilization of histidinylated biomolecuels. *Electrochimica Acta*, 110:4–8, 2013.

[175] Mallikarjunarao Ganesana, Georges Istarnboulie, Jean louis Marty, Thierry Noguer, and Silvana Andreescu. Site-specific immobilization of a ( his ) 6-tagged acetylcholinesterase on nickel nanoparticles for highly sensitive toxicity biosensors. *Biosensors and Bioelectronics*, 30:43–48, 2011.

[176] Quang Thuan Tran, Jacques De Sanoit, Sylvie Pierre, Jean Charles Arnault, and Philippe Bergonzo. Diamond electrodes for trace alpha pollutant sequestration via covalent grafting of nitrilotriacetic acid (nta) ligand. *Electrochimica Acta*, 136:430–434, 2014.

[177] Da Young Lee, Seung Yun Lee, Seung Hyeon Yun, Jae Won Jeong, Jae Hyeon Kim, Hyun Woo Kim, Jung Seok Choi, Gap Don Kim, Seon Tea Joo, Inho Choi, and Sun Jin Hur. Review of the current research on fetal bovine serum and the development of cultured meat, 2022.

[178] O. A. Williams, A. Kriele, J. Hees, M. Wolfer, W. Müller-Sebert, and C. E. Nebel. High young's modulus in ultra thin nanocrystalline diamond. *Chemical Physics Letters*, 495:84–89, 7 2010.

# Appendix A

## Material properties used in simulations

**Quartz LH 1978 IEEE**

Density $\rho = 2651$ kg/m$^3$

Elastic constants in $10^9$ N/m$^2$

$$\left[c^E\right] = \begin{bmatrix} 86.73 & 6.98 & 11.91 & 17.9 & 0 & 0 \\ 6.98 & 86.73 & 11.91 & -17.9 & 0 & 0 \\ 11.91 & 11.91 & 107.19 & 0 & 0 & 0 \\ 17.9 & -17.9 & 0 & 57.94 & 0 & 0 \\ 0 & 0 & 0 & 0 & 57.94 & 17.9 \\ 0 & 0 & 0 & 0 & 17.9 & 39.9 \end{bmatrix} \tag{6.1}$$

Piezoelectric constants in C/m$^2$ and dieletric constants in $10^{-11}$ F/m

$$\left[e\right] = \begin{bmatrix} -0.171 & 0.171 & 0 & -0.04 & 0 & 0 \\ 0 & 0 & 0 & 0 & 0.04 & 0.171 \\ 0 & 0 & 0 & 0 & 0 & 0 \end{bmatrix} \tag{6.2}$$

$$\left[\epsilon^S\right] = \begin{bmatrix} 4.428 & 0 & 0 & \\ & 0 & 4.428 & 0 \\ 0 & 0 & 4.428 & \end{bmatrix} \tag{6.3}$$

**Lithium tantalate**

Density $\rho = 7450$ kg/m$^3$

Elastic constants in $10^{10}$ N/m$^2$

$$\left[c^E\right] = \begin{bmatrix} 23.29 & 4.69 & 8.02 & -1.1 & 0 & 0 \\ 4.69 & 23.29 & 8.02 & 1.1 & 0 & 0 \\ 8.02 & 8.02 & 27.53 & 0 & 0 & 0 \\ -1.1 & 1.1 & 0 & 9.39 & 0 & 0 \\ 0 & 0 & 0 & 0 & 9.39 & -1.1 \\ 0 & 0 & 0 & 0 & -1.1 & 9.3 \end{bmatrix} \tag{6.4}$$

Piezoelectric constants in C/m$^2$ and dieletric constants in $10^{-11}$ F/m

$$\left[e\right] = \begin{bmatrix} 0 & 0 & 0 & 0 & 2.596 & -1.59 \\ -1.59 & 1.59 & 0 & 2.596 & 0 & 0 \\ 0.08 & 0.08 & 1.88 & 0 & 0 & 0 \end{bmatrix} \tag{6.5}$$

$$\left[\epsilon^S\right] = \begin{bmatrix} 40.9 & 0 & 0 \\ 0 & 40.9 & 0 \\ 0 & 0 & 43.3 \end{bmatrix} \tag{6.6}$$

**Lithium niobate**

Density $\rho = 4700$ kg/m$^3$

Elastic constants in $10^9$ N/m$^2$

$$\left[c^E\right] = \begin{bmatrix} 202.9 & 52.9 & 74.92 & 8.998 & 0 & 0 \\ 52.9 & 202.9 & 74.92 & -8.998 & 0 & 0 \\ 74.92 & 74.92 & 243.08 & 0 & 0 & 0 \\ 8.998 & -8.998 & 0 & 59.9 & 0 & 0 \\ 0 & 0 & 0 & 0 & 59.9 & 8.998 \\ 0 & 0 & 0 & 0 & 8.998 & 74.88 \end{bmatrix} \tag{6.7}$$

Piezoelectric constants in C/m$^2$ and dieletric constants in $10^{-11}$ F/m

$$\left[e\right] = \begin{bmatrix} 0 & 0 & 0 & 0 & 3.696 & -2.54 \\ -2.54 & 2.54 & 0 & 3.696 & 0 & 0 \\ 0.19 & 0.19 & 1.3 & 0 & 0 & 0 \end{bmatrix} \tag{6.8}$$

$$\left[\epsilon^S\right] = \begin{bmatrix} 43.6 & 0 & 0 \\ 0 & 43.6 & 0 \\ 0 & 0 & 29.16 \end{bmatrix} \tag{6.9}$$

**Zinc oxide**

Density $\rho = 5680$ kg/m$^3$

Young's modulus $E = 210$ GPa

Elastic constants in $10^{10}$ N/m$^2$

$$\left[c^E\right] = \begin{bmatrix} 20.97 & 12.11 & 10.54 & 0 & 0 & 0 \\ 12.11 & 20.97 & 10.54 & 0 & 0 & 0 \\ 10.54 & 10.54 & 21.12 & 0 & 0 & 0 \\ & 0 & 0 & 0 & 4.24 & 0 & 0 \\ 0 & 0 & 0 & 0 & 4.21 & 0 \\ 0 & 0 & 0 & 0 & 0 & 4.42 \end{bmatrix} \tag{6.10}$$

Piezoelectric constants in C/m$^2$ and dieletric constants in $10^{-11}$ F/m

$$\left[e\right] = \begin{bmatrix} 0 & 0 & 0 & 0 & -0.48 & 0 \\ 0 & 0 & 0 & -0.48 & 0 & 0 \\ -0.57 & -0.57 & 1.32 & 0 & 0 & 0 \end{bmatrix} \tag{6.11}$$

$$\left[\epsilon^S\right] = \begin{bmatrix} 8.54 & 0 & 0 \\ 0 & 8.54 & 0 \\ 0 & 0 & 10.2 \end{bmatrix} \tag{6.12}$$

**Silicon oxide**

Density $\rho = 2200$ kg/m$^3$

Young's modulus $E = 70$ GPa

Relative permittivity $\epsilon_r = 4.2$

**PMMA**

Density $\rho = 1190$ kg/m$^3$

Young's modulus $E = 3$ GPa

Relative permittivity $\epsilon_r = 3$

**Diamond**

Density $\rho = 3515$ kg/m$^3$

Young's modulus $E = 1150$ GPa

Relative permittivity $\epsilon_r = 5.1$

**Silicon carbide**

Density $\rho = 3216$ kg/m$^3$

Young's modulus $E = 748$ GPa

Relative permittivity $\epsilon_r = 9.7$